A Framework for Cyclic Simulation of Thin-Walled Cold-Formed Steel Members in Structural Systems

by
David A. Padilla-Llano

Dissertation submitted to the faculty of the Virginia Polytechnic Institute and State University in partial fulfillment of the requirements for the degree of

Doctor of Philosophy
In
Civil Engineering

Cristopher D. Moen, Chair
Matthew R. Eatherton, Co-Chair
Carin L. Roberts-Wollmann
Roberto T. Leon
Benjamin W. Schafer

May 8, 2015
Blacksburg, VA

Keywords: *Cold-formed steel, Seismic energy dissipation, Hysteretic behavior, Buckling, Thin-walled, Cold-formed steel studs, Cold-formed steel joists.*

A Framework for Cyclic Simulation of Thin-Walled Cold-Formed Steel Members in Structural Systems

David A. Padilla-Llano

ABSTRACT

The objective of this research is to create a computationally efficient seismic analysis framework for cold-formed steel (CFS) framed-buildings supported by hysteretic nonlinear models for CFS members and screw-fastened connections. Design of CFS structures subjected to lateral seismic forces traditionally relies on the strength of subassemblies subjected to lateral loading of systems, such as strapped/sheathed shear walls and diaphragms, to provide adequate protection against collapse. Enabling performance-based seismic design of CFS buildings requires computationally efficient and accurate modeling tools that predict the nonlinear cyclic behavior of CFS buildings, the individual CFS components and connections. Such models should capture the energy dissipation and damage due to buckling and cross-sectional deformations in thin-walled CFS components subjected to cyclic loads such as those induced by earthquakes. Likewise, models for screw-fastened CFS connections should capture the energy dissipation and damage due to tilting, bearing, or screw shear when subjected to cyclic loading.

In this dissertation, an analysis framework for CFS structures that captures the nonlinear cyclic behavior of critical components including axial members, flexural members, and screw fastened connections is presented. A modeling approach to simulate thin-walled behavior in CFS members is introduced where parameters were developed using results from an experimental program that investigated the cyclic behavior and energy dissipation in CFS axial members and flexural members. Energy dissipation and cyclic behavior of CFS members were characterized for members experiencing global, distortional and local buckling. Cyclic behavior and energy dissipation in thin steel plates and members was further investigated through finite element analysis in ABAQUS to provide a strategy for modeling steel columns cyclic behavior including local buckling. Model parameters were developed as generalized functions of the hysteretic energy dissipated and slenderness. The capabilities of the analysis framework are demonstrated through simulations of CFS wood sheathed shear wall cyclic responses validated with experimental results from full scale shear wall tests.

Publications Record

Peer-Reviewed Journal Articles:

(-) **Padilla-Llano, D.**, Moen, C. D., Eatherton, M. R., "A framework for cyclic simulation of thin-walled cold-formed steel members in structural systems." (In progress).

(-) **Padilla-Llano, D.**, Moen, C. D., Eatherton, M. R., "Modeling steel columns axial cyclic response including local buckling deformations." (In progress).

(2) **Padilla-Llano, D.**, Eatherton, M. R., Moen, C. D., "Cyclic flexural response and energy dissipation of cold-formed steel framing members", *Thin-Walled Structures*, (in Review).

(1) **Padilla-Llano, D. A.**, Moen, C. D., Eatherton, M. R., "Cyclic axial response and energy dissipation of cold-formed steel framing members", *Thin-Walled Structures*, 78, 95-107, ISSN 0263-8231, 2014.

Articles in Conference Proceedings:

(12) **Padilla-Llano, D.**, Moen, C. D., Eatherton, M. R., "OpenSees simulation of steel column axial cyclic response including local buckling." Proceedings of the *SSRC Stability Conference*, March 24-27, 2015, Nashville, Tennessee, 2015.

(11) Bian, G., **Padilla-Llano, D.**, Buonopane, S.G., Moen, C.D., Schafer, B.W., "OpenSees modeling of wood sheathed cold-formed steel framed shear walls." Proceedings of the *SSRC Stability Conference*, March 24-27, 2015, Nashville, Tennessee.

(10) **Padilla-Llano, D.**, Moen, C. D., Eatherton, M. R., "Local buckling hysteretic nonlinear models for cold-formed steel axial members." *Proceedings of the 22nd International Specialty Conference on Cold-Formed Steel Structures*, November 2014, St. Louis, Missouri.

(9) Moen, C. D., **Padilla-Llano, D.**, Corner S., Ding C., "Towards load-deformation models for screw-fastened cold-formed steel-to-steel shear connections." *Proceedings of the 22nd International Specialty Conference on Cold-Formed Steel Structures*, November 2014, St. Louis, Missouri.

(8) **Padilla-Llano, D.**, Moen, C. D., Eatherton, M. R., "Cyclic flexural hysteretic models for cold-formed steel seismic simulation." *EuroSteel 2014*, Sept. 2014, Naples, Italy.

(7) Schafer, B. W., Ayhan D., Leng J., Liu P., **Padilla-Llano, D.**, Peterman K., Stehman M., Buonopane S., Eatherton, M. R., Madsen R., Manley B., Moen, C. D., Nakata N., Rogers C., Yu C., "The CFS-NEES Effort: Advancing Cold-Formed Steel Earthquake Engineering." *10th U.S. National Conference on Earthquake Engineering*, July 21-25, 2014, Anchorage, AK.

(6) McAnallen, L., **Padilla-Llano, D.**, Zhao, X., Moen, C. D., Schafer, B. W., Eatherton, M. R., "Initial geometric imperfection measurement and characterization of cold-formed steel C-section structural members with 3D non-contact measurement techniques." *SSRC Stability Conference*, March 2014, Toronto, Canada.

(5) **Padilla-Llano, D.**, Eatherton, M., Moen, C., "Axial Hysteretic Modeling of Cold-Formed Steel Members for Computationally Efficient Seismic Simulation." *Structures Congress 2013*, ASCE, 948–959, (doi: 10.1061/9780784412848.084), 2013.

(4) **Padilla-Llano, D.**, Moen, C.D., Eatherton, M.R., "Cyclic Lateral-Torsional Buckling Response of Cold-Formed Steel C-Section Joists." *SSRC Stability Conference*, April 2013, St. Louis, MO.

(3) **Padilla-Llano, D.**, Moen, C. D. D., Eatherton, M. R., McAnallen L., Bruce T., "Compression-Tension hysteretic response of cold-formed steel C-section framing members." *Proceedings of the 21st International Specialty Conference on Cold-Formed Steel Structures*, October 24-25, 2012, St. Louis, Missouri.

(2) **Padilla-Llano, D.**, Eatherton, M., Moen, C. D., "Cyclic Energy Dissipation of Cold-Formed Steel Structural Studs." *Proceedings of the 15th World Conference on Earthquake Engineering*, September 24-28, 2012, Lisbon, Portugal.

(1) **Padilla-Llano, D.**, Eatherton, M., Moen, C., Bruce, T., and McAnallen, L., "Cyclic Energy Dissipation of Cold-Formed Steel Studs Experiencing Euler Buckling." *Structures Congress 2012*: ASCE, 1518-1528, (doi: 10.1061/9780784412367.135), 2012.

Acknowledgements

I express my sincere gratitude to Dr. Cristopher Moen and Dr. Matthew Eatherton, my advisors for giving me the opportunity to pursue my doctoral research at Virginia Tech, and in a project that involved two of my main topics of interest stability of structures and earthquake engineering. Their support, guidance and friendship has been very valuable in the completion of my studies and during my life in Blacksburg.

I would like to thank my fiancée Holly DeLong for her support, patience and company during the last five years. Her constant support and companionship despite the distance helped me to carry on with my dream. I also would like to thank my siblings Santiago, Samuel and Kelly for their support and sharing this dream. And I deeply thank my father Joaquin who gave me at first all the tools and motivation that I needed to set high goals, keep perseverant and to not desist on pursuing my objectives.

I would like to express my gratitude to Dennis Huffman, Brett Farmer and Dr. David Mokarem at the Thomas M. Murray Structures and Materials Laboratory for their help during the time I spent at the lab conducting my experiments. Also I express gratitude to the many friends that accompanied me during my stay in Blacksburg, especially Jerron Walker, Karen Black, Amber Verma, and Rafic El Helou.

Table of Contents

List of Figures

List of Tables

Chapter 1: Introduction

The objective of this research work is to develop a computationally efficient analysis framework for cold-formed steel (CFS) framed buildings subjected to extreme loading (e.g., seismic loading) supported by hysteretic nonlinear models that can capture the nonlinear cyclic behavior of all the critical components. The steel industry increasing interest on using cold-formed steel for multi-story building construction able to withstand extreme loads such as earthquake induced lateral loads, requires development of analysis tools and guidelines that allow flexibility in modeling and safe design of actual CFS structures. Furthermore, the shift towards performance-based earthquake engineering has created considerable interest in understanding and controlling building seismic performance at different seismic hazard levels. Current analysis and prescriptive design procedures for CFS lateral load-resisting systems (e.g., steel/wood sheathed CFS shear walls and diaphragms), are expected to provide adequate protection against collapse [1], but lack the ability to predict and design for performance levels. These prescriptive procedures provide no information about energy dissipation, strength degradation, and stiffness degradation of these systems and their components (e.g., floor joists, drag struts and boundary chord studs). They also neglect the resistance from other CFS components that are not part of the lateral-load resisting system (e.g., gravity load supporting walls).

To develop seismic performance factors (i.e., R, Ω_0, and C_d) and include different hazard levels in addition to collapse, it is necessary to consider ground motions suites, many ground motion intensities, as well as, different structural layouts [2]. This in turn translates into a sizable number of analyses (i.e., thousands of nonlinear response history analyses) that require computationally efficient and reasonably accurate modeling tools. These tools should allow flexibility on modeling different structural layouts and capture the energy dissipation and the major response characteristics in CFS systems (e.g., shear walls, diaphragms), their components (i.e., studs and joists) and connections subjected to cyclic loading. Developing such models requires characterizing the cyclic behavior and energy dissipation in CFS systems, members and connections through experiments and analysis.

Research efforts to understand seismic behavior of cold-formed steel structures traditionally focus on studies of shear wall response. These include experimental and analytical studies of the most common CFS shear wall configurations used in construction including wood,

steel or gypsum sheathed and steel strapped shear walls (e.g., [3-14]). More recent efforts grouped under the CFS-NEES projects, seek to advance understanding in the seismic behavior of cold-formed steel buildings and the building blocks (e.g., members, connections, shear walls, floor diaphragm) for developing nonlinear models and response history analysis [15]. These projects include shear wall tests [6,7,12,13], characterization of sheathing to steel connections [16,17], characterization of moment-rotation responses including the post-buckling part of the response in CFS flexural members exhibiting local and distortional buckling [18], and the recently completed shake table tests of the full scale CFS-NEES building that was subjected to various ground motions at different stages of construction to evaluate the different structural element contributions to the seismic response [19,20]. Detailed background information pertinent to the research presented in this dissertation is summarized in the corresponding chapters.

Within this framework towards a better understanding of CFS building seismic behavior, there is still a need to expand the knowledge of the behavior at the more basic levels, i.e., member cyclic behavior including buckling deformations, screw-fastened connections behavior, and how they contribute to systems (e.g., shear walls, diaphragms) energy dissipation, and overall building response. Understanding at the member and connection level facilitates consideration of different structural layouts, lateral-force resisting systems, and hazard levels in analysis and design. For example, the cold-formed steel structure in Fig. 1.1 comprises numerous CFS members forming shear walls, floor diaphragms and gravity load carrying walls that during an earthquake are subjected to cyclic axial and flexural loads. The seismic behavior and performance of this building can be assessed using computationally efficient models that account for the behavior of the individual components (i.e., joist, studs, and connections). In Fig. 1.1 for instance, joists, studs and connections can be modeled using nonlinear hysteretic models that are assembled to simulate the cyclic behavior of the whole building. This dissertation introduces a computationally efficient component based analysis framework for cold-formed steel framed buildings supported by nonlinear hysteretic models for CFS members and screw-fastened connections. The proposed analysis framework contributes to advancing performance-based seismic analysis and design of cold-formed steel framed buildings.

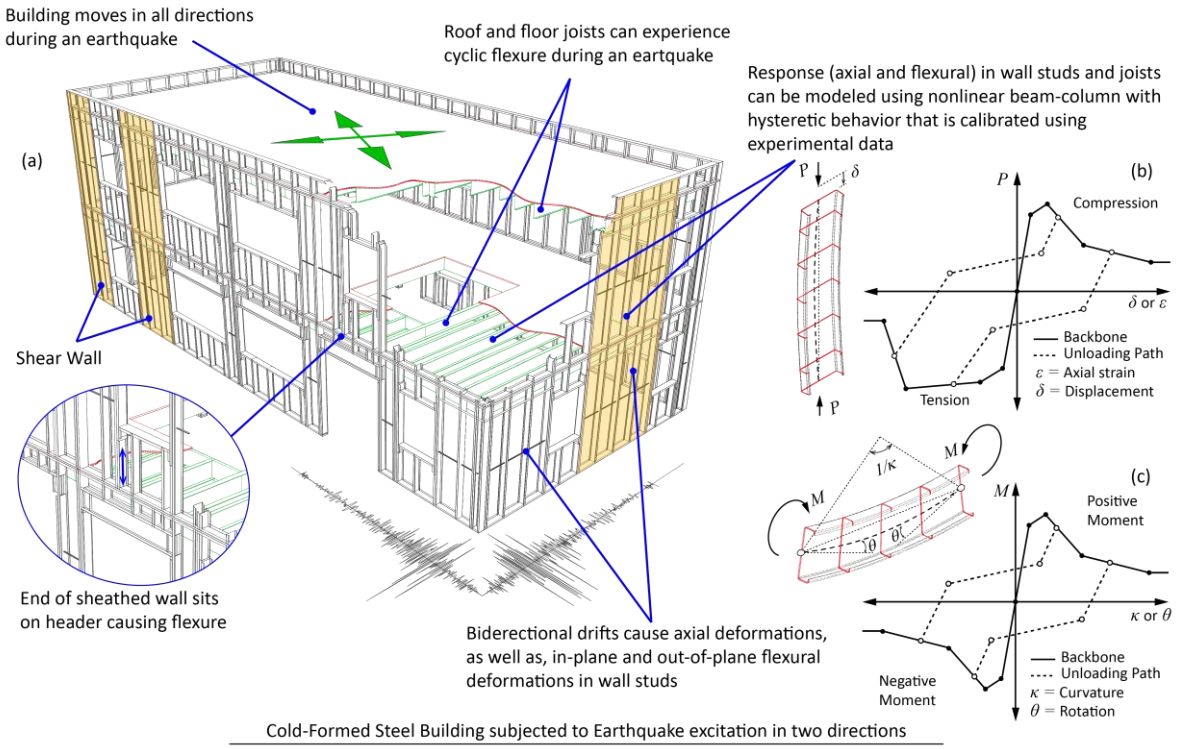

Fig. 1.1. Cold-formed steel framing members experience cyclic axial and flexure forces during earthquake excitations (adapted from CFS-NEES building model [19]) with behavior that can be represented by phenomenological models [21].

Thin-walled cold-formed steel members subjected to compressive stresses are prone to inelastic buckling deformations that reduce stiffness and affect their post-peak strength behavior. When subjected to cyclic loading, buckling deformations reverse and combine with yielding strains in tension at the highly stressed locations. Energy dissipates through accumulation of these inelastic strains that can lead to fracture and tearing of the material (see Fig. 1.2).

The types of buckling deformations experienced by thin-walled members are different depending on the geometry and elastic buckling properties. For common cold-formed steel members the AISI Direct Strength Method (DSM) [22] identifies three types of buckling limit states: global (Fig. 1.2a and 1.2d), distortional (Fig. 1.2b and 1.2e), and local buckling (Fig. 1.2c and 1.2f). Depending on which of these limit states governs, the distribution (or concentration) of inelastic strains as well as cyclic strength and stiffness deterioration may vary. For example Fig. 1.2a shows inelastic strains due to buckling of the stiffening lips in a CFS stud experiencing global buckling while Fig. 1.2f shows inelastic strains concentration from local buckling in the web of a CFS joist subjected to uniform bending. Characterizing the relationship between the different types

of buckling deformations and the cyclic behavior is one of the objectives of this research towards providing the analytical tools for the seismic analysis framework for CFS structures.

Fig. 1.2. Cold-formed steel member failure modes: (a) global buckling in axial member; (b) distortional buckling in axial member; (c) local buckling in axial member; (d) global buckling in flexural member; (e) distortional buckling in flexural members; (f) local buckling.

Two approaches are introduced in this dissertation to model the cyclic response of cold-formed steel axial and flexural members experiencing local, distortional and global buckling deformations: a *nonlinear spring* model with concentrated nonlinear *axial load-displacement* (P-δ) or *moment-rotation* (M-θ) behavior, and a *nonlinear beam-column* with distributed nonlinear section *axial load-strain* (P-ε) or *moment-curvature* M-κ behavior. Model parameters are derived as functions of the hysteretic energy dissipated, unbraced length, and member elastic buckling properties. These models are then used together with a nonlinear spring model for screw-fastened connections to illustrate the capabilities of simulation framework.

The research progression starts with Chapter 2 studying the energy dissipation in thin plates subjected to axial and flexural cyclic loading. The study provides insight on the cyclic behavior of thin-walled cross-section elements, such as webs and stiffened elements. The effects of slenderness, imperfections, and loaded end boundary conditions on the cyclic response and energy dissipation are explored through nonlinear finite element modeling in ABAQUS [23]. Chapter 3 and 4 describe the results from an experimental program that investigated the cyclic behavior of cold-formed steel axial and flexural members experiencing local, distortional and global buckling deformations. Chapter 5 describes the axial and flexural cyclic response characterization including strength and stiffness degradation as well as pinching behavior. Chapter 6 describes a framework to model cyclic behavior in thin-walled cold-formed steel axial and flexural members. The approach for CFS members described in Chapter 6 is specialized in Chapter 7 to model the axial cyclic behavior in steel columns including local buckling. The library *asymPinching* is implemented for OpenSees [24] or MATLAB [25] that allows for the approximate simulation of local buckling in cyclic frame-type analyses. This research concludes in Chapter 8 demonstrating the potential of the nonlinear *asymPinching* model for CFS members in the analysis of CFS shear walls that are validated against experimental responses of wood-sheathed shear walls used in the CFS-NEES building [19,20] tested at the University of North Texas [12,13]. Summaries of literature pertinent to the research presented in this dissertation are summarized in the corresponding chapters as needed.

Additional information that supplements the work in this research is supplied in the appendices. Appendix A describes the background and reasoning for developing the displacement-controlled loading protocol for cyclic testing of cold-formed steel members. Appendix B includes the test setup drawings for both axial and flexural tests. Summaries of the experimental results for

each of the members tested are included in Appendix C and Appendix D. In Appendix E a member imperfections study is described using contact and non-contact measuring techniques that was presented as a conference paper at the SSRC 2014 Stability Conference [26]. Finally the MATLAB version code for the *asymPinching* is provided in Appendix F. Fundamental studies on thin-walled steel cyclic behavior begin in the following chapter.

Chapter 2: Cyclic Behavior and Energy Dissipation in Cold-Formed Steel Thin-Walled Members

In this chapter, cyclic behavior and energy dissipation in thin steel plates are studied through nonlinear finite element modeling to explore answers to the research questions: 1) *What are the energy dissipation mechanisms in cold-formed steel members?* and 2) *How do damage and inelastic strains accumulate during cyclic loading?*. The results from this study provide insights into the cyclic behavior of thin-walled cross-section elements (e.g., webs and stiffened elements) subjected to stresses from axial and flexural loading.

Thin-walled cold-formed steel members subjected to compressive stresses experience buckling deformations that will reduce their stiffness and affect the post-peak behavior. As the applied compressive stresses increase, these buckling deformations appear and their effects translate to the axial load-deformation curve by changes in stiffness and peak-strength values. For example, Fig. 2.2 compares the response of two axially loaded studs with fixed ends subjected on the top to a displacement δ. This figure shows that the more slender member (λ_ℓ =2.04) shows larger buckling deformations that translate into smaller pre-peak stiffness (segment *a*-*b* vs. segment *d*-*e*) and peak strength compared to the less slender stud, λ_ℓ =1.14, [$\lambda_\ell = (P_y/P_{cr\ell})^{0.5}$, $P_y = AF_y$, F_y=yield stress, A=cross-section area, $P_{cr\ell}$=local buckling load]. Depending on the elastic buckling properties and yield stress, these buckling deformations will be reversible (i.e., elastic) or will include permanent plastic strains. As the member reaches its maximum strength, inelastic deformations spread across the mid-height cross-section so that the response beyond this point softens with a gradually decreasing negative stiffness and inelasticity spreading along the member (see *b*, *e*, *c*, and *f* in Fig. 2.2). Whether the post peak strength decreases more or less gradually depends on the properties (slenderness) of the member as illustrated in Fig. 2.2. The drop in strength from peak strength (20% drop) is steeper for the less slender member (point *b* to *c*) compared to the more slender member (point *e* to *f*).

Similar behavior can be observed in thin-walled members subjected to cyclic loading. Buckling deformations appear as compressive stresses are applied and inelastic strains accumulate around the buckled cross-section. When the loading direction reverses, more inelastic strains accumulate at the buckled cross-sections which translate into strength and stiffness reduction in the subsequent cycles as shown in Fig. 2.3. The amount of inelastic strains that accumulate, or

more precisely the damage accumulated along the member length, translates into hysteretic energy dissipated.

The hysteretic energy dissipated can be equated to the work done by the applied loads/moments using the concept of energy balance in a structural member [27]. The energy input by external loading in a member (see, Fig. 2.1) can be equated to the sum of the kinetic energy $E_{kinetic}$, energy dissipated by additional damping or friction $E_{damping}$, and the energy dissipated by deformation of the components E_{deform}, as shown in Eq. 2.1. If additional damping is not provided and friction is neglected the corresponding term $E_{damping}$ can be dropped from Eq. 2.1. Since in the research discussed herein members are loaded in a quasi-static manner, the kinetic energy term $E_{kinetic}$ is also neglected. The remaining energy term E_{deform} can be separated in two components, the recoverable elastic strain energy E_{strain} and the hysteretic energy dissipated $E_{hysteretic}$. The input energy is equal to the work done by the external loads/moments applied to the structure (W_{ext}), which is calculated as the area enclosed by the load-deformation response, see Fig. 2.1. The hysteretic energy dissipated is approximated by equating it to the input energy, and thus it becomes the area enclosed by the load-deformation response. This approach is adopted throughout this dissertation to calculate the energy dissipated within a CFS member during cyclic loading.

$$E_{input} = E_{kinetic} + E_{damping} + E_{deform} \qquad 2.1$$

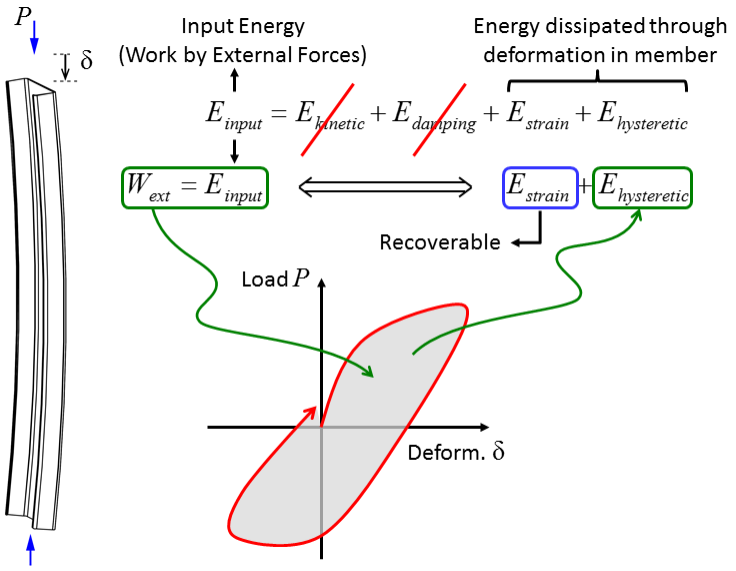

Fig. 2.1. Energy dissipated within the member is equated to the work done by external loads.

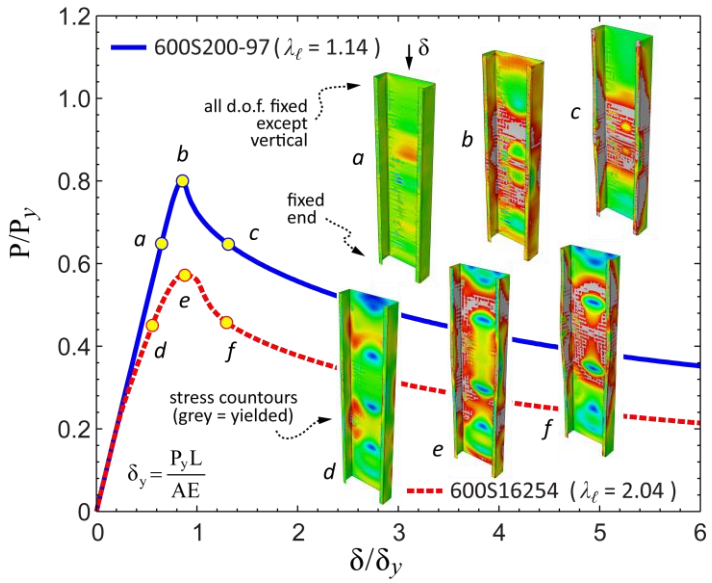

Fig. 2.2. Monotonic axial load-deformation (*P*-*δ*) response where the more slender member experiences larger buckling deformations which translate in smaller pre-peak stiffness (segment *a*-*b* vs. segment *d*-*e*) and peak strength.

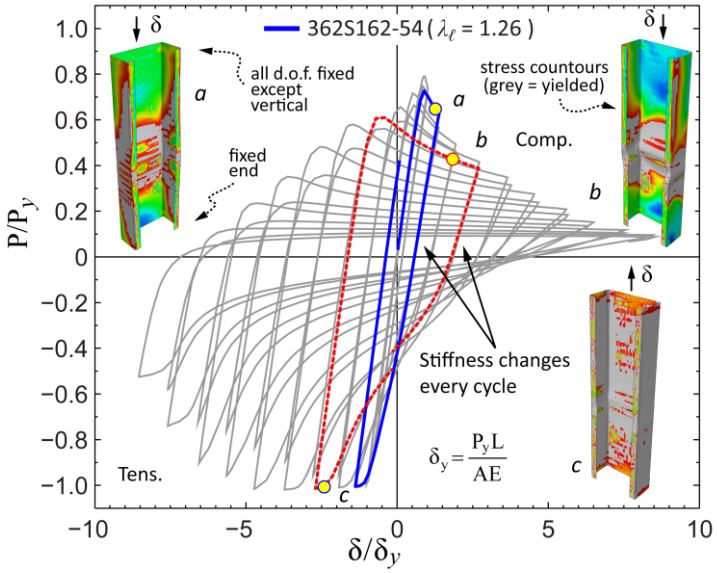

Fig. 2.3. Cyclic load deformation response. Inelasticity accumulates around the mid-span due to buckling deformations and yielding in tension.

The amount of energy dissipation can vary depending on the elastic buckling properties of the thin-walled members but also on the boundary conditions at the end of the members. The following two sections describe an analytical study of the cyclic behavior of thin steel plates subjected to stresses from axial and flexural loading. The study explores initial answers to the questions formulated at the beginning of this chapter and provided insight into how energy

dissipates and how damage accumulates in CFS cross-section elements (e.g., webs and stiffened elements) during cyclic loading.

2.1 Cyclic behavior and energy dissipation in thin steel plates

Cyclic behavior and energy dissipation in thin steel plates subjected to in-plane axial and flexural loading was studied through finite element analyses in ABAQUS [23]. The models are implemented using S9R5 thin shell elements for two sets of plates summarized in Table 2.1. The S9R5 shell element is a nine node, doubly-curved, reduced integration, quadratic element with five degrees of freedom per node, flexible shear strain definition, and numerically imposed Kirchhoff constraints (classical plate theory with no transverse shear deformation) [23]. Two widths (h) to thickness (t) ratios were selected with values matching the flat web width and thickness of common CFS channels. Plate lengths were selected as multiples of the buckled half-wavelength L_{cr}.

Two boundary condition cases for the loaded edges are considered to simulate pinned and fixed end conditions as shown in Fig. 2.4. In the pinned end condition, the translational degrees of freedom at the loaded edges are constrained to move as a rigid body while rotations at each node are unconstrained. For the fixed end condition, all degrees of freedom at the loaded edges are constrained to move as a rigid body. The out of plane displacement (*2 direction*) around all edges is restrained while free to move in the 1 and 3 directions, and free to rotate about direction 3. Initial geometric imperfections are imposed based on the lowest elastic buckling mode (see Fig. 2.6a and 2.6c) with magnitudes d_0/t=0.17 and d_0/t=0.54 (d_0=imperfection magnitude). These magnitudes respectively correspond to occurrence probabilities $P(d<d_0)$=0.25 and $P(d<d_0)$=0.75 that the actual imperfection, d, will be less than d_0 [28,29]. The geometry and boundary conditions are summarized in Fig. 2.4.

The elastic modulus of elasticity was assumed as E=203.4GPa and Poisson's ratio ν=0.3. Material nonlinearity was implemented using two true stress-strain (σ-ε) curves (Fig. 2.5) and isotropic hardening behavior. The stress-strain curves correspond to actual measured stress-strain curves from cold-formed steel tension coupon tests of the selected thicknesses. The plates are loaded from both ends by imposing a displacement or rotation history using the cyclic loading protocol for cold-formed steel members described in Appendix A. The protocol is symmetric with steps of increasing amplitude and two cycles per step. Each step's amplitude is 40% larger than the previous (i.e., δ_i=1.4δ_{i-1} and θ_i=1.4 θ_{i-1}). The protocol is anchored at the fourth step to the

elastic displacement $\delta_e=(0.673)^2P_{cr}L/AE$ for uniform axial loading where P_{cr} is the elastic plate buckling load and $A=th$ the plate cross section area (see Table 2.1). For the in-plane bending case (i.e., stress gradient) the protocol is anchored at the fourth step to the elastic rotation $\theta_e=(0.673)^2M_{cr}L/2EI$ where M_{cr} is the elastic plate buckling moment and $I= ht^3/12$, is the plate cross-section moment of inertia. Energy dissipated, equated herein to external work done by the axial force in the direction of the applied displacement/rotation (or strain energy), will be compared between models for every cycle, and total length, half-wave length, plate slenderness effects will be discussed.

Table 2.1. Cold-formed steel thin plate analysis matrix.

Model[a]	t (mm)	h (mm)	L_{cr} (mm)	L	F_y (MPa)	P_{cr}[b] (kN)	M_{cr}[b] (kN-mm)
P60-33-i##-A	0.879	147	147	1, 2, 3, ... 10 times L_{cr},	334	3.24	-
P36-54-i##-A	1.367	85	85	305 and 2740mm	398	20.95	-
P120-97-i##-F	2.583	292	168	1, 2, 3, ... 10 times L_{cr},	422	-	13005
P100-33-i##-F	0.879	248	188	1625 and 3048mm	410	-	514

(a) i## = imperfection magnitude (i25:$d_0=0.17t$; i75: $d_0=0.54t$) [28], A = Axial, F = Flexural.
(b) Plate buckling load/moment

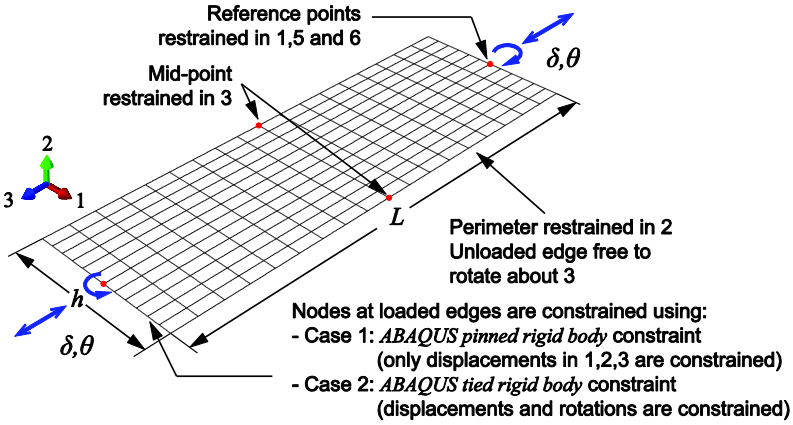

Fig. 2.4. Plate model geometry and boundary conditions.

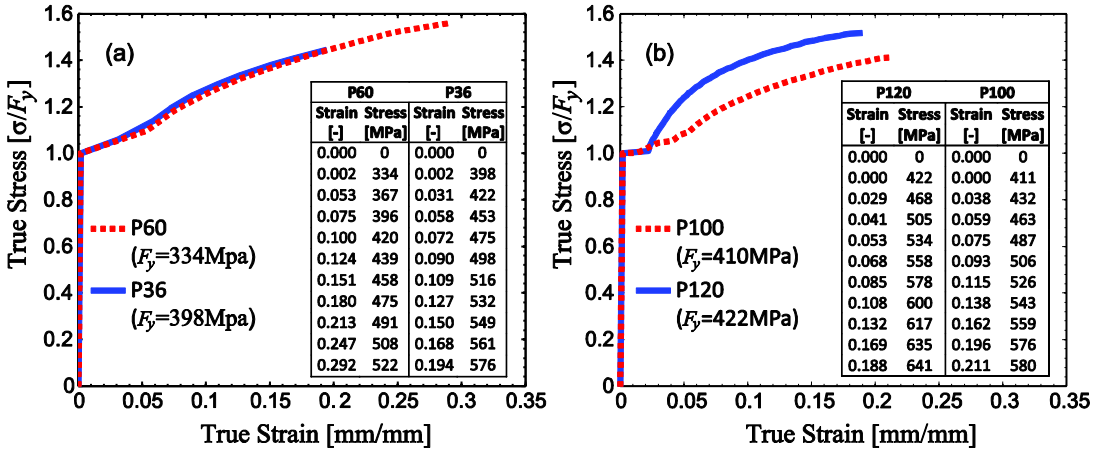

Fig. 2.5. True stress-strain curves assumed for plate models (a) in compression; and (b) in bending.

2.1.1 Cyclic axial behavior in thin plates

The axial cyclic responses obtained show elastic behavior for all cycles before reaching the peak compression load. At the peak compression load, energy dissipation starts as plastic strains concentrate at one or more locations leading to full cross-section and plate collapse (i.e., no load carrying capacity either in compression or tension). Damage accumulated in these zones that are approximately one half-wave (L_{cr}) long for all the plates analyzed irrespective of the plate length and generally happened at the mid-length (see, Fig. 2.6b). Only in four plates, corresponding to the longer plates with ratio h/t=62.12, fixed ends (case 2 in Fig. 2.4), and symmetric imposed imperfection patterns, the damaged zones happened closer to the loaded ends as shown in Fig. 2.6d. Energy dissipation occurs through plastic deformation at the damaged zones.

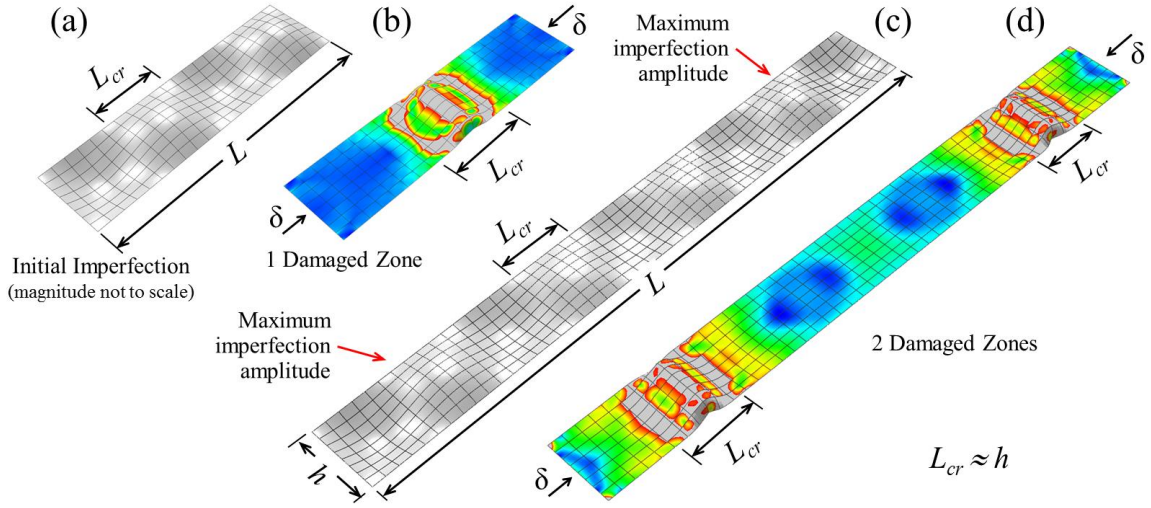

Fig. 2.6. Initial imperfection shape and damaged zone relationship in plates subjected to cyclic axial load.

Cumulative energy dissipation is compared in Fig. 2.7 for all lengths and for the two imperfection magnitudes considered. The energy dissipated was normalized to $P_y\delta_{cr}$ ($P_y=AF_y$, $\delta_{cr}=P_yL_{cr}/AE$, $A=th$) and plotted as a function of the cumulative post-peak applied displacement divided by the half-wave length $\Sigma(\delta/L_{cr})$. It can be seen that all the curves are grouped and therefore energy dissipation is independent of the plate length and is confined to a damaged zone that extends approximately one half-wave length L_{cr}. In the four long plates (L=849mm and 2743mm) that exhibited two damaged zones close to the loaded edges as shown in Fig. 2.6d, the amount of energy dissipation was about twice as much the plates that exhibited only one damaged zone (see Fig. 2.7b). Thus, the amount of energy dissipated is proportional to the number of

damaged zones developed in the plate (i.e., zones with concentration of plastic strains). The presence of two damaged zones is related to the initial geometric imperfection field imposed to the plates. The imperfection field imposed to the long plates (i.e., lowest buckling mode) presents maximum amplitudes towards the loaded edges encouraging larger strains at that locations. The magnitude of the imperfection (i.e., d_0/t=0.17 and d_0/t=0.54) has no effect on the amount of energy dissipated or location of the damage zone. The effect from the different boundary conditions is almost negligible for both plate groups because damaged accumulated at least one half-wave length away from the loaded edges.

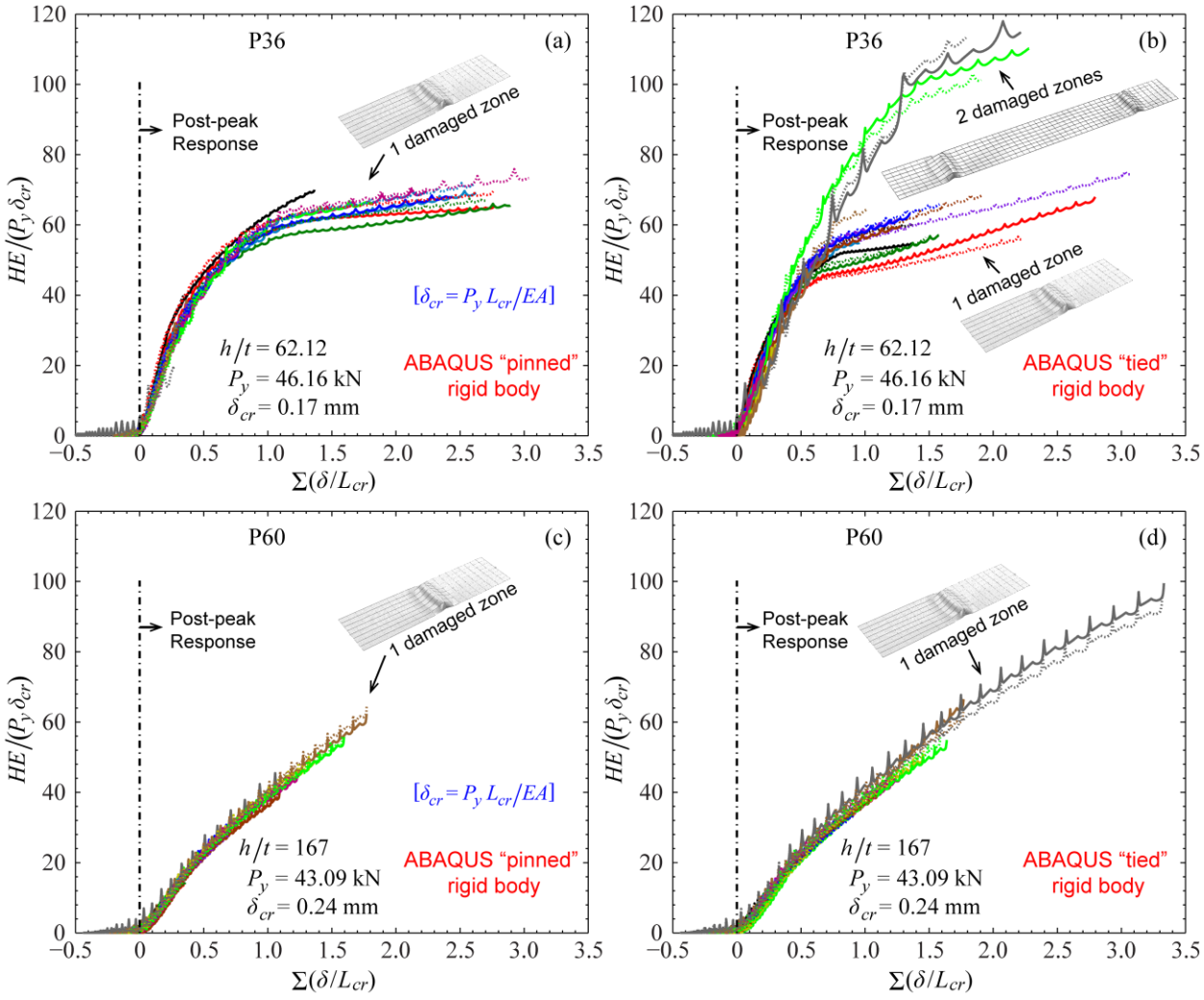

Fig. 2.7. Cumulative hysteretic energy (*HE*) dissipated in cyclic axially loaded thin plates of various lengths: (a) width *h*=85mm pinned ends; (b) width *h*=85mm tied ends; (c) width *h*=147mm pinned ends; (d) width *h*=147mm tied ends (see Table 2.1).

2.1.2 Cyclic flexural behavior in thin plates

The flexural responses obtained were mostly elastic in all cycles before reaching the peak moment. After peak moment, buckling inelastic deformations appear due to compressive stresses and energy dissipates as plastic strains extend at more than one location along the plates. Inelastic strains appear first on the side of the plate that is in compression right after peak moment and when the load direction reverses, inelastic strains may appear right at the opposite side (Fig. 2.8b) or at some other location due to redistribution of stresses (Fig. 2.8e). Damage accumulates in these zones that can extend a length less or equal to the buckled half-wavelength (L_{cr}) irrespective of the plate length. All plates in series P100 showed two damaged zones (Fig. 2.8c) while plates in series P120 showed one (Fig. 2.8b), two (Fig. 2.8c) and three damage zones (Fig. 2.8e) as the length of the plate increased as shown in Fig. 2.9. Energy dissipation occurs through plastic deformation at the damaged zones.

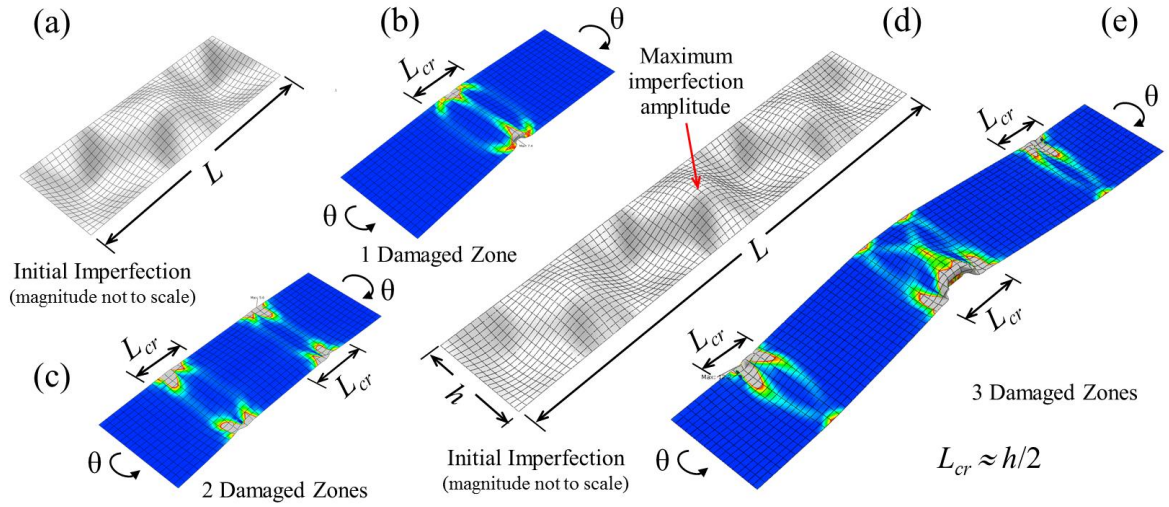

Fig. 2.8. Initial imperfection shape and damaged zone relationship in plates subjected to cyclic flexure.

Cumulative energy dissipation is compared in Fig. 2.9 for all lengths and for the two imperfection magnitudes considered. The energy dissipated was normalized to $M_y\theta_{ycr}$ ($M_y=SF_y$, $\theta_{ycr}=M_yL_{cr}/2EI$, $I=th^3/12$, $S=2I/h$) and plotted as a function of the cumulative post-peak applied rotation divided by the rotation θ_{ycr} $\Sigma(\theta/\theta_{ycr})$. The rotation θ_{ycr} at the end of a plate of length L_{cr} due to a moment M_y. In Fig. 2.9a is shown that all the curves in series P100 are grouped together and that the number of damaged zones (two) is the same for all the plates. Thus, energy dissipation is independent of the plate length and is confined to the two damaged zones that extend each approximately a half-wave length L_{cr}. As the number of damaged zones increases due to stress

redistribution, more sections of the plate accumulate inelastic strains and thus the amount of energy dissipated increases. The cumulative energy dissipated is proportional to the number of damaged zones where plates exhibiting two damaged zones dissipated about twice the energy of those in which only one damaged zone occurred.

There is not an observed relationship as to what triggers the formation of more than one damaged zone on the analyzed plates. The plates are subjected to uniform bending right before peak moment, and theoretically maximum compressive stresses are the same along the farthest fiber. Thus, the likelihood that a damaged zone appears is the same for any cross-section along the plate and it only increases if the magnitude of the imperfection at such cross-section is bigger than in adjacent cross-sections. Once inelasticity starts accumulating at one of the damaged zones other damaged zones are less likely to appear on the same side (see Fig. 2.8e) unless plastic strains have spread across the cross-section full depth. The magnitude of the imperfection (i.e., d_0/t=0.17 and d_0/t=0.54) had no effect on the amount of energy dissipated or location of the damage zone.

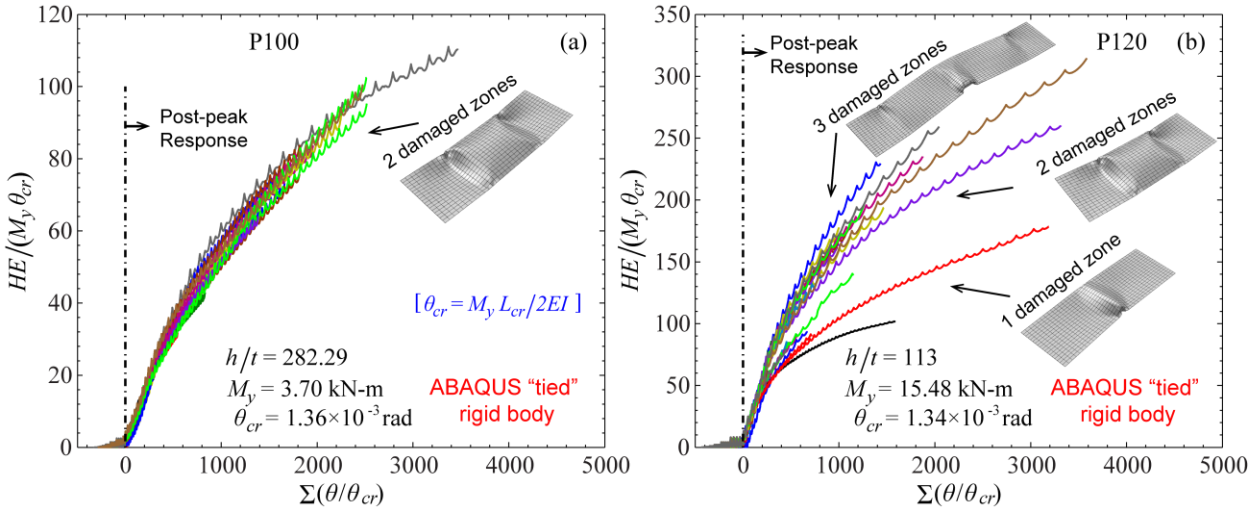

Fig. 2.9. Cumulative hysteretic energy (*HE*) dissipated in thin plates of various lengths subjected to cyclic bending load: (a) width *h*=248mm tied ends; (b) width *h*=292mm tied ends (see Table 2.1).

2.2 Remarks on the cyclic behavior of thin steel plates and cold-formed steel members

The previous sections showed that energy dissipation is independent of the plate length and that it occurs through accumulation of plastic deformations at localized damaged zones. Also they showed that damaged zones are confined to areas of approximately one half-wave long and that multiple damaged zones may occur either because of the initial imperfection's shape or stress redistribution (e.g., case of flexural stresses). These results provide insights into the cyclic behavior

and energy dissipation in thin-walled cross-section elements, such as webs and stiffened elements. For example, the behavior illustrated in Fig. 2.8e is similar to the behavior exhibited by the top flange of the cold-formed steel member experiencing lateral-torsional buckling in Fig. 1.2d. Likewise, the web buckling deformations in Fig. 1.2d can be compared to the behavior shown in Fig. 2.8b. In the next two sections an experimental program that investigated the cyclic behavior and energy dissipation in cold-formed steel axial and flexural members (studs and joists) is summarized.

Chapter 3: Cyclic and Monotonic Experiments on Cold-Formed Steel Axial Members [1]

This chapter summarizes results from an experimental program that investigated the cyclic axial behavior and energy dissipation of cold-formed steel structural framing members experiencing local, distortional and global buckling. Twelve cyclic axial tests, twelve monotonic axial tests in compression, and two monotonic axial tests in tension, were conducted on common CFS C-section studs without perforations. Cross-section dimensions and specimen length are varied to isolate specific buckling modes (i.e., local, distortional or global buckling), and a loading protocol adapted from FEMA 461 [30] is employed where the target displacements are calculated using the member elastic buckling properties. Local and global buckling slenderness are key parameters influencing energy dissipation of thin-walled steel components, and these trends are explored in a review of existing literature in the next section.

3.1 Background - Cyclic response of axial members including buckling

Existing cyclic axial tests focused on hot-rolled steel structural sections used for steel-framed buildings and offshore oil platforms. The cyclic axial behavior of globally slender steel members (struts, braces) was studied starting in the early 1970s, both analytically and with experimental programs. Hysteretic load-deformation response models for columns experiencing a plastic hinge were developed for finite element models [31-34]. Some of the models included cross-sectional slenderness as a softening parameter [35,36]. The analytical models were combined with experimental data in a few cases to develop semi-empirical equations that predict bracing member fracture life, i.e., the number of cycles to tensile fracture [37].

The viability of these numerical models was established by experiments on structural sections ranging from solid steel bars [31] to hollow thin-walled tubes [38], W-sections [39], and angles [40]. A few experiments even considered the influence of cold-bending on energy dissipation [41]. These studies have shown that, inelastic elongation of the members during tensile excursions occurred in a relatively predictable manner [31,39,40]; that tension strength remained fairly constant during inelastic cycles, but compression strength degraded with the number of

---

[1] This work is published in *Thin-Walled Structures Journal, Vol 78 (2014), 95-107*, with the title "**Cyclic Axial Response and Energy Dissipation of Cold-Formed Steel Framing Members"** (http://dx.doi.org/10.1016/j.tws.2013.12.011).

cycles (implying damage accumulation in compression) [38-40]; when local buckling accompanied global deformation, the member failure mode was typically tensile fracture caused by stress concentrations at a fold [38]; that inelastic deformation of the steel was the key contributor to energy dissipation as compared to inherent material damping [40]; that the total energy dissipation appears to be independent of initial loading direction (tension then compression or compression and then tension) [40]; and, that the amount of total hysteretic energy dissipated decreases as the global slenderness increases [38,40].

Only a few experimental programs focused on energy dissipation from local buckling [42-45]. These studies showed that local buckling compression strength degraded to a constant magnitude with increasing cycles because of inherent post-buckling capacity, which is different and potentially more beneficial to seismic performance than global buckling cyclic behavior where compressive strength decreases to zero as the plastic hinge develops. The experimental program described below explores these post-buckling benefits and documents the cyclic behavior of CFS axial members with a focus on thin-walled member buckling limit states, i.e., global, distortional and local buckling.

3.2 Experimental program

An experimental program was conducted to study the cyclic response of CFS axial members experiencing local, distortional and global buckling. Cyclic tests were conducted to determine the effects of reversed cyclic loading (i.e., tension and compression) and cumulative axial deformation on damage and hysteretic energy dissipation of members experiencing global, distortional or local buckling. Monotonic tests were performed to establish a load-deformation envelope for comparison to the cyclic test response.

3.2.1 Specimen selection strategy

Specimens were selected such that their predicted monotonic capacity in compression is governed either by local, distortional or global buckling as predicted by the American Iron and Steel Institute (AISI) Direct Strength Method (AISI-S100-12, [22]). The cross-sections considered, five (5) in total with web widths of 92mm and 152mm and nominal thicknesses ranging from 0.88 to 2.58mm, were chosen from standard sizes as listed in the Structural Stud Manufacturers Association (SSMA) catalog [46]. Cross-section dimensions and length (L) varied to isolate each buckling limit state. Global buckling specimens have a length L=2286mm, while

for distortional buckling tests L=610mm and for local buckling L=305mm. The test program included two specimens subjected to quasi-static cyclic displacement and two specimens subjected to monotonic displacement (in compression) per specimen type. Two monotonic tests in tension were included to define the representative tension side load-deformation envelope. Specimen nomenclature is explained in Fig. 3.1a.

3.2.2 Specimen dimensions, material properties and elastic buckling loads

Cross-section dimensions were measured at member mid-height using methods described in [47], see Table 3.1 and Fig. 3.1b. These values were input to the finite strip eigen-buckling analysis software CUFSM [48] to calculate the elastic buckling loads for local buckling, $P_{cr\ell}$, distortional buckling, P_{crd}, and global buckling, P_{cre}, and the associated half-wavelengths ($L_{cr\ell}$, L_{crd}, and L_{cre} respectively). Boundary conditions were assumed to be warping fixed (i.e., fixed-fixed) when calculating the elastic buckling loads, i.e., an effective length of 0.5L is considered when calculating P_{cre}. In addition, P_{crd} was calculated including the effects of warping-fixed ends [47] and considering the increase in P_{crd} when L_{crd} is longer than the total member length [22].

The tension yield load, P_y, was determined using the measured cross-section area and the average yield stress F_y obtained from three coupon tests per specimen. Coupon tests were conducted in accordance with ASTM E8M-04 [49] with one coupon taken from each flange and web flat. The monotonic compression capacity, P_n, was calculated using the AISI-S100-12 Direct Strength Method [22]. These values are summarized in Table 3.2.

3.2.3 Test setup and instrumentation

A uniaxial loading frame was assembled to perform the cyclic tests (see Fig. 3.2). End plates were welded to both ends of the specimens to transfer axial forces while providing rotation fixed, twist fixed, and longitudinal warping fixed end boundary conditions. Specimen axial deformations were measured using two LVDTs connected between the top and bottom end plates as shown on the right inset of Fig. 3.2. Specimens were subjected to a cyclic displacement history at a constant displacement rate of 0.008(mm/mm)/(min). Based on previous monotonic tension coupon tests, it is expected that this displacement rate will produce yield stresses approximately 2% larger than the static yield stress while minimizing strain-rate related effects [50]. The displacement rate for the monotonic tests was set to 0.0001(mm/mm)/(min), which corresponds to

the maximum rate of 21MPa per minute recommended in the AISI-S910-08 test method for column distortional buckling [51].

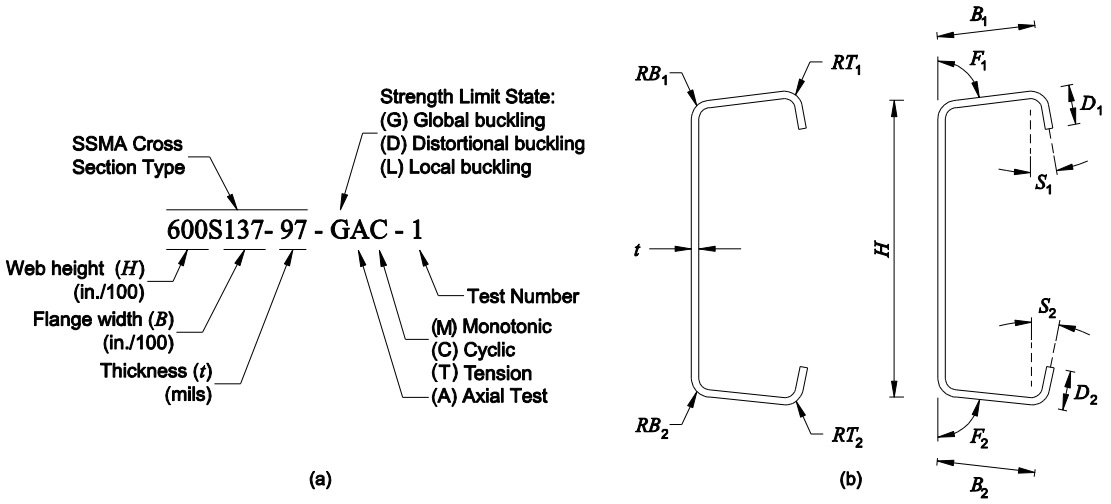

Fig. 3.1. Specimen naming notation (a); and cross-section dimension (b).

Table 3.1. Measured specimen dimensions.

Specimen	L	A_g	D_1	D_2	B_1	B_2	H	RT_1	RB_1	RT_2	RB_2	F_1	F_2	S_1	S_2	t
	(mm)	(mm^2)					(mm)						(°)			(mm)
600S137-97-GAM-1	2286	631	19.1	17.3	36.2	35.8	152.7	5.2	5.8	4.8	5.2	84.1	89.3	1.7	1.6	2.59
600S137-97-GAM-2	2286	632	19.1	17.5	36.1	35.7	152.2	5.0	6.0	4.8	5.2	83.8	87.9	1.6	1.9	2.60
600S137-97-GAC-1	2286	634	17.6	19.5	35.8	36.0	152.1	4.8	5.6	4.8	5.4	87.6	84.3	1.0	1.4	2.60
600S137-97-GAC-2	2286	629	17.6	18.9	35.6	35.9	152.5	4.8	5.2	5.2	6.0	87.6	85.1	3.1	2.0	2.58
362S137-68-GAM-1	2286	315	11.6	13.4	34.5	33.5	93.3	4.0	4.0	4.4	4.4	88.4	87.6	-2.5	4.8	1.82
362S137-68-GAM-2	2286	316	11.7	13.5	34.5	33.3	93.2	4.0	3.8	4.4	4.4	86.6	87.8	-3.5	3.6	1.82
362S137-68-GAC-1	2286	315	11.8	13.3	34.4	33.6	93.3	4.0	4.0	4.4	4.4	86.6	88.1	-2.0	3.4	1.82
362S137-68-GAC-2	2286	315	11.8	13.3	34.4	33.4	93.3	4.0	4.0	4.4	4.4	88.5	88.2	-2.5	4.1	1.82
600S137-68-DAM-1	610	416	10.9	11.5	34.8	33.8	152.7	4.0	3.6	4.4	4.2	90.5	88.6	-1.5	0.6	1.80
600S137-68-DAM-2	610	415	10.7	11.5	34.8	33.8	152.7	4.0	4.0	4.4	4.0	90.5	89.5	-1.4	-0.7	1.80
600S137-68-DAC-1	610	416	10.8	11.3	34.4	34.2	152.7	4.0	4.0	4.2	4.0	91.9	88.1	-1.1	5.0	1.80
600S137-68-DAC-2	610	415	10.5	11.9	34.9	33.8	152.5	4.0	4.0	4.4	4.2	89.9	89.6	-1.1	-0.1	1.80
362S137-68-DAM-1	610	318	11.9	13.4	34.8	33.5	94.0	4.0	4.0	4.4	4.4	88.8	86.9	-4.7	5.4	1.82
362S137-68-DAM-2	610	317	12.0	12.9	34.5	33.9	93.3	4.0	4.0	4.4	4.4	89.8	86.4	-2.0	4.2	1.82
362S137-68-DAC-1	610	313	11.5	13.2	34.5	33.5	93.2	4.0	4.0	4.4	4.4	87.6	88.1	-2.3	4.1	1.81
362S137-68-DAC-2	610	314	11.6	13.4	34.4	33.9	93.2	4.0	4.0	4.4	4.4	89.7	86.2	-2.1	4.0	1.81
600S162-33-LAM-1	305	215	12.9	13.6	42.1	41.7	149.9	3.6	4.2	3.4	4.4	84.4	90.7	5.2	1.6	0.86
600S162-33-LAM-2	305	215	13.0	13.5	42.0	41.5	150.3	3.6	4.0	3.6	4.4	88.1	91.9	2.0	-0.2	0.86
600S162-33-LAC-1	305	215	12.7	13.6	41.9	41.7	150.6	3.6	4.0	3.6	4.4	84.6	91.1	6.0	1.5	0.86
600S162-33-LAC-2	305	215	12.7	13.6	41.9	41.5	150.3	3.6	4.0	3.2	4.4	86.6	89.1	3.1	3.6	0.86
362S162-54-LAM-1	305	272	12.0	11.6	41.6	42.3	93.1	3.6	4.4	4.2	4.4	90.2	89.8	0.9	2.4	1.44
362S162-54-LAM-2	305	273	11.7	12.2	42.3	41.6	92.7	4.2	4.4	3.6	4.4	89.2	89.2	3.2	2.2	1.44
362S162-54-LAC-1	305	272	11.7	11.8	42.0	41.6	92.7	4.0	4.4	3.6	4.4	88.9	89.5	1.0	2.0	1.44
362S162-54-LAC-2	305	273	11.8	12.0	42.3	41.7	92.9	4.2	4.4	3.8	4.4	89.0	89.2	5.1	2.3	1.44
362S162-54-LAMT-1	305	272	11.8	12.3	41.1	42.2	92.8	3.6	4.2	4.0	4.2	92.4	88.8	-3.6	3.6	1.46
362S162-54-LAMT-2	305	274	11.7	12.2	41.3	42.3	93.9	3.6	4.4	4.2	4.3	90.1	88.1	1.4	3.9	1.46

See the dimension definitions in Fig. 3.1

Table 3.2. Elastic buckling properties and predicted compressive capacity.

Specimen	F_y (MPa)	F_u (MPa)	P_y (kN)	P_n (kN)	P_{cre} (kN)	λ_e	P_{crd} (kN)	λ_d	L_{crd} (mm)	$P_{cr\ell}$ (kN)	λ_ℓ	$L_{cr\ell}$ (mm)	δ_e ($\times 10^{-3}$mm)
600S137-97-GAM-1	388	529	245	121	147	1.29	228	1.04	314	198	0.78	119	654
600S137-97-GAM-2	394	529	249	122	147	1.30	232	1.04	314	201	0.78	118	653
600S137-97-GAC-1	382	523	242	121	147	1.28	233	1.02	318	202	0.78	118	650
600S137-97-GAC-2	388	528	244	120	145	1.30	225	1.04	315	196	0.78	119	647
362S137-68-GAM-1	392	531	123	60	71	1.32	165	0.86	253	130	0.68	71	636
362S137-68-GAM-2	387	529	122	59	70	1.32	167	0.86	252	131	0.67	71	624
362S137-68-GAC-1	389	535	123	59	70	1.32	166	0.86	254	130	0.67	71	626
362S137-68-GAC-2	386	529	121	60	71	1.30	165	0.86	254	130	0.68	71	638
600S137-68-DAM-1	427	558	177	91	1249	0.38	76	1.53	260	62	1.64	123	173
600S137-68-DAM-2	427	558	177	90	1243	0.38	75	1.53	258	62	1.64	124	172
600S137-68-DAC-1	427	558	177	91	1270	0.37	76	1.53	259	62	1.64	124	172
600S137-68-DAC-2	427	558	177	91	1256	0.38	76	1.53	259	62	1.64	123	173
362S137-68-DAM-1	389	529	124	103	968	0.36	180	0.83	256	130	0.95	72	533
362S137-68-DAM-2	389	529	123	103	961	0.36	180	0.83	255	132	0.94	71	537
362S137-68-DAC-1	389	528	122	101	933	0.36	175	0.83	252	128	0.95	71	529
362S137-68-DAC-2	389	528	122	102	947	0.36	177	0.83	254	128	0.95	71	531
600S162-33-LAM-1	333	398	72	27	4138	0.13	62	1.08	515	8	3.04	111	32
600S162-33-LAM-2	333	398	72	32	4307	0.13	53	1.16	462	11	2.49	108	48
600S162-33-LAC-1	333	398	72	27	4125	0.13	60	1.09	512	8	3.05	112	32
600S162-33-LAC-2	333	398	72	27	4147	0.13	60	1.09	511	8	3.05	111	32
362S162-54-LAM-1	416	476	113	81	3704	0.17	157	0.85	330	70	1.26	72	232
362S162-54-LAM-2	416	476	113	81	3674	0.18	160	0.84	333	71	1.26	71	234
362S162-54-LAC-1	416	476	113	81	3626	0.18	157	0.85	328	70	1.26	71	233
362S162-54-LAC-2	416	476	113	81	3683	0.18	158	0.85	332	70	1.26	72	232
362S162-54-LAMT-1	416	476	113	81	3717	0.17	161	0.84	334	70	1.26	71	233
362S162-54-LAMT-2	416	476	114	81	3720	0.17	159	0.85	332	69	1.27	72	228

$\lambda_e = (P_y/P_{cre})^{0.5}$; $\lambda_d = (P_y/P_{crd})^{0.5}$; $\lambda_\ell = (P_{ne}/P_{cr\ell})^{0.5}$.

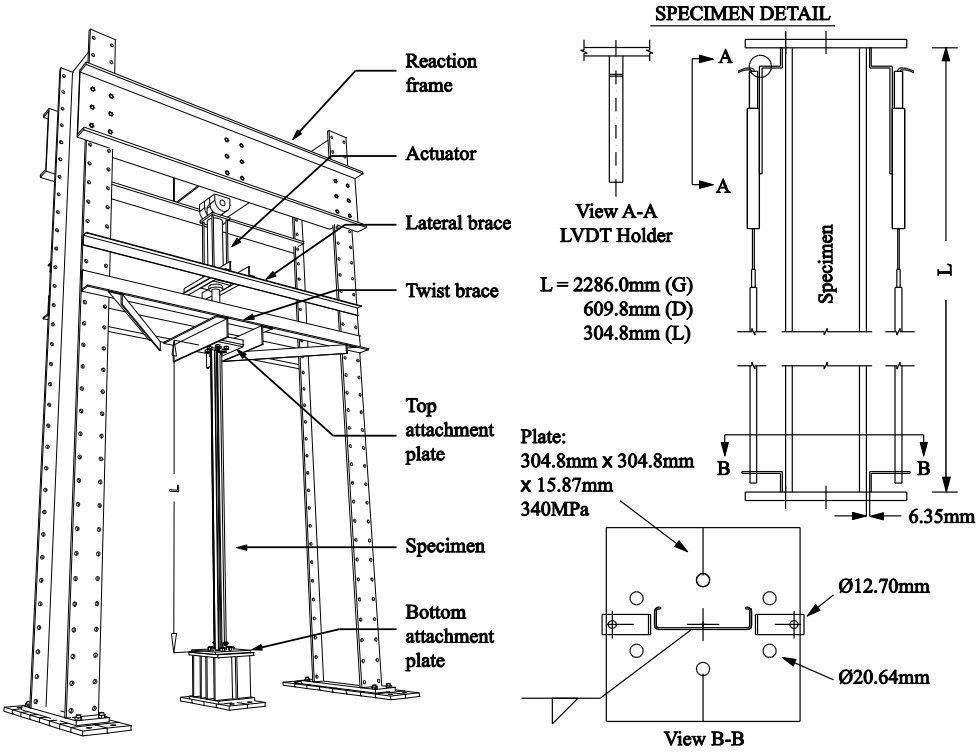

Fig. 3.2. Test setup and specimen detail.

3.2.4 Displacement-controlled testing protocol

The loading protocol (see Fig. 3.3) was adapted from FEMA 461 quasi-static cyclic deformation-controlled testing protocol. The FEMA 461 protocol is used to obtain fragility data and hysteretic load-deformation response characteristics of building components for which damage is best predicted by imposed deformations [30]. CFS axial members may experience asymmetrical loading because of end connections (e.g., screwed or welded connection) and the location within a building system (e.g., end stud compared to an inside stud in a shear wall). Using a symmetric protocol with equal deformation demands in compression and tension captures the damage and energy dissipation from cross-sectional deformation of the thin-walled channel sections under compression and damage and tearing that can occur by the reversal of these deformations under tension loading. Hysteretic numerical models built based on the responses obtained from this protocol are expected to be capable of capturing the behavior under different loading patterns such as on-sided loading.

The loading protocol consists of amplitude increasing steps with two cycles per step. Each step amplitude is related to the previous by the equation $\delta_i = 1.4\delta_{i-1}$ (see Fig. 3.3). The anchor point is the elastic axial displacement, $\delta_e = P_eL/AE$, that defines the amplitude of the fourth step (i.e., 7th and 8th cycles). The compressive load, P_e, at which buckling deformations influence the load-deformation response is calculated using slenderness limits defined in the AISI-S100-12 DSM [22]. The DSM approach predicts that local buckling deformation initiates at λ_ℓ =0.776 and the distortional buckling deformation initiates at λ_d=0.561. Using $\lambda=(P_e/P_{cr})^{0.5}$, then P_e=0.60$P_{cr\ell}$ and P_e=0.31P_{crd}. The load where global buckling deformation influences load-deformation response is assumed to be P_e=0.50P_{cre}. Values of δ_e are listed in Table 3.2 for all specimens.

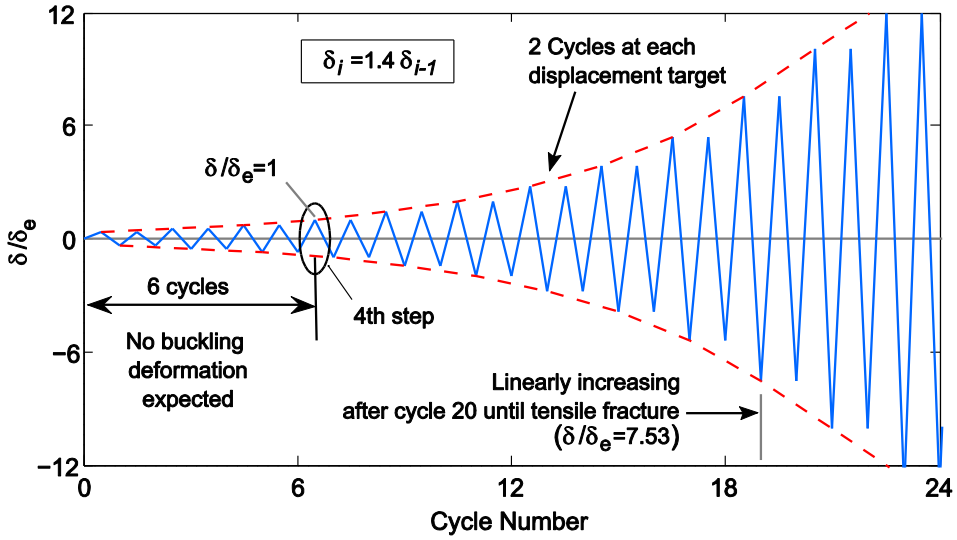

Fig. 3.3. Cyclic compression-tension cold-formed steel loading protocol.

3.2.5 Specimen imperfections

Initial geometric imperfections in CFS members reduce axial strength and initial stiffness in compression. The measured strength, as well as the predicted strength from a FEM analysis that includes imperfections, decreases the most if the shape of imperfections resemble the governing buckling modes [47,52,53]. Member imperfections are defined as the specimen geometry deviations from the straight "perfect" member before attaching it to the loading frame (see Fig. 3.4). Imperfections were measured using methods described in [54].

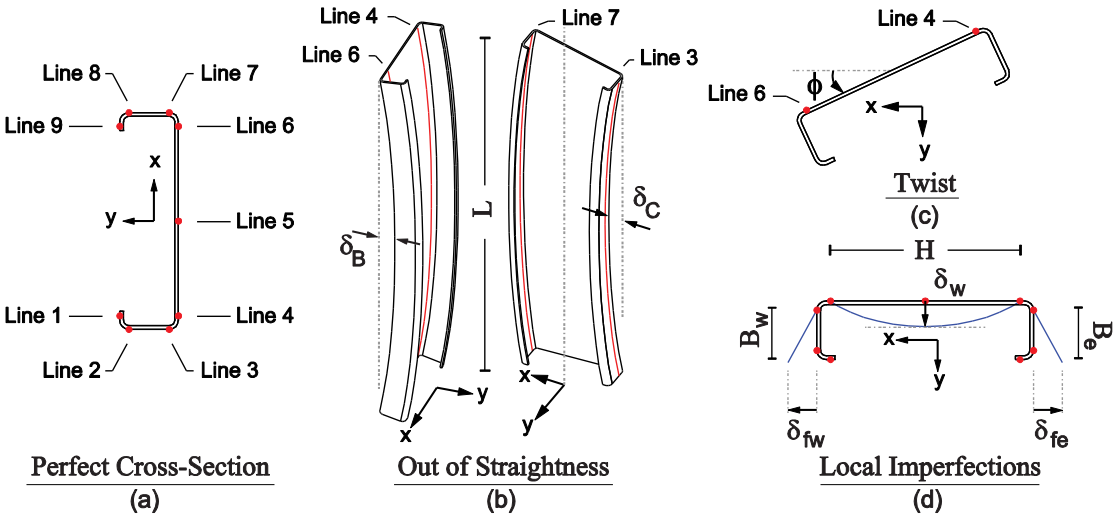

Fig. 3.4. Global and local imperfection definition.

The average maximum measured imperfections were generally smaller than the tolerance limits given in ASTM C955-09 [55] as shown in Table 3.3. However, for some specimens the

global imperfections were larger than the ASTM limit and affected their strength. For instance, the strength of specimen 600S137-97-GAM-2 was 17% lower than the predicted strength (see Table 3.4 and Fig. 3.6b) due to large initial global imperfections (δ_B=L/452, see Table 3.3) in the weak axis direction. Global imperfection magnitudes in CFS members are known to increase with sheet thickness because of plastic strains and associated residual curvature caused by coiling the sheet for transportation and manufacturing [56,53]. Initial global imperfections also affected the buckling mode. For example, specimen 362S137-68-GAM-1 experienced flexural-torsional buckling due to an initial twist ϕ=3.93°, the largest observed. Out-of-straightness in the strong axis direction, δ_C, for local buckling specimens was on average larger than the ASTM limits; however, its effect on compressive strength and buckling mode is negligible.

Local imperfections were all lower than ASTM limits and smaller than δ_w/t = 0.66 and δ_f/t = 3.44 associated with occurrence probabilities P(δ<δ_w)=0.75 and P(δ<δ_f)=0.95 respectively in [28]. The influence of local imperfections on the strength was negligible for all specimens, however it affected the initial stiffness of the 362DAM and the LAM specimens. Imperfection influence was negligible for members under cyclic loading because during the first elastic tension excursions the imperfections straighten out. The result is equal initial stiffness in compression and tension (see Fig. 3.5a, 3.7a, and 3.90a). A detailed discussion about the measured imperfections from this testing program and their characterization can be found in [54].

Table 3.3. Maximum measured imperfections.

		Member imperfections									
		δ_B/L (×10^{-3})		**δ_C/L** (×10^{-3})		**ϕ** (°)	**δ_W/H** (×10^{-3})		**δ_{FE}/B_e** (×10^{-3})		**δ_{FW}/B_w** (×10^{-3})	
Global	Mean	1.04	(L/961)	-		2.64	8.16	(H/123)	48.16	(B/21)	46.27	(B/22)
	Max	2.21	(L/452)	-		3.93	44.45	(H/22)	76.40	(B/13)	86.99	(B/11)
	Min	0.22	(L/4556)	-		1.66	1.67	(H/598)	19.14	(B/52)	26.91	(B/37)
	St.Dev	0.70		-		0.78	14.69		18.65		21.49	
	COV	0.68		-		0.29	1.80		0.39		0.46	
Distortional	Mean	0.60	(L/1678)	0.56	(L/1771)	1.39	3.25	(H/308)	41.50	(B/24)	28.25	(B/35)
	Max	0.97	(L/1028)	0.95	(L/1052)	3.48	6.14	(H/163)	54.10	(B/18)	51.22	(B/20)
	Min	0.23	(L/4389)	0.30	(L/3288)	0.10	0.81	(H/1231)	14.58	(B/69)	9.68	(B/103)
	St.Dev	0.23		0.27		1.13	1.95		12.77		13.40	
	COV	0.38		0.49		0.81	0.60		0.31		0.47	
Local	Mean	0.46	(L/2187)	1.63	(L/612)	0.77	3.74	(H/267)	43.87	(B/23)	37.57	(B/27)
	Max	0.78	(L/1277)	3.22	(L/311)	2.16	10.58	(H/95)	79.92	(B/13)	51.46	(B/19)
	Min	0.20	(L/5080)	0.80	(L/1252)	0.02	1.66	(H/604)	12.24	(B/82)	22.45	(B/45)
	St.Dev	0.20		1.09		0.71	2.87		23.98		12.50	
	COV	0.44		0.67		0.92	0.77		0.55		0.33	
ASTM C955 Tol.		L/960		L/960		L/H/384	2 x 1.59mm (max)		2 x 1.59mm (max)		2 x 1.59mm (max)	

3.3 Experimental Results

3.3.1 Monotonic and cyclic response

Cyclic and monotonic load-deformation responses were obtained for specimens experiencing local, distortional, and global buckling. From the monotonic tests, the average ratio of test peak load (in compression) to predicted load P_{min}/P_n was 1.00 with a coefficient of variation of 0.09 (see Table 3.5). This result confirms that the actual boundary conditions accurately represent the assumed constraints of rotational fixity and warping fixity at the specimen ends. The cyclic response is linear during the first six cycles with equal stiffness in tension and compression for all specimens (see Fig. 3.5a, 3.7a, and 3.90a). As expected, the cyclic response is asymmetric due to the presence of buckling deformations in compression. Strength and stiffness in compression degraded under cycling loading due to inelastic deformations. Additional details for each of the limit states are discussed in the following sections and test videos are available at the Virginia Polytechnic Institute and State University digital repository [57].

Table 3.4. Test maximum loads.

Specimen	P_{max} (kN)	δ_{Pmax} ($\times10^{-3}$mm)	P_{min} (kN)	δ_{Pmin} ($\times10^{-3}$mm)	δ_y	P_{max}/P_y	P_{min}/P_n	δ_{Pmax}/L ($\times10^{-3}$)	δ_{Pmin}/L	δ_{Pmax}/δ_y	δ_{Pmin}/δ_y
600S137-97-GAM-1	-	-	-117	-2413	4358	-	0.97	-	-1.06	-	-0.55
600S137-97-GAM-2	-	-	-101	-2921	4424	-	0.83	-	-1.28	-	-0.66
600S137-97-GAC-1	236	8890	-129	-2362	4289	0.98	1.06	3.89	-1.03	2.07	-0.55
600S137-97-GAC-2	237	16180	-127	-2388	4361	0.97	1.06	7.08	-1.04	3.71	-0.55
362S137-68-GAM-1	-	-	-56	-2718	4400	-	0.94	-	-1.19	-	-0.62
362S137-68-GAM-2	-	-	-53	-2362	4355	-	0.90	-	-1.03	-	-0.54
362S137-68-GAC-1	122	8331	-50	-2464	4376	1.00	0.84	3.64	-1.08	1.90	-0.56
362S137-68-GAC-2	123	9068	-49	-2261	4339	1.01	0.83	3.97	-0.99	2.09	-0.52
600S137-68-DAM-1	-	-	-97	-1829	1277	-	1.07	-	-3.00	-	-1.43
600S137-68-DAM-2	-	-	-97	-1626	1279	-	1.08	-	-2.67	-	-1.27
600S137-68-DAC-1	175	3226	-96	-1295	1279	0.99	1.06	5.29	-2.13	2.52	-1.01
600S137-68-DAC-2	174	2769	-100	-1118	1278	0.98	1.10	4.54	-1.83	2.17	-0.87
362S137-68-DAM-1	-	-	-100	-1778	1166	-	0.96	-	-2.92	-	-1.52
362S137-68-DAM-2	-	-	-98	-1499	1166	-	0.95	-	-2.46	-	-1.28
362S137-68-DAC-1	127	5512	-99	-1168	1167	1.05	0.98	9.04	-1.92	4.72	-1.00
362S137-68-DAC-2	128	5766	-96	-991	1167	1.05	0.94	9.46	-1.63	4.94	-0.85
600S162-33-LAM-1	-	-	-31	-406	499	-	1.12	-	-1.33	-	-0.82
600S162-33-LAM-2	-	-	-33	-559	499	-	1.04	-	-1.83	-	-1.12
600S162-33-LAC-1	66	838	-29	-457	499	0.92	1.06	2.75	-1.50	1.68	-0.92
600S162-33-LAC-2	67	991	-32	-457	499	0.94	1.19	3.25	-1.50	1.99	-0.92
362S162-54-LAM-1	-	-	-88	-813	623	-	1.08	-	-2.67	-	-1.31
362S162-54-LAM-2	-	-	-86	-889	623	-	1.05	-	-2.92	-	-1.43
362S162-54-LAC-1	109	1295	-88	-508	623	0.97	1.08	4.25	-1.67	2.08	-0.82
362S162-54-LAC-2	110	1270	-90	-635	623	0.97	1.11	4.17	-2.08	2.04	-1.02
362S162-54-LAMT-1	110	1719	-	-	623	0.97	-	5.64	-	2.76	-
362S162-54-LAMT-2	115	9896	-	-	623	1.01	-	32.47	-	15.89	-

P_{max}, δ_{Pmax}= test max. tension and corresponding displacement;
P_{min}, δ_{Pmin}= test max. compression and corresponding displacement.
$\delta_y = P_yL/EA_g$ the elastic yielding displacement.

Table 3.5. Test-to-predicted statistics.

Specimen Group	P_{max}/P_y		P_{min}/P_n		δ_{Pmax}/L		δ_{Pmin}/L		δ_{Pmax}/δ_y		δ_{Pmin}/δ_y	
	μ	*cov*	μ	*cov*	μ	*cov*	μ	*cov*	μ	*cov*	μ	*cov*
Global	0.99	0.02	0.93	0.10	4.64	0.35	1.09	0.09	2.44	0.35	0.57	0.08
Distortional	1.02	0.03	1.02	0.07	7.08	0.36	2.32	0.22	3.59	0.40	1.16	0.22
Local	0.95	0.02	1.09	0.04	3.60	0.20	1.94	0.30	1.95	0.09	1.04	0.22
Monotonic	-	-	1.00	0.09	-	-	2.03	0.40	-	-	1.05	0.36
Cyclic	0.99	0.04	1.03	0.11	5.11	0.43	1.53	0.27	2.66	0.43	0.80	0.25
All Spec.	0.99	0.04	1.01	0.10	5.11	0.43	1.78	0.38	2.66	0.43	0.92	0.35

μ = mean value; *cov* = coefficient of variation; Tension tests are not included.

3.3.1.1 Global buckling limit state

Cyclic response of global buckling (GAC) specimens was characterized by weak-axis flexural buckling, which in later cycles led to folding of the stiffening lips near the mid-height as shown in Fig. 3.5d. Damage from strain reversal accumulated at the mid-height in the C-section flange stiffening lips during subsequent excursions in tension and compression. Compressive strength degraded rapidly in the cycles after the peak compressive load was reached due to the damaged accumulated at the folded lips. This deterioration is quantified as the difference between the monotonic curves and the compression side of the cyclic responses in Fig. 3.6.

Unloading stiffness also deteriorated during cyclic loading and the member unloaded nonlinearly from the compression side as shown in Fig. 3.5b. Web inelastic buckling occurred near the supports after damage accumulated at the mid-height folded lips. Excursions in tension after peak compressive load is reached were characterized by very low stiffness until the member straightens out as shown in Fig. 3.5b. Ductile yielding at a consistent tension yield capacity was observed at the mid-height cross-section as shown in bottom-left quadrant of Fig. 3.5c. The final failure mode was gradual tearing of the section starting at the folded lips and propagating through the cross section, or in some cases fracture near the welded connection.

The monotonic response of the global buckling (GAM) specimens was generally characterized by weak axis flexural buckling, with folding of the stiffening lips at mid-height. Specimen 362S137-68-GAM-1 however, exhibited flexural-torsional buckling due to torsional initial imperfections in the member. This resulted in a higher peak compression load and higher monotonic envelope as shown in Fig. 3.6a and Table 3.4.

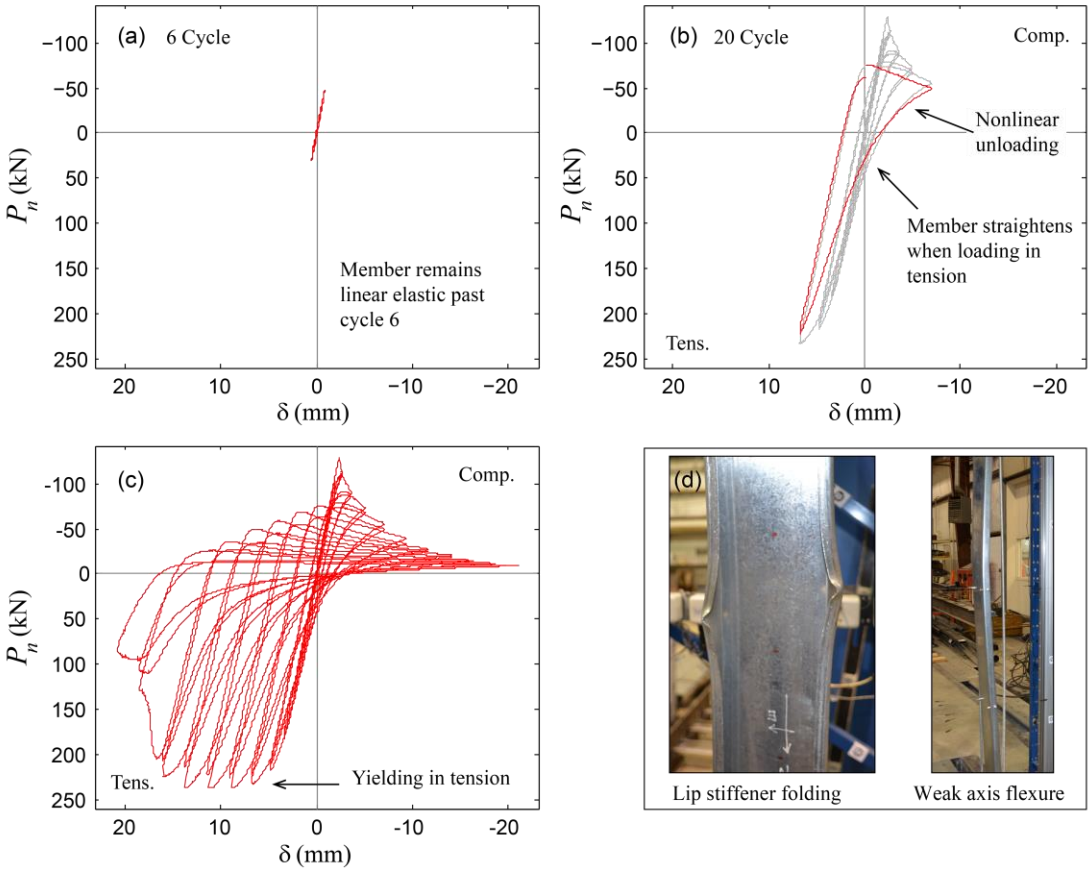

Fig. 3.5. Cyclic load-deformation response specimen 600S137-97-GAC-1, (a) 6 cycles, (b) 20 cycles, (c) complete response, (d) failure mode.

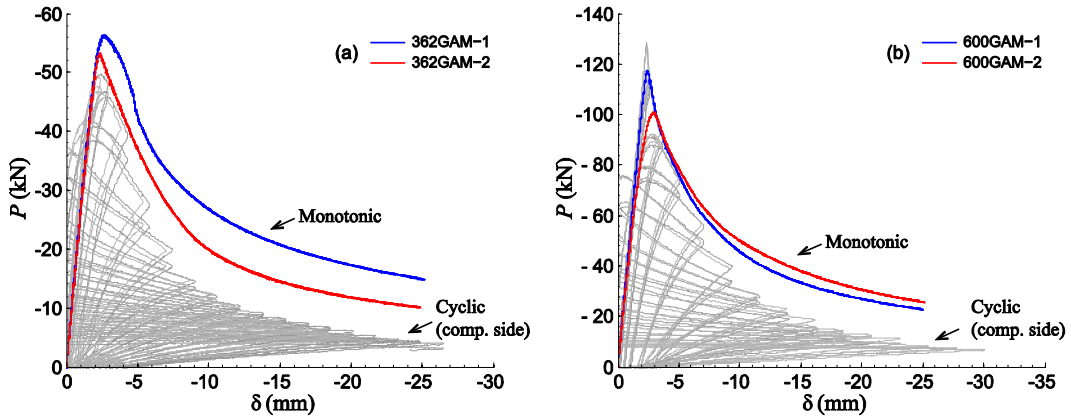

Fig. 3.6. Global buckling monotonic response envelope, (a) 362 series, (b) 600 series (Tension side of the cyclic responses has been omitted).

3.3.1.2 Local buckling limit state

Cyclic response of the local buckling (LAC) specimens was characterized by web buckling with at least two half-waves occurring before reaching the peak compressive load. After the peak load in compression, one half-wave locked around mid-height and damage accumulated at that location (see Fig. 3.7d). Compressive strength and unloading stiffness then degraded quickly on the compression side as shown in Fig. 3.7(b-c); however unlike global buckling members, unloading from compression was linear for all excursions (see Fig. 3.8). The difference between the monotonic curves and the compression side of the cyclic responses in Fig. 3.8 demonstrates this deterioration. Strength in tension deteriorated faster in the 600LAC specimens than for the 362LAC specimens. The 362LAC specimens experienced yielding close to the rounded corners and a yield line across the web. Tearing started thereafter at the center of the web and propagated to the corners and then to the rest of the cross-section. The 600LAC specimens exhibited similar behavior, but as shown in Fig. 3.7d, two yield lines formed around mid-height where tearing occurred. The 600LAC specimens underwent approximately 100 cycles after which the web was still carrying some tensile load.

The monotonic response of the local buckling (LAM) specimens demonstrated similar deformations as their cyclic counterpart; however, in the 362LAM specimens these deformations occurred closer to the top end plate. Initial stiffness for the 362LAM specimens was lower than for their cyclic counterparts from initial imperfections (see Fig. 3.8a). Both cyclic and monotonic tests exceeded the predicted compressive capacity P_n, but the maximum tensile strength fell below the yield load P_y for the 600LAC specimens (see Table 3.4). It is hypothesized that for thinner members (e.g., 600S162-33-LAC) the flanges and corners carried more of the tensile load than the web, and therefore, the cross-section was not fully effective in tension. This as a consequence of the large web buckling deformations during compression excursions that did not fully straightened out when loading in tension leading to non-uniform tension yielding around the cross-section.

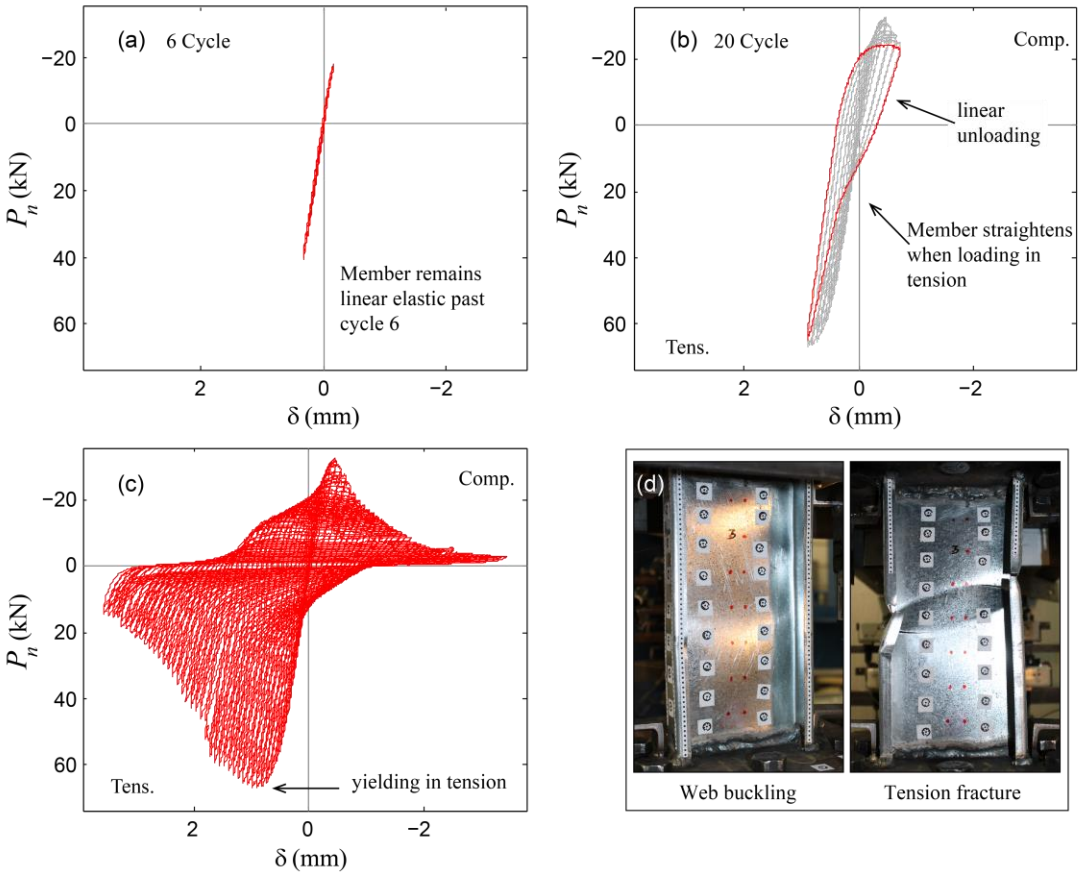

Fig. 3.7. Cyclic load-deformation response specimen 600S162-33-LAC-2, (a) 6 cycles, (b) 20 cycles, (c) complete response, (d) failure mode.

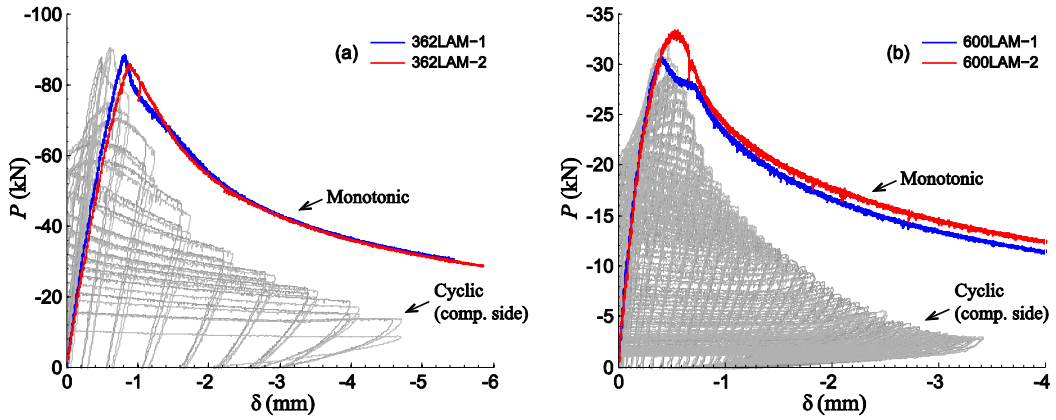

Fig. 3.8. Local buckling monotonic response envelope, (a) 362 series, (b) 600 series (Tension side of the cyclic responses has been omitted).

3.3.1.3 Distortional buckling limit state

Cyclic response of the distortional buckling 600DAC specimens was characterized by the formation of at least one half-wavelength centered at mid-height as seen in Fig. 3.9d. Damage accumulated from inelastic strains at the rounded corners as the member stretched and compressed. Strength in compression and unloading stiffness degraded from inelastic strains accumulating in the damaged half-wave as shown by the difference between the monotonic curves and the cyclic envelopes in Fig. 3.10. The strength in tension remained constant until tearing started at the rounded corners and propagated around the cross section. The deformations experienced by the 362DAC specimens were a combination of distortional and local buckling of the web near one of the end plates. However, web buckling deformations were more visibly noticeable than opening of the flanges. The behavior of the 362DAC members was found to be similar to the behavior of the local buckling 362LAC specimens. The monotonic response of the DAM specimens demonstrated similar deformations as their cyclic counterpart. Their initial stiffness however, is lower than for the DAC specimens, as seen in Fig. 3.10, due to initial imperfections.

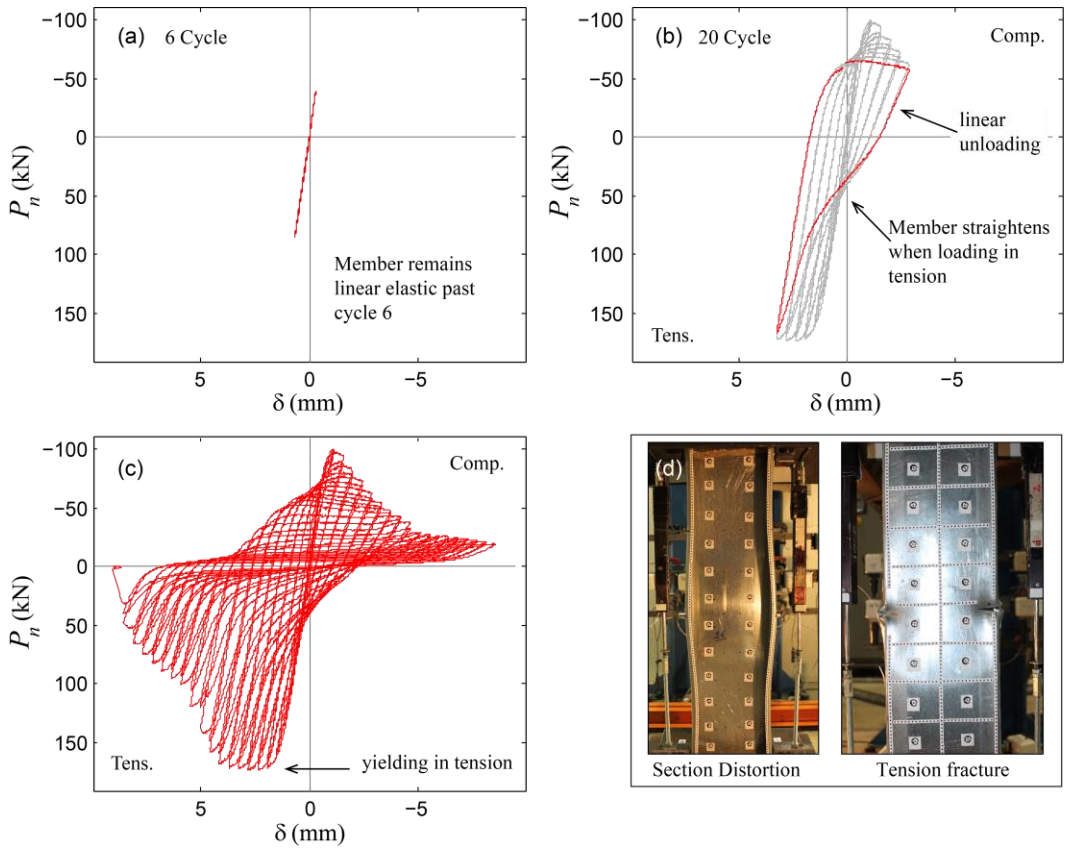

Fig. 3.9. Cyclic load-deformation response specimen 600S137-68-DAC-2, (a) 6 cycles, (b) 20 cycles, (c) complete response, (d) failure mode.

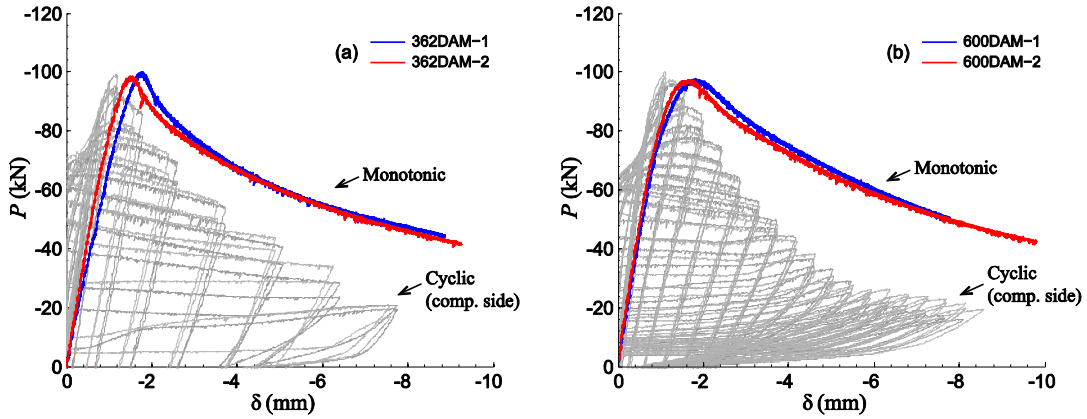

Fig. 3.10. Distortional buckling monotonic response envelope, (a) 362 series, (b) 600 series (Tension side of the cyclic responses has been omitted).

3.3.1.4 Monotonic tension response

The monotonic tension response of the 362LAMT specimens was linear up to 80% of the peak tension load (P_{max}) when yielding starts in the web, then a short nonlinear segment occurs caused by the propagation of yielding around the cross-section. A linear segment with decreased stiffness and large axial deformations followed to the peak tension load (see Fig. 3.11). Strength reduced rapidly when tearing started. The normalized axial deformations δ/δ_y far exceeded (~300% at rupture) the maximum normalized deformations reached during the tension excursions by any of the specimens that underwent cyclic loading (see Table 3.4). Thus, ductility in axial tension is highly reduced as a consequence of the reversal of inelastic strains at the damaged half-wave during cyclic loading (see Fig. 3.5c, 3.7c, and 3.9c). The monotonic responses when normalized to P_y and δ_y shown in Fig. 3.11 are considered here as representative of the behavior in tension of all the tested CFS members.

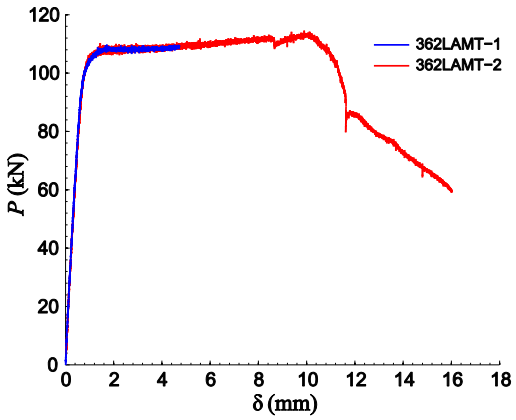

Fig. 3.11. Monotonic tension response of 362LAMT specimens.

3.3.2 Hysteretic load-deformation response and energy dissipation comparisons

Strength degradation, stiffness degradation, and pinching of the load-deformation response varies for the different specimens; however, trends can be identified by focusing in on cross-sectional slenderness. Fig. 3.12 compares the normalized envelopes of the cyclic response of all the specimens in this study. It can be seen that all the specimens have the same normalized pre-buckling stiffness k/k_e ($k_e = AE/L$). Strength in compression, compared to the peak compression load, decreased in all specimens at similar rates as the axial deformation δ/δ_y increased ($\delta_y = P_y/k_e$). The maximum normalized axial deformations δ/δ_y for compression and tension excursions was similar for all the specimens. This result will be useful in the future for defining load-deformation hysteretic numerical models for CFS axial members based on a common displacement criteria.

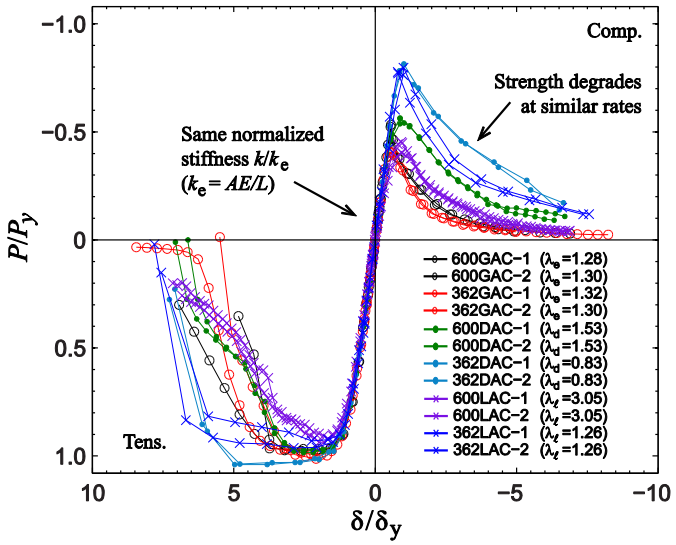

Fig. 3.12. Cyclic response envelopes.

Even though the cyclic envelopes in Fig. 3.12 and in general the cyclic behavior is similar for all the specimens, there are differences in the cyclic response. Specimens with smaller cross-sectional slenderness exhibited less pinching of the load-deformation response and differences in the amount of hysteretic energy dissipated. Fig. 3.13 compares the normalized hysteretic energy per cycle as a function of cumulative axial displacement $\Sigma\delta/L$. The hysteretic energy dissipated each cycle $E_{c,i}$ was normalized to the area of the rectangle E_{cr} bounded by the maximum and minimum axial deformation experienced in that cycle and the predicted strengths in compression and tension (see inset in Fig. 3.13). The energy curves for the 362LAC and 362DAC specimens show the largest per cycle energy dissipation values (higher than 0.35), with less cumulative axial

deformation before tensile rupture, see Table 3.6. The global buckling specimens (GAC) exhibit the least energy dissipation because of severe pinching in the load-deformation response. Post-peak deformations for the GAC specimens involved out-of-plane member deformations and development of plastic hinges all through the cross-section at mid-height that reduced axial stiffness. For instance, for the GAC specimens the unloading stiffness on average reduced to $0.13k_e$ for just 10% of the total energy dissipated. Full plastic hinges did not form in the local (LAC) and distortional (DAC) buckling specimens, and therefore the axial stiffness degraded less. In this case, the unloading stiffness reduced on average to $0.47k_e$ for the same 10% of the total energy dissipated (compared to 87% in the GAC specimens). The higher post-peak unloading stiffness from compression to tension in the LAC and DAC specimens led to less pinching of the load-deformation response and more energy dissipated per cycle.

Energy dissipation (per cycle and total) decreased with increasing cross-sectional slenderness within the damaged half-wave as shown in Fig. 3.14 and Table 3.6, results consistent with previous studies, see [42-45]. Specimens with lower cross-sectional slenderness, e.g., 362LAC (λ_ℓ =1.26) and 362DAC (λ_d =0.83), dissipate more energy within the damaged half-wave. Less slender members (λ_ℓ, $\lambda_d \leq 1.3$ – locally stocky) experience more inelastic buckling strains that translate to more damage accumulated per cycle and less cumulative axial deformation before fracture ($\Sigma\delta/L<0.7$). In contrast, specimens with higher cross-sectional slenderness, e.g., 600LAC (λ_ℓ =3.05) and 600DAC (λ_d =1.53), dissipate less energy within the damaged half-wave. Locally slender members (λ_ℓ, λ_d >1.3) experience elastic buckling strains that lead to less damage accumulated per cycle and more cumulative axial deformation before fracture ($\Sigma\delta/L>1.0$). Specimens experiencing global buckling (e.g., 600GAC and 362GAC) have the lowest energy dissipation capacity per half-wavelength and low cumulative axial deformations before tensile rupture when compared to the other buckling limit states.

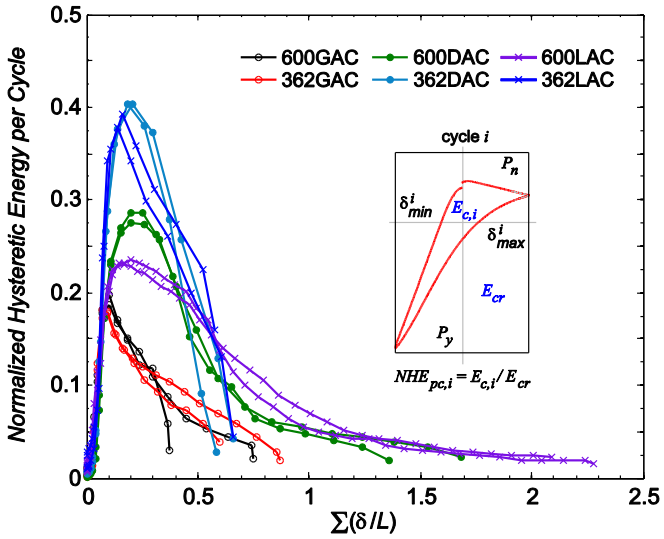

Fig. 3.13. Hysteretic energy per cycle (normalized) vs. cumulative axial deformation.

Table 3.6. Hysteretic energy dissipation.

Specimen	$HE_{0.25}$	$HE_{0.5}$	$HE_{1.0}$	HE_T	$HE_{0.25}/L_{cr}$	$HE_{0.5}/L_{cr}$	$HE_{1.0}/L_{cr}$	HE_T/L_{cr}	max $\Sigma\delta/L$
	(kN-mm)				(kN-mm/mm)				(×100)
600S137-97-GAC-1	12234	-	-	16063	10.70	-	-	14.05	37
600S137-97-GAC-2	12339	19327	-	22983	10.79	16.91	-	20.11	75
362S137-68-GAC-1	5676	10176	-	14952	4.97	8.90	-	13.08	87
362S137-68-GAC-2	5508	9078	-	10009	4.82	7.94	-	8.76	60
600S137-68-DAC-1	3125	6191	8234	8935	12.06	23.90	31.78	34.49	136
600S137-68-DAC-2	2844	5800	7598	8960	11.00	22.43	29.38	34.65	168
362S137-68-DAC-1	3131	5846	-	6458	44.02	82.20	-	90.81	66
362S137-68-DAC-2	3614	6195	-	6368	50.81	87.11	-	89.55	58
600S162-33-LAC-1	630	1313	2033	2550	5.64	11.75	18.19	22.82	209
600S162-33-LAC-2	593	1248	1863	2344	5.33	11.22	16.74	21.07	228
362S162-54-LAC-1	1580	3270	-	3839	22.21	45.98	-	53.98	57
362S162-54-LAC-2	1767	3316	-	3773	24.67	46.29	-	52.68	66

HE_{xx} = cumulative hysteretic energy dissipated up to $\Sigma\delta/L$ = xx.
HE_T = cumulative hysteretic energy dissipated until failure.

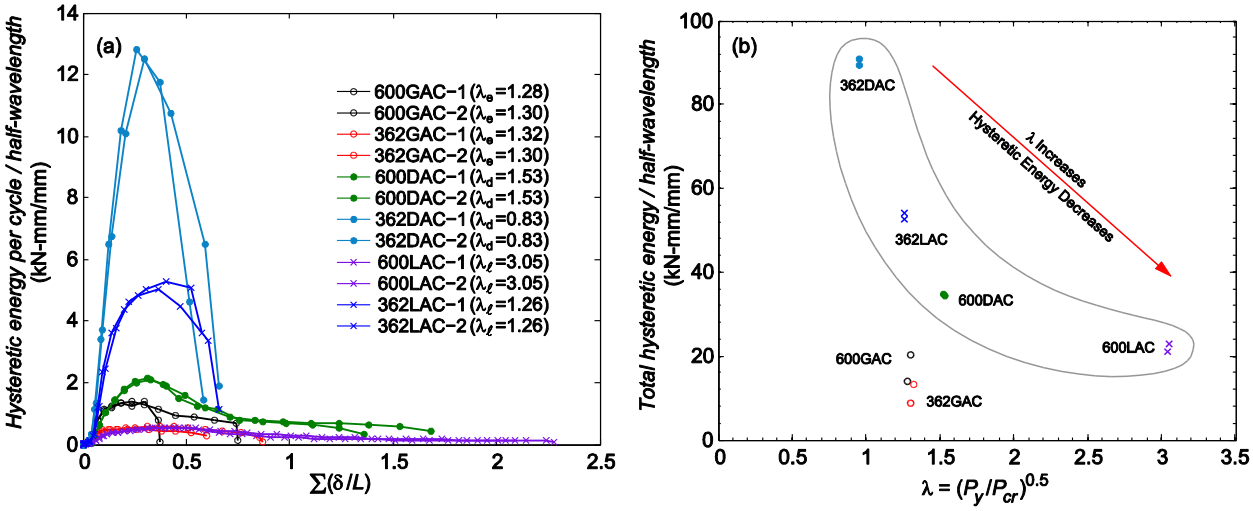

Fig. 3.14. Hysteretic energy per half-wavelength (HE_T/L_{cr}) vs. (a) cumulative axial deformation, (b) cross-sectional or global slenderness.

3.4 Conclusions

The axial cyclic response of cold-formed steel C-section framing members experiencing local, distortional and global buckling was investigated. Twelve cyclic tests, twelve monotonic tests in compression, and two monotonic tests in tension were performed to evaluate the hysteretic load-deformation response, strength degradation and energy dissipation characteristics of CFS axial members. The new cyclic loading protocol was adapted from the FEMA 461 quasi-static cyclic loading protocol for structural components. The protocol anchor point is defined as the axial deformation that initiates buckling deformation in the seventh cycle, calculated with the global or cross-sectional slenderness before a test.

The amount of strength degradation, stiffness degradation, and pinching of the load-deformation response varies for the different specimens; however, the behavior is similar across the different buckling modes, lengths and cross-sections considered. The total energy dissipated within a damaged half-wave decreases with increasing cross-sectional slenderness. Strength degradation in compression occurred at similar rates for all the specimens, regardless of buckling mode. Unloading stiffness from compression was different for the different buckling modes and affected the amount of hysteretic pinching when reloading in tension.

The results of these chapter are adapted to nonlinear hysteretic models for CFS axial members in Chapter 5and Chapter 6 for use in computational simulation and analysis-based seismic design of cold-formed steel framed structures

Chapter 4: Cyclic and Monotonic Experiments on Cold-Formed Steel Flexural Members [2]

This chapter summarizes results from an experimental program that investigated the cyclic flexural behavior and energy dissipation of cold-formed steel structural framing members with focus on thin-walled member buckling limit states (i.e., global, distortional and local buckling). Twelve cyclic flexural tests, twelve monotonic flexural tests, were conducted on common CFS C-section studs without perforations. Specimen cross-section dimensions and lengths were selected to isolate specific buckling modes (i.e., local, distortional or global buckling), and a loading protocol adapted from FEMA 461 [30] is employed where the target displacements are calculated using the member elastic buckling properties. Local and global buckling slenderness are key parameters influencing energy dissipation of thin-walled steel components, and these trends are explored in a review of existing literature in the next section.

4.1 Background - Cyclic response of flexural members including buckling

Existing research on cyclic behavior of cold-formed steel flexural members is scarce and primarily focuses on flexural response as part of bolted steel moment connections (e.g. [58-60]). Cyclic tests on hot-rolled steel I-beams experiencing global buckling (i.e., lateral-torsional buckling) demonstrated that strength deteriorates after buckling initiates with localized inelastic strains accumulating at the compression flange [61,62]. Strength decreases even more rapidly if flexure is combined with axial loading. Post-buckling strength degradation in thin-walled cold-formed steel I-beams that exhibited lateral-torsional buckling is more severe for stiffer members, and stiffness degradation was more severe for beams with lower flexural rigidity [63]. This suggests that there is a relationship between slenderness and cyclic flexural behavior of thin-walled members as described in Chapter 3 for axial CFS members.

Local buckling deformations define thin-walled member cyclic behavior. Experiments on steel circular and rectangular tubes under constant amplitude cyclic uniform bending showed that strength deteriorated due to tube wall local buckling [64-66], and that performance of rectangular steel tubes deteriorated due to inelastic buckling deformations accumulation in the compression

[2] This chapter has been formatted into a journal paper and submitted to *Thin-Walled Structures Journal,* with the title "**Cyclic Flexural Response and Energy Dissipation of Cold-Formed Steel Framing Members"**.

face with collapse when kinks developed at the dominant local buckling half-wave [68]. More recent studies investigating energy dissipation associated with local buckling deformations in cold-formed steel beams subjected to constant amplitude cyclic bending [69-71] showed that strength degrades rapidly in the first cycles and reduces to an almost constant magnitude. This is a consequence of localized inelastic buckling deformations (and subsequent fracture) slowly spreading throughout the cross-section as number of cycles increased. Residual strength after several cycles can be beneficial in the context of collapse analysis and design of CFS systems.

This chapter summarizes an experimental program that investigated the cyclic behavior and energy dissipation of CFS flexural members with focus on thin-walled buckling limit states. Specimen cross-section dimensions, unbraced lengths, and test boundary conditions were strategically selected to isolate thin-walled member buckling limit states common to open cross-section thin-walled CFS joists (i.e., lateral-torsional, distortional and local buckling). Strength and stiffness degradation were carefully documented, and trends related to cross-sectional slenderness and energy dissipation are discussed. The next section introduces the experimental program, specimen selection strategy, test setup and loading protocol.

4.2 Experimental program

An experimental program was conducted to study the cyclic behavior of CFS flexural members (lipped channels without perforations) experiencing local, distortional and global buckling deformations. Specimens were subjected to four-point bending with a constant moment region of length L_u. Shear and axial (catenary) forces in the unbraced length (L_u) were prevented with custom designed test fixtures described in this section. The program included monotonic and cyclic tests where the monotonic tests served as a baseline moment-rotation response to quantify cyclic strength and stiffness degradation.

4.2.1 Specimen selection strategy

Specimens cross-sections and unbraced lengths, L_u, were selected such that their monotonic flexural strength was governed either by local, distortional or global buckling as predicted by the American Iron and Steel Institute (AISI) Direct Strength Method [22]. Six cross-sections were selected from standard sizes listed in the Structural Stud Manufacturers Association (SSMA) catalog [46] with web widths ranging from 203 to 305mm and nominal thicknesses between 0.88mm and 2.58mm. Global buckling specimens had an unbraced length L_u=3048mm, while local

and distortional buckling specimens had an unbraced length of L_u=1626mm. The test matrix is summarized in Table 4.1 (with nominal dimensions) and specimen nomenclature and cross-section variables are defined in Fig. 4.1.

Table 4.1. Test matrix with nominal dimensions, number of tests, and displacement loading rate.

Specimen [(a)]	Buckling Limit [(b)]	L_u (mm)	H (mm)	B (mm)	t (mm)	No. of Cyclic Tests	No. of Monotonic Tests	Cyclic Disp. Rate (mm/min)	Monotonic Disp. Rate (mm/min)
800S200-33-LF#	Local	1626	203	51	0.88	2	2	20.57	0.35
1000S200-43-LF#	(λ_ℓ>>λ_d, λ_e)	1626	254	51	1.15	2	2	30.85	0.52
800S250-68-DF#	Distortional	1626	203	64	1.81	2	2	28.55	0.48
1200S250-97-DF#	λ_d>>λ_ℓ and λ_e	1626	305	64	2.58	2	2	42.82	0.73
800S162-97-GF#	Global	3048	203	41	2.58	2	2	34.26	0.58
1200S162-97-GF#	λ_e>>λ_ℓ and λ_d	3048	305	41	2.58	2	2	42.82	0.73

(a) F= Flexural, G= Global, D= Distortional, L= Local, # indicates Cyclic or Monotonic.
(b) λ_ℓ, λ_d and λ_e = local, distortional and global slenderness parameter respectively [22].

4.2.2 Specimen dimensions, material properties and elastic buckling moments

Cross-section dimensions were measured at the member's mid-span using methods described in [47]. See Fig. 4.1b for definitions of measured quantities and Table 4.2 for values. The measured dimensions were input in the finite strip eigen-buckling analysis software CUFSM [48] to calculate the elastic buckling moment for local buckling, $M_{cr\ell}$, distortional buckling, M_{crd}, and global buckling, M_{cre}, along with the associated half-wavelengths ($L_{cr\ell}$, L_{crd}, and L_{cre} respectively). Warping, twist and minor axis flexure were assumed fixed at loading points when calculating the elastic buckling moments, i.e., an effective length of $0.5L_u$ was used when calculating M_{cre}. The yield moment, M_y, was determined using the cross-section moment of inertia (calculated using measured dimensions) at mid-span and the average measured yield stress F_y obtained from three coupon tests per specimen. Coupon tests were conducted in accordance with ASTM E8M-13a [49] with one coupon taken from each flange and one from the web. The monotonic flexural capacity, M_n, was calculated using the AISI Direct Strength Method [22]. These values are summarized in Table 4.3.

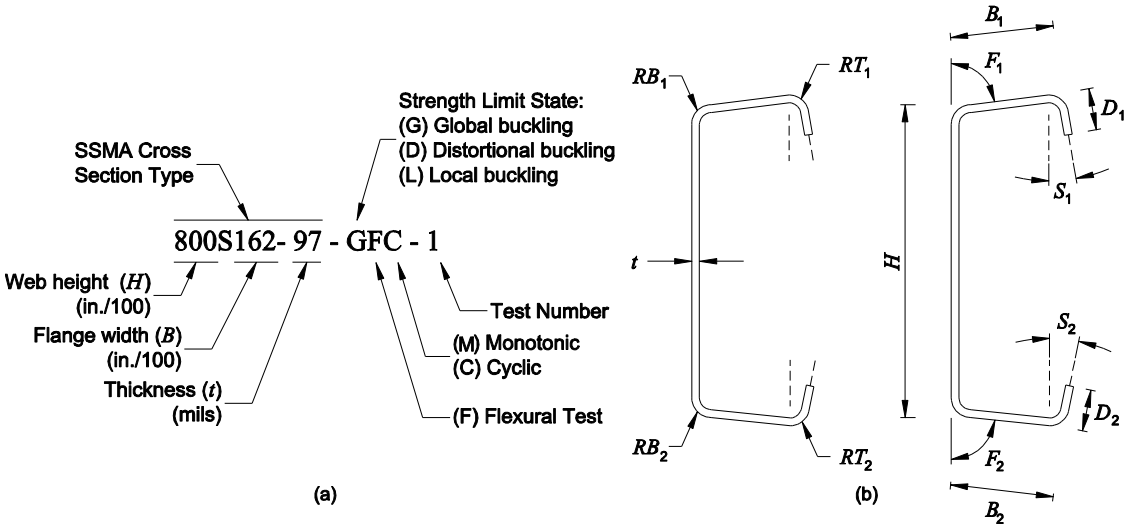

Fig. 4.1. Specimen naming notation (a); and cross-section dimension (b).

Table 4.2. Measured specimen dimensions.

Specimen	L (mm)	A_g[a] (mm^2)	I_x[a] (cm^4)	D_1 (mm)	D_2 (mm)	B_1 (mm)	B_2 (mm)	H (mm)	RT_1 (mm)	RB_1 (mm)	RT_2 (mm)	RB_2 (mm)	F_1 (°)	F_2 (°)	S_1 (°)	S_2 (°)	t (mm)
1200S162-97-GFC-1	3048	995	1111	9.8	11.3	42.5	43.1	305.7	4.8	5.6	5.2	5.6	91.2	88.0	-2.8	2.6	2.52
1200S162-97-GFC-2	3048	993	1111	10.1	10.9	42.8	43.1	305.7	5.0	5.6	5.2	5.6	90.9	87.5	-2.8	3.0	2.51
1200S162-97-GFM-1	3048	991	1105	10.0	11.1	42.3	43.2	305.9	4.8	5.6	5.2	5.6	91.2	88.2	-3.7	-3.1	2.51
1200S162-97-GFM-2	3048	992	1104	10.8	10.0	42.8	42.0	305.7	5.2	5.6	4.8	5.6	88.7	90.7	2.5	-4.0	2.52
800S162-97-GFC-1	3048	734	400	9.7	11.4	42.9	42.5	203.9	4.4	5.6	5.2	5.2	90.6	88.8	-2.3	0.7	2.50
800S162-97-GFC-2	3048	734	398	12.4	13.0	40.6	40.2	203.9	5.0	5.4	5.2	5.4	90.3	88.8	0.5	2.1	2.50
800S162-97-GFM-1	3048	732	398	9.9	11.4	42.4	42.3	204.0	4.8	5.4	5.2	5.2	90.6	88.8	-2.7	-1.1	2.50
800S162-97-GFM-2	3048	735	400	12.2	13.6	40.3	39.9	203.8	4.8	5.4	5.2	5.2	89.0	87.7	0.7	2.1	2.51
1200S250-97-DFC-1	1626	1148	1427	12.9	14.5	65.8	64.9	306.6	5.2	5.6	5.6	5.6	92.2	89.8	-4.2	-3.7	2.57
1200S250-97-DFC-2	1626	1140	1421	12.6	14.5	65.1	65.7	306.5	5.2	5.6	5.6	5.6	91.4	89.5	-4.0	-4.1	2.56
1200S250-97-DFM-1	1626	1154	1437	12.7	14.7	65.7	65.9	306.8	5.2	5.6	5.6	5.6	92.7	89.5	-5.3	-2.9	2.58
1200S250-97-DFM-2	1626	1148	1434	12.8	14.7	66.0	66.4	306.8	5.2	5.6	5.6	5.6	92.0	89.7	-4.6	-5.7	2.56
800S250-68-DFC-1	1626	618	377	12.2	14.2	63.2	64.4	204.2	4.0	4.0	4.2	4.6	91.9	89.3	-5.3	-5.0	1.79
800S250-68-DFC-2	1626	615	373	14.6	11.5	63.8	63.0	204.2	8.7	4.8	4.2	4.0	90.6	90.5	-4.1	-4.1	1.80
800S250-68-DFM-1	1626	623	378	14.2	12.4	63.8	63.8	204.3	4.4	4.8	4.0	4.0	91.7	91.0	-3.2	-3.8	1.81
800S250-68-DFM-2	1626	625	382	14.4	12.1	65.0	63.7	204.1	4.4	4.4	4.2	4.0	90.6	90.6	-4.6	-4.1	1.81
1000S200-43-LFC-1	1626	418	360	10.2	11.8	49.2	50.3	254.0	3.6	3.2	3.6	3.6	89.6	87.0	1.0	0.9	1.14
1000S200-43-LFC-2	1626	422	364	10.3	12.0	49.1	50.1	254.4	3.6	3.2	3.6	3.6	90.5	86.8	0.7	2.0	1.15
1000S200-43-LFM-1	1626	422	364	10.3	12.0	49.2	50.2	254.5	3.6	3.2	3.6	3.6	90.4	87.4	0.2	1.1	1.15
1000S200-43-LFM-2	1626	424	365	10.1	12.0	49.2	50.3	254.4	3.6	3.2	3.6	3.6	90.8	87.2	0.3	1.5	1.16
800S200-33-LFC-1	1626	285	168	14.5	14.7	49.9	49.9	204.7	3.6	3.2	3.6	3.2	90.7	90.6	1.9	0.1	0.88
800S200-33-LFC-2	1626	302	178	14.0	14.1	52.8	50.2	203.7	3.6	3.2	4.4	3.2	90.1	90.5	-0.7	1.0	0.93
800S200-33-LFM-1	1626	286	169	14.5	15.2	49.5	49.9	204.5	3.6	3.2	3.6	3.2	91.5	88.9	-1.7	1.1	0.88
800S200-33-LFM-2	1626	287	170	14.7	14.7	50.0	49.3	204.7	3.6	3.0	3.6	3.4	90.7	89.6	-0.8	-0.2	0.88

(a) See the dimension definitions in Fig. 4.1.

Table 4.3. Elastic buckling properties and predicted flexural capacity.

Specimen	F_y [a]	F_u [a]	M_y	M_n [b]	M_{cre}	λ_e [c]	M_{crd}	λ_d [c]	L_{crd}	$M_{cr\ell}$	λ_ℓ [c]	$L_{cr\ell}$	δ_e
	(MPa)			(kN-mm)			(kN-mm)		(mm)	(kN-mm)		(mm)	($\times 10^{-3}$mm)
1200S162-97-GFC-1	448	574	32664	15524 (11435)	15524	1.45	23387	1.18	252	28195	0.74	141	3871
1200S162-97-GFC-2	464	575	33835	15835 (11689)	15835	1.46	23557	1.20	254	28379	0.75	141	3951
1200S162-97-GFM-1	451	566	32668	15272 (11296)	15272	1.46	23276	1.18	252	28028	0.74	141	3830
1200S162-97-GFM-2	440	568	31850	16530 (11986)	16530	1.39	24544	1.14	260	29561	0.75	139	4149
800S162-97-GFC-1	452	578	17786	10005 (7416)	10006	1.33	24668	0.85	221	34810	0.54	92	6937
800S162-97-GFC-2	454	575	17752	9854 (7393)	9854	1.34	27939	0.80	249	36219	0.52	92	6867
800S162-97-GFM-1	452	579	17711	9721 (7261)	9721	1.35	24901	0.84	220	34704	0.53	92	6770
800S162-97-GFM-2	462	580	18182	9623 (7274)	9623	1.37	27902	0.81	244	36195	0.52	92	6664
1200S250-97-DFC-1	411	537	38450	27721	208449	0.43	31050	1.11	376	39466	0.99	141	10537
1200S250-97-DFC-2	385	531	35914	26249	199162	0.42	30076	1.09	367	38276	0.97	141	10255
1200S250-97-DFM-1	389	530	36673	26845	206543	0.42	30839	1.09	370	39349	0.97	141	10393
1200S250-97-DFM-2	404	532	37977	27340	208425	0.43	30546	1.12	375	38865	0.99	141	10316
800S250-68-DFC-1	385	466	14292	10247	81992	0.42	11373	1.12	410	15650	0.96	117	14595
800S250-68-DFC-2	377	462	13833	10575	82729	0.41	13084	1.03	451	16544	0.91	113	16995
800S250-68-DFM-1	376	465	14007	10658	88723	0.40	13079	1.03	462	16680	0.92	113	16739
800S250-68-DFM-2	377	464	14148	10719	91237	0.39	13057	1.04	469	17022	0.91	113	16570
1000S200-43-LFC-1	424	478	12034	6056	36445	0.57	3997	1.74	363	3378	1.89	139	6037
1000S200-43-LFC-2	421	476	12047	6125	36989	0.57	4098	1.71	365	3443	1.87	139	6098
1000S200-43-LFM-1	418	479	11983	6114	37083	0.57	4110	1.71	365	3454	1.86	139	6111
1000S200-43-LFM-2	419	476	12045	6090	36932	0.57	4045	1.73	358	3468	1.86	140	6123
800S200-33-LFC-1	335	403	5550	3197	26252	0.46	3136	1.33	582	1797	1.76	109	6881
800S200-33-LFC-2	307	371	5377	3358	30191	0.42	3417	1.25	578	2184	1.57	109	7907
800S200-33-LFM-1	335	404	5575	3208	25679	0.47	3190	1.32	575	1799	1.76	110	6858
800S200-33-LFM-2	337	405	5632	3257	26365	0.46	3257	1.31	586	1843	1.75	109	7001

(a) F_y , F_u = yielding and ultimate stresses respectively measured from coupon tests.
(b) M_n = predicted capacity using AISI-S100-12 [22], values in parentheses are predicted capacity using Eurocode-3 [72].
(c) $\lambda_e = (M_y/M_{cre})^{0.5}$; $\lambda_d = (M_y/M_{crd})^{0.5}$; $\lambda_\ell = (M_{ne}/M_{cr\ell})^{0.5}$; M_{ne} = predicted flexural capacity for lateral-torsional buckling.

4.2.3 Test setup and instrumentation

Tests were conducted in a four point bending configuration to produce constant moment along the unbraced length. All members span 4877mm from end support to support and are loaded through an adjustable spreader beam that accommodates variation in loading point location to change the unbraced length L_u (see Fig. 4.2). Loading attachments and end supports were detailed to allow rotation about the cross-section major bending axis. Slotted holes were used at the supports and at one of the loading points to prevent axial forces from developing in the specimen. Lateral braces were placed along the shear spans of length *a*, to develop longitudinal warping and minor axis flexure fixed conditions at the loading points that defined the unbraced length.

A cyclic displacement history was applied at the loading points using a customized control program receiving feedback from two vertical linear potentiometric transducers placed at the load points. A displacement rate was derived such that the strain rate at the extreme fiber remained constant at 0.002 mm/mm/min. Based on monotonic tension coupon tests described in the literature, this displacement rate is expected to produce yield stresses approximately 2% larger

than the static yield stress [50]. The displacement rate for the monotonic tests was derived based on a constant strain rate at the extreme fiber of 0.00003 mm/mm/min, which corresponds to 1/3 of the maximum rate of 21MPa per minute recommended in the AISI test method for flexural testing of cold-formed steel beams [74]. The derived displacement rates applied at the loading points for each type of specimen are listed in Table 4.1.

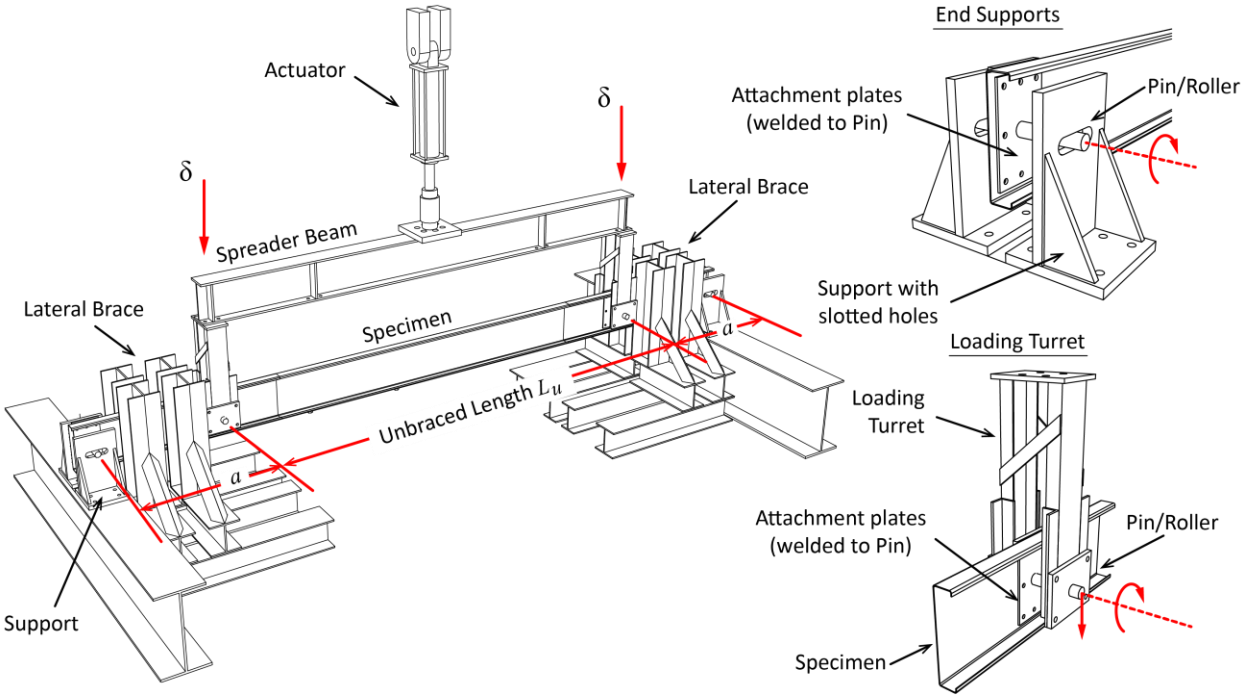

Fig. 4.2. Test setup with support and loading details.

4.2.4 Displacement-controlled testing protocol

The displacement-controlled testing protocol (see Fig. 4.3) is adapted from the FEMA 461 quasi-static cyclic deformation-controlled testing protocol. The FEMA 461 protocol was developed to obtain fragility data and hysteretic response characteristics of building components for which damage is best predicted by imposed deformations [30]. CFS flexural members can experience symmetrical or asymmetrical loading depending on the end connections (e.g., screwed or welded connection), bracing conditions, and location within a building system (e.g., floor joist compared to a stud in a shear wall). The adapted protocol is fully reversed with symmetric displacement amplitudes. The loading protocol comprises steps of increasing amplitude with two cycles per step. Each step's displacement amplitude is 40% larger than the previous, i.e., $\delta_i = 1.4\delta_{i-1}$ (see Fig. 4.3). The loading protocol is anchored to the elastic displacement, $\delta_e = M_e a(3L_u + 2a)/6EI$

(EI = elastic bending stiffness), at the fourth step (i.e., 7th and 8th cycles). The moment associated with stiffness degradation from buckling deformations, M_e, is estimated using slenderness limits defined in the AISI Direct Strength Method (DSM) [22]. The DSM approach predicts that local buckling initiates at λ_ℓ=0.776 and the distortional buckling initiates at λ_d=0.673. Calculating the slenderness $\lambda=(M_e/M_{cr})^{0.5}$, the moments associated with stiffness degradation from buckling deformations are M_e=0.60$M_{cr\ell}$ and M_e=0.45M_{crd} for local and distortional buckling respectively. The DSM approach estimates that global buckling deformations initiate at M_e=0.36M_{cre}. Elastic displacements, δ_e, are listed in Table 4.3 for all specimens.

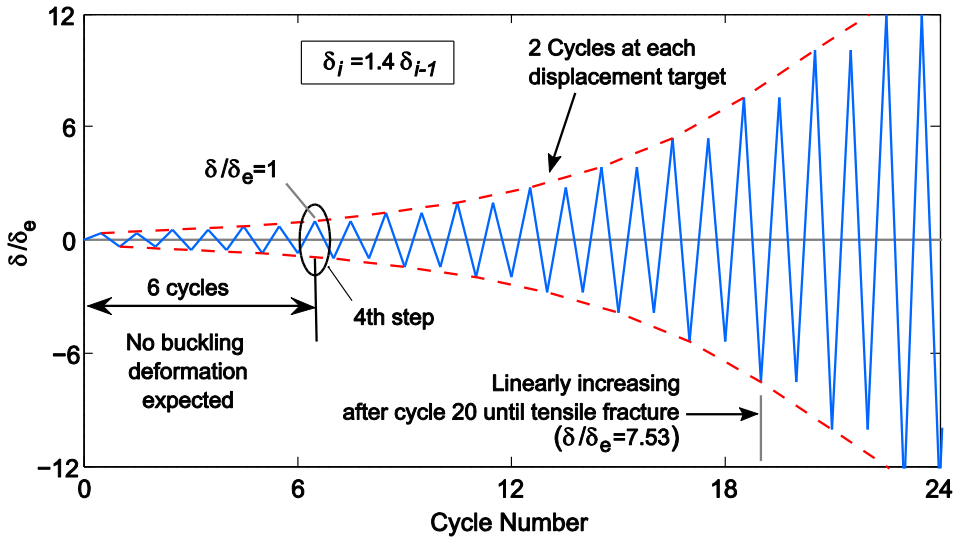

Fig. 4.3. Cyclic flexural cold-formed steel loading protocol.

4.2.5 Specimen imperfections

Initial geometric imperfections in CFS members reduce flexural strength and initial stiffness. The predicted strength decreases the most if the imperfections resemble the governing buckling modes [47,52,53]. Member imperfections are defined as the specimen geometry deviations from the straight "perfect" member before attaching it to the supports (see Fig. 4.4). Imperfections were measured and characterized using methods described in [54].

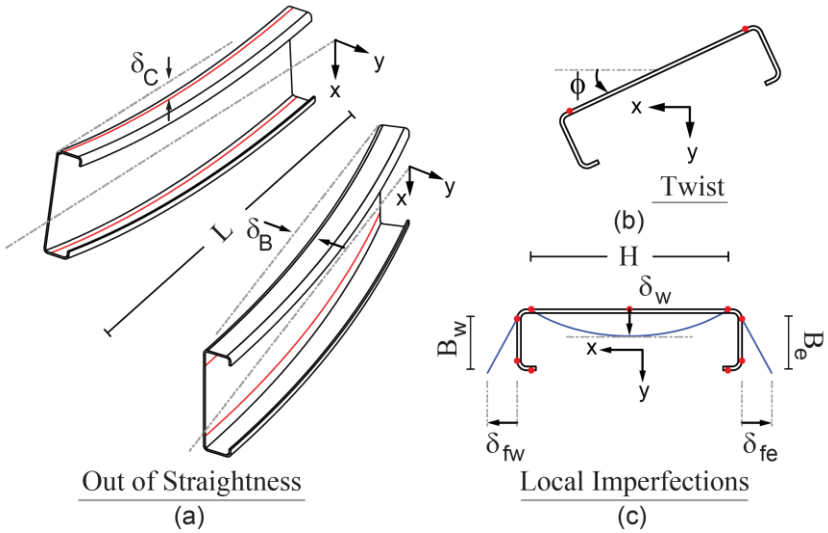

Fig. 4.4. Member imperfections: (a) global out-of-straightness (sweep); (b) initial twist; and (c) local web and flange imperfections.

The average global sweep imperfections δ_B in distortional and local buckling specimens (short members) were smaller than the tolerance limits given in ASTM C955-09 [55] as shown in Table 4.4. For global buckling specimens (long members), the average sweep δ_B was larger than the ASTM limit of $L/960$ leading to measured flexural strengths, M_{max}, less than the predicted M_n (see section 4.3.1). Global buckling specimens (L_u=3048mm) with the highest thickness t=2.51 mm have the largest sweep imperfections. Imperfection magnitudes in CFS members are known to increase with sheet thickness because of plastic strains and associated residual curvature caused by coiling the sheet for transportation and manufacturing [56,53]. Out-of-straightness in the strong axis direction δ_C was smaller than the ASTM limits for all specimens. Local imperfections were also all lower than ASTM limits and smaller than δ_w/t = 1.35 and δ_f/t = 3.44 associated with occurrence probabilities P($\delta<\delta_w$) = 0.95 and P($\delta<\delta_f$) = 0.95 in [28]. A detailed discussion about the measured imperfections and their characterization from this testing program can be found in [54].

Table 4.4. Test specimen measured imperfections statistics.

Specimen group		δ_B/L ($\times10^{-3}$)	δ_C/L ($\times10^{-3}$)	ϕ (°)	δ_W/H ($\times10^{-3}$)	δ_{FE}/B_e ($\times10^{-3}$)	δ_{FW}/B_w ($\times10^{-3}$)
Global	Mean	1.45 (L/689)	0.37 (L/2710)	0.49	2.25 (H/444)	33.55 (B/30)	55.78 (B/18)
	Max	2.02 (L/495)	0.63 (L/1570)	0.64	2.84 (H/352)	60.13 (B/17)	66.30 (B/15)
	Min	1.01 (L/986)	0.15 (L/6770)	0.32	1.67 (H/600)	17.59 (B/57)	35.88 (B/28)
	St.Dev	0.52	0.25	0.16	0.59	23.17	17.24
	COV	0.36	0.67	0.34	0.26	0.69	0.31
Distortional	Mean	0.12 (L/8250)	0.35 (L/2880)	0.29	2.60 (H/385)	16.31 (B/61)	20.51 (B/49)
	Max	0.17 (L/5940)	0.55 (L/1820)	0.51	3.67 (H/272)	22.49 (B/44)	31.69 (B/32)
	Min	0.09 (L/11500)	0.16 (L/6370)	0.08	1.80 (H/557)	11.27 (B/89)	13.70 (B/73)
	St.Dev	0.04	0.16	0.19	0.93	4.74	8.01
	COV	0.29	0.47	0.67	0.36	0.29	0.39
Local	Mean	0.24 (L/4130)	0.29 (L/3500)	0.29	4.87 (H/205)	23.66 (B/42)	28.21 (B/35)
	Max	0.44 (L/2260)	0.46 (L/2200)	0.45	5.30 (H/189)	26.78 (B/37)	33.77 (B/30)
	Min	0.12 (L/8420)	0.18 (L/5630)	0.21	4.32 (H/231)	19.96 (B/50)	20.66 (B/48)
	St.Dev	0.14	0.12	0.11	0.42	3.39	6.29
	COV	0.59	0.42	0.39	0.09	0.14	0.22
ASTM C955 Tol.		*L*/960	*L*/960	*L*/*H*/384	1.59mm (max)	1.59mm (max)	1.59mm (max)

See imperfection definition in Fig. 4.4.

4.3 Experimental Results

Moment-rotation (M–θ) responses were obtained for all specimens. Experimental values for rotation $\theta=\delta/a$, were calculated as the average displacement measured at the loading points, δ, divided by the shear span, a. This approximation is consistent with lumped-spring models for CFS flexural members, e.g. [18]. Rotations are normalized to the yield rotation, $\theta_y = \delta_y/a$, [$\delta_y=aM_y(3L_u+2a)/6EI$], which corresponds to the yield moment $M_y=SF_y$ (S is the elastic section modulus). Experimental values of the moment are calculated as $M=aP$, where P is half of the measured vertical load. Positive moment and rotations correspond to downward loading and the negative values correspond to upward loading. The loading protocol was continued to the maximum stroke of the hydraulic actuator or until the distance available to slide at the supports was expended. All members were deformed to a maximum downward/upward displacement of at least 63mm. The following sections describe details of the monotonic and cyclic tests for each buckling limit state. Test videos are available in Virginia Tech's digital repository [75].

4.3.1 Monotonic flexural responses

Monotonic flexural responses of members that experienced global (GFM), distortional (DFM), and local (LFM) buckling are shown in Fig. 4.5. The pre-peak responses are linear past 50% of the peak moment for all members and became nonlinear when buckling deformations appeared. Buckling in all members started before the peak moment and cross-section failure

happened close to the mid-span (see Fig. 4.6), with the exception of specimen 8DFM-2 where failure occurred half way between the mid-span and loading point; however, the moment-rotation behavior was still consistent with the other specimen in the group, 8DFM-1.

The average ratio of measured peak moment to predicted nominal capacity M_{max}/M_n was 0.96 with a coefficient of variation (COV) of 0.21 for all monotonic tests (see Table 4.5 and 4.6). When considering only local and distortional buckling specimens, the average test-to-predicted moment ratio is 1.09 and coefficient of variation is 0.08 (see Table 4.6 and 4.6) while for global buckling the test-to-predicted mean was 0.70. The low test-to-predicted M_{max}/M_n ratios for global buckling specimens resulted from large sweep imperfections on average of $L/767$ coupled with the unconservative AISI code treatment (e.g., AISI-S100-12 Section C.3.1.2.1 or Appendix 1.2.2.1, [22]) that equates the capacity to the critical elastic buckling moment without consideration of initial imperfections. If M_n is calculated using Eurocode-3, which includes an imperfection factor $\alpha = 0.49$ for lateral-torsional buckling [72], the average M_{max}/M_n ratio for global buckling members becomes 0.94 with a COV=0.04 (see Table 4.3, 4.5 and 4.6).

The measured initial stiffness k is not influenced by imperfections for all specimens as the average test-to-predicted stiffness ratio k/k_e was 0.95 (COV=0.04), with the global buckling specimens showing the lowest average $k/k_e = 0.93$ (COV=0.04), see Table 4.5 and 4.6. With these statistics the member initial stiffness is shown to be accurately characterized by $k_e = 6EI/(3L_u+2a)$.

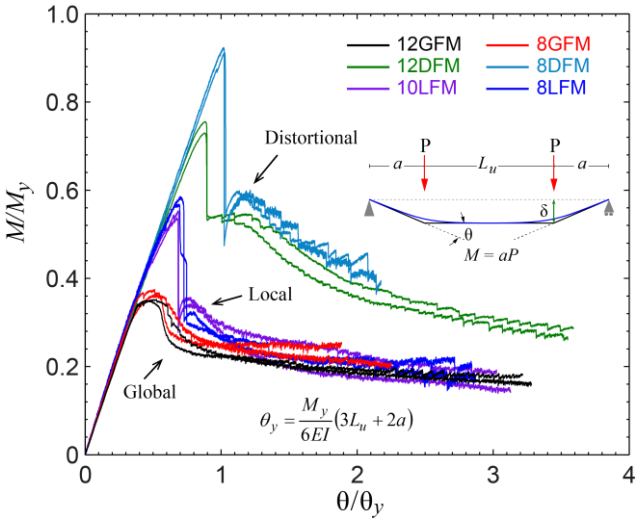

Fig. 4.5. Monotonic flexural responses normalized to the yield moment and rotation. Flexural capacity and post-peak response are least affected by buckling deformations for specimens 8DFM and 12DFM.

Fig. 4.6. Flexural buckling modes, (a) lateral torsional buckling;
(b) distortional buckling; (c) local buckling.

4.3.1.1 Global buckling members GFM

Global buckling flexural members (GFM) exhibited lateral-torsional buckling deformation that started before the maximum flexural strength M_{max}, see Fig. 4.6a. At peak moment, the top flange at intersection with the stiffening lip experienced inelastic local buckling and strength dropped rapidly to about 70% of the peak-moment. The moment-rotation response stabilized around $0.2M_y$ for both cross-section types (Fig. 4.5). Even though the top flanges buckled and did not contribute to the flexural-torsional stiffness, the members were still able to carry load for large deformations because the web and web-flange intersections maintained their shape without plastic deformations spreading across the cross section. Inelastic deformations developed close to the loading points as the second hinge formed in the later test stages.

4.3.1.2 Distortional buckling members DFM

Specimens in group 8DFM exhibited distortional buckling of the top flange and top portion of the web with three half-waves similar to the ones showed in Fig. 4.6b. Once the maximum moment strength, M_{max}, was reached, the top flange failed locally and strength dropped almost

instantly to 65% the peak moment. Inelastic strains accumulated around the failed cross-section and the section folded into itself as deformations increased. Out-of-plane deformations related to lateral-torsional buckling were not observed and no hinges formed at the loading points.

Distortional buckling specimens in group 12DFM experienced buckling of the top portion of the web and flanges with four half-waves as seen in Fig. 4.6b. The top flange failed locally at the maximum strength, M_{max}, and strength dropped almost instantly to 75% of the peak moment (Fig. 4.5). The post-peak behavior resembled lateral-torsional buckling with large out-of-plane deformation. Inelastic deformations developed close to the loading points as additional hinges formed in the later stages of the test with strength degrading to values around $0.3M_y$.

4.3.1.3 Local buckling members LFM

Local buckling specimens 8LFM showed buckling of the top portion of the web with 14 half-waves before the maximum flexural strength, M_{max}. At peak moment, the top part of the web close to the junction with the flange yielded and the mid cross-section buckled (Fig. 4.6c) accompanied by a sudden drop, to 50% of the peak moment. The strength then degraded slowly and stabilized around $0.2M_y$ (Fig. 4.5). After the mid-span cross-section buckled the response resembled lateral torsional buckling. Inelastic deformation developed close to the loading points in the later test stages.

Local buckling specimens 10LMF buckled with about eight half-waves at the top portion of the web in the early cycles, and this quickly changed to distortional buckling with four half-waves in the top flange before the maximum flexural strength M_{max}. These members had top flange stiffening lips shorter than the nominal values (10.2 mm measured as compared to nominal 15.8mm). Because of these shorter lips, the average predicted strength by DSM for distortional buckling, M_{nd} =6096kN-mm, was less than predicted strength for local buckling, $M_{n\ell}$ =6624kN-mm, which was also reflected in the observed buckling mode. At peak moment, the top flange locally buckled and strength dropped almost instantly to 65% of M_{max}. The post-peak behavior resembled the behavior of the 8LMF members with large deformations and gradual strength degradation to values around $0.2M_y$.

Table 4.5. As tested peak moments, rotations, and initial stiffness.

Specimen	M_{max}	M_{min}	θ_{Mmax}	θ_{Mmin}	θ_y	k_e	k	M_{max}/M_n	M_{min}/M_n	θ_{Mmax}/θ_y	θ_{Mmin}/θ_y	k/k_e
	(kN-mm)		($\times 10^{-3}$rad)			(kN-m/rad)						
1200S162-97-GFC-1	10290	-10450	13	-13	27	1200	1050	0.66 (0.90)	0.67 (0.91)	0.48	-0.48	0.87
1200S162-97-GFC-2	11270	-11255	12	-11	28	1200	1065	0.71 (0.96)	0.71 (0.96)	0.42	-0.38	0.89
1200S162-97-GFM-1	11505		13	-	27	1195	1075	0.75 (1.02)	-	0.47	-	0.90
1200S162-97-GFM-2	11305		14	-	27	1190	1085	0.68 (0.94)	-	0.52	-	0.91
800S162-97-GFC-1	6905	-6630	20	-20	41	430	415	0.69 (0.93)	0.66 (0.89)	0.50	-0.50	0.97
800S162-97-GFC-2	7065	-6775	21	-20	41	430	415	0.72 (0.96)	0.69 (0.92)	0.50	-0.48	0.97
800S162-97-GFM-1	6500		21	-	41	430	415	0.67 (0.90)	-	0.51	-	0.96
800S162-97-GFM-2	6905		21	-	42	430	420	0.72 (0.95)	-	0.50	-	0.97
1200S250-97-DFC-1	28505	-29080	17	-16	19	2060	1940	1.03	1.05	0.91	-0.85	0.94
1200S250-97-DFC-2	28120	-28590	16	-16	18	2050	1900	1.07	1.09	0.94	-0.90	0.93
1200S250-97-DFM-1	26885		16	-	18	2075	1920	1.00	-	0.88	-	0.93
1200S250-97-DFM-2	28850		16	-	18	2070	1955	1.06	-	0.88	-	0.94
800S250-68-DFC-1	12030	-13405	23	-26	26	545	530	1.17	1.31	0.89	-0.99	0.97
800S250-68-DFC-2	13245	-11175	26	-22	26	540	520	1.25	1.06	1.02	-0.85	0.96
800S250-68-DFM-1	13070		26	-	26	545	525	1.23	-	1.02	-	0.96
800S250-68-DFM-2	12990		26	-	26	550	510	1.21	-	1.02	-	0.93
1000S200-43-LFC-1	6390	-7180	14	-15	23	520	515	1.05	1.19	0.61	-0.67	0.99
1000S200-43-LFC-2	6940	-7425	16	-16	23	525	525	1.13	1.21	0.69	-0.70	1.00
1000S200-43-LFM-1	6705		16	-	23	525	530	1.10	-	0.68	-	1.01
1000S200-43-LFM-2	6555		15	-	23	525	505	1.08	-	0.67	-	0.96
800S200-33-LFC-1	3490	-3325	16	-15	23	245	240	1.09	1.04	0.71	-0.64	0.98
800S200-33-LFC-2	3210	-3475	14	-14	20	255	250	0.96	1.03	0.73	-0.72	0.98
800S200-33-LFM-1	3355		16	-	23	245	245	1.05	-	0.70	-	1.01
800S200-33-LFM-2	3300		15	-	23	245	235	1.01	-	0.66	-	0.97

(a) M_{max}, θ_{Mmax}= maximum moment and corresponding rotation; M_{min}, θ_{Mmin}= minimum moment and corresponding rotation.
(b) $k_e = 6EI_x/(3L_u+2a)$, the initial elastic stiffness; k = measured initial stiffness $\theta_y = M_y/k_e$, the yielding rotation.
(c) Values between parentheses are calculated using Eurocode-3 [72].

Table 4.6. Test-to-predicted statistics.

Specimen Group	M_{max}/M_n		M_{min}/M_n		θ_{Mmax}/θ_y		θ_{Mmin}/θ_y		k/k_e	
	μ	COV	μ	COV	μ	COV	μ	COV	μ	COV
Global	0.70 (0.94)	0.04	0.68 (0.92)	0.03	0.49	0.06	0.46	0.11	0.93	0.04
Distortional	1.13	0.09	1.13	0.11	0.95	0.07	0.90	0.07	0.95	0.02
Local	1.06	0.05	1.12	0.08	0.68	0.05	0.68	0.05	0.99	0.02
L & D	1.09	0.08	1.12	0.09	0.81	0.18	0.79	0.18	0.97	0.03
Cyclic	0.96	0.22	0.98	0.24	0.70	0.30	0.68	0.28	0.96	0.04
Monotonic	0.96	0.21	-	-	0.71	0.28	-	-	0.95	0.04
All Spec.	0.96	0.21	0.98	0.24	0.71	0.28	0.68	0.28	0.95	0.04

(a) μ = mean value; COV= coefficient of variation; L&D= Local and Distortional.
(b) Values between parentheses are calculated using M_n from Eurocode-3 [72].

4.3.2 Cyclic flexural responses

For all cyclic tests, the moment-rotation response was linear elastic past the first six cycles with similar stiffness in both loading directions (see, Fig. 4.7a, 4.9a, and 4.11a). Buckling deformations typically started after cycle 10 in a pattern similar to the monotonic members and as illustrated in Fig. 4.7, 4.9, and 4.11. Specimens generally buckled at different locations during positive and negative flexure due to strain hardening and redistribution of stresses around the first buckled cross-section. Despite this, the cyclic moment-rotation response was symmetric for most of the members with three exceptions described in the following sections. The average ratio of test

peak moment to predicted moment for cyclic tests was 0.96 (COV=0.22) and 0.98 (COV=0.24) for positive and negative moment respectively.

4.3.2.1 Flexural members experiencing global buckling (GFC)

Global buckling members subjected to cyclic loading (GFC) exhibited lateral-torsional buckling similar to their monotonic counterparts as illustrated in Fig. 4.7d. Strength decreased rapidly after the peak to about 65% M_{max}, then continued to degrade slowly. The moment-rotation response stabilized around $0.2M_y$ for both cross-section types, which could have implications in seismic design with regards to residual load-carrying capacity, see Fig. 4.7c. Even though the flanges have buckled and are not contributing to the flexural-torsional stiffness, the members are still able to sustain moment at large deformations because of redistribution of the stresses towards the loading supports through the web and web-flange intersections. Pinching of the response (Fig. 4.7b) occurred because upon unloading, the member straightened out (towards the unbuckled initial position) before starting to load in the opposite direction. Damage due to inelastic strains accumulated at the buckled flanges close to the stiffening lips which led to tearing during the last cycles. This tearing did not propagated to the flanges. Cyclic strength degradation is minimal when comparing monotonic cyclic responses in Fig. 4.8.

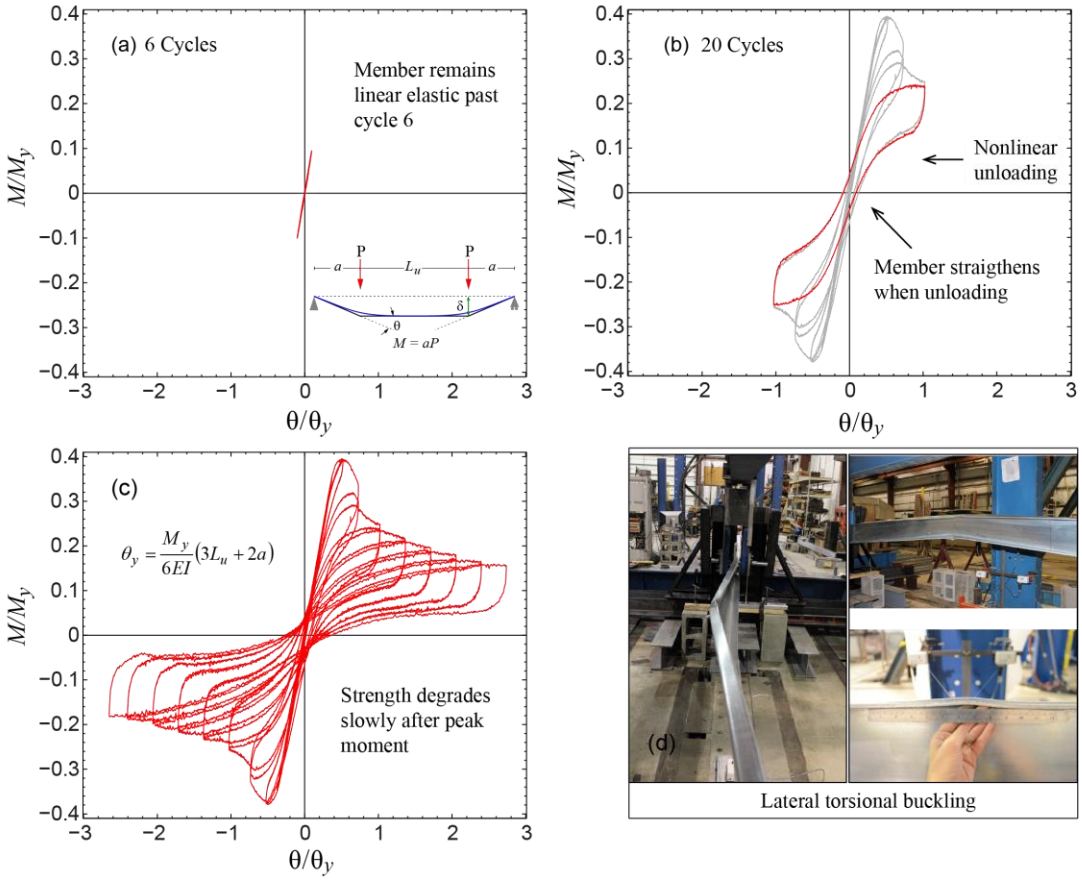

Fig. 4.7. Cyclic moment-rotation response specimen 800S162-97-GFC-2 at: (a) 6 cycles, (b) 20 cycles, (c) complete response, (d) failure mode.

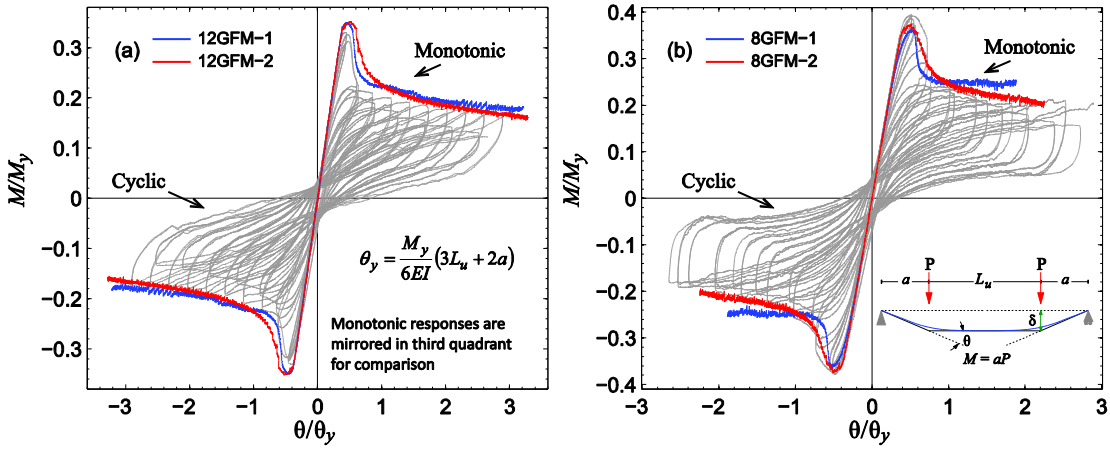

Fig. 4.8. Global buckling monotonic response envelope: (a) 12 series, (b) 8 series. Cyclic strength degradation is minimal when comparing monotonic cyclic responses.

4.3.2.2 Flexural members experiencing distortional buckling (DFC)

Distortional members (DFC) showed buckling of the top flange and top portion of the web similar to their monotonic counterparts as illustrated in Fig. 4.9d. Moment strength dropped almost

instantly after the peak moment to about 60% and 70% of the peak for the 8DFC and 12DFC members respectively. Cyclic strength degradation occurred as damage accumulated at the buckled flanges as evidenced by the gap between the monotonic curves and cyclic envelopes in Fig. 4.10. Stiffness degraded with every cycle as well. Slight pinching of the hysteretic response occurred as the buckled flange straightened out during load reversal (Fig. 4.9b). The 12DFC members moment response was symmetric where top and bottom flanges buckled at the mid-span cross-section and subsequent large deformations occurred while sustaining moments around $0.2M_y$ (Fig. 4.9c). Damage also accumulated close to the loading points for the 12DFC as hinges formed in the last cycles creating a shape resembling lateral-torsional-buckling. The response of the 8DFC members was slightly asymmetric because buckling occurred at two different locations, the mid-span cross-section in positive moment and close to the loading point in negative moment. This ultimately affected their post-peak behavior which consisted of folding of the buckled cross-sections without formation of additional hinges.

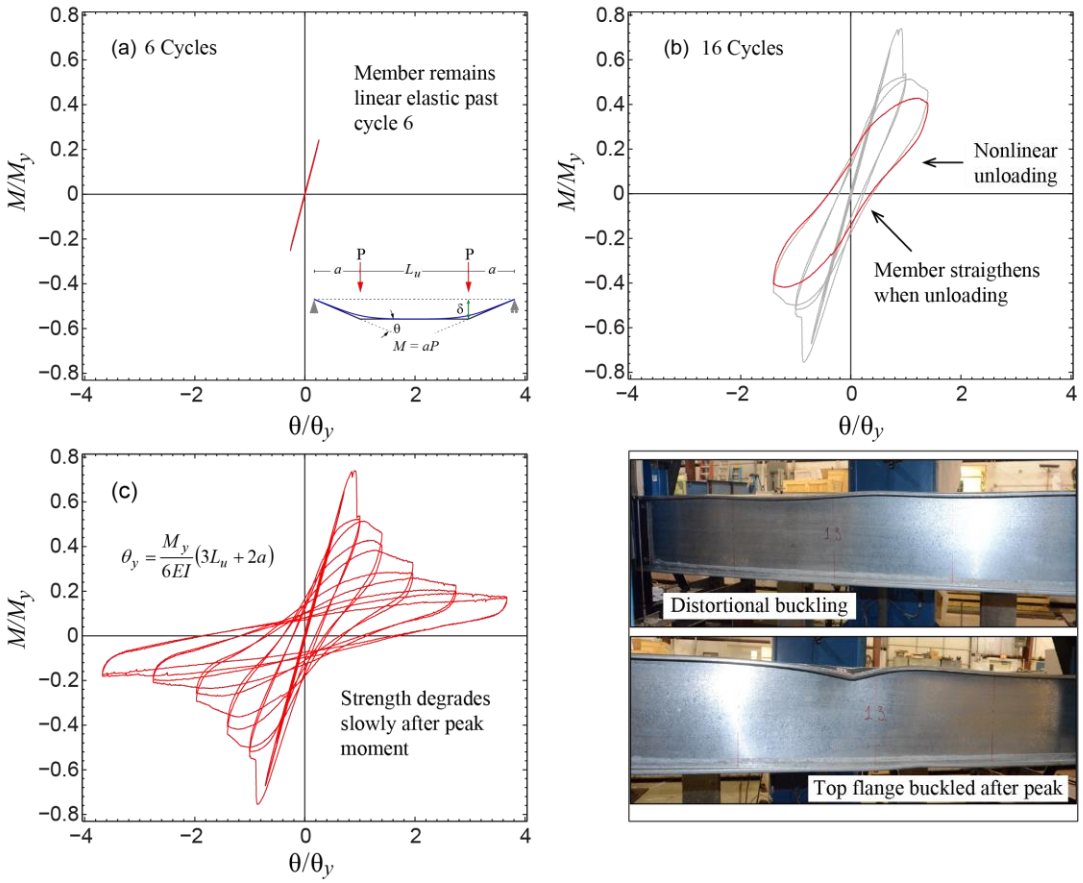

Fig. 4.9. Cyclic moment-rotation response specimen 1200S250-97-DFC-1 at:
(a) 6 cycles, (b) 16 cycles, (c) complete response, (d) failure mode.

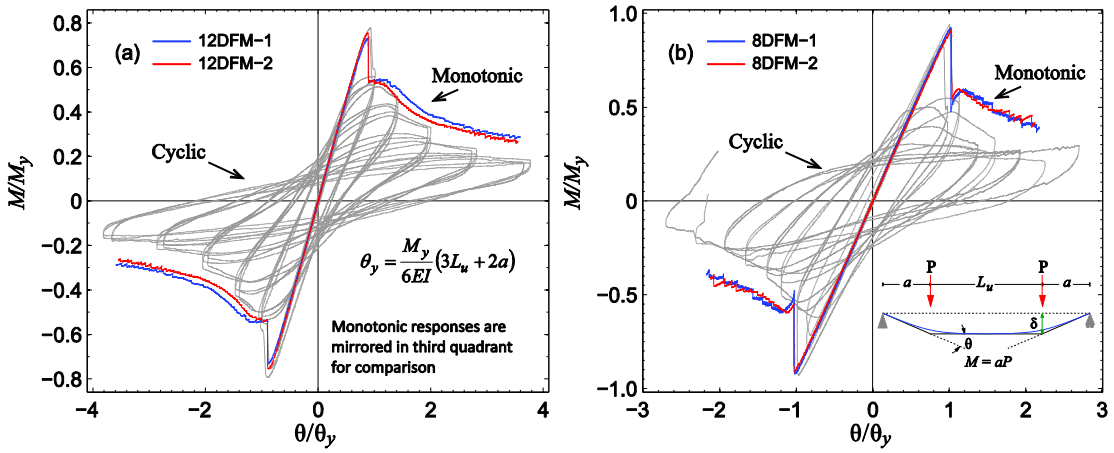

Fig. 4.10. Distortional buckling monotonic response envelope: (a) 12 series, (b) 8 series. Cyclic strength deterioration at the end of test is around 56% and 64% of the corresponding strength under monotonic loading for 8DFC and 12DFC specimens respectively.

4.3.2.3 Flexural members experiencing local buckling (LFC)

Local members (8LFC) buckled similar to their monotonic counterparts as illustrated in Fig. 4.11d. Strength dropped almost instantly after the peak moment to about 40% of M_{max}, then degraded as the inelastic deformations accumulated at the top part of the web close to the web-flange junction. Slight pinching of the hysteretic response occurred as the member straightened during load reversal (Fig. 4.11b). The response of the 8LFC-1 member was symmetric where web buckling occurred at the mid-span followed by large deformations while carrying moments around $0.1M_y$ (Fig. 4.11c). Damage also accumulated close to one of the loading points for this member. The response of member 8LFC-2 shown in Fig. 4.12b, was similar to 8LFC-1 however, the cross-section at the only hinge folded into itself as post-peak deformations increased, providing stiffness and strength gains in both directions during the last cycles.

Local members 10LFC exhibited local web buckling before peak load that quickly shifted to a distortional buckling pattern similar to their monotonic counterparts. These members also had stiffening lips shorter than the nominal values (10.3 mm measured as compared to nominal 15.8mm). Strength dropped nearly instantaneously after the peak moment to about 55% of M_{max} and then degraded as damaged accumulated at the mid span and in later cycles close to the loading points. The response of specimen 10LFC-2 was asymmetric because of the different directions that the out-of-plane deformations formed in positive and negative moment. The out-of-plane deformations in the positive moment direction favored higher strengths because of compatibility-

based membrane tension stiffening. This stiffening effect was not present in the negative moment direction because the bottom flange buckled close to the loading supports forming additional hinges.

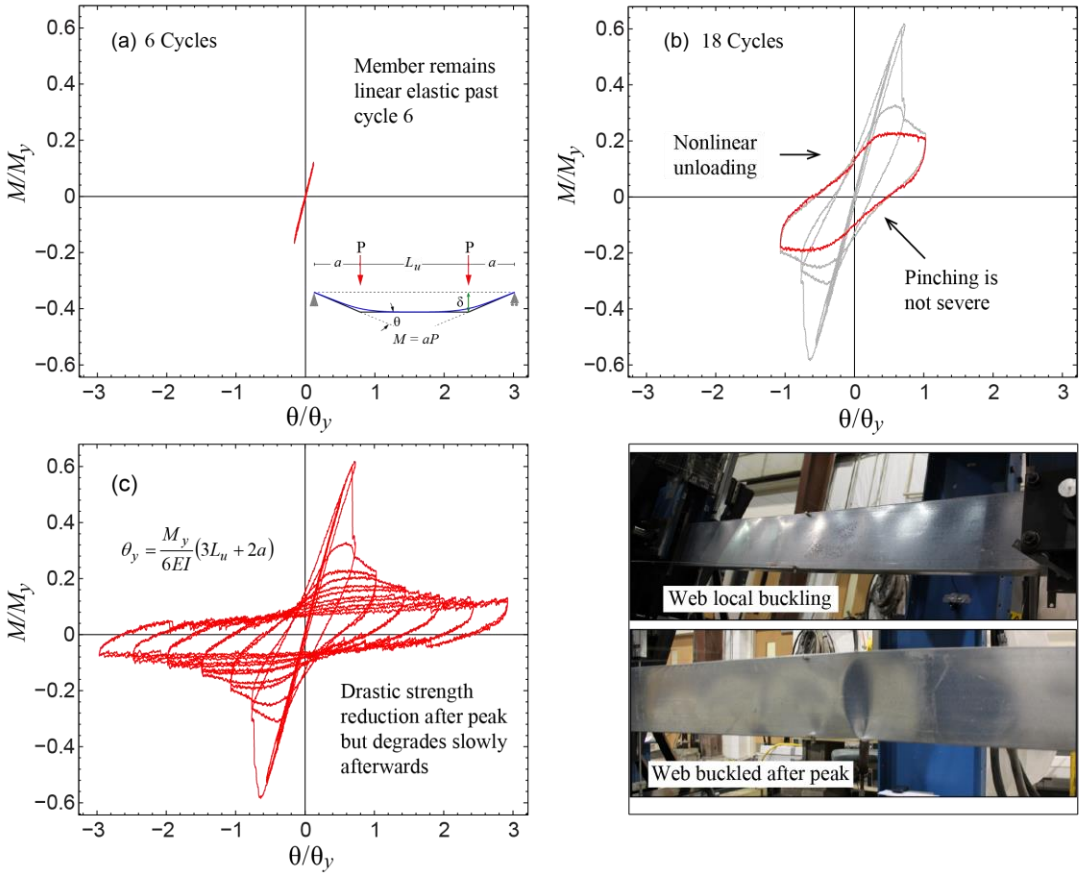

Fig. 4.11. Cyclic moment-rotation response specimen 800S200-33-LFC-1 at: (a) 6 cycles, (b) 18 cycles, (c) complete response, (d) failure mode.

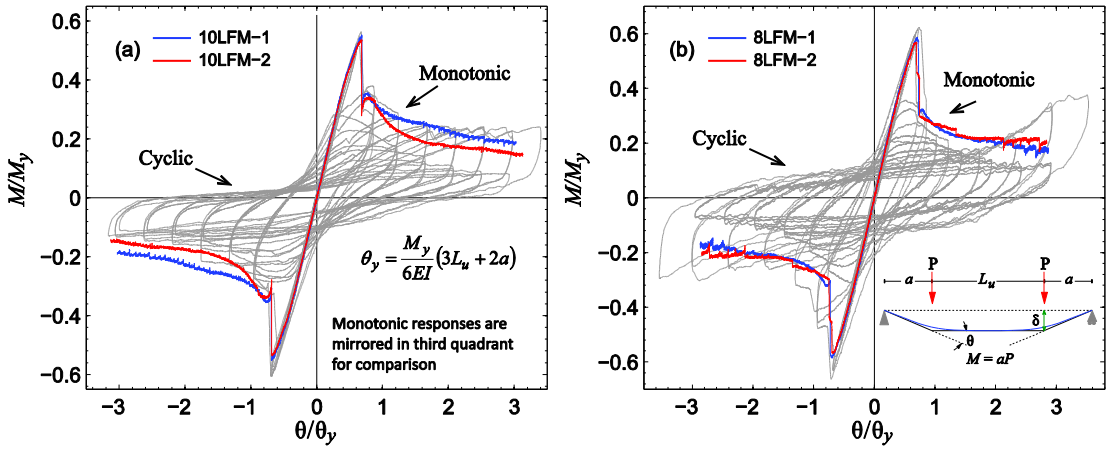

Fig. 4.12. Local buckling monotonic response envelope, (a) 10 series, (b) 8 series. Strength degrades no more than 40% the corresponding strength under monotonic loading for both 10LFC and 8LFC specimens.

4.3.3 Moment-rotation response comparisons

Comparing the hysteretic response across limit states is challenging because of the different cross-sections, specimen lengths, and buckling failure modes considered in this study. The amount of strength degradation, stiffness degradation, and pinching of the hysteretic response varies for the different specimens; however, if one compares normalized cyclic response envelopes, similar characteristics can be observed across the different buckling modes, unbraced lengths and cross-sections considered.

Cyclic response envelopes were normalized to the respective yield rotation, $\theta_y = \delta_y/a$, and yield moment, M_y, as shown in Fig. 4.13. It can be seen that the average slope k/k_e for all envelopes is 0.96 (COV = 0.04) between peak positive and negative moments, and it demonstrates that the pre-peak stiffness is well characterized by $k_e = 6EI/[3L_u+2a]$ (see Table 4.5 and 4.6). Strength decreased after the peak moment by at least 35%, and then degraded at different rates as the flexural deformation, θ/θ_y, increased. All specimens had some residual load carrying capacity, on average $0.2M_y$, in both loading directions after sustaining large flexural deformations ($\theta/\theta_y \geq 2$). This result could be useful in characterizing post-peak behavior in seismic design and collapse analysis of CFS structures.

The differences observed between the moment-rotation responses associated with different buckling modes relate to the amount of stiffness degradation and pinching. There is less stiffness degradation and pinching of the hysteretic response for distortional (Fig. 4.9b) and local buckling (Fig. 4.11b) members than for global buckling members (Fig. 4.7b). This difference correlates to the failure mechanism in global buckling members, which involves inelastic local buckling deformations at the compression lip-flange accompanied by large twist plus lateral deflections at the mid-span cross-section. Accumulation of inelastic deformations at the compression lip-flange every cycle amplifies second-order effects that increase twist and lateral deflections and decrease flexural stiffness. Straightening upon unloading of the increasing large torsional deformations translates into more pinching of the moment-rotation response.

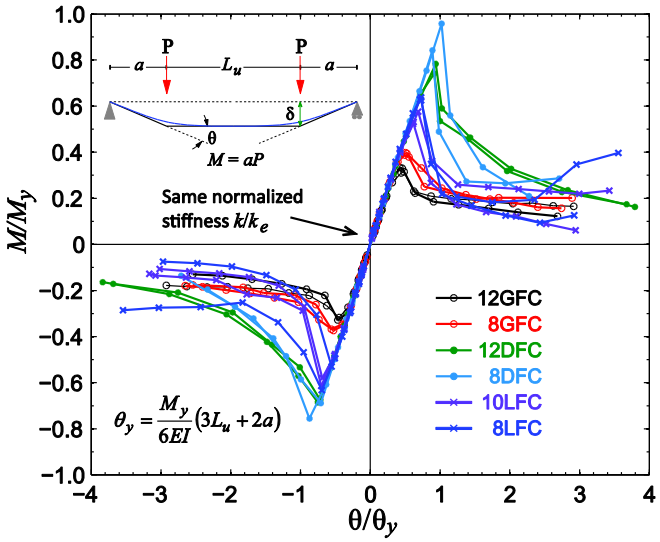

Fig. 4.13. Cyclic M-θ response envelopes show post-peak strengths dropping at least 35% of peak moments where local and distortional buckling specimens experience less strength degradation when compared to global buckling specimens.

4.3.4 Energy dissipation of CFS flexural members

Energy dissipation characteristics in global buckling specimens were different than those of local and distortional buckling specimens. Fig. 4.14 compares the normalized energy dissipated per cycle (NHE_{pc}) as a function of the cumulative flexural deformation $\Sigma\theta/\theta_y$. The energy dissipated in each cycle, $E_{c,i}$, is normalized to the area of the rectangle, E_{cr}, bounded by the maximum and minimum flexural deformation experienced in that cycle and the predicted moment strength, M_n (see inset in Fig. 4.14). Global buckling members (GFC) dissipated less energy every cycle than local or distortional members. The amount of pinching of the moment-rotation response, which was more pronounced in the GFC specimens, translated to less energy dissipated per cycle. However, energy dissipation capabilities for the GFC specimens remained relatively constant ($NHE_{pc} \approx 0.1$) with increasing flexural deformations. Conversely, energy dissipation capabilities in local and distortional buckling members reached higher NHE_{pc} values (≥ 0.2) compared to global buckling specimens, and decreased rapidly as flexural deformations increased (Fig. 4.14).

The observed differences between global buckling specimens and local and distortional buckling specimens are related to the failure mechanism and how damage accumulated after peak moment at the failed cross-sections and along the unbraced length. Damage in global buckling members was concentrated in the buckled flanges at the mid-span for most of the cycles and close to the loading points at the final cycles when additional hinges formed. In local and distortional

buckling specimens, damage initially accumulated at the compression portion of the cross section (web/flange) and quickly spread across the cross section creating yield lines with folding during every cycle. Because in global buckling members, damage did not spread to the web and folding was absent, the energy dissipation capabilities remained relatively constant.

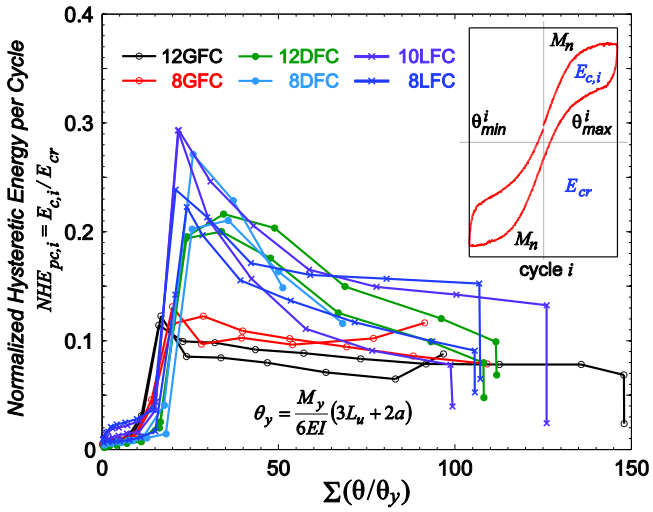

Fig. 4.14. Normalized energy dissipated per cycle (NHE_{pc}) is less and remains relatively constant in global buckling specimens compared to local and distortional buckling members as cumulative flexural deformations $\Sigma\theta/\theta_y$ increase.

Energy dissipation (per cycle and cumulative) within the damage half-wave decreases for higher cross-sectional slenderness (λ_d and λ_ℓ) and increases with the cross-section elastic modulus S as shown in Fig. 4.15 and Table 4.7. A convenient representation for these trends is to compare S/λ^2 at different cumulative flexural deformations $\Sigma\theta/\theta_y$. Energy dissipation is higher for specimens with small slenderness and large section elastic modulus compared to specimens with larger λ or smaller section modulus S. For instance, 12DFC specimens have the largest S/λ^2 (= 76.9×10^3 mm^3) values with average cumulative energy dissipated 7.45 kN-mm/mm compared to 1.29 kN-mm/mm of the 10LFC specimens (S/λ^2 = 9.58×10^3 mm^3) for the same cumulative deformation $\Sigma\theta/\theta_y$ = 50 (see Table 4.7). The inversely proportional relationship between energy dissipation and cross-sectional slenderness described is consistent with results from cyclic loaded cold-formed steel axial members observed in [77]. In the case of specimens where damage accumulated at more than one location, energy dissipation remained relatively unaffected despite having the similar slenderness and S/λ^2 values. For example, damage accumulated at two locations

in specimen 8LFC-1 but dissipated less energy compared to specimen 8LFC-2 where damage accumulated at only one location close to the mid-span (see Table 4.7). Because there is higher rotation demand in a member with a single hinge (compared to two), plastic strains accumulation is higher, which translates into more energy dissipated. The 10LFC specimens behavior at peak load was controlled by distortional buckling, therefore the respective L_{crd} and λ_d were used in the normalizations shown in Fig. 4.15.

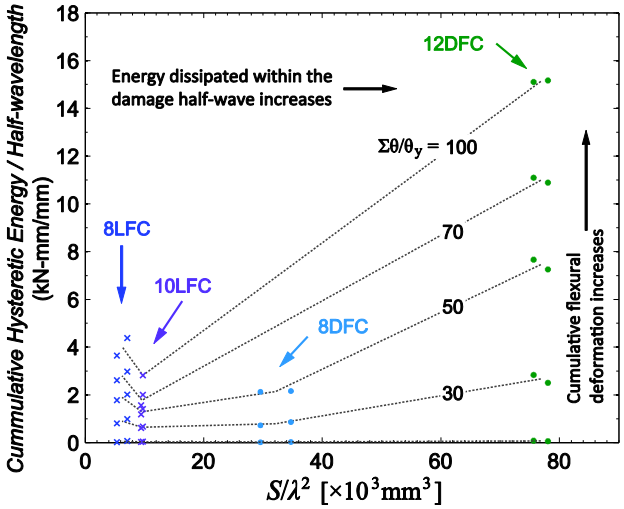

Fig. 4.15. Cumulative energy dissipated in the damaged half-wave(s) (HE_{pc}/L_{cr}) increases as a function of the section modulus S and cross-section slenderness λ for local and distortional buckling specimens.

Table 4.7. Cumulative hysteretic energy magnitudes.

Specimen	λ	S/λ^2	HE_{20}	HE_{40}	HE_{60}	HE_{80}	HE_T	HE_{20}/L_{cr}	HE_{40}/L_{cr}	HE_{60}/L_{cr}	HE_{80}/L_{cr}	HE_T/L_{cr}	max
		(×10³mm³)	(kN-mm)					(kN-mm/mm)					$\Sigma\theta/\theta_y$
1200S162-97-GFC-1	1.45	34.66	306	982	1639	2255	4258	0.201	0.644	1.075	1.479	2.794	148
1200S162-97-GFC-2	1.46	34.11	296	879	1443	1960	2497	0.194	0.577	0.947	1.286	1.639	97
800S162-97-GFC-1	1.33	22.13	276	965	1622	2279	2811	0.181	0.633	1.064	1.495	1.845	91
800S162-97-GFC-2	1.34	21.73	238	939	1630	2291	3196	0.156	0.616	1.070	1.503	2.097	109
1200S250-97-DFC-1	1.11	75.64	165	2003	3550	4690	6038	0.439	5.322	9.431	12.458	16.041	108
1200S250-97-DFC-2	1.09	78.07	132	1781	3337	4518	6098	0.360	4.856	9.097	12.318	16.625	112
800S250-68-DFC-1	1.12	29.56	56	1212	2177	-	2537	0.068	1.476	2.652	-	3.091	68
800S250-68-DFC-2	1.03	34.71	126	1413	-	-	2019	0.140	1.567	-	-	2.238	51
1000S200-43-LFC-1	1.74	9.42	135	677	1004	1251	1460	0.186	0.932	1.382	1.723	2.010	99
1000S200-43-LFC-2	1.71	9.74	150	774	1254	1663	2530	0.206	1.061	1.719	2.280	3.469	126
800S200-33-LFC-1	1.76	5.36	37	289	482	649	835	0.169	1.322	2.206	2.972	3.824	106
800S200-33-LFC-2	1.57	7.11	76	330	546	755	1028	0.352	1.517	2.511	3.473	4.727	107

HE_{xx} = cumulative hysteretic energy dissipated up to $\Sigma\theta/\theta_y = xx$;
HE_T = cumulative hysteretic energy dissipated end of test;
max($\Sigma\theta/\theta_y$) = cumulative deformation at the end of the test;
λ = governing slenderness from Table 4.3;
S = cross-section elastic modulus.

4.4 Conclusions

Cold-formed steel flexural members can dissipate energy and provide post-buckling strength and stiffness even though the flanges and/or web have buckled because of redistribution of stresses to regions next to the damaged half-wave(s). Flexural strength decreased rapidly after peak moment but some residual load carrying capacity remained, on average $0.2M_y$, while sustaining large deformations ($\theta/\theta_y>2$).

Cyclic strength degradation, cyclic stiffness degradation, and pinching of the hysteretic response varied across the different buckling modes. The unloading and reloading mechanisms affected the amount of pinching observed, which was larger in members experiencing lateral-torsional buckling and reflected in the lowest energy dissipation compared those members experiencing local and distortional buckling.

Energy was dissipated through inelastic strains and cold-bending at the buckled cross-section(s), and varied depending on the buckling mode as well as the number of locations where damage accumulated along the unbraced length. Energy dissipation capabilities remained constant for members experiencing lateral-torsional buckling while enduring large deformations. Members experiencing local and distortional buckling dissipated more energy per cycle than members experiencing lateral-torsional buckling, but the dissipation capabilities rapidly decreased as flexural deformations increased. When damage accumulated at more than one location along the unbraced length (i.e., two flexural hinges), the cumulative energy dissipated was less compared to members with similar slenderness that only exhibited one flexural hinge. Higher rotation demand in a member with a single hinge, translates into more plastic strains accumulation and more energy dissipation.

A key observation was that energy dissipation within a damaged half-wave for local and distortional buckling decreases with increasing cross-sectional slenderness (λ_d and λ_ℓ) and increases with the cross-section elastic modulus S. The results of these chapter are adapted to nonlinear hysteretic models for CFS flexural members in the next two chapters for use in computational simulation and analysis-based seismic design of cold-formed steel framed structures.

Chapter 5: Cold-Formed Steel Members Cyclic Response Characterization

In this chapter the experimental load-deflection and moment-rotation responses from Chapter 3 and 4 are characterized through calibration to a zero-length *nonlinear hysteretic spring* model that includes strength degradation, unloading stiffness degradation and pinching behavior of the observed experiments. Model parameters and damage rules are calibrated for local, distortional and global buckling as functions of the hysteretic energy dissipated. The underlying model for members behavior consist of, a *backbone curve*, *unloading-reloading paths* that account for pinching, and a *damage model* for strength and stiffness degradation.

5.1 Axial member cyclic response characterization [3]

Hysteretic models to accurately simulate the CFS axial member behavior need to capture the asymmetric nature of the cyclic response, strength and stiffness degradation, as well as the pinching of the load-deflection curve. Herein, cyclic response characterization and calibration of the hysteretic *nonlinear spring model* for CFS axial members (Fig. 5.1) is pursued using the hysteretic model *Pinching4* [21] as implemented in OpenSees [24]. The backbone curves are derived from normalized monotonic responses and the damage model for strength and stiffness deterioration is calibrated by comparing the monotonic and cyclic responses. The responses are normalized to the yield axial load P_y ($P_y=F_yA$) and the elastic yield displacement δ_y ($\delta_y = P_yL/AE$).

The typical monotonic compression response exhibits a pre-peak branch where nonlinear behavior appears as the compressive load approaches the peak load and a nonlinear post-peak branch where strength rapidly degrades as shown in Fig. 5.2a. the differences between compression backbones of the different buckling modes with global buckling reaching only $0.4P_y$ to $0.5P_y$, distortional buckling occurring at $0.5P_y$ to $0.6P_y$ and local buckling occurring around $0.8P_y$. The buckling mode also has distinct effects on the character of the strength degradation. In tension, the response is linear up to about 80% of the peak tension load when yielding starts, then a short nonlinear segment followed by a linear segment with decreased stiffness and large axial deformations up to peak load (Fig. 5.2b). Strength reduces rapidly after peak load until fracture of

---

[3] This work is published in the *2013 Structures Congress Proceedings*, with the title "**Axial Hysteretic Modeling of Cold-Formed Steel Members for Computationally Efficient Seismic Simulation**" (http://dx.doi.org/10.1061/9780784412848.084).

the cross section occurs. Cyclic responses are highly asymmetric due to buckling deformations (Fig. 5.3a-c). The amount of hysteretic energy dissipation can be related to the cross-sectional slenderness, where members experiencing inelastic buckling dissipate more energy per cycle within the damage half-wave [77]. The cyclic envelopes in Fig. 5.3d show that the members have the same pre-buckling normalized stiffness k/k_e ($k_e = AE/L$). The shape of the hysteretic pinching as the specimen was reloaded in compression is different from when the specimen is reloaded in tension, but the general pinching behavior is similar across the different buckling modes. The monotonic responses are used to define the backbone curves and to characterize the strength and stiffness degradation during the cyclic tests.

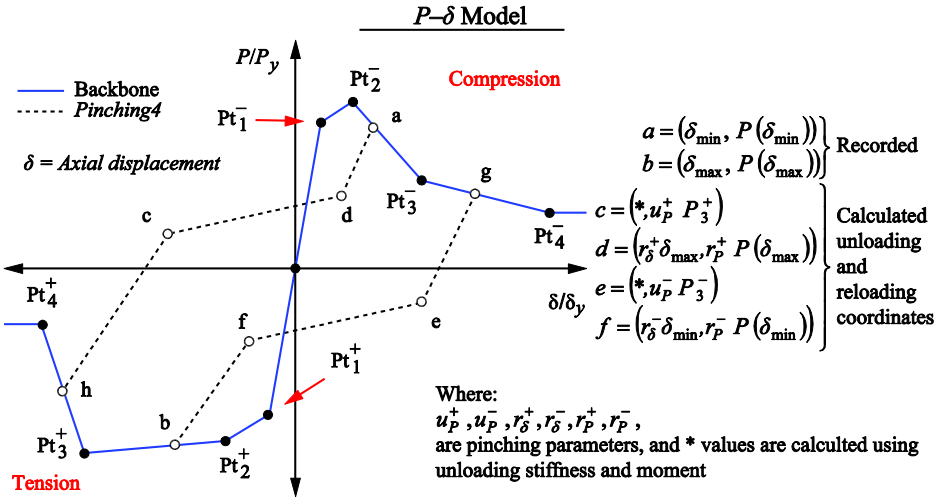

Fig. 5.1. Hysteretic spring model (*Pinching4*) for CFS axial members.

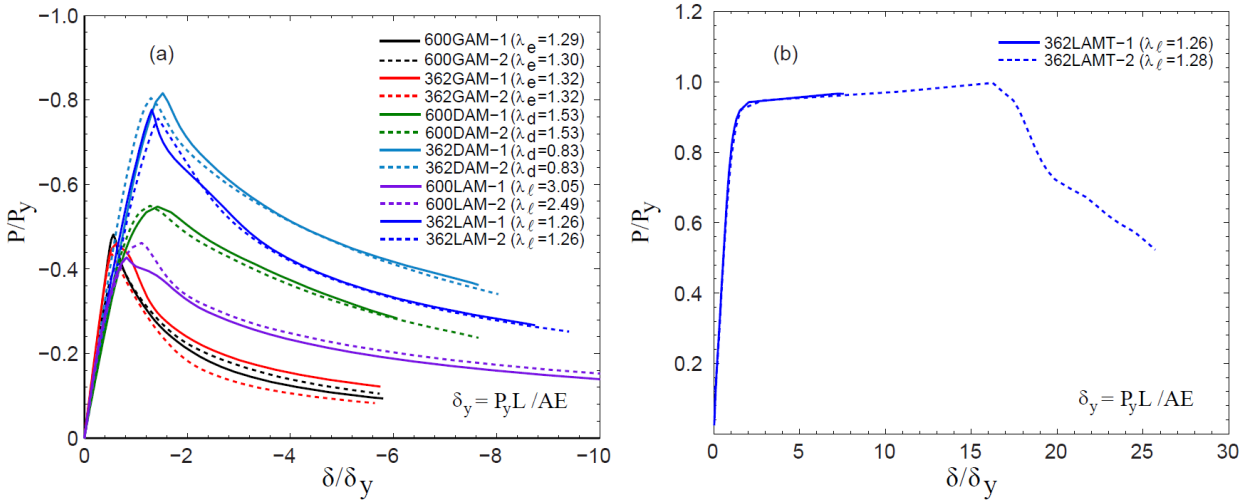

Fig. 5.2. Monotonic test sampled curves: compression (a), and tension (b).

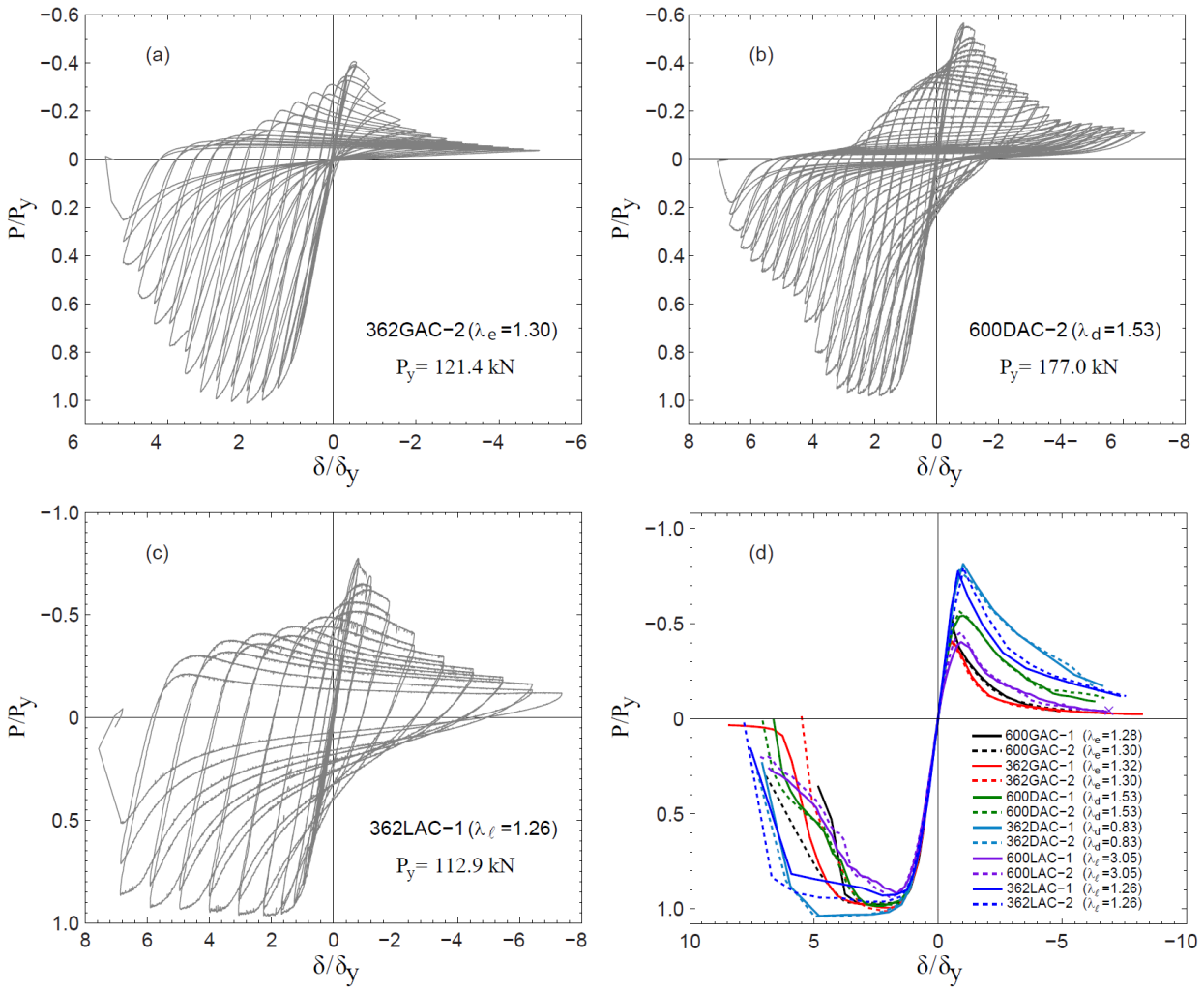

Fig. 5.3. Cyclic test: global buckling (a), distortional buckling (b), local buckling (c), and cyclic envelopes (d).

5.1.1 Axial Backbone – Monotonic Response Characterization

Backbone curves were fit to the monotonic test data using a combination of defined anchor points and fit values to match the energy represented by the area under the monotonic load-deformation curve. The backbone consists of load and displacement coordinates, labeled as δ_i, P_i in Fig. 5.1, for eight unique points, four in compression and four in tension. It is noted that the hysteric modeling is conducted in normalized coordinates (δ/δ_y, and P/P_y) to allow more direct comparison between specimens and to facilitate application of the hysteric parameters to different configurations. The anchor points for tension and compression are described in the following sections and the remaining values were selected using a least squares method to minimize the error between the energy dissipated in the monotonic tests and the energy dissipated by the multi-linear

model. The fit was performed separately for pre-peak and post-peak energy to prevent over or under compensation of the dissipated energy [18]. Additional constraints were utilized to encourage the model backbone to resemble the experimental curve.

5.1.1.1 Compression Side

Two line segments prior to the peak load were used to capture the elastic and pre-buckling nonlinearities in the response. Backbone point (δ_2^-,P_2^-) as shown in Fig. 5.1 was anchored to the point of maximum compression load and corresponding displacement. Two post-peak segments with negative slope were included to account for the softening and post-peak strength loss as observed from the tests. Point (δ_4^-,P_4^-) was anchored to an axial deformation δ=6.0δ_y and associated force obtained from the test data. This point corresponds to strength loss of at least 50% for all tested specimens and a zero-slope is assumed beyond this point. The coordinates for backbone point 1 and 3 were found using a least squares fit to create the same amount of area under the pre-peak, and post-peak curves respectively. The coordinates defining the fit compression backbones are summarized in Table 5.1.

5.1.1.2 Tension Side

For tension, the backbone is calibrated from the two monotonic tests listed in Chapter 3. These tests are considered here to be representative of the tension behavior of the tested CFS members. Three segments prior to peak load are intended to capture the initial yielding and post-yielding part of the response. A fourth segment with negative slope is included to represent the loss of strength due to tearing and fracture observed from the tests. The coordinates defining the tension backbone are summarized at the bottom of Table 5.1.

One of the shortcomings of the *Pinching4* hysteretic model is that while the backbone can be separately defined in compression and tension, the strength and stiffness degradation parameters are universal to both compression and tension. The effect of the accumulation of damage on compression and tension response of cold-formed steel members is significantly different. An attempt was made therefore to improve the behavior of the hysteretic model by adjusting the tension backbone. The adjusted tension backbone was developed as a hybrid between the monotonic tests and the tension side of the cyclic envelopes shown in Fig. 5.3d. As a result the adjusted backbone is defined using larger forces and smaller normalized deformations than the

backbones fit to the monotonic tension tests. The adjusted tension backbone is given at the bottom of Table 5.1.

Table 5.1. Backbone definition points for axial specimens.

	Specimen	P_y (kN)	k_e [(a)] (kN/mm)	δ_y [(b)] (mm)	δ_1/δ_y	δ_2/δ_y	δ_3/δ_y	δ_4/δ_y	P_1/P_y	P_2/P_y	P_3/P_y	P_4/P_y	k_1/k_e	k_2/k_e $\times 10^{-3}$	k_3/k_e $\times 10^{-3}$	k_4/k_e $\times 10^{-3}$
1	600S137-97-GAM-1	245	56.13	4.36	0.463	0.562	1.394	5.600	0.433	0.482	0.210	0.096	935	490	-326	-27
2	600S137-97-GAM-2	249	56.23	4.42	0.452	0.664	1.815	5.600	0.373	0.414	0.205	0.107	826	195	-182	-26
3	362S137-68-GAM-1	123	28.04	4.40	0.440	0.618	1.642	5.600	0.414	0.460	0.233	0.124	942	258	-222	-28
4	362S137-68-GAM-2	122	28.08	4.35	0.419	0.535	1.528	5.600	0.391	0.435	0.181	0.083	933	374	-256	-24
5	600S137-68-DAM-1	177	138.86	1.28	0.837	1.427	3.779	6.000	0.493	0.548	0.377	0.286	589	93	-72	-41
6	600S137-68-DAM-2	177	138.36	1.28	0.758	1.278	3.438	6.000	0.495	0.549	0.379	0.284	652	106	-79	-37
7	362S137-68-DAM-1	124	106.13	1.17	1.144	1.523	3.045	6.000	0.735	0.816	0.556	0.417	642	215	-171	-47
8	362S137-68-DAM-2	123	105.68	1.17	0.935	1.293	3.100	6.000	0.724	0.804	0.549	0.411	774	225	-141	-48
9	600S162-33-LAM-1	72	143.49	0.50	0.526	0.816	2.913	6.000	0.385	0.427	0.259	0.188	731	147	-80	-23
10	600S162-33-LAM-2	72	143.56	0.50	0.608	1.110	2.234	6.000	0.416	0.462	0.298	0.203	684	92	-146	-25
11	362S162-54-LAM-1	113	181.80	0.62	1.017	1.309	2.877	6.000	0.699	0.777	0.478	0.333	688	266	-190	-47
12	362S162-54-LAM-2	113	181.92	0.62	1.108	1.434	2.791	6.000	0.681	0.756	0.489	0.331	614	232	-197	-49
	Tension															
14	362S162-54-LAMT-1	113	181.46	0.62	0.976	1.669	7.232	-	0.823	0.953	0.967	-	847	213	3	-
15	362S162-54-LAMT-2	114	182.79	0.62	1.126	2.880	16.168	25.633	0.870	0.957	0.997	0.450	779	102	3	-58
16	**Tension Adjusted**	**114**	**182.79**	**0.62**	**1.128**	**1.488**	**6.000**	**8.000**	**1.044**	**1.134**	**1.172**	**0.872**	**926**	**250**	**9**	**-150**

(a) $k_e = A_g E/L$ (E=203.4GPa); (b) $\delta_y = P_y/k_e$

5.1.2 Cyclic Response Characterization

Strength and stiffness deterioration are simulated in *Pinching4* using damage rules that are a function of the hysteretic energy dissipated and the historic deformation demand [21,24]. Three damage rules are available in *Pinching4*, to simulate strength, unloading stiffness and reloading stiffness deterioration. Both strength (Eq. 5.1) and unloading stiffness (Eq. 5.2) degradation were incorporated in the proposed hysteretic model whereas reloading stiffness deterioration was neglected. The damage rules were defined using the damage index for backbone strength, $\eta_{f,i}$, and damage index for stiffness, $\eta_{k,i}$, as follows:

$$f_{\max,i} = (1-\eta_{f,i})\, f_{\max,o} \tag{5.1}$$

$$k_i = (1-\eta_{k,f})k_o \tag{5.2}$$

$$\eta_i = \beta_1(\tilde{d}_{\max,i})^{\beta_3} + \beta_2\left(E_i/\gamma_E E_m\right)^{\beta_4} \le \gamma_{\text{limit}} \tag{5.3}$$

where the index i = current load excursion value; o = value achieved if damage were not included (i.e. monotonic backbone curve); f_{max} = maximum strength for the current excursion, k = unloading stiffness, E_i = cumulative hysteretic energy dissipated during previous excursions, E_m = maximum of the energy dissipated under monotonic loading in achieving point P_4 in Fig. 5.1; γ_E = parameter to define the maximum energy dissipated during cyclic loading; and β_i = parameters fitted from

experimental data. In general experimental values of the damage index η_i are calculated from the tests, and a least squares fit using Eq. 5.3 is employed to obtain values β_i for each tested member. For the proposed hysteretic model, the damage was computed as a function of energy rather than peak deformations so the term relating damage to peak displacements was removed by setting $\beta_1 = \beta_3 = 0$.

5.1.2.1 Strength degradation

Strength deterioration was calculated as the positive difference in strength between the monotonic backbone force ($f_{max,o}$) and the cyclic force envelope ($f_{max,i}$). The strength degradation behavior differs substantially between compression and tension excursions as shown in Fig. 5.4. In compression, strength deteriorates faster with a reduction at the end of the test of more than 50% the maximum strength. The curves in Fig. 5.4a suggest that compression strength degradation is cross-section and length independent. In tension the strength deterioration was more gradual, almost negligible, until tearing started and most or all strength was lost (i.e., fracture, see Fig. 5.4b). In the *Pinching4* hysteretic model, the accumulation of damage is defined to be the same in both tension and compression loading directions; hence, it was necessary to use the average of the strength deterioration in compression and tension to define the degradation parameters. The fitted β_i values fitted to each specimen's curve are listed in Table 5.2.

5.1.2.2 Stiffness degradation

Unloading stiffness values were obtained by fitting a line to the unloading paths of the cyclic responses. The model is fit using a least squares method to minimize the error on the predicted load. The unloading stiffness is therefore the slope of segments *g*-*e* and *h*-*c* as shown in Fig. 5.1. The differences between unloading stiffness degradation in tension and compression are even greater than the differences in strength degradation as shown in Fig. 5.5a. Unloading stiffness in compression rapidly decreases soon after the maximum compression is reached. Fig. 5.5a shows that unloading stiffness in compression for global buckling members is more pronounced than it is for local and distortional buckling members. A reduction of more than 80% occurs before 20% of the hysteretic energy is dissipated for global members. In tension, unloading stiffness deterioration happens more gradually than in compression and there is little distinction between the different buckling modes (i.e., global, local, or distortional, see Fig. 5.5b). As it was the case with strength degradation, both experimental tension and compression values of $\eta_{k,i}$ were used to

develop the stiffness degradation parameters since the hysteretic model does not allow definition of different tension and compression degradation. The fitted β_i values are listed in Table 5.2.

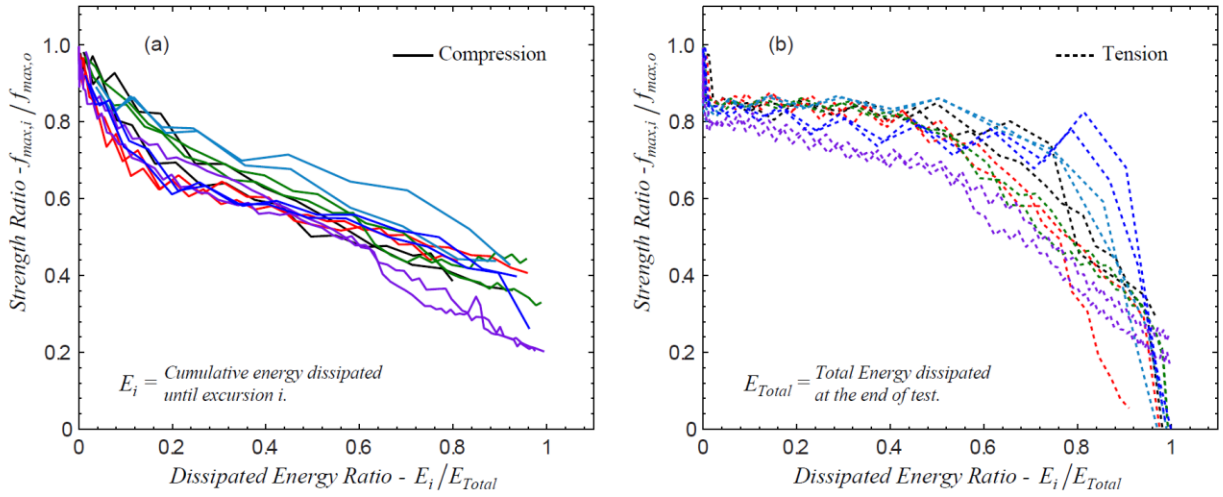

Fig. 5.4. Strength degradation, (a) compression; (b) tension.

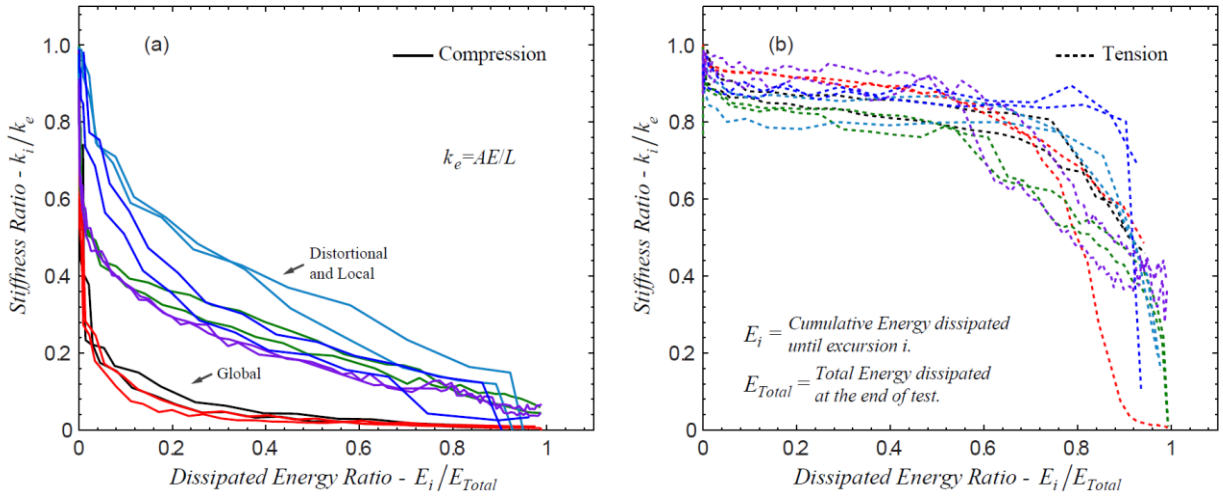

Fig. 5.5. Stiffness degradation, (a) compression; (b) tension.

5.1.2.3 Pinching behavior

Pinching behavior is defined by a set of parameters, u_{F+}, u_{F-}, r_{D+}, r_{D-}, r_{F+}, and r_F. The parameters r_{D-} and r_{D+} are the ratio of the deformation at which reloading starts (points *d* and *f* in Fig. 5.1) to the maximum/minimum historic deformation, d_{min} and d_{max}. Parameters r_{F-} and r_{F+} are the corresponding ratios of the load at the point at which reloading starts (points *d* and *f*) to the load corresponding to the maximum historic displacement, $f(d_{min})$ and $f(d_{max})$. Parameters u_{F-} and u_{F+} are the ratios of the load developed after unloading (point *c* and *e* in Fig. 5.1) to the load coordinate of backbone point 3, P_{3-} and P_{3+}.

An initial attempt to characterize pinching was made by fitting a tri-linear model to each unloading and reloading curve using a least squares method. The coordinates of the fitted points defining each segment were used to derive a first estimate of parameters r_{D+}, r_{D-}, r_{F+}, r_{F-}, u_{F+}, and u_{F-} for every cycle. It was found, however, that these values are not constant and varied as the number of cycles increased. Since the pinching behavior in *Pinching4* is defined using constant pinching parameters, a second method was developed to consider the entire data set from a test. The second method consisted of minimizing the error between the dissipated hysteretic energy produced by the model and the experimentally observed energy dissipation. The optimization problem was implemented in MATLAB [25] using the average values of r_{D+}, r_{D-}, r_{F+}, r_{F-}, u_{F+}, and u_{F-} from the first estimate described above as seed values. Constraints were set to ensure the modeled load-deformation shape approximated the test data while minimizing the error in energy. The slopes of segments *h-c*, *c-d*, and *d-a* were constrained such that they decrease in that order (i.e. $k_{hc} > k_{cd} > k_{da}$). The load at point *c* was constrained to remain negative. The obtained values for r_{D+}, r_{D-}, r_{F+}, r_{F-}, u_{F+}, and u_{F-} are listed in Table 5.2 and a statistical summary of the pinching parameters as well as the damage parameters is given in Table 5.3.

Table 5.2. *Pinching4* model parameters for axial specimens.

Specimen[a]	Damage Parameters						Pinching Parameters						
	Strength [b]		Stiffness [b]				Compression			Tension			Backbone
	β_2	β_4	β_2	β_4	γ_E	E_M[c]	r_{D-}	r_{F-}	u_{F-}	r_{D+}	r_{F+}	u_{F+}	Used [d]
600S137-97-GAC-1	0.70	0.98	0.69	0.20	1.88	8541	0.40	0.92	0.50	0.55	0.25	-0.10	1, 16
600S137-97-GAC-2	0.58	0.60	0.73	0.22	2.62	8761	0.40	0.92	0.50	0.75	0.25	-0.10	1, 16
362S137-68-GAC-1	0.69	0.71	0.90	0.33	3.39	4417	0.40	0.92	0.50	0.35	0.25	-0.03	4, 16
362S137-68-GAC-2	0.66	0.70	0.70	0.22	2.25	4450	0.48	0.92	0.50	0.50	0.25	-0.03	4, 16
600S137-68-DAC-1	0.71	1.04	0.68	0.30	4.78	1868	0.66	0.92	0.50	0.80	0.30	-0.10	6, 16
600S137-68-DAC-2	0.68	0.82	0.72	0.27	4.86	1863	0.66	0.92	0.50	0.80	0.26	-0.10	6, 16
362S137-68-DAC-1	0.68	1.04	0.70	0.52	5.05	1260	0.65	0.92	0.50	0.45	0.62	-0.03	8, 16
362S137-68-DAC-2	0.67	1.09	0.67	0.40	4.95	1270	0.60	0.92	0.50	0.53	0.62	-0.03	8, 16
600S162-33-LAC-1	0.71	0.55	0.68	0.33	8.68	294	0.48	0.92	0.50	0.80	0.30	-0.10	10, 16
600S162-33-LAC-2	0.78	0.73	0.73	0.33	8.47	293	0.48	0.92	0.50	0.80	0.30	-0.10	10, 16
362S162-54-LAC-1	0.55	0.49	0.66	0.43	6.63	579	0.48	0.92	0.50	0.53	0.62	-0.03	11, 16
362S162-54-LAC-2	0.56	0.46	0.62	0.32	6.49	581	0.49	0.92	0.50	0.53	0.62	-0.03	11, 16

(a) SSMA profiles [46]; AC= axial cyclic test; G, D and L are = Global, Distortional, and Local buckling [22].
(b) Fit using positive and negative excursions; (c) Energy in units of kN-mm; (d) Backbone curve from Table 5.1

Table 5.3. Statistics for *Pinching4* parameters.

	Damage Parameters						Pinching Parameters					
	Strength		Stiffness				Compression			Tension		
	β_2	β_4	β_2	β_4	γ_E	E_M	r_{D-}	r_{F-}	u_{F-}	r_{D+}	r_{F+}	u_{F+}
μ	0.66	0.77	0.71	0.32	5.00	2848	0.52	0.92	0.50	0.62	0.39	-0.07
cov	0.10	0.29	0.09	0.29	0.45	1.07	0.20	0.00	0.00	0.26	0.45	-0.56

μ = mean value; cov = coefficient of variation.

5.1.2.4 Generalized hysteretic model

It is desirable to develop generalized hysteretic models that can be applied to a wide range of cold-formed steel sections of varying length. Two options are explored here for calibration of a generalized hysteretic model to simulate the axial behavior of cold-formed members.

5.1.2.4.1 Generalized compression backbone curves

Generalized backbone curves for the compression side derived from the values in Table 5.1 require identifying a functional relationship between these values and cross-sectional slenderness. A power regression of the form $P_i/P_y = C\lambda^r$ was pursued as an initial hypothesis for such a relationship where λ is the slenderness corresponding to the governing buckling limit state (i.e., λ_e, λ_d or λ_ℓ). This approach is similar to the AISI Direct Strength Method approach in which strength in compression is a function of the governing slenderness member slenderness. A similar power regression $\delta_i/\delta_y = C\lambda^r$ was pursued for the displacements. The resulting expressions are summarized in the lower half of Table 5.4 and shown in Fig. 5.6 along with the corresponding backbone coordinates from Table 5.1. Points corresponding to global buckling do not follow the trends observed, and regression including these points would result in very low backbones for the distortional and local buckling specimens. These points, therefore were excluded when fitting the coefficients *C* and *r* for the power regressions in Fig. 5.6. However, excluding these points also makes the obtained expressions applicable to members experiencing local and distortional buckling, but not global buckling.

Generalized expressions that could be applicable to all members irrespective of the governing buckling mode should be functions of all three slenderness values λ_e, λ_d and λ_ℓ. A power regression of the form $P_i/P_y = C\lambda_e^r\lambda_d^s\lambda_\ell^t$ was pursued where λ_e, λ_d and λ_ℓ are the corresponding slenderness calculated using DSM for a specific member. The resulting expressions are summarized in Table 5.4 and shown in Fig. 5.7 along with the corresponding backbone coordinates from Table 5.1. The resulting expression allows estimating backbone curves for compression side using the same set of coefficients irrespective of the governing buckling mode.

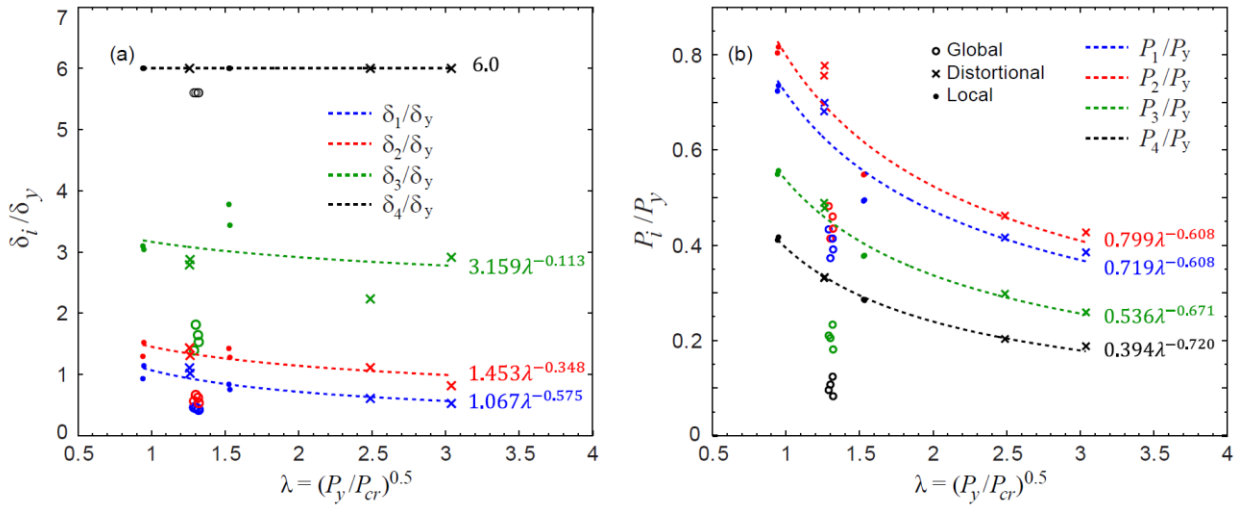

Fig. 5.6. Compression backbone coordinates as a function of governing λ.
(Global buckling data not included in the fit)

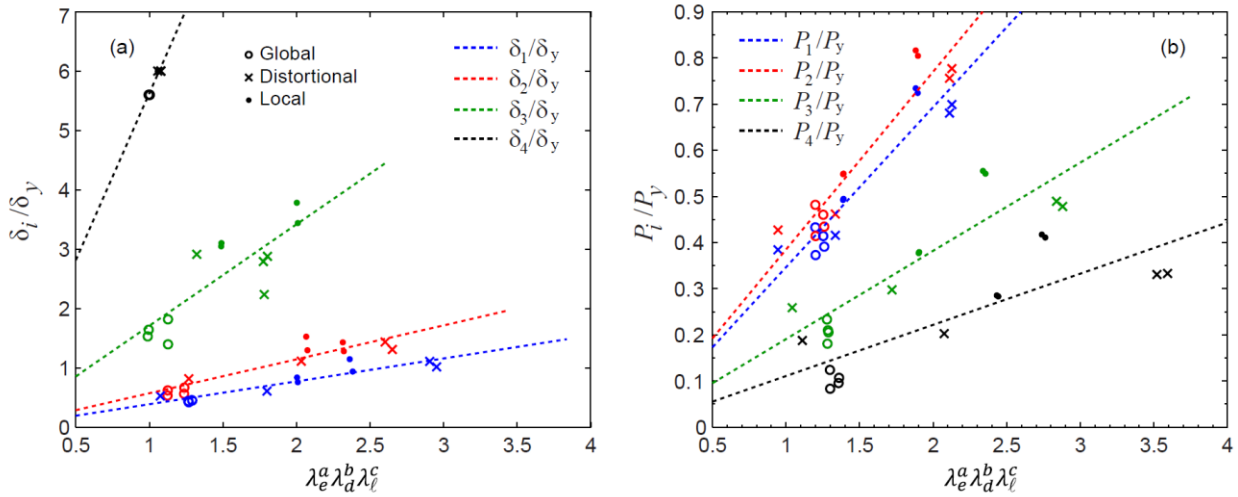

Fig. 5.7. Compression backbone coordinates as a function of λ_e, λ_d and λ_ℓ.

Table 5.4. Coefficients for generalized axial backbones.

Equation	**δ_1/δ_y**	**δ_2/δ_y**	**δ_3/δ_y**	**δ_4/δ_y**	**P_1/P_y**	**P_2/P_y**	**P_3/P_y**	**P_4/P_y**
C	0.386	0.571	1.708	5.626	0.347	0.385	0.191	0.111
r	-1.014	-0.933	-0.585	-0.059	-0.687	-0.687	-0.988	-1.215
s	1.509	1.704	1.352	0.079	0.777	0.777	1.415	1.932
t	-1.886	-1.602	-0.908	-0.062	-1.357	-1.357	-1.860	-2.253
R^2 (a)	0.876	0.853	0.687	0.915	0.889	0.889	0.804	0.716
C	1.067	1.453	3.159	6.000	0.719	0.799	0.536	0.394
r	-0.575	-0.348	-0.113	0.000	-0.608	-0.608	-0.671	-0.720
R^2 (a)	0.789	0.684	0.100	-	0.884	0.885	0.969	0.995

(a) Coefficient of determination

5.1.2.4.2 Generalized strength, stiffness and pinching parameters

In section 5.1.2 it was mentioned that strength degradation in compression appears to be cross-section and length independent and that tension degradation was almost negligible and seemed independent of cross-section and specimen length as well. The stiffness degradation curves in compression on the other hand, suggests a relationship with the cross-section slenderness, and the stiffness degradation behavior for global buckling specimens appeared to be different than local or distortional buckling. In addition, some of the parameters for *Pinching4* in Table 5.2 show large variations, *cov* values 20%, across the different specimens (see Table 5.3). Large variations suggest that the use of the average values might be inappropriate. For these reasons and because *Pinching4* requires the use of one set of strength/stiffness degradation parameters to be used in both compression and tension; the relationship between the values in Table 5.2 with the global and cross-sectional slenderness was investigated.

Trends between each parameter with the slenderness corresponding to the governing buckling mode (i.e., λ_e, λ_d or λ_ℓ) are not clear as shown in Fig. 5.8a, and Fig. 5.9a. The scatter for each curve suggests that the generalized expression cannot be represented as a function of only the governing slenderness. A power regression of the form $\beta = C\lambda_e^a \lambda_d^b \lambda_\ell^c$ was pursued and the resulting curves are shown in Fig. 5.8b and Fig. 5.9b and the corresponding coefficients are summarized in Table 5.5. These expressions allow an approximation of the degradation coefficients β_2 and β_4 as well as pinching parameters r_{D+}, r_{D-}, r_{F+}, r_{F-}, u_{F+}, and u_{F-} for use with the *Pinching4* hysteretic model, irrespective of the governing buckling mode.

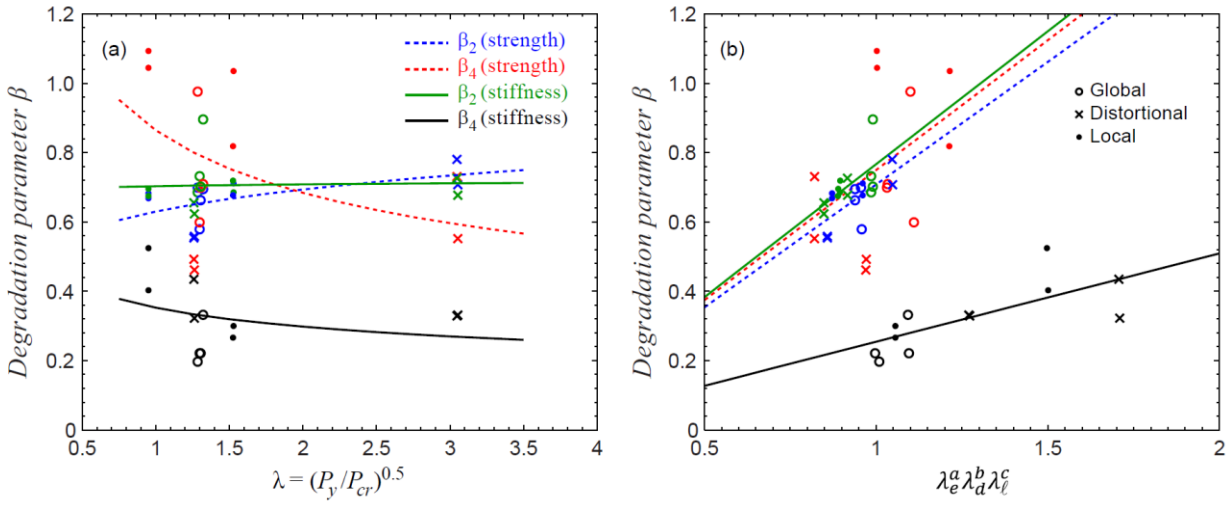

Fig. 5.8. Strength and Stiffness degradation parameter β as a function of slenderness.

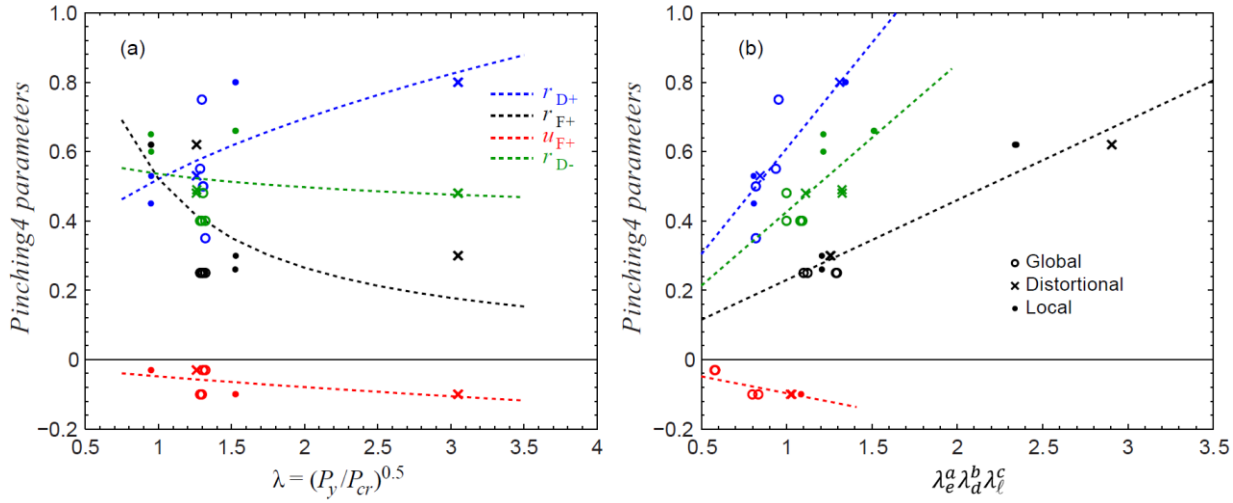

Fig. 5.9. *Pinching4* parameters as function of slenderness.

Table 5.5. Coefficients for generalized axial *Pinching4* parameters.

	Damage Parameters					Pinching Parameters					
	Strength		Stiffness			Compression			Tension		
Equation	**β_2**	**β_4**	**β_2**	**β_4**	**γ_E**	**r_{D-}**	**r_{F-}**	**u_{F-}**	**r_{D+}**	**r_{F+}**	**u_{F+}**
C	0.708	0.749	0.766	0.255	3.083	0.426	0.92	0.50	0.609	0.230	-0.097
r	0.142	-0.108	0.134	-0.340	-0.410	-0.322	0.00	0.00	0.104	-0.782	1.108
s	-0.127	0.710	-0.159	-0.207	-0.140	0.889	0.00	0.00	0.480	0.057	0.417
t	0.309	-0.431	0.179	-0.387	0.182	-0.563	0.00	0.00	0.393	-1.223	2.006
R^2 (a)	0.468	0.175	0.384	0.543	0.972	0.564	-	-	0.807	0.929	0.831
C	0.630	0.864	0.703	0.353	3.635	0.536	0.92	0.50	0.521	0.522	-0.048
r	0.139	-0.338	0.011	-0.243	0.738	-0.107	0.00	0.00	0.417	-0.977	0.712
R^2 (a)	0.271	0.147	0.002	0.068	0.462	0.039	-	-	0.435	0.313	0.341

(a) Coefficient of determination

5.1.3 Simulated Axial Cyclic Responses

The calibrated hysteretic models are capable of capturing the observed response characteristics such as the post-peak degradation of strength and stiffness in compression and tension as shown in Fig. 5.10. However, the *Pinching4* hysteretic model is not capable of accurately representing the unloading-reloading from tension to compression (path *h-c-d-a* in Fig. 5.1). This is because the *Pinching4* model requires that the maximum load along the reloading path occurs at point *a*, whereas the observed cyclic responses suggest that the maximum load in segment *h-c-d-a* should occur at point *c*. Strength and stiffness degradation were captured reasonably well by the calibrated hysteretic model. However, since the *Pinching4* model utilizes the same set of degradation coefficients irrespective of the loading direction, the model tends to under-predict and over predict the amount of degradation in compression and tension respectively (Fig. 5.10).

The hysteretic energy dissipated by the simulated response develops slower than the experiments as evidenced by Fig. 5.11. The difference stems largely from the inability of the *Pinching4* hysteretic model to approximate the unloading-reloading path from tension to compression. At the end of the tests, the average ratio of energy dissipated for the model to energy dissipated for the tests E_{model}/E_{Test} was 0.91 with a coefficient of variation of 0.09 (see Table 5.6). The objective of the hysteretic shape calibration described above was to minimize the error in dissipated energy while remaining on the conservative side of underestimating energy dissipation and associated hysteretic damping. Other criteria for calibration are possible and may be considered in the future.

The performance of the expression for the generalized backbones and *Pinching4* parameters is illustrated in Fig. 5.12. The modeled responses share the same characteristics described above for the responses modeled using parameters from Table 5.1 and Table 5.2. However, in some cases the generalized model could overestimate or underestimate the strength and damage accumulated by the member. This is a natural consequence of using values calibrated to a small data set. More points obtained from additional cyclic testing or finite element analysis would improve the calibration of the fitted coefficients and therefore the accuracy of the generalized expressions.

Table 5.6. Test and model hysteretic energy.

Specimen	E_{Test} (kN-mm)	E_{Model} (kN-mm)	E_{Model}/E_{Test} -	**Backbone Used** [(a)]
600S137-97-GAC-1	16063	12010	0.75	1, 16
600S137-97-GAC-2	22983	20982	0.91	1, 16
362S137-68-GAC-1	14952	12465	0.83	4, 16
362S137-68-GAC-2	10009	9129	0.91	4, 16
600S137-68-DAC-1	8935	8697	0.97	6, 16
600S137-68-DAC-2	8960	8836	0.99	6, 16
362S137-68-DAC-1	6458	5845	0.91	8, 16
362S137-68-DAC-2	6368	5812	0.91	8, 16
600S162-33-LAC-1	2550	2408	0.94	10, 16
600S162-33-LAC-2	2344	2457	1.05	10, 16
362S162-54-LAC-1	3839	3244	0.85	11, 16
362S162-54-LAC-2	3773	3442	0.91	11, 16

(a) Backbone curve from Table 5.1

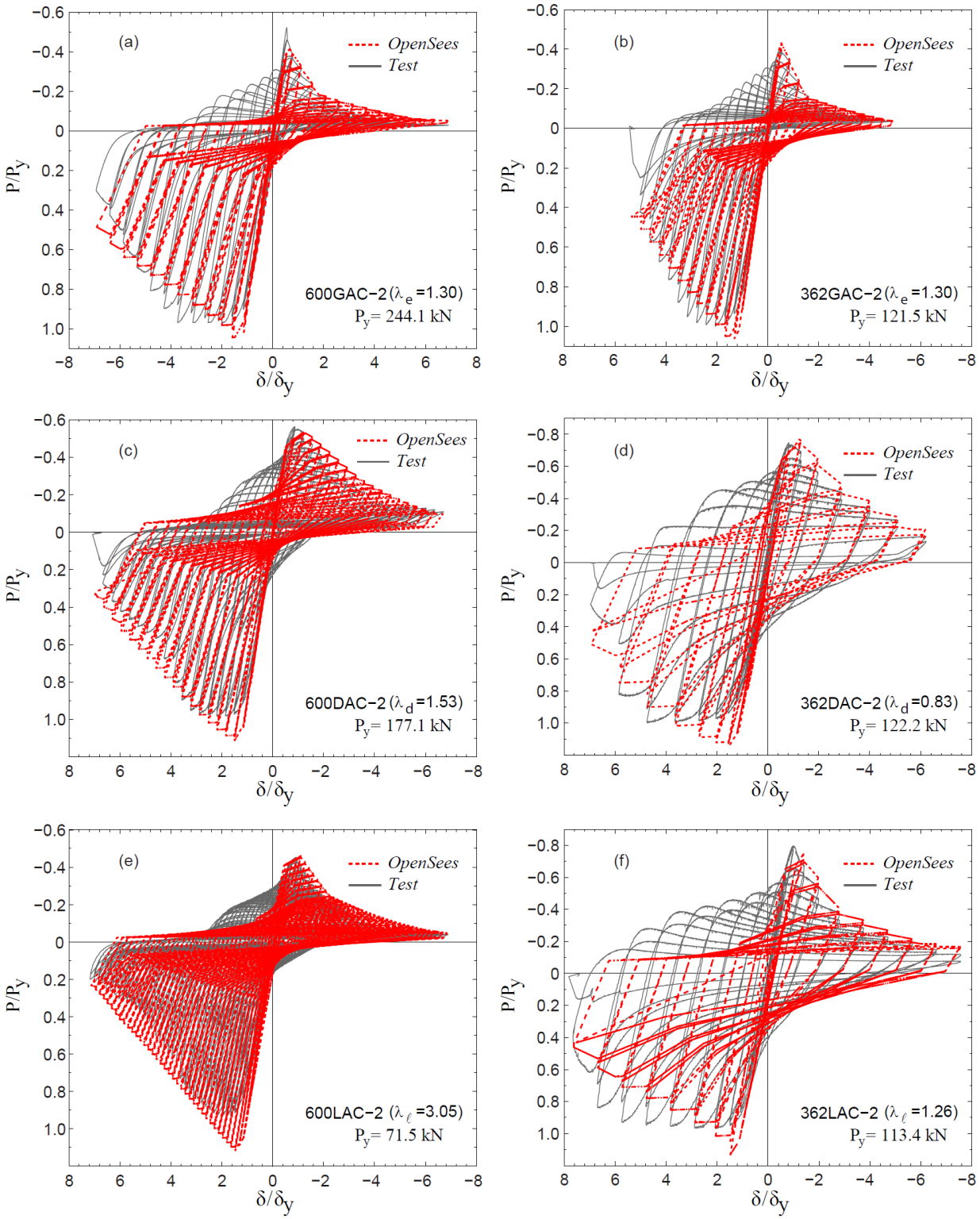

Fig. 5.10. Simulated axial response using *Pinching4*.

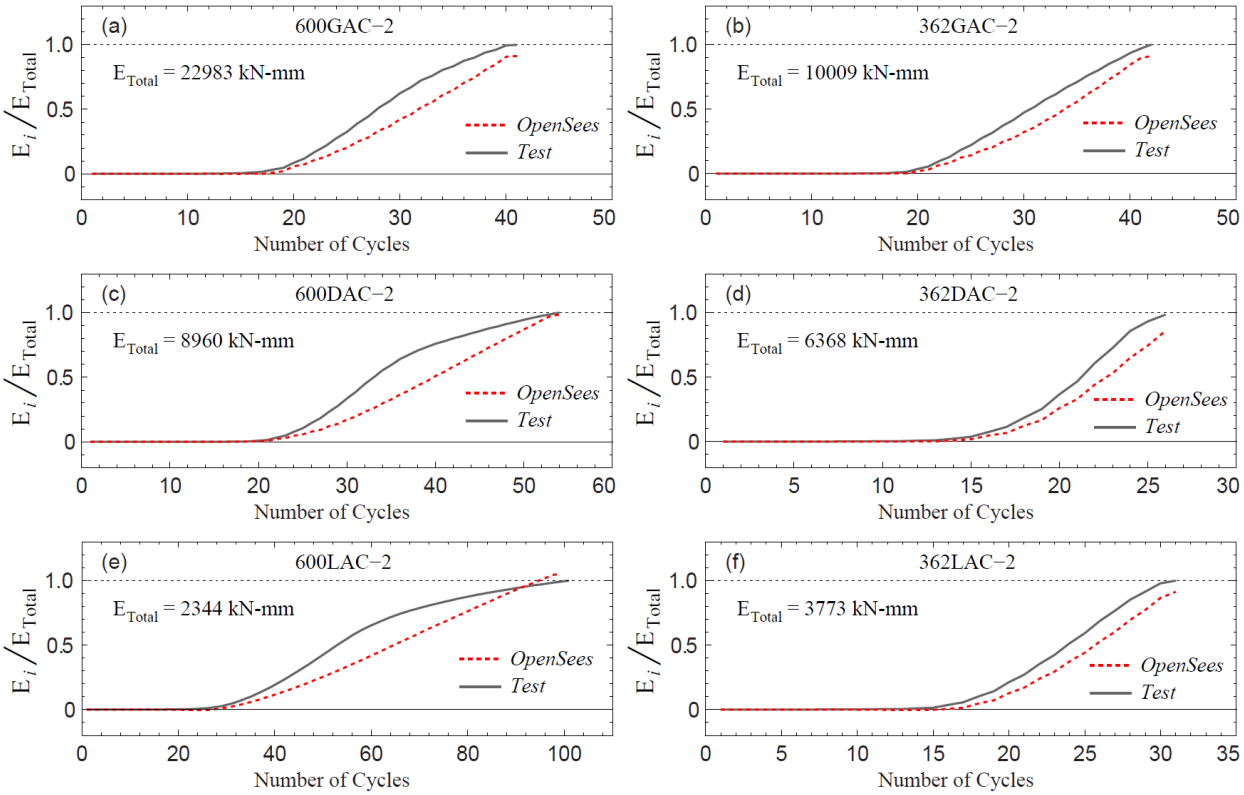

Fig. 5.11. Hysteretic energy comparison.

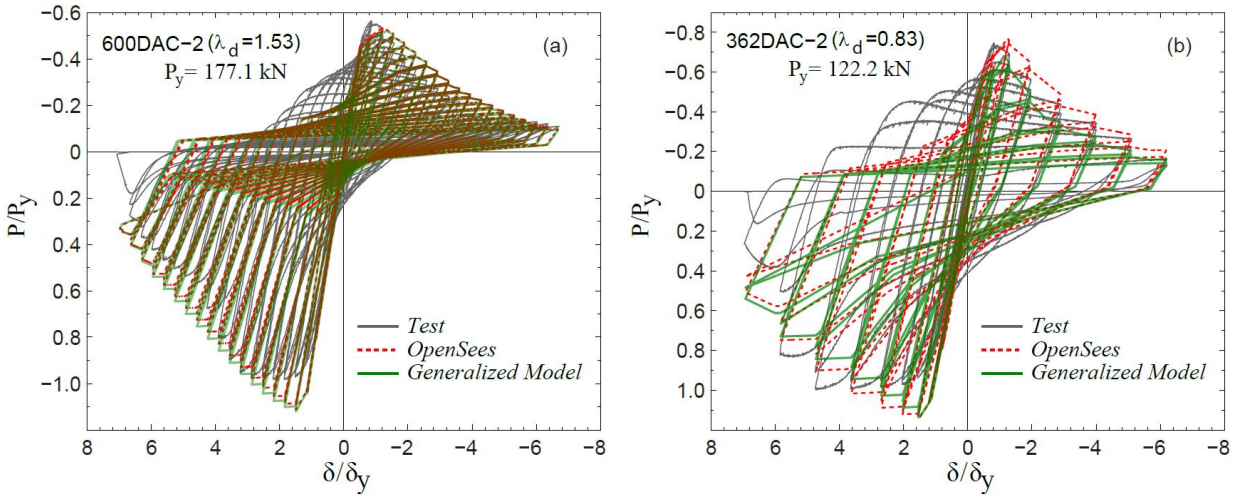

Fig. 5.12. Generalized model expressions comparisons.

5.2 Flexural member cyclic response characterization [4]

Hysteretic models for CFS flexural members should accurately simulate the moment-rotation response including strength and stiffness degradation, as well as, pinching when unloading and reloading in the opposite direction. Herein, cyclic response characterization and calibration of the hysteretic *nonlinear spring model* for CFS flexural members (Fig. 5.13) is pursued using the hysteretic model *Pinching4* [21] as implemented in OpenSees [24]. The backbone curves are derived from normalized monotonic responses and the damage model for strength and stiffness deterioration is calibrated by comparing the monotonic and cyclic responses. The responses are normalized to the yield moment M_y (M_y = SF_y) and the elastic yield rotation θ_y (θ_y = M_y(3Lu+2a)/*6EI*, see Chapter 4).

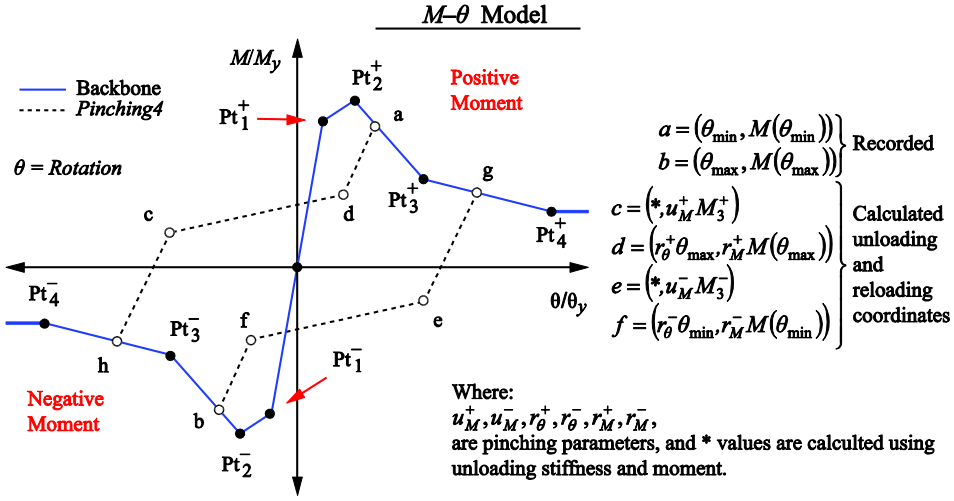

Fig. 5.13. Hysteretic spring model (*Pinching4*) for CFS flexural members.

Cyclic responses are symmetric, show equal pre-buckling stiffness k/k_e (k_e =*6EI*/[$3L_u$+*2a*]) in both loading directions, and exhibit pinching when loading in the opposite direction (Fig. 5.14). The amount of pinching observed was different for the different buckling modes and unloading mechanism. Energy dissipation varied depending on buckling mode with local and distortional members dissipating more energy per cycle while enduring less cumulative rotations than the global buckling members. Total cumulative rotation was less in members where damage accumulated at more than one location along the unbraced length (see Chapter 4). The monotonic

[4] This section is part of a paper presented at the *7th European Conference on Steel and Composite Structures 2014*, as part of the paper titled "**Cyclic Flexural Hysteretic Models for Cold-Formed Steel Seismic Simulation**".

responses are used to define the backbone curves and to characterize the strength and stiffness degradation during the cyclic tests. The typical monotonic response is linear past 50% of the peak strength and becomes nonlinear when buckling deformations appear up to the peak moment (Fig. 5.15). The maximum strength depends on the buckling mode where global buckling specimens reached 0.34M_y to 0.38M_y, distortional buckling specimens 0.75M_y to 0.91M_y, and local buckling specimens 0.55M_y to 0.6M_y. Strength decreased significantly, almost instantly, after the peak moment, at least 35% of the peak moment followed by a gradual strength reduction as rotations increase (Fig. 5.15).

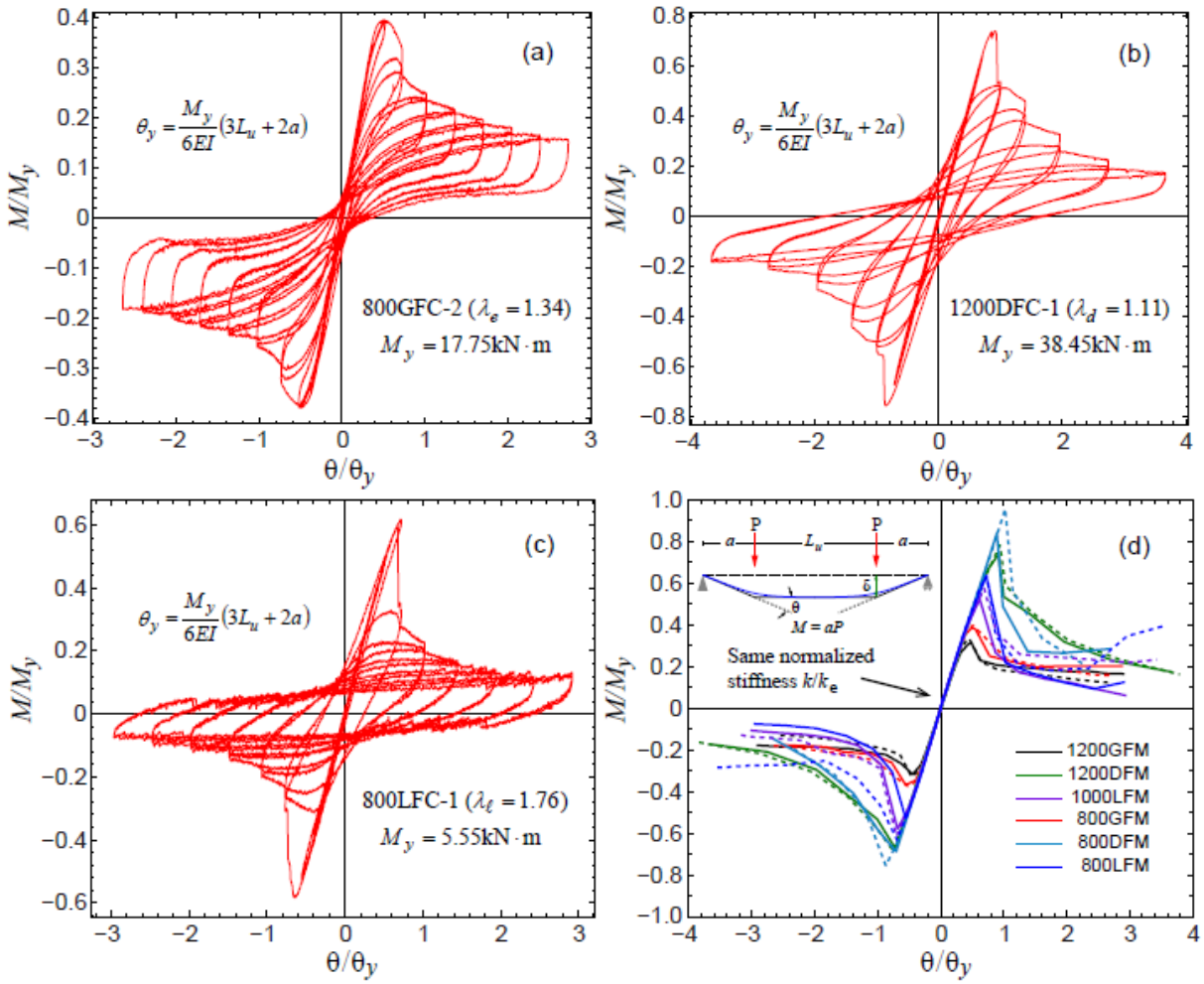

Fig. 5.14. Cyclic response: (a) global buckling, (b) distortional buckling, and (c) local buckling.

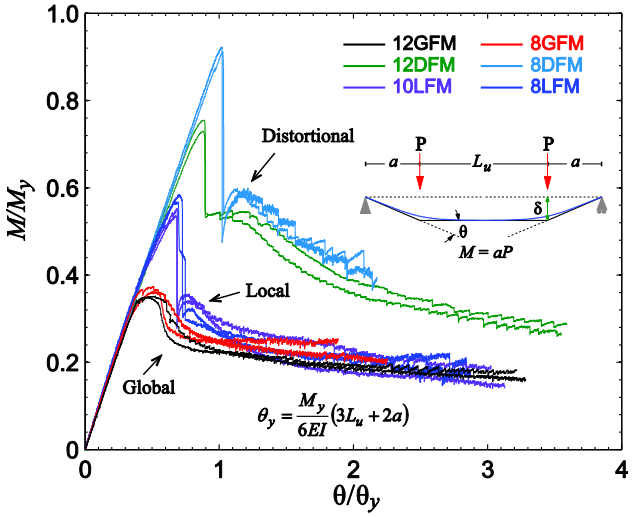

Fig. 5.15. Monotonic flexural Response.

5.2.1 Flexural Backbone – Monotonic Response Characterization

Backbone curves were fit to the monotonic test data using a combination of defined anchor points and fit values to match the energy represented by the area under the monotonic load-deformation curve. The backbone consists of load and displacement coordinates, labeled as θ_i, M_i in Fig. 5.15, for eight unique points, four for positive moment, and four for negative moment. It is noted that the backbone characterization is conducted in normalized coordinates (θ/θ_y, and M/M_y) to allow more direct comparison between specimens and to facilitate application of the hysteric parameters to different configurations. The anchor points of the backbone for positive and negative moment were set at points (θ_2,M_2) and (θ_4,M_4). Point (θ_2,M_2) as shown in Fig. 5.15 was fixed to the point of maximum normalized moment and corresponding normalized rotation. Point (θ_4,M_4) was fixed based on an flexural deformation $\theta = 2\theta_y$ and associated moment. This point corresponds to post-peak strength loss of at least 40% for all tested specimens and a zero-slope is assumed beyond this point. The remaining values were selected using a least squares method to minimize the error between the energy dissipated in the monotonic tests and the energy dissipated by the multi-linear model. The fit was performed separately for pre-peak and post-peak energy to prevent over or under compensation of the dissipated energy [18]. Additional constraints were utilized to encourage the model backbone to resemble the experimental curve.

Two segments prior to the peak load were used to capture the elastic and pre-buckling nonlinearities in the response. Two post-peak segments with negative slope were included to account for the softening and post-peak strength loss as observed from the tests. Point (θ_3,M_3) was

constrained to be slightly to the right/left of point (θ_2,M_2) for distortional and local members to avoid convergence problems caused by a close to infinity slope. The coordinates defining the fitted backbones are summarized in Table 5.7. The obtained points are used to establish the backbone for both sides of the moment-rotation hysteretic model.

Table 5.7. Backbone definition points for flexural specimens.

	Specimen [a]	M_y (kN-mm)	k_e [b] (MN-mm/rad)	θ_y [c] (rad×10^{-3})	θ_1/θ_y	θ_2/θ_y	θ_3/θ_y	θ_4/θ_y	M_1/M_y	M_2/M_y	M_3/M_y	M_4/M_y
1	1200S162-97-GFM-1	32668	1193.1	27.38	0.328	0.443	0.631	2.000	0.314	0.349	0.237	0.193
2	1200S162-97-GFM-2	31850	1192.2	26.72	0.325	0.515	0.761	2.000	0.317	0.352	0.236	0.185
3	800S162-97-GFM-1	17711	429.6	41.22	0.332	0.495	0.625	1.880	0.326	0.363	0.258	0.252
4	800S162-97-GFM-2	18182	432.1	42.08	0.347	0.511	0.808	2.000	0.337	0.374	0.253	0.211
5	1200S250-97-DFM-1	36673	2073.8	17.68	0.725	0.879	0.905	2.000	0.656	0.729	0.577	0.387
6	1200S250-97-DFM-2	37977	2069.5	18.35	0.732	0.883	0.925	2.000	0.680	0.755	0.538	0.361
7	800S250-68-DFM-1	14007	546.1	25.65	0.881	1.018	1.089	2.000	0.830	0.923	0.571	0.408
8	800S250-68-DFM-2	14148	550.7	25.69	0.892	1.023	1.109	2.000	0.821	0.912	0.538	0.440
9	1000S200-43-LFM-1	11983	525.2	22.81	0.532	0.685	0.737	2.000	0.497	0.552	0.307	0.230
10	1000S200-43-LFM-2	12045	526.2	22.89	0.524	0.675	0.738	2.000	0.483	0.536	0.279	0.176
11	800S200-33-LFM-1	5575	243.8	22.87	0.550	0.698	0.752	2.000	0.526	0.585	0.283	0.193
12	800S200-33-LFM-2	5632	244.6	23.02	0.549	0.684	0.751	2.000	0.510	0.567	0.274	0.218

(a) SSMA profiles [46]; FM= flexural monotonic test; G, D and L are = Global, Distortional, and Local buckling [22].
(b) $k_e = 6EI/(3L_u+2a)$, E=203.4GPa, L=4876.8mm, a = 832mm for GFM, a = 1543mm for DFM and LFM
(c) $\theta_y = M_y/k_e$

5.2.2 Cyclic Response Characterization

Strength and stiffness deterioration are simulated in *Pinching4* using damage rules that are a function of the hysteretic energy dissipated and the historic deformation demand [21,24]. Three damage rules are available in *Pinching4*, to simulate strength, unloading stiffness and reloading stiffness deterioration. Both strength (Eq. 5.1) and unloading stiffness (Eq. 5.2) degradation were incorporated in the proposed hysteretic model whereas reloading stiffness deterioration was neglected. Experimental values of the damage index η_i are calculated from the tests, and a least squares fit using Eq. 5.3 is employed to obtain values β_i for each tested member. For the proposed model, the damage was computed as a function of energy dissipated rather than peak deformations so the term relating damage to peak displacements was removed by setting $\beta_1 = \beta_3 = 0$.

5.2.2.1 Strength degradation

Strength deterioration was calculated as the positive difference on strength between the monotonic backbone moment ($m_{max,o}$) and the cyclic moment envelope ($m_{max,i}$). The strength degradation behavior is less pronounced for global buckling members than it is for the other members, see Fig. 5.16. The $m_{max,i}/m_{max,o}$ values close to one indicate that the cyclic envelope is close to the monotonic envelope, and the strength has not been reduced due to damage accumulated

during cyclic loading. For local and distortional buckling members strength degrades no more than 40% the corresponding strength under monotonic loading. It appears strength degrades more for members with higher cross-sectional slenderness (compare the averages λ_d =1.09 for distortional, and λ_ℓ = 1.77 for local buckling members); however, this correlation is not clear. In the *Pinching4* hysteretic model, the accumulation of damage is defined to be the same in both loading directions; hence, to define the degradation parameters β_2 and β_4, the average of the strength deterioration in both directions was used. The fitted β_i values fitted for each specimen are listed in Table 5.7.

5.2.2.2 Stiffness degradation

Unloading stiffness values were obtained by fitting a line to the unloading paths of the cyclic responses. A tri-linear model is fit using a least squares method to minimize the error on the predicted load to this unloading-reloading path. The unloading stiffness is therefore the slope of segments *g-e* and *h-c* shown in Fig. 5.1. Stiffness degradation for global buckling members is more pronounced than it is for the local and distortional buckling members. A reduction of more than 60% occurs before 20% of the hysteretic energy is dissipated for global members. For local and distortional members stiffness degradation is less than the global buckling members. It appears from Fig. 5.17 that there is no correlation between the amount of degradation and the cross-section slenderness besides the difference between global buckling members and the other members. As in the case with strength degradation, the average of the stiffness deterioration in both directions was used to develop the stiffness degradation parameters. The fitted β_i values fitted for each specimen are listed in Table 5.7 and a statistical summary in Table 5.9.

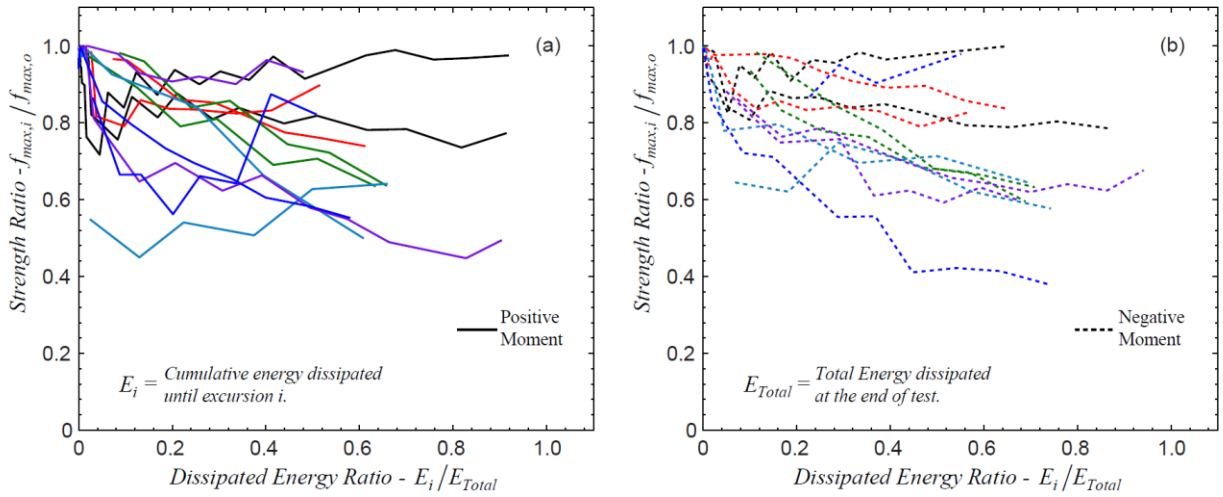

Fig. 5.16. Strength degradation, (a) positive moment; (b) negative moment.

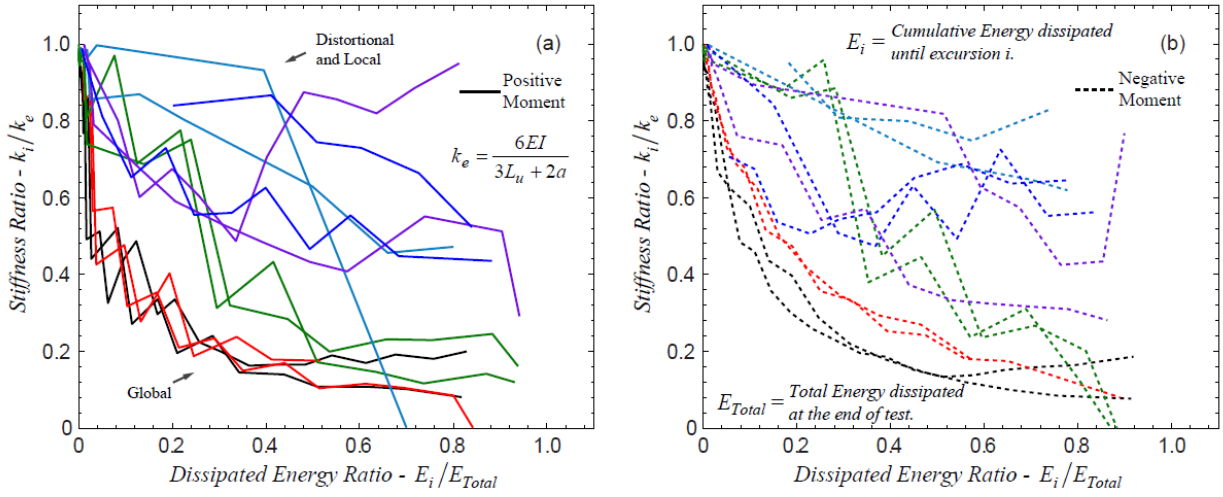

Fig. 5.17. Stiffness degradation, (a) positive moment; (b) negative moment.

Table 5.8. *Pinching4* model parameters for flexural specimens.

Specimen[a]	Damage Parameters						Pinching Parameters						Backbone
	Strength[b]		Stiffness[b]				Positive Moment			Negative Moment			
	β_2	β_4	β_2	β_4	γ_E	E_M[c]	$r_{\theta-}$	r_{M-}	u_{M-}	$r_{\theta-}$	r_{M-}	u_{M-}	Used [d]
1200S162-97-GFC-1	0.067	0.000	1.012	0.320	11.32	374.0	0.175	0.291	-0.176	0.205	0.324	-0.208	2
1200S162-97-GFC-2	0.250	0.347	1.113	0.382	6.51	381.3	0.226	0.334	-0.174	0.234	0.348	-0.208	2
800S162-97-GFC-1	0.237	0.318	1.184	0.459	7.71	360.2	0.218	0.333	-0.177	0.223	0.333	-0.190	4
800S162-97-GFC-2	0.304	0.806	1.077	0.394	8.51	372.3	0.207	0.324	-0.177	0.261	0.362	-0.211	4
1200S250-97-DFC-1	0.581	1.096	0.953	0.665	10.45	577.0	0.190	0.339	-0.203	0.196	0.382	-0.193	5
1200S250-97-DFC-2	0.510	0.694	1.041	0.722	10.83	562.4	0.104	0.265	-0.209	0.226	0.418	-0.168	5
800S250-68-DFC-1	0.398	0.000	0.491	0.735	7.16	353.7	0.224	0.359	-0.145	0.225	0.358	-0.195	7
800S250-68-DFC-2	0.519	0.572	0.916	1.613	5.74	351.1	0.149	0.288	-0.162	0.242	0.383	-0.193	7
1000S200-43-LFC-1	0.481	0.416	0.748	0.479	9.21	158.1	0.090	0.280	-0.188	0.213	0.411	-0.170	10
1000S200-43-LFC-2	0.486	0.736	0.351	0.307	17.86	141.1	0.074	0.213	-0.164	0.221	0.403	-0.178	9
800S200-33-LFC-1	0.703	0.495	0.584	0.406	11.95	69.8	0.107	0.302	-0.140	0.226	0.449	-0.185	11
800S200-33-LFC-2	0.212	0.000	0.349	0.018	14.68	69.9	0.108	0.286	-0.162	0.280	0.475	-0.114	11

(a) SSMA profiles [46]; FC= flexural cyclic test; G, D and L are = Global, Distortional, and Local buckling [22].
(b) Fit using positive and negative values; (c) Energy in units of kN-mm; (d) Backbone curve from Table 5.7.

Table 5.9. Statistics for *Pinching4* parameters.

	Damage Parameters						Pinching Parameters					
	Strength		Stiffness				Compression			Tension		
	β_2	β_4	β_2	β_4	γ_E	E_M	r_{D-}	r_{F-}	u_{F-}	r_{D+}	r_{F+}	u_{F+}
μ	0.40	0.46	0.82	0.54	10.16	314	0.16	0.30	-0.17	0.23	0.39	-0.18
cov	0.46	0.76	0.37	0.72	0.35	0.54	0.37	0.13	-0.12	0.10	0.12	-0.14

μ = mean value; cov = coefficient of variation.

5.3 Conclusions

The cyclic responses of CFS axial and flexural members were characterized and a *nonlinear spring* model was calibrated including strength and stiffness degradation. Backbone curves were developed from monotonic tests and parameters for the hysteretic model *Pinching4* were derived based on the hysteretic energy dissipated for each specimen. Generalized parameters

for the *axial spring model* were calculated as a function of the three slenderness λ_e, λ_d and λ_ℓ. The derived models captured reasonably well the main characteristics of the experimental response such as strength degradation, stiffness degradation, and pinching behavior. This study identified improvements that could be made to the *Pinching4* model formulation to better capture the hysteretic response of CFS axial members. The study suggests different sets of coefficients β_2 and β_4 to capture the inherently different modes of damage accumulation (different in tension than in compression). The shape of the unloading-reloading curve from tension to compression could also be modified to better capture the cyclic axial buckling response. For flexural members the derived parameters show good agreement between the experiments and the models. The calibrated parameters from this chapter are used in the next chapter to implement a *nonlinear beam-column* modeling framework for CFS axial and flexural members.

Chapter 6: Nonlinear Beam-Column Models for Cold-Formed Steel Members

This chapter presents the development of a modeling approach for cold-formed steel axial and flexural members under cyclic loading including local, distortional and global buckling. Two approaches to model the response are introduced, a *nonlinear spring* model with concentrated nonlinear P-δ (Fig. 6.1b) or M-θ (Fig. 6.4b) behavior, and a *nonlinear beam-column* with distributed nonlinearity using load-strain P-ε (Fig. 6.1c) or moment-curvature M-κ (Fig. 6.4c) to model cross-section behavior. Model parameters and damage rules are calibrated for local, distortional and global buckling as functions of the hysteretic energy dissipated, unbraced length (i.e., global slenderness λ_e) and cross-sectional slenderness (λ_d, and λ_ℓ). The underlying hysteretic model for members behavior consist of, a *backbone curve*, *unloading-reloading paths* that account for pinching, and a *damage model* for strength and stiffness degradation. This formulation is based on the hysteretic model *Pinching4* [21] as implemented in OpenSees [24].

6.1 Axial hysteretic modeling of CFS members

In this section, the results from calibration of the axial response in section 5.1 are used to formulate the nonlinear *spring* and *beam-column* models depicted in Fig. 6.1. The two models are formulated to simulate the cyclic response of CFS axial members spanning between two nodes as in the case of frame elements in common analysis tools.

6.1.1 Spring model - concentrated nonlinearity

The spring modeling approach uses axially rigid beam elements connected to a P-δ *nonlinear spring* where all the nonlinear behavior concentrates. The spring is located at one end of the modeled member. Fig. 6.1b illustrates this concept where the CFS axial member subjected to uniform axial force in Fig. 6.1a is modeled using a *nonlinear spring* at the top end. Parameters defining the nonlinear spring behavior are obtained by direct calibration of *Pinching4* to match experimental load-deformation responses and energy dissipation as described in section 5.1. Using nonlinear springs is a computationally inexpensive approach but requires adjusting the calibrated model parameters depending on possible different member lengths and loading conditions. For example, a member subjected to non-uniform axial load can be modeled using multiple springs

along the length where the backbone displacement coordinates are scaled accordingly to the distance between springs.

6.1.2 Nonlinear beam-column model – distributed nonlinearity

In this modeling approach, a *nonlinear beam-column element* with distributed nonlinearity is formulated using a load-deflection *P*-ε formulation to model the cross-section behavior (Fig. 6.1c). This approach allows modeling of damage spreading due to buckling deformations along the member length as observed in Chapter 3, and lets modeling different axial loading conditions using the same set of parameters that define the cross-section behavior. The parameters to define the load-strain behavior of the cross-section can be derived from the values obtained for the nonlinear spring model. The applied displacement δ_i from tests in Chapter 3 is converted to axial strain ε_i by dividing by the member length, thus $\varepsilon_i = \delta_i / L$. This defines the axial load-strain backbone *P*-ε at any cross section of the CFS axial member assuming a uniform strain distribution along the member. Thus, as described, this approach assumes that damaged and inelastic strains are averaged along the member length. This assumption does not directly reflect the results observed in Chapter 2 where inelastic strains concentrate in localized damaged zones; however, energy dissipation and the load-deflection response *P*-δ are still captured as illustrated in the next subsection. Parameters to model strength and stiffness degradation are defined in section 5.1 and do not differ from those of the nonlinear spring model.

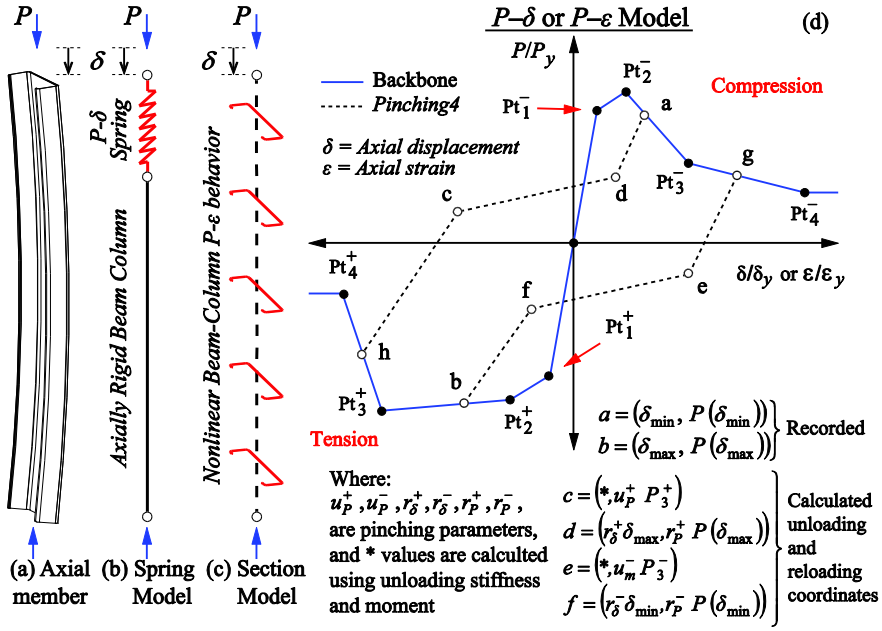

Fig. 6.1. a) Axial member; b) spring model; c) nonlinear beam-column model; d) hysteretic model.

6.1.3 Simulating CFS members axial cyclic response

This section illustrates the application of the hysteretic model to simulate the axial response of CFS members. The two models, *nonlinear springs* and the *nonlinear beam-column* element with distributed nonlinearity illustrated in Fig. 6.1 are used to simulate the experimental response of the axial members described in Chapter 3. The *nonlinear spring* model is implemented in OpenSees using an axially rigid beam element connected to a *zeroLength* element located at the loading point (see Fig. 6.2b). For these models, one spring will suffice and values from Table 5.1 and 5.2 are used directly without further adjustment that would be required for example if additional springs were to be placed along the member length *L*. The *nonlinear beam-column* model is implemented in OpenSees using a *dispBeamColumn* element connected between the two end nodes (see Fig. 6.2b). The Gauss-Lobatto quadrature rule with seventh integration points, two at the element ends, is used for numerical integration within the element. Axial load-strain section behavior is implemented using values in Table 5.1 and 5.2.

Comparison between the two models shows that they both produce similar results as far as modeling the load-deformation cyclic response P-δ of the tests in Chapter 3 as illustrated in Fig. 6.2a. Moreover the root mean-squared deviation between the predicted load responses to the tests is between 8% and 14% as shown in Fig. 6.3a. Likewise, both methods show very similar energy dissipation cycle by cycle (Fig. 6.2c) and the total energy dissipated is almost identical yet smaller than the tests (Fig. 6.3b). One main disadvantage of using spring models attached to axially rigid beam elements arises when modeling elements in which non-uniform axial loads may arise, like the case of a shear wall chord-stud where the fasteners may subject the member to a non-uniform axial loads. In such cases proper scaling, as previously described, of the backbone displacement coordinates is required to avoid any displacement incompatibilities. Adjusting the backbone to accommodate other than uniform axial loads using hysteretic springs can be troublesome, however this inconvenience can be avoided by using the distributed nonlinearity approach. Using a beam-column element with distributed nonlinearity P-ε does not require adjusting the backbone curve displacements to accommodate non-uniform axial loads or other combined loading cases (axial +moment).

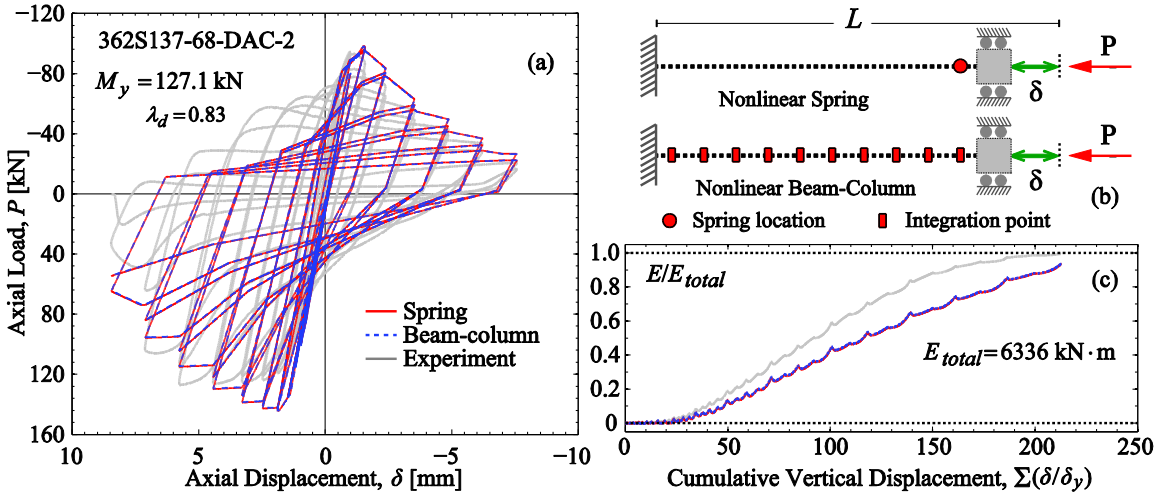

Fig. 6.2. a) Simulated and experimental response; b) Spring and beam-column models; c) Energy dissipated.

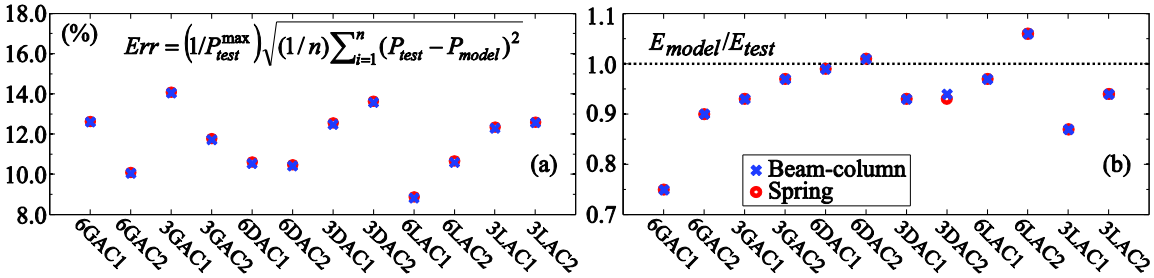

Fig. 6.3. Model to tests load a) and energy b) dissipation ratio for all test in Chapter 3 (see member labels in Table 5.1).

6.2 Flexural hysteretic modeling of CFS members [5]

In this section, the results from calibration of the flexural response in *Section* 5.2 are used to formulate the nonlinear *spring* and *beam-column* models depicted in Fig. 6.4. The two models are formulated to simulate the cyclic response of CFS flexural members spanning between two nodes as in the case of frame elements in common analysis tools.

6.2.1 Spring model - concentrated nonlinearity

The spring modeling approach uses rigid beam elements connected to *M-θ nonlinear springs* where all the nonlinear behavior concentrates. Springs are located at preselected locations along the modeled member length and their number and distribution would depend on the loading conditions. Fig. 6.4b illustrates this concept where the CFS member under constant moment in Fig. 6.4a is modeled using a *nonlinear spring* at the mid-span. Parameters defining the nonlinear spring behavior are obtained by direct calibration of *Pinching4* to match experimental moment rotation responses and energy dissipation as described in *Section 5.2.* Using nonlinear springs is a computationally inexpensive approach but requires adjusting the hysteretic model parameters depending on possible different loading conditions.

6.2.2 Nonlinear beam-column model – distributed nonlinearity

In this modeling approach, a *nonlinear beam-column element* with distributed nonlinearity is formulated using a moment curvature *M-κ* formulation to model the cross-section behavior (Fig. 6.4c). This approach allows modeling damage spreading due to buckling deformations along the member length as observed in Chapter 4, and lets modeling different loading conditions using the same set of parameters that define the cross-section behavior. The parameters to define the moment-curvature behavior of the cross-section can be derived from the values obtained for the nonlinear spring model. Backbone rotations, $\theta_i=\delta_i/a$, from Chapter 5 are converted to backbone curvature values κ_i using Eqs. 6.1-6.2 (see Fig. 6.4c),

$$\kappa_1 = \theta_1\left(\frac{6}{3L_u + 2a}\right) \qquad 6.1$$

$$\kappa_i = \left(\frac{2}{L_u}\right)\left(\theta_i - \frac{aM_i}{3M_1/\kappa_1}\right), \quad i = 2...4 \qquad 6.2$$

---

[5] This section is part of a paper presented at the *7th European Conference on Steel and Composites Structures* in Napoli, Italy 2014, with the title "**Cyclic Flexural Hysteretic Models for Cold-Formed Steel Seismic Simulation**".

These expressions define the moment-curvature backbone M-κ at any cross section of the CFS flexural member. Parameters to model strength and stiffness degradation are defined in section 5.2 and do not differ from those of the nonlinear spring model.

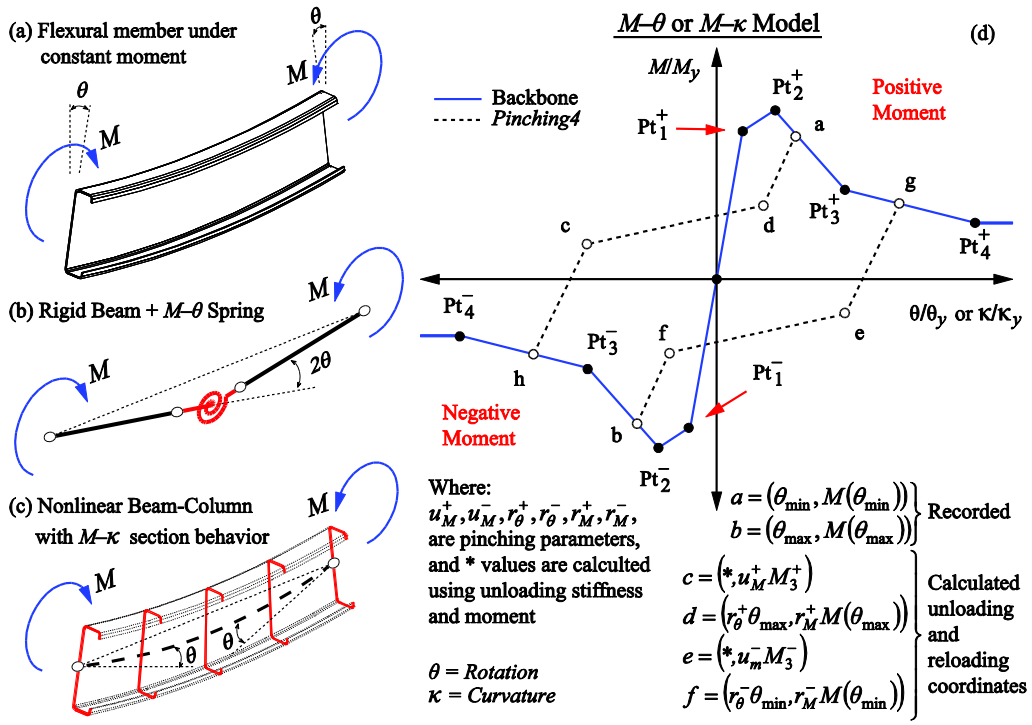

Fig. 6.4. a) Flexural member; b) spring model; c) nonlinear beam-column model; d) hysteretic model.

6.2.3 Simulating CFS members flexural cyclic response

This section illustrates the application of the hysteretic model to simulate the flexural response of CFS members. The two models, *nonlinear springs* and the *nonlinear beam-column* element with distributed nonlinearity illustrated in Fig. 6.4 are used to simulate the experimental response of the flexural members described in Chapter 4. The *nonlinear spring* model is implemented in OpenSees using rigid beam elements connected to *zeroLength* elements located at the loading points (see Fig. 6.5b). For these models, two springs will suffice and values from Table 5.7 and 5.8 are used directly without further adjustment that would be required for example if additional springs were to be placed along the unbraced length L_u. The *nonlinear beam-column* model is implemented in OpenSees using *dispBeamColumn* elements, one for each shear span of length a, and one for the unbraced length L_u (see Fig. 6.5b). The Gauss-Lobatto quadrature rule with seventh integration points, two at the element ends, is used for numerical integration within

each element. Moment-curvature behavior is implemented using values in Table 5.7 and 5.8 and Eqs. (6.1-6.2).

Comparison between the two models shows that both produce similar results as far as modeling the load-deformation cyclic response P-δ of the tests in Chapter 4 as illustrated in Fig. 6.5a. Moreover the root mean-squared deviation between the predicted load responses to the tests is between 5% and 12% as shown in Fig. 6.6a. Likewise, both methods show very similar energy dissipation cycle by cycle (Fig. 6.5c) and the total energy dissipated is almost identical yet smaller than the tests (Fig. 6.6b). Evident differences on the deflections and rotations along the member arise from the nature of each model as illustrated in Fig. 6.5b for rotations and vertical deflections. Spring models with rigid bars have the disadvantage of displacement and rotations incompatibility depending on the spring arrangement and would require adjustments of spring definition parameters when modeling different type of loading. A solution commonly used in analysis of frames under lateral loads consists of using elastic-beam elements combined with springs that model the nonlinear behavior at the plastic hinge locations; however this approach requires to define a priori the springs location, could lead to numerical instability problems and makes it difficult to express stiffness degradation as a fraction of the elastic stiffness [78]. In this regard, using a beam-column element with distributed nonlinearity M-κ is an efficient approach that does not require additional adjustment of parameters in Table 5.7 and 5.8, and lends itself to further generalization and use with other loading configurations such as those producing moment gradients.

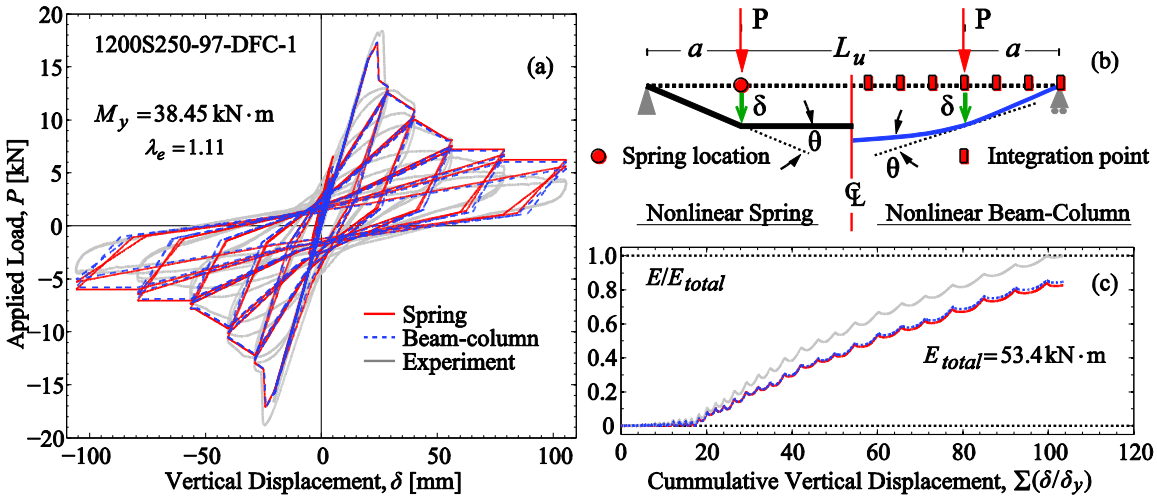

Fig. 6.5. a) Simulated and experimental response; b) Spring and beam-column models; c) Energy dissipated.

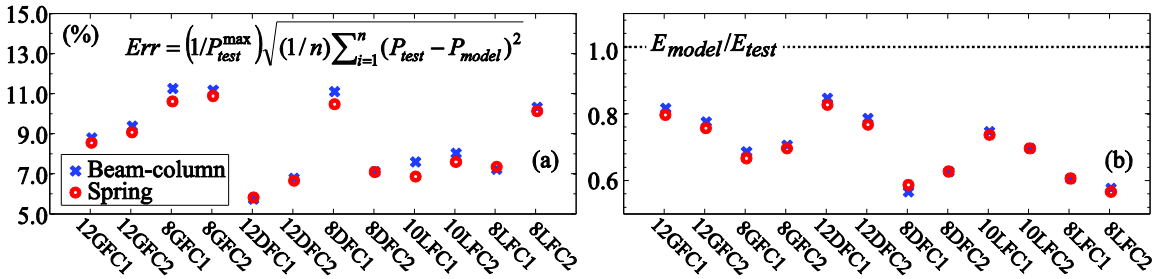

Fig. 6.6. Model to tests load a) and energy b) dissipation ratio for all test in Chapter 4 (see member labels in Table 5.7).

6.3 Conclusions

The modeling approach described allows modeling CFS member cyclic behavior in systems and different loading scenarios as illustrated later in Chapter 8. Some shortcomings arise with the modeling approach using nonlinear beam-columns with hysteretic behavior modeled at the cross-section level as described in this chapter. The first one is related to the axial load-bending interaction in the case where both axial loads and bending moments are applied at member ends. This type of interaction is not included for the behavior at the cross-section level formulated here and would not be addressed in this dissertation. However, the approach remains relevant to model the behavior of several components that are subjected to mainly axial loads or bending moments in a light-framed steel building like the one shown in Fig. 1.1.

The second shortcoming is related to the underlying cross-section behavior model (*Pinching4*). As pointed out in section 5.1 for axial members, the modeled unloading-reloading behavior from tension to compression does not reflect the observed behavior from the experiments where the amount strength or stiffness degrades in compression excursions is independent from that in tension excursions. Because damage accumulation in *Pinching4* is defined using the same sets of parameters for both loading directions, damage accumulated during compression excursions is used to reduce the strength envelope for the subsequent excursions in tension (and vice versa). This results in underestimation or overestimation of the strength or stiffness degradation depending on the loading direction. In the next chapter these two issues are addressed by modifying *Pinching4* to include damage accumulation independent of the loading directions and redefining the unloading-reloading path from tension to compression for axial members.

Chapter 7: Nonlinear Beam-Column Model for Thin-Walled Steel Columns Including Local Buckling [6]

Steel columns subjected to dynamic loading such as those resulting from earthquake, wind, and other hazards, can experience cyclic local buckling deformations. During cyclic loading, buckling deformations reverse and combine with yielding in tension at the highly stressed locations compromising the member's strength and stiffness and affect their ductility. Local buckling deformations develop under compression and stretch during tension, and are more pronounced, as well as their effects, in thinner cross-sections (e.g., thin-walled cold-formed steel).

The framework described in Chapter 6 for modeling the axial cyclic behavior in CFS members is generalized in this chapter for thin-walled steel columns including local buckling. The nonlinear-beam column approach previously described is combined with a hysteretic cross-section behavior model that describes the behavior observed in the experimental responses described in Chapter 3. Generalized expressions for backbones, strength degradation, stiffness degradation and unloading-reloading parameters are presented as a function of the member cross-section slenderness λ_ℓ and the hysteretic energy dissipated. The model parameters are derived using P-δ responses obtained from finite element analysis of thin-walled cold-formed steel members conducted in ABAQUS [23]. Parameters are calibrated so that the model matched the simulated axial load-displacement (P-δ) monotonic and cyclic responses of each column in the finite element analysis set.

7.1 Simulated axial monotonic and cyclic responses database

Twenty two thin-walled C-shaped columns were modeled using ABAQUS [23] to study the monotonic and cyclic behavior of axial members exhibiting local buckling deformations. The cross-sections were selected from the SSMA catalog [46] such that the capacity in compression is governed by local buckling as predicted using the AISI-S100-07 Direct Strength Method [22]. The cross-sections properties and length were selected to cover a range of local cross-section slenderness $\lambda_\ell = (P_y/P_{cr\ell})^{0.5}$ from 0.69 to 3.39 ($P_y=AF_y$, A=cross-section area; F_y=yield stress and $P_{cr\ell}$=local buckling load calculated using for example CUFSM [48]). The analyses were setup to

[6] Parts of this chapter are part of a paper accepted and presented at the *2015 SSRC Annual Stability Conference* with the title "**OpenSees Simulation of Steel Column Axial Cyclic Response Including Local Buckling**" [85].

simulate similar boundary conditions and loading as those described in Chapter 3 for testing CFS axial members. Table 7.1 summarizes the selected cross-sections and their elastic buckling properties.

The column models are implemented using S9R5 thin-shell elements that allow double-curvature within one element, a feature that facilitates definition of initially curved geometries with smaller mesh size (as compared to using S4 or S4R elements). The length of each column was set such that at least five buckling half-waves could develop in compression. The half-wavelength $L_{cr\ell}$ was calculated using the finite strip eigen-buckling analysis software CUFSM [48]. The aspect ratio (length/width) for each element was about 4:1 with the long side aligned along the length of the column. End boundary conditions were modeled as fixed ends with one end allowed to move along the axial direction 3, see Fig. 7.1a. Loading was applied at the free end by imposing a displacement history derived using the displacement-controlled testing protocol for cold-formed steel members described in Appendix A.

Initial geometric imperfections are simulated using the 1D spectral approach described by Zeinoddini et al. [28]. In this approach the imperfection field imposed is formed using a linear combination of five buckling mode shapes where the amplitude of each mode along the length is given by a one-dimensional power spectrum. The 1D spectrum accounts for the frequency content and variability of the distribution of each mode along the length. The mode shapes used to generate the imperfection field where calculated using CUFSM [48] and are illustrated in Fig. 7.1b.

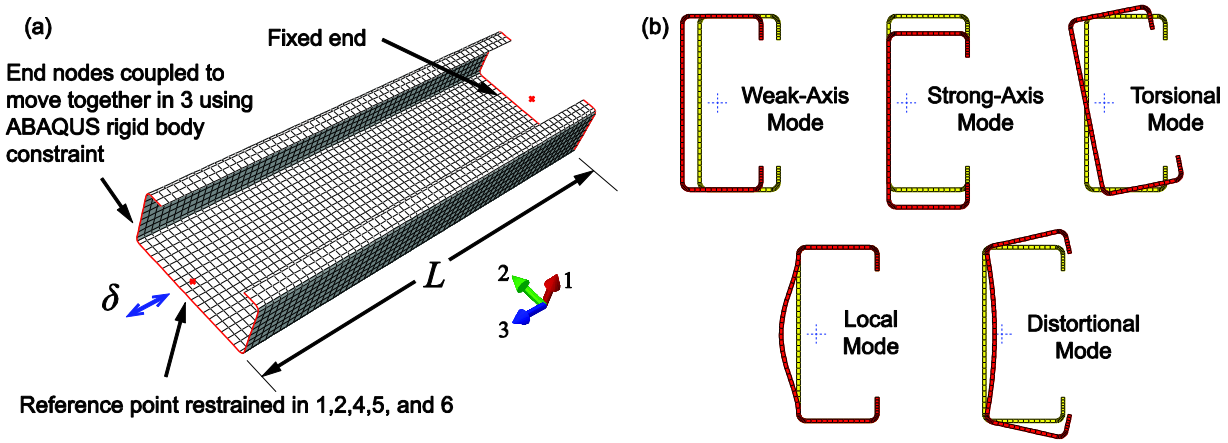

Fig. 7.1. Column model geometry with warping fixed-fixed ends boundary conditions (a), and buckling modes used with the 1D spectral approach to construct the imperfection field imposed to the model (b).

Table 7.1. Column model elastic buckling properties and compressive capacity.

Specimen	L (mm)	$L_{cr\ell}$	F_y (MPa)	P_y (kN)	$P_{cr\ell}$ (kN)	λ_ℓ	P_n (kN)
250S162-68	260	52	417	119	244	0.694	117
250S162-54	269	54	417	96	122	0.881	87
350S162-68	316	63	417	138	149	0.957	119
362S162-68	328	66	417	141	141	0.989	118
400S162-68	366	73	417	148	122	1.091	117
600S200-97	551	110	417	287	216	1.139	218
350S162-54	323	65	417	111	74	1.215	82
362S137-54	335	67	417	102	64	1.245	73
362S162-54	335	67	417	113	71	1.255	81
362S162-54	305	67	417	113	71	1.257	81
362S200-54	335	67	417	128	78	1.271	92
400S137-54	373	75	417	108	56	1.372	72
550S162-68	516	103	417	177	78	1.488	111
600S162-68	567	113	417	186	69	1.617	110
550S162-54	524	105	417	142	39	1.878	76
600S162-54	574	115	417	149	35	2.039	75
600S250-54	574	115	417	180	40	2.093	90
800S200-68	767	153	417	244	51	2.146	117
800S250-68	767	153	417	263	54	2.180	126
800S200-54	775	155	417	195	26	2.705	79
800S250-54	775	155	417	210	27	2.751	85
1000S250-54	976	195	417	241	20	3.387	82

$\lambda_\ell = (P_y/P_{cr\ell})^{0.5}$.

The steel modulus of elasticity is assumed as E=203GPa and Poisson's ratio ν=0.3. Steel plasticity is implemented using the Armstrong-Frederick plasticity model [79] (combined nonlinear isotropic-kinematic hardening with one backstress, α, in ABAQUS) as given by Eq. 7.1-7.2. Isotropic hardening parameters Q_∞ and b and kinematic hardening parameters C_1 and γ_1 were calibrated using true strain-stress curves obtained from steel coupon tests. The steel plasticity model parameters are kept the same for all columns in the simulation database and are summarized in Table 7.2.

$$\bar{\sigma} = \sigma_y + Q_\infty(1 - e^{-b\bar{\varepsilon}_p}) \tag{7.1}$$

$$\dot{\alpha} = \frac{C_1}{\bar{\sigma}}(\sigma - \alpha)\dot{\bar{\varepsilon}}_p - \gamma_1 \alpha \dot{\bar{\varepsilon}}_p \tag{7.2}$$

Material damage is also simulated to capture the strength and stiffness reduction from tearing and fracture caused by cold-bending and stretching during cyclic loading. The onset of damage and propagation until tearing/fracture of the material is modeled in ABAQUS using the DAMAGE INITIATION and DAMAGE EVOLUTION commands. Damage initiation is implemented using the Bao-Wierzbicki fracture criteria for metal sheets [80,81] to define the

fracture locus. This model defines the equivalent strain to fracture $\bar{\varepsilon}_f$ for different average stress triaxiality values $\rho = \sigma_m/\bar{\sigma}$ (σ_m= hydrostatic stress and $\bar{\sigma}$ = von-misses stress) as given by Eq. 7.3,

$$\bar{\varepsilon}_f = \begin{cases} \infty & ,\rho \le -1/3 \\ A/(1+3\rho) & ,-1/3 \le \rho \le 0 \\ A+9(B-A)\rho^2 & ,0 \le \rho \le 1/3 \\ B/3\rho & ,\rho > 1/3 \end{cases} \quad 7.3$$

where $A = B(3/4)^{1/2n}$ is the equivalent fracture strain in pure shear, B is the equivalent strain to fracture in uniaxial tension, and n is the hardening exponent if the true stress-strain curve is approximated by the power law $\bar{\sigma} = K\bar{\varepsilon}^n$ (K is a constant). The fracture locus parameters were calibrated using the same stress-strain curves used to calibrate the steel plasticity model following the procedure described in [81]. The values obtained are listed in Table 7.2. The plasticity model and fracture locus were validated by comparing cyclic responses obtained from ABAQUS for two of the local buckling specimens in Chapter 3 (362S164-54-LAC# specimens) to the corresponding experimental curves.

Table 7.2. Steel material properties for ABAQUS simulations

σ_y [MPa]	C_1 [MPa]	γ_1 -	Q_∞ [MPa]	b -	A -	B -
416.6	114.7	3.012	295.9	3.468	0.146	0.269

Axial load-displacement (P-δ) monotonic and cyclic responses were obtained for each model in the database. The responses were characterized to obtain the amount of strength degradation, stiffness degradation, hysteretic energy dissipated, and pinching following the procedures described in Chapter 5. These results are used in the next section to include local buckling in modeling steel column cyclic behavior.

7.2 Axial thin-walled cross-section hysteretic model - asymPinching

This section introduces the asymmetric pinching hysteretic model (herein referred as *asymPinching*) for modeling the axial cyclic behavior in thin-walled steel columns. The model includes a *backbone curve*, a *damage model* with independent definitions for tension and compression excursions, and *unloading-reloading paths* with a tension-to-compression unloading-reloading path definition that reflects the actual behavior observed Chapter 3 (see Fig. 7.2). The model follows the same format of the original *Pinching4* model introduced by Lowes et al. [21] with redefined variables to make damage accumulation independent for negative and positive

excursions. The generalized expressions for each parameter (as a function of the cross-section local slenderness λ_ℓ) are described next.

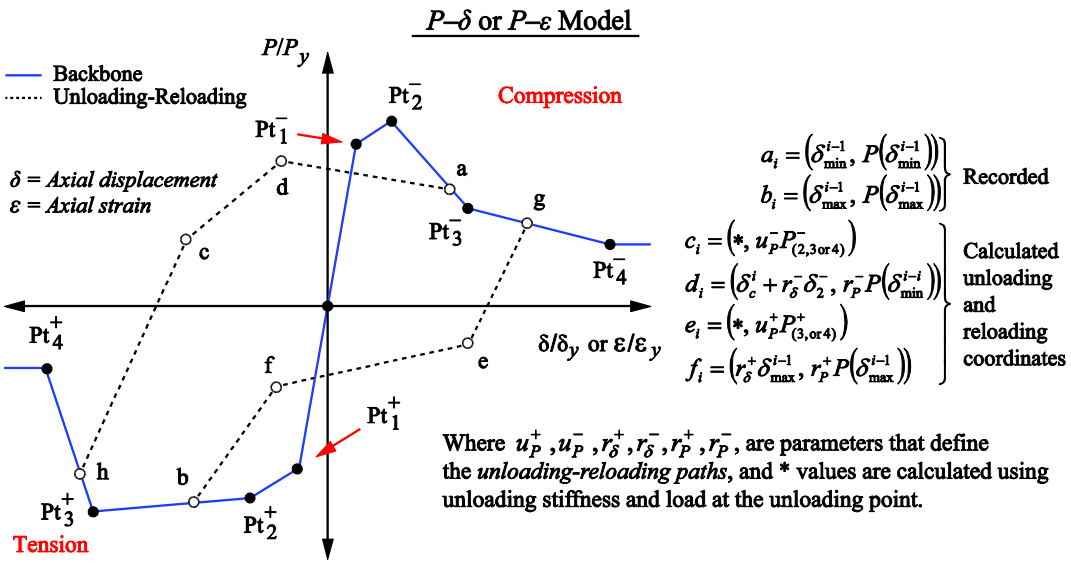

Fig. 7.2. Cross-section hysteretic behavior model for axial members.

7.2.1 Backbone curve

The compression backbone coordinate pairs (δ_i, P_i) [or (ε_i, P_i)] were derived as described in Chapter 5 from the monotonic responses. The load values P_i are set as a function of the local slenderness λ_ℓ where the peak load P_2 is set equal to the DSM strength expression in AISI-S100-12 [22]. All values of P_i are limited to a maximum of P_y with the case where all P_i/P_y = 1.0 corresponding to a column with a very stocky cross-section (i.e. compact cross-section). To determine the displacement δ_1 (strain ε_1) that marks the end of the elastic range in compression (point 1 in Fig. 7.2), it is necessary to calculate the initial stiffness k_1 expressed as a fraction (that depends on λ_ℓ) of the elastic stiffness k_e=AE/L as shown in Fig. 7.3. The expressions for the initial stiffness k_1 and the compressive load P_1 suggests that the cross-section is considered fully effective for $\lambda_\ell \leq 0.689$, and considered slender if $\lambda_\ell > 1.23$. The expressions for the four coordinate pairs (δ_i, P_i) [or (ε_i, P_i)] that define the compression backbone are summarized in Table 7.3 and illustrated in Fig. 7.4.

The tension backbone coordinate pairs (δ_i, P_i) [or (ε_i, P_i)] are set as a function of the yield load P_y and the corresponding elastic yield displacement δ_y (or strain ε_y). Because the *asymPinching* model includes independent damage accumulation for each loading direction, it was not necessary to overestimate the loads P_i in the backbone as described in Chapter 5. The load P_2

was set equal to P_y and some hardening is allowed to account for material hardening that may occur after the cross-section yields by setting the load P_3 =1.039P_y. The tension backbone coordinates are listed in Table 7.4.

Table 7.3. Compression backbone general expressions for local buckling.

Load	Displacement/Strain
$\frac{P_1}{P_y}=\begin{cases}1.0 & ,\lambda_\ell \le 0.689\\ 0.760\lambda_\ell^{-0.737} & ,\lambda_\ell > 0.689\end{cases}$	$\frac{\delta_1}{\delta_y}=\frac{\varepsilon_1}{\varepsilon_y}=\begin{cases}1.0 & ,\lambda_\ell \le 0.689\\ P_1/k_1 & ,\lambda_\ell > 0.689\end{cases}$
$\frac{P_2}{P_y}=\begin{cases}1.0 & ,\lambda_\ell \le 0.776\\ \left[1-0.15\lambda_\ell^{-2(0.4)}\right]\lambda_\ell^{-2(0.4)} & ,\lambda_\ell > 0.776\end{cases}$	$\frac{\delta_2}{\delta_y}=\frac{\varepsilon_2}{\varepsilon_y}=\begin{cases}1.0 & ,\lambda_\ell \le 0.814\\ 0.774\left(\lambda_\ell-0.776\right)^{-0.078} & ,\lambda_\ell > 0.814\end{cases}$
$\frac{P_3}{P_y}=\begin{cases}1.0 & ,\lambda_\ell \le 0.523\\ 0.552\lambda_\ell^{-0.915} & ,\lambda_\ell > 0.523\end{cases}$	$\frac{\delta_3}{\delta_y}=\frac{\varepsilon_3}{\varepsilon_y}=\begin{cases}2.0 & ,\lambda_\ell \le 0.623\\ 1.339+0.345\lambda_\ell^{-1.371} & ,\lambda_\ell > 0.623\end{cases}$
$\frac{P_4}{P_y}=\begin{cases}1.0 & ,\lambda_\ell \le 0.379\\ 0.338\lambda_\ell^{-1.119} & ,\lambda_\ell > 0.379\end{cases}$	$\frac{\delta_4}{\delta_y}=\frac{\varepsilon_4}{\varepsilon_y}=\begin{cases}6.0 & ,\lambda_\ell \le 0.857\\ 5.048+0.491\lambda_\ell^{-4.287} & ,\lambda_\ell > 0.857\end{cases}$
	$\frac{k_1}{k_e}=\begin{cases}1.0 & ,\lambda_\ell \le 1.23\\ 1.075\lambda_\ell^{-0.349} & ,\lambda_\ell > 1.23\end{cases}$

Table 7.4. Tension backbone general expressions for local buckling.

Load	Displacement/Strain
$P_1/P_y=0.910$	$\delta_1/\delta_y=\varepsilon_1/\varepsilon_y=0.910$
$P_2/P_y=1.000$	$\delta_2/\delta_y=\varepsilon_2/\varepsilon_y=1.270$
$P_3/P_y=1.039$	$\delta_3/\delta_y=\varepsilon_3/\varepsilon_y=8.000$
$P_4/P_y=0.739$	$\delta_4/\delta_y=\varepsilon_4/\varepsilon_y=10.00$

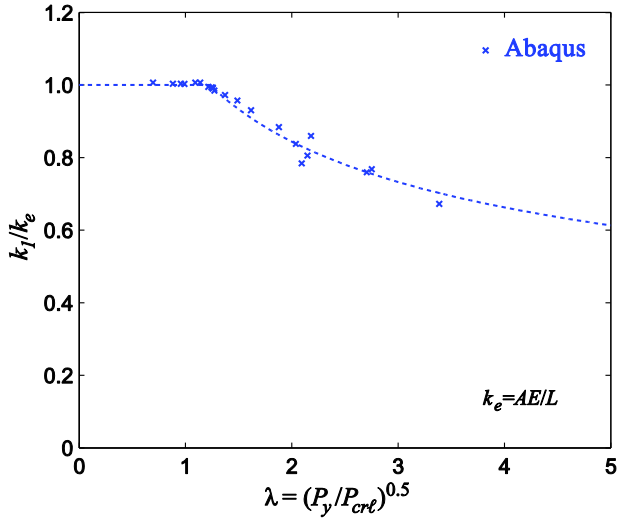

Fig. 7.3. Initial member stiffness as a function of local slenderness.

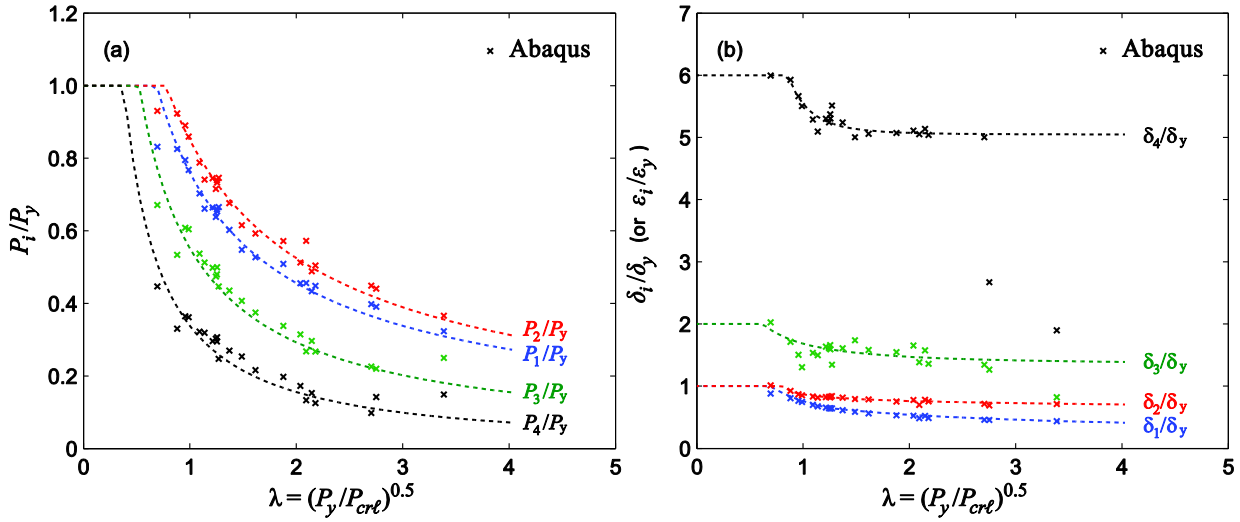

Fig. 7.4. Compression backbone general expressions for local buckling.

7.2.2 Cyclic strength and stiffness degradation

Cyclic strength and stiffness degradation is simulated as a function of the *cumulative hysteretic energy dissipated* in each excursion E_i and the *total energy dissipation capacity* E_T (see section 7.2.3). As more hysteretic energy is dissipated, the ratio E_i/E_T approaches unity where further deterioration is not expected. The functional form for strength and stiffness degradation is given by Eq. 7.4 where the coefficients β_i are calibrated as described further below in this section.

As discussed in Chapter 5, cyclic strength and stiffness degradation differ substantially between compression and tension excursions. In *Pinching4*, deterioration of the strength envelope (and stiffness) is defined using the same β_i values for tension and compression. Further, damage accumulated during compression excursions is used to reduce the strength envelope (or stiffness) in subsequent excursions in tension (and vice versa). If damage accumulated from the previous excursion is used in the current (but opposite in direction) excursion, then strength degradation (and stiffness degradation) will be underestimated and overestimated during the compression and tension excursions respectively. In the improved *asymPinching* model, the degradation parameters β_i are defined independently for tension and compression to overcome this shortcoming. Thus, the accumulated damage during compression excursions is not used to reduce the strength envelope (or stiffness) in the subsequent excursions in tension (and vice versa). In CFS axial members, strength degradation develops independently in both loading directions, where loads in tension can reach the yield load P_y despite having experienced deterioration of the compression strength from

buckling deformations unless fracture has been initiated. This is the case for example in a member subjected to one sided compression cyclic loading followed by one large tension excursion, where loads close to P_y should be expected. Strains and stresses in tension loading tend to distribute evenly across the member cross-section and compared to compression loading when buckling occurs.

$$\eta_i = \beta_2 \left(E_i / E_T\right)^{\beta_4} \leq 1.0 \tag{7.4}$$

$$f_{\max,i} / f_{\max,o} = 1 - \eta_{is} \geq 0 \tag{7.5}$$

$$k_i / k_1 = 1 - \eta_{ik} \geq 0 \tag{7.6}$$

Strength degradation is characterized as the positive difference in strength between the monotonic backbone force ($f_{max,o}$) and the cyclic force envelope ($f_{max,i}$). Fig. 7.5 shows how strength degrades as a function of the cumulative hysteretic energy E_i where lighter color curves indicate larger slenderness values. It can be seen that strength degradation is cross-section slenderness and member length independent (see Fig. 7.5). Because of this independence, two separate expression for η_{is} are set with constant parameters β_{is} to describe how strength deteriorates as a function of the energy dissipated. Note that there is some residual strength after the energy dissipation capacity is exhausted (i.e., E_i/E_T =1.0). The parameters for strength degradation are listed in Table 7.5.

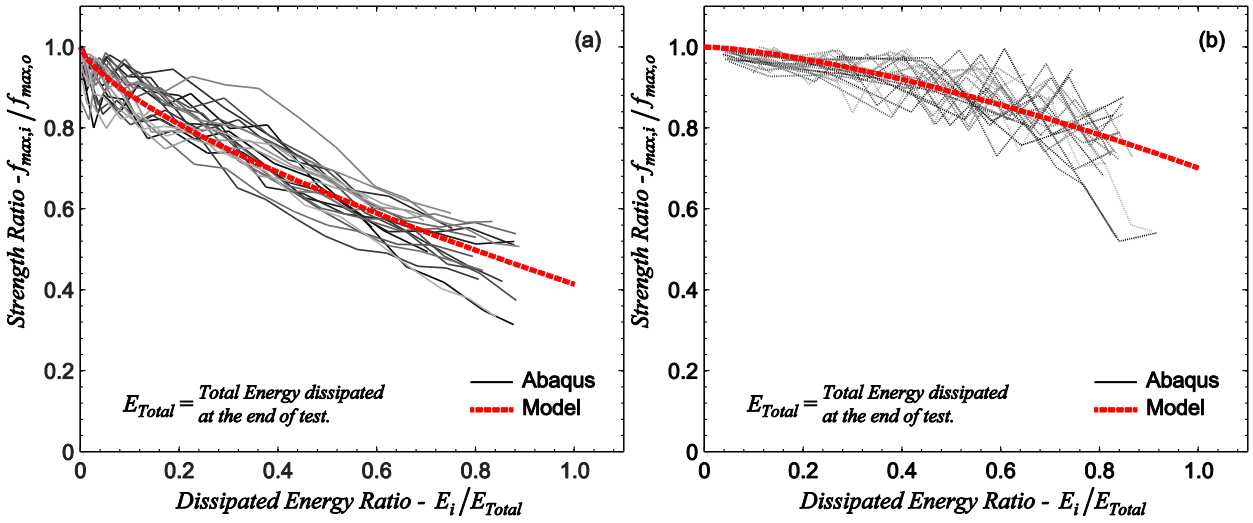

Fig. 7.5. Strength degradation in compression (a) and tension (b) are member length and cross-section slenderness independent

Stiffness degradation is characterized as the ratio between the unloading stiffness in every excursion k_i and the initial stiffness k_1. Fig. 7.6 shows how unloading stiffness degrades as a function of the cumulative hysteretic energy E_i. From the figure it is noted how stiffness in

compression degrades faster as the slenderness increases indicated by the lighter colors, while in tension degradation is independent of the member length and cross-section slenderness. In addition, stiffness appears to reduce to zero as the cumulative energy dissipated E_i reaches the maximum value E_T. Therefore, expressions for the parameters β_{is} as a function of the cross-section slenderness were derived for the case of stiffness degradation in compression and are shown in Fig. 7.7. In tension an expression for η_{ik} with constant parameters β_{2s} and β_{4s} is set to describe how stiffness degrades as a function of the energy dissipated. The parameters to define stiffness degradation are listed in Table 7.5.

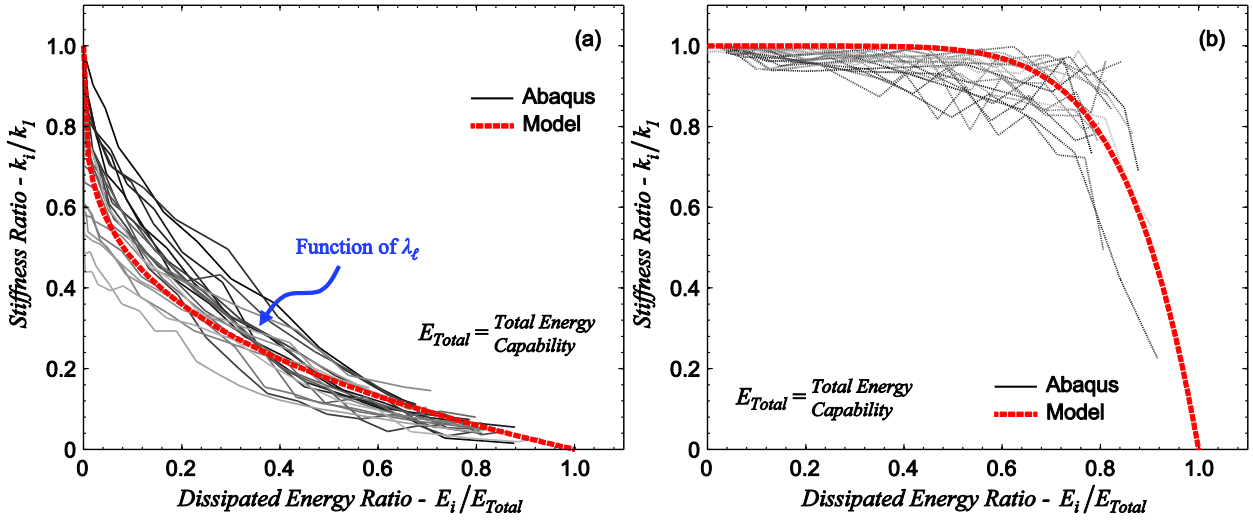

Fig. 7.6. Stiffness degradation in compression (a) is a function of the cross-section slenderness λ_ℓ, while in tension (b) it is member length and slenderness independent.

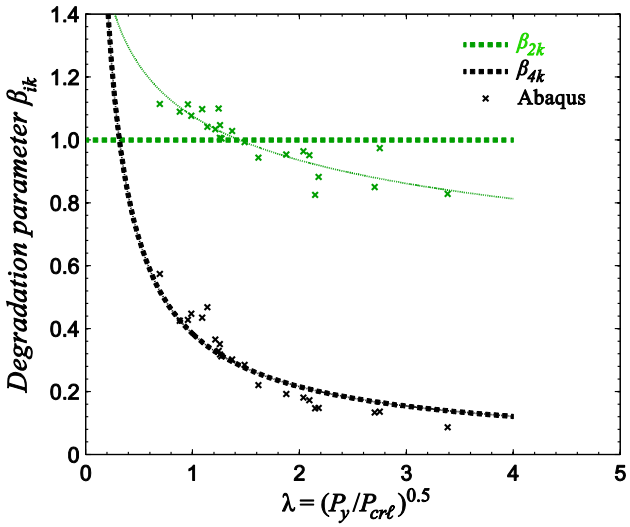

Fig. 7.7. Stiffness degradation parameters as a function of the cross-section slenderness.

Table 7.5. Strength and stiffness degradation parameters.

Loading Direction	Strength Degradation	Stiffness Degradation
Compression	$\beta_{2s} = 0.586,$ $\beta_{4s} = 0.697$	$\beta_{2k} = 1.0,$ $\beta_{2k} = 0.384\lambda_{\ell}^{-0.832}$
Tension	$\beta_{2s} = 0.299,$ $\beta_{4s} = 1.438$	$\beta_{2k} = 1.0,$ $\beta_{4k} = 6.797$

7.2.3 Total energy E_T

It was shown previously that stiffness and strength degrade as a function of the *cumulative hysteretic energy dissipated* in each excursion E_i and the *total energy dissipation capacity* E_T. The total energy dissipation capacity E_T is the maximum value of cumulative hysteretic energy the element is allowed to dissipate. A general expression to calculate E_T for any given member represents a challenge as this value cannot be tied easily to the member strength and properties in a mechanics based manner. However, a heuristic procedure based on the hysteretic energy dissipated per excursion was developed to obtain an expression for E_T given the member cross-section slenderness λ_ℓ.

The procedure to obtain E_T starts by calculating the *hysteretic energy dissipated* per excursion $E_{e,i}$ normalized to an area defined by the maximum load in the corresponding loading direction and the range of deformations of the current excursion (see inset in Fig. 7.8a). If this normalized energy dissipated per excursion ($NHE_{pe,i}$) is plotted versus the cumulative normalized axial deformation ($\sum\delta/\delta_y$), the plot will look like the one shown in Fig. 7.8a. It can be seen that $NHE_{pe,i}$ increases up to a maximum value and then decreases towards zero as cumulative normalized deformation increases. This is a typical behavior observed in all the cyclic responses from the simulation database as shown in Fig. 7.9 and also observed in the experiments described in Chapter 3 (see Fig. 3.13). Note that the normalized energy dissipated per excursion $NHE_{pe,i}$ decreases with the cross-section slenderness. This is indicated in Fig. 7.9 where slenderness increases from the lighter to darker colors curves.

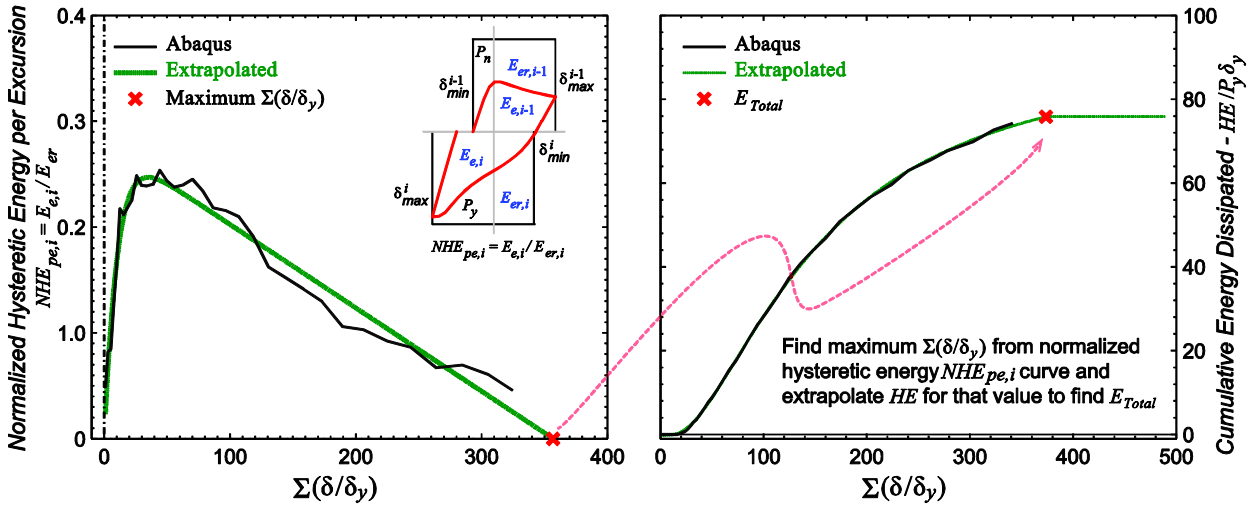

Fig. 7.8. The total energy dissipation capacity E_T is obtained as the cumulative energy dissipated corresponding to a cumulative normalized deformation CDF_0. The cumulative deformation CDF_0 is the value where the normalized hysteretic energy per excursion $NHE_{pe,i}$ vanishes.

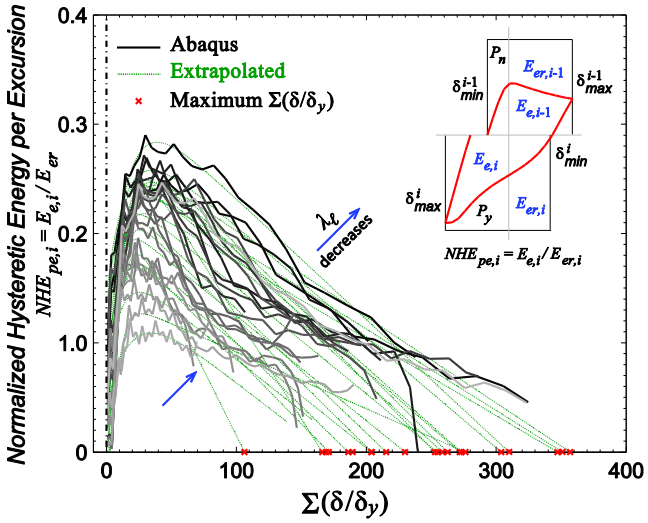

Fig. 7.9. Normalized hysteretic energy dissipated per excursion $NHE_{pe,i}$.

The rationale for estimating E_T therefore is: there should be a cumulative normalized deformation CDF_0 for which $NHE_{pe,i}$ is equal to zero and beyond that point the member is unable to dissipate more energy (see Fig. 7.8). The value for E_T is determined as the cumulative hysteretic energy E_i corresponding to the cumulative normalized axial deformation CDF_0. Values for E_T were estimated for all members in the simulation database and used to obtain the expression in Eq. 7.7 (see Fig. 7.10). Note that E_T increases rapidly to infinite as slenderness λ_ℓ becomes smaller. It is assumed that for the members with a fully effective cross-section (i.e., $\lambda_\ell \leq 0.689$), the slenderness effects on the total energy dissipation capacity are negligible and E_T depends only on the material

properties, member length and cross-section area. Thus a maximum limit for the total energy dissipation capacity is proposed at $E_T \leq 113.2 P_y \delta_y$ for all members with fully effective cross-section. This limit is set somewhat arbitrarily and the proposed value requires experimental validation not addressed in this dissertation.

$$\frac{E_T}{P_y \delta_y} = \begin{cases} 113.2 & , \lambda_\ell \leq 0.689 \\ 64.991 \lambda_\ell^{-1.489} & , \lambda_\ell > 0.689 \end{cases} \qquad 7.7$$

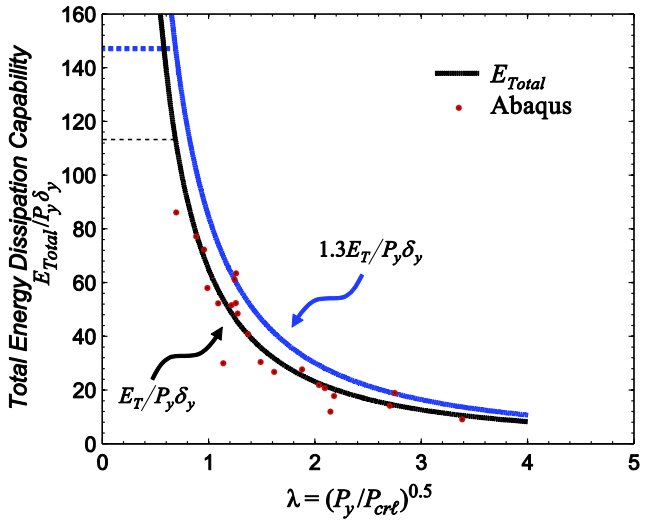

Fig. 7.10. Total energy dissipation capability as a function of the cross-section slenderness.

7.2.4 Unloading-reloading paths

The tension-to-compression reloading path was redefined such that the slopes of segments *h*-*c*, *c*-*d* are positives and decrease in that order (i.e., $k_{hc} > k_{cd}$) to reflect the unloading and reloading up to the peak compressive force in the current excursion. The slope of segment *d*-*a* was set negative to represent the subsequent softening observed in the experimental responses. The points in the tension-compression unloading-reloading path are defined by three parameters u_{P-}, r_{P-} and $r_{\delta-}$. The parameter u_{P-} is the ratio (u_{P-}<1.0) of the load at the point at which reloading in compression starts (point *c* in Fig. 7.2) to the current excursion degraded envelope load P_3 (if $\delta_{min} < \delta_{2+}$), P_4 (if $\delta_{min} < \delta_{3+}$) or P_5 (if $\delta_{min} < \delta_{4+}$). The parameter r_{P-} is the ratio ($r_{P-} \geq 1.0$) of the maximum compression load in the current excursion (point *d*) to the load $P(\delta_{min})$ corresponding to the minimum historic displacement at point *a* (see Fig. 7.2). The load at point *d* is restricted to the maximum load of the current degraded backbone envelope. The displacement at point *d* is defined

as the displacement at point *c* plus a fraction $r_{\delta-}$ of the displacement at the peak compression load of the non-degraded backbone envelope ($r_{\delta-} \leq 1.0$).

The compression-to-tension unloading-reloading path is defined using the original definitions from *Pinching4* model. Parameter $r_{\delta+}$ is the ratio of the deformation at which reloading starts (point *f* in Fig. 7.2) to the maximum historic deformation δ_{max}. Parameter r_{P+} is the ratio of the load at the point at which reloading starts (points *f*) to the load corresponding to the maximum historic displacement $P(\delta_{max})$. Parameter u_{P+} is the ratio of the load developed after unloading (point *e* in Fig. 7.2) to the load coordinate at point 3 of the degraded backbone P_{3+}. Unloading-reloading parameters were obtained as described in Chapter 5 for each of the responses in the simulation database and are shown in Fig. 7.11. The figure shows no trend of any of the six parameters with slenderness as well as a lot of scatter. A second calibration exercise was performed to obtain values that worked for all responses in the simulation database resulting in the values summarized in Table 7.9. During the calibration exercise it was necessary to increase 30% the value for the total energy dissipation capacity to be able to match the simulated responses in ABAQUS. Thus, the new design expression for the total energy dissipation capacity is to $1.3E_T$ with E_T as given in Eq. 7.7. Appendix F includes the source code implementing the tension-to-compression unloading-reloading path for the *asymPinching* model.

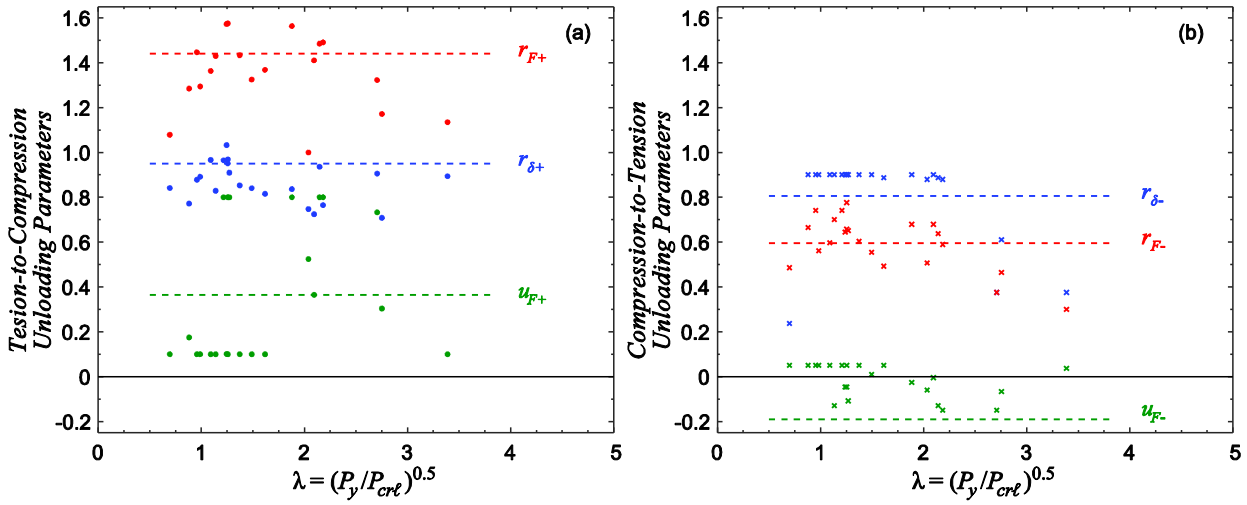

Fig. 7.11. Unloading-reloading path parameters for (a) tension-to-compression and (b) compression-to-tension.

Table 7.6. Unloading-reloading parameters for *asymPinching*.

Parameter	$r_{\delta+}$	r_{P+}	u_{P+}	$r_{\delta-}$	r_{P-}	u_{P-}
Mean	0.652	1.372	0.527	0.418	0.457	-0.022
COV	0.211	0.104	0.236	0.132	0.081	1.702
Adopted	*0.950*	*1.440*	*0.364*	*0.806*	*0.596*	*-0.019*

7.3 Modeling hysteretic behavior including local buckling using Pinching4

The approach presented in the preceding section introduced new definitions for the tension-to-compression unloading-reloading path, and introduced independence in the damage definition for tension and compression excursions. Even though the *asymPinching* model overcomes the difficulties described in Chapter 5 and 6 when using *Pinching4* to model the cyclic behavior in CFS axial members, the model still requires further validation and code stability checks for different loading cases and boundary conditions. Conversely the *Pinching4* model has been used in several cases for different type of loadings since first introduced that probe the stability of the model and code. For this reason in this section, degradation and pinching parameters are provided to use with *Pinching4* to model cyclic behavior of steel columns including local buckling.

7.3.1 Backbone curve

The backbone curve definitions in compression are defined using the same expressions given in Table 7.3. However, the backbone in tension needs to be modified to overcome the damage underestimation and overestimation issues associated with *Pinching4* when modeling CFS members axial cyclic behavior. The tension backbone coordinates in Table 7.7 are proposed herein for used with *Pinching4*. This backbone in tension is defined based on the tension side of the cyclic envelopes obtained from the simulation database.

Table 7.7. Tension backbone for steel column modeling using *Pinching4*.

Load	Displacement/Strain
$P_1/P_y = 1.044$	$\delta_1/\delta_y = \varepsilon_1/\varepsilon_y = 1.044$
$P_2/P_y = 1.134$	$\delta_2/\delta_y = \varepsilon_2/\varepsilon_y = 1.404$
$P_3/P_y = 1.172$	$\delta_3/\delta_y = \varepsilon_3/\varepsilon_y = 8.0$
$P_4/P_y = 0.872$	$\delta_4/\delta_y = \varepsilon_4/\varepsilon_y = 10.0$

7.3.2 Cyclic strength and stiffness degradation

Cyclic strength and stiffness degradation parameters for *Pinching4* were derived in the same fashion as previously described for the *asymPinching* model. Degradation is defined as a

function of the *cumulative hysteretic energy dissipated* in each excursion E_i and the *total energy dissipation capacity*, where E_T is defined by Eq. 7.7. Unlike the *asymPinching* model, and as pointed out in Chapter 5, strength and stiffness degradation in *Pinching4* is defined using the same set of parameters for both loading directions. These parameters are calibrated using the average of the strength and stiffness degradation in both excursions.

Strength and stiffness degradation as a function of the energy dissipated is compared Fig. 7.12 to the expressions (blue dashed-lines) proposed herein to model deterioration in *Pinching4* (see Eq. 7.4-7.6). Damage parameters β_{2s} and β_{4s} are set constant as strength degradation is member length and cross-section slenderness independent in both tension and compression. Stiffness degradation parameters β_{2k} and β_{4k} on the other hand are defined as a function of the cross-section slenderness λ_ℓ as shown in Fig. 7.13. The strength and stiffness degradation parameters are derived after taking the average of the degradation curve in compression and the respective curve in tension. The expressions for strength and stiffness degradation parameters β_2 and β_4 are summarized in Table 7.8.

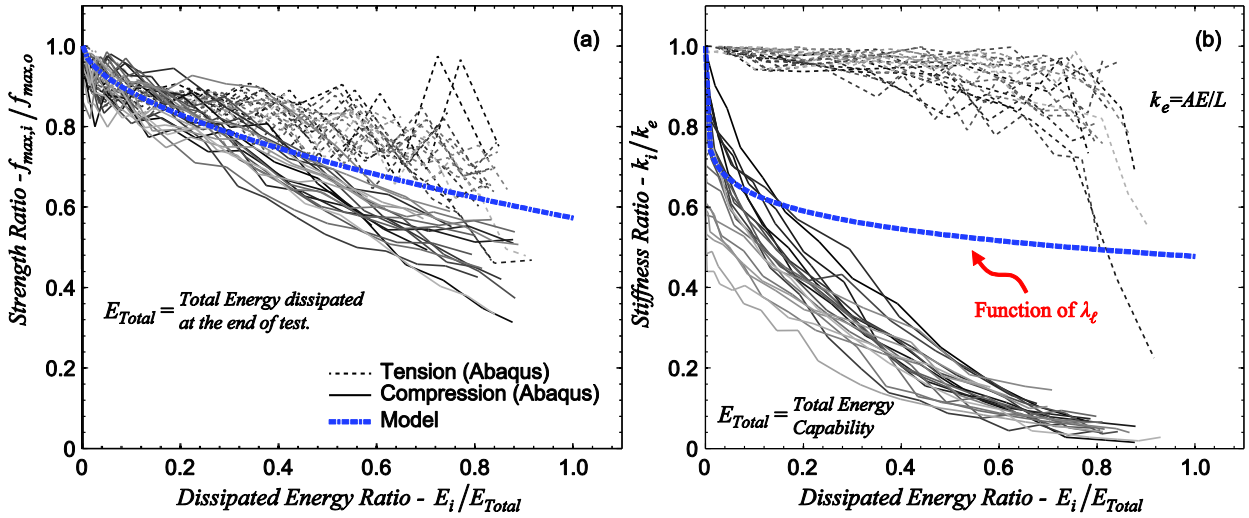

Fig. 7.12. Strength degradation (a) is member length and cross-section slenderness independent, while stiffness degradation (b) is a function of the member cross-section slenderness. Damage parameters are defined using the average damage in tension and compression (blue dashed-lines).

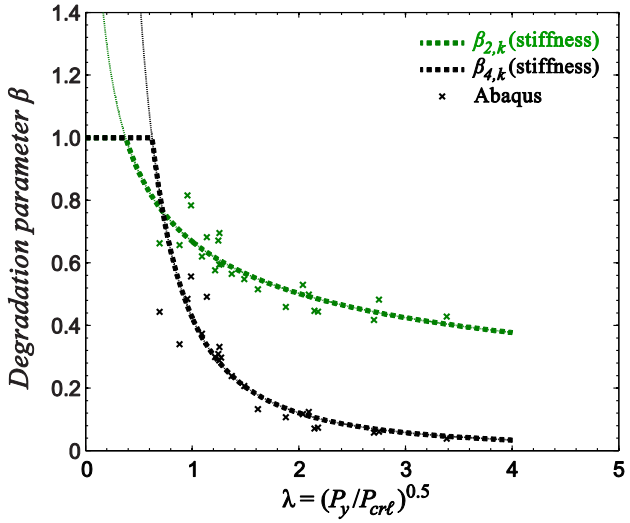

Fig. 7.13. Stiffness degradation parameters for *Pinching4* as a function of the cross-section slenderness.

Table 7.8. Strength and stiffness degradation parameters for *Pinching4*.

Strength Degradation	Stiffness Degradation
$\beta_{2s} = 0.427$	$\beta_{2k} = \begin{cases} 1.0 & ,\lambda_\ell \le 0.377 \\ 0.669\lambda_\ell^{-0.412} & ,\lambda_\ell > 0.377 \end{cases}$
$\beta_{4s} = 0.569$	$\beta_{4k} = \begin{cases} 1.0 & ,\lambda_\ell \le 0.624 \\ 0.425\lambda_\ell^{-1.814} & ,\lambda_\ell > 0.624 \end{cases}$

7.3.3 Unloading-reloading paths

The six parameters, u_{P+}, u_{P-}, $r_{\delta+}$, $r_{\delta-}$, r_{P+} and r_{P-} that define the unloading-reloading paths in *Pinching4* are shown in Fig. 7.14. The parameters $r_{\delta-}$ and $r_{\delta+}$ are the ratio of the deformation at which reloading starts (points *d* and *f* in Fig. 5.1) to the maximum/minimum historic deformation, δ_{min} and δ_{max}. Parameters r_{P-} and r_{P+} are the corresponding ratios of the load at the point at which reloading starts (points *d* and *f*) to the load corresponding to the maximum historic displacement, $f(d_{min})$ and $f(d_{max})$. Parameters u_{P-} and u_{P+} are the ratios of the load developed after unloading (point *c* and *e* in Fig. 5.1) to the load coordinate of backbone point 3, P_{3-} and P_{3+}. Note that the definitions of these parameters apply for both loading directions, however values for tension-to-compression different than compression-to-tension unloading-reloading can be specified. The values in Fig. 7.14 show that u_{P+}, u_{P-}, $r_{\delta+}$, $r_{\delta-}$, r_{P+} and r_{P-} are similar for all members in the simulation database and therefore and average value was adopted (see Table 7.9).

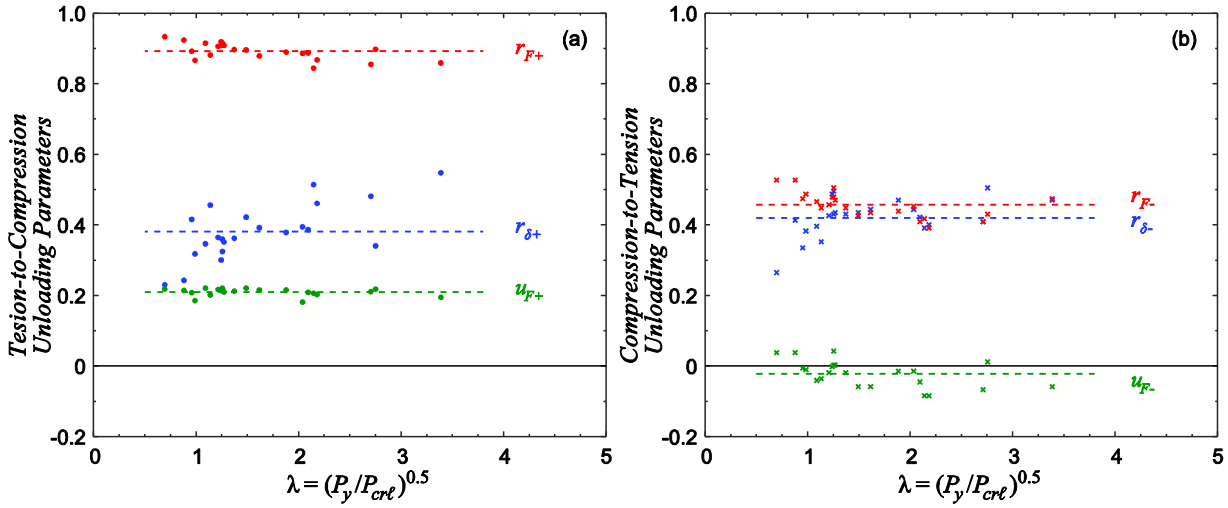

Fig. 7.14. *Pinching4* unloading-reloading path parameters for (a) tension-to-compression and (b) compression-to-tension.

Table 7.9. Unloading-reloading parameters for *Pinching4*.

Parameter	$r_{\delta+}$	r_{P+}	u_{P+}	$r_{\delta-}$	r_{P-}	u_{P-}
Mean	0.381	0.892	0.210	0.419	0.457	-0.022
COV	0.207	0.026	0.052	0.130	0.081	-1.702

7.4 Simulating the axial cyclic response including local buckling using asymPinching

Modeling the cyclic response of the local buckling members in Chapter 3 using the *asymPinching* model shows the capabilities of the latter to describe properly the response. The load-deformation *P-δ* response of the four axial members tested and those in the simulation database were calculated using *asymPinching* and previously derived expressions. The response was also calculated using *Pinching4* to evaluate the performance of the proposed model. Comparison of the responses in Fig. 7.15 shows that *asymPinching* captures the response more accurately than *Pinching4* including the unloading-reloading from tension-to-compression as well as the cumulative energy dissipation. The energy dissipated at the end of the simulations when using the *asymPinching* is in average 10% to 20% higher compared to the responses from the database and the experimental response for members 362LAC in Chapter 3 (see Fig. 7.16a). Additionally, the root mean-squared deviation between the predicted load responses using *asymPinching* to the ABAQUS simulations and tests is less than 15% and the responses for the 362LAC members (8% and 9%) falls within the trend shown in Fig. 7.16b. The model does not capture well the energy dissipated at the end of the test for the 600LAC members as E_{model}/E_{test} was very small and the root mean-squared deviation fell away from the error trend shown in Fig. 7.16b. The observed errors in energy and load steam mostly from the fact that the unloading-

reloading path is defined with the same parameters for all cycles the member may experience. As noted in Chapter 5 these parameters vary every cycle and accounting for this variation should reduce the errors observed.

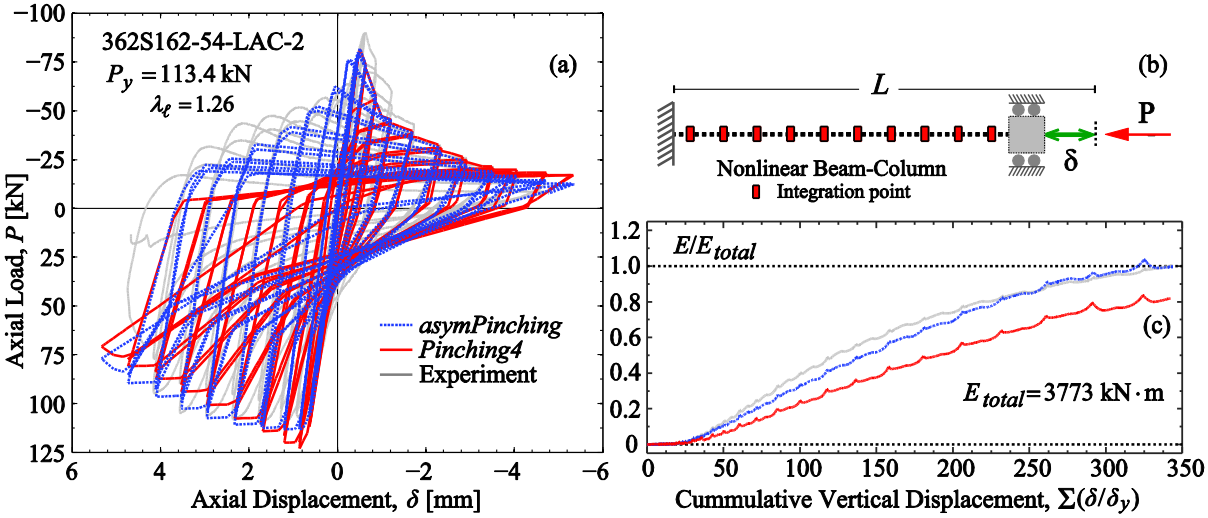

Fig. 7.15. Simulated response using the *asymPinching* model captures better the response (a) and energy dissipated (b) when compared to *Pinching4*.

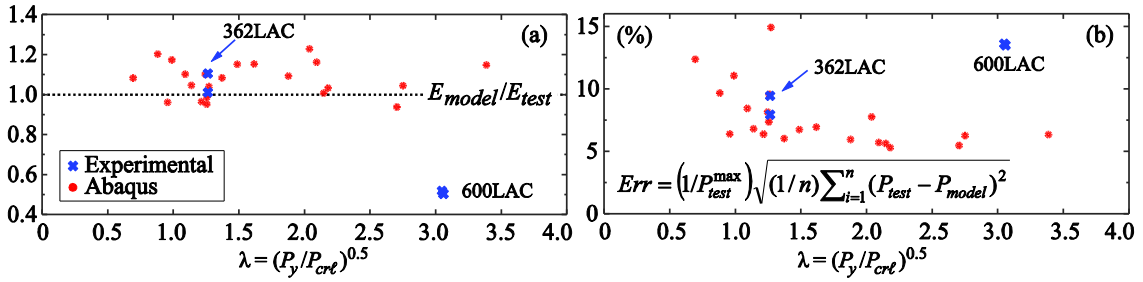

Fig. 7.16. Energy dissipation (a) from the *asymPinching* model is slightly higher than in ABAQUS simulations. The root mean-squared deviation (b) of the predicted load using *asymPinching* to the ABAQUS simulations is between 5% to 15%.

The following observation needs mentioning when using the *dispBeamColumn* (or similar) element from OpenSees in conjunction with the distributed nonlinearity approach to model thin-walled axial members. Since this approach assumes a uniform distribution of the axial strains along the member, the damage and inelastic strains localization behavior observed in the plate study from Chapter 2 and experiments is not captured. This can be visualized from the example in Fig. 7.17 which compares monotonic responses of a uniformly axially loaded member modeled using both the spring and the distributed nonlinearity approach. The curves show the displacement δ applied at the top end versus the axial reaction P at the bottom support. The two models produce

the same *P-δ* response, however from Fig. 7.18 can be seen that localization of inelastic behavior does not occur in the member with distributed nonlinearity since all cross-sections deform the same. On the other hand the spring model inherently concentrates all nonlinear behavior at the bottom end.

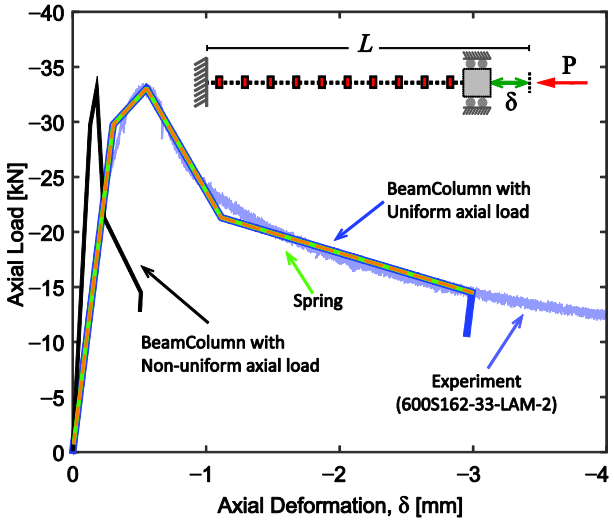

Fig. 7.17. Comparison between spring model and nonlinear beam-column model.

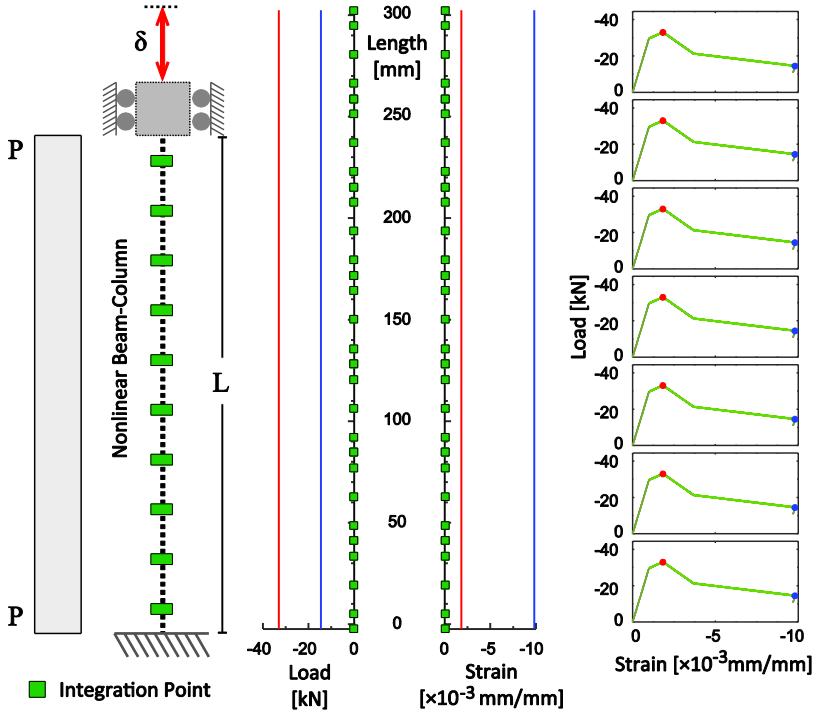

Fig. 7.18. Axial member subjected to uniform load showing all cross-sections deforming the same amount and localization of inelastic strains is not present.

Now comparing the response for same the column but subjected to non-uniform distributed axial load, the *P-δ* responses obtained using both approaches are not the same, see Fig. 7.17. The response from the spring model is exactly the same as for the uniform load case since the parameters defining its behavior are kept the same as the uniform load. This results suggest the displacement backbone coordinates need modification to accommodate this loading case. For the distributed nonlinearity model, the response appears stiffer than the uniform load case, and with displacements at the top end smaller than those from the spring model. Localization is observed for the distributed nonlinearity approach as shown in Fig. 7.19 where cross-sections towards the bottom end are in the inelastic range while towards the top cross-sections unloaded and remained linear elastic.

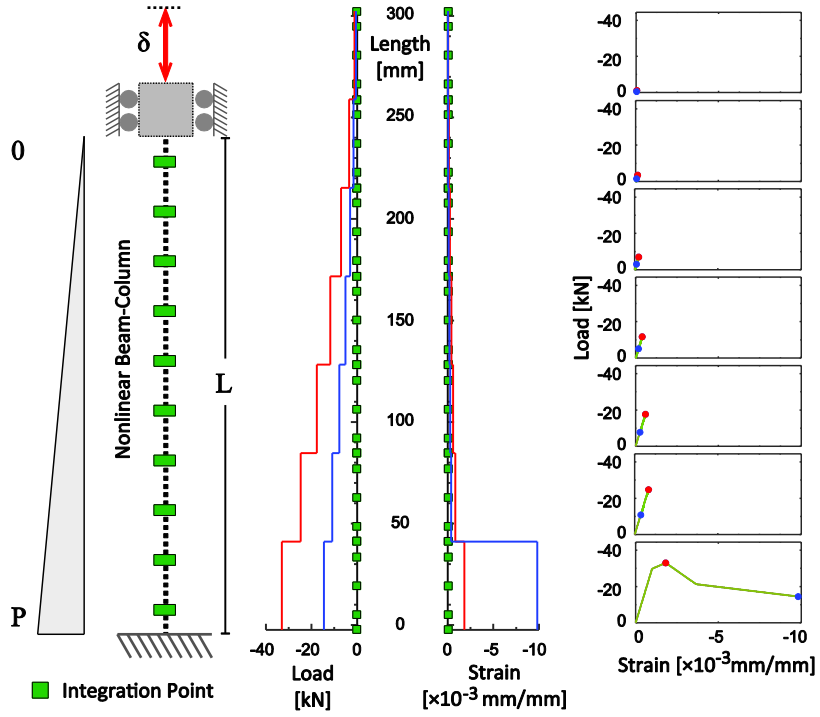

Fig. 7.19. Axial member subjected to non-uniform load showing localization of inelastic behaviour at the bottom end.

One can conclude from the two comparisons that because of the uniform axial strain distribution assumption used in the *dispBeamColumn* (or similar) element, the localization behavior cannot be captured for the case of uniform axial load using the distributed nonlinearity approach. If capturing localization is of interest, then using the spring modeling approach is suggested and the user is required to select a priori the location where all nonlinearity will

concentrate. Selecting the location of the spring can be difficult if the axial load can become non-uniformly distributed along the member at any time during the analysis.

For members subjected to non-uniform distributed axial load, inelastic behavior localization may occur automatically when the most stressed/loaded cross-cross-section starts softening resulting in unloading of the adjacent cross-sections. This type of behavior can be simulated with the *dispBeamColumn* element (or similar) and does not require the user to consider where nonlinear behavior will concentrate before running an analysis. Even tough localization cannot be captured using the distributed nonlinearity approach for the case of uniform axial load, the energy dissipation and the load-deflection response P-δ are still properly captured.

The proposed methodology is established for thin-walled cold-formed steel members, however the *asymPinching* parameters are presented generally as a function of local buckling slenderness λ_ℓ and could be extended to hot-rolled steel members and cross-sections with future validation. Moreover, the methodology presented can be applied to thin-walled cold-formed steel members that experience distortional and global buckling deformations with further finite element validation. In the next chapter the *asymPinching* model is used to explore local buckling effects in the response of sheathed cold-formed steel shear walls and demonstrate how to implement this into structural system analyses.

Chapter 8: Simulation Framework for Cold-Formed Steel Structures

Cold-formed steel structures subjected to extreme loads, like those due to seismic loading, are designed such that lateral loads are resisted by shear wall systems and floor diaphragms. The behavior of these systems is governed by the components individual behavior (e.g., chord studs, floor joists, and sheathing), and their interaction within the system through the connections (e.g. screw-fastened connections). The components and connections can exhibit nonlinear behavior that needs to be considered for performance and analysis based design of CFS framed structures. This chapter introduces a computationally efficient component-based framework for the analysis of cold-formed steel structures that captures the nonlinear behavior in all critical components in detail.

8.1 Simulation framework

The component-based simulation framework is supported by nonlinear models for framing members, screw-fastened connections and other components in light-framed steel structures assembled in finite element models for accurate gravity load analysis, wind analysis, seismic design and other extreme loading conditions. The modeling approach described herein complements the efforts from the CFS-NEES projects to advance analysis and performance based design of cold-formed steel structures described in [15,82] by introducing the nonlinear behavior in the framing members. The framework provides the ability to simulate behavior including limit states related to framing members (e.g., local buckling), single screw-fastened connection limit states and/or sheathing buckling/failure in CFS structures. An outline of the simulation framework for CFS subsystems is illustrated in Fig. 8.1 where the framing members in a sheathed CFS shear wall are modeled using nonlinear-beam columns, and connections between framing members (CFS studs and tracks) and sheathing are modeled using nonlinear hysteretic springs.

The supporting models necessary for the framework are those that govern the behavior of each component, i.e., framing members, sheathing elements, and connections. To model framing elements the approach in Chapter 6 is used to include thin-wall behavior into the analysis of framing members for the three buckling limit states described by AISI-S100-12 [22] (see Fig. 6.1 and 6.4). In Chapter 7 this approach was expanded to provide general expressions and the

asymPinching model to simulate steel columns including local buckling. A similar approach to the one described in Chapter 7 together with the procedure described in Chapter 6 can be adopted to simulate framing members governed by distortional or global buckling using the *asymPinching* model.

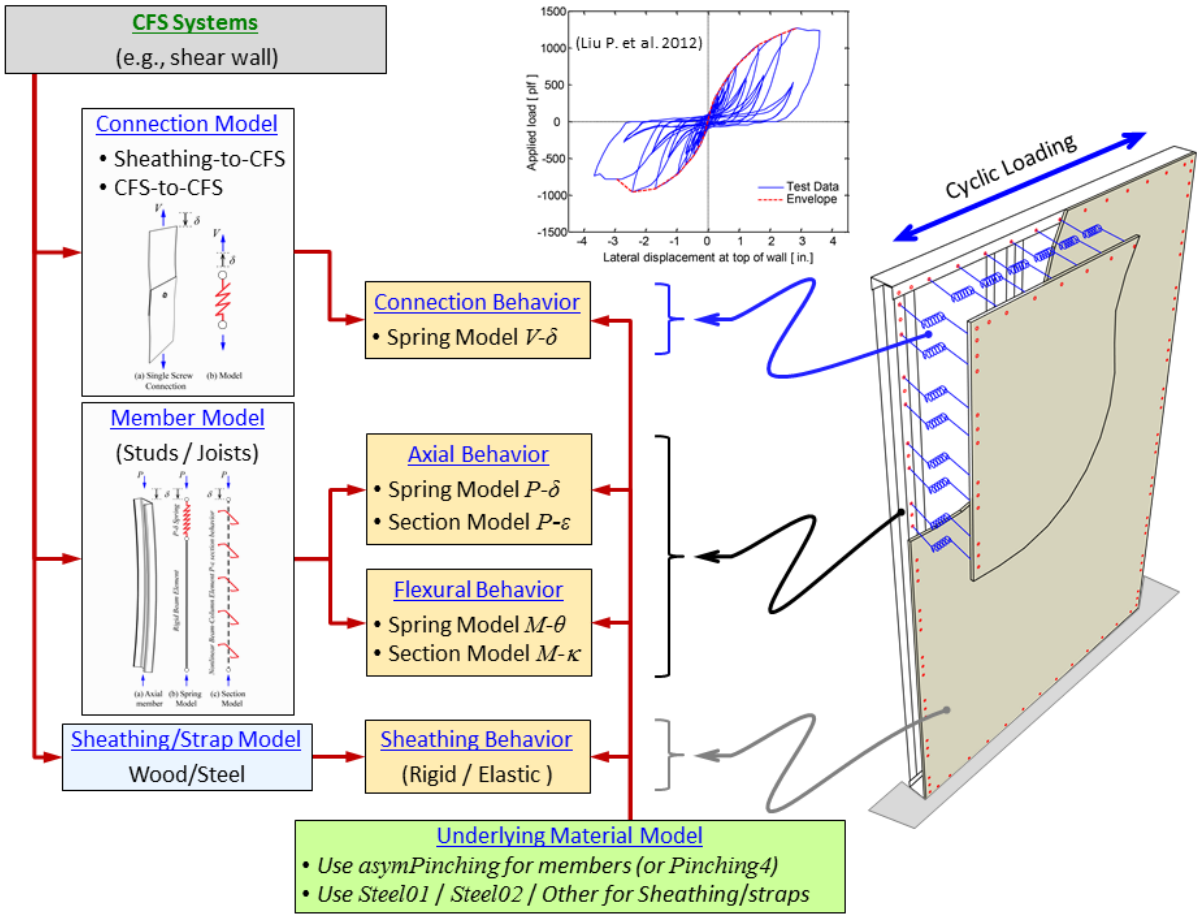

Fig. 8.1. Simulation framework outline for cold-formed steel systems where hysteretic models for members, single screw-fastened connections, and sheathing can be assembled to explore different limit states in CFS shear walls.

Models to simulate the connections between components depend on the type of connection and should provide flexibility to model different types of structural systems. In cold formed steel structures connections between components are usually screw-fastened connections and less commonly welded. Modeling welded connections can be approached in a simplified manner by constraining the appropriate degrees of freedom unless damage of the connection and respective limit states are of interest. In this last case, the proper models need to be provided. In the case of the most used type of connection in cold-formed steel structures, the screw-fastened connections,

a single screw-fastened connection model is suggested. For the proposed framework, single screw-fastened connections are modeled using nonlinear zero length springs with parameters derived from experiments (e.g., [83]). Fig. 8.2 illustrates the spring model with behavior modeled using *Pinching4*. Modeling each fastener involved in a connection can provide the flexibility needed for this type of connection and eases the formulation of a model.

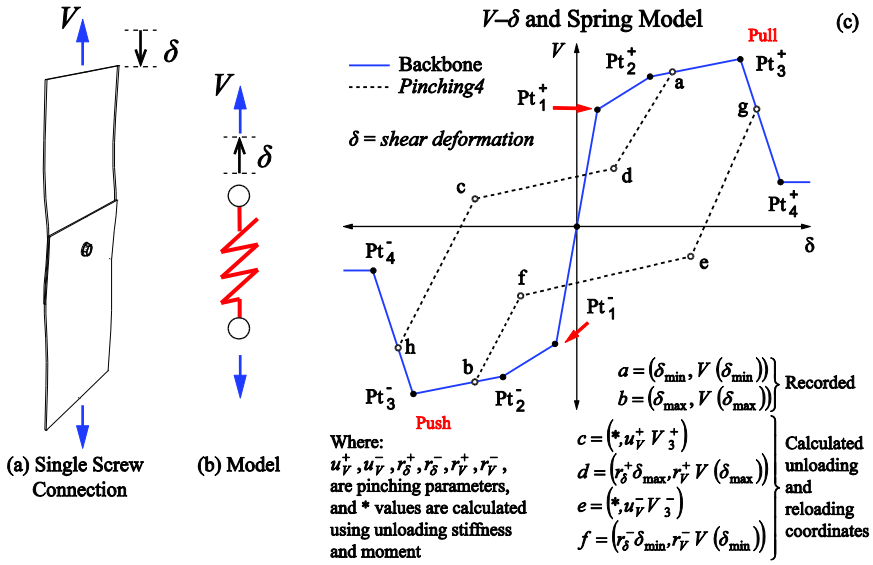

Fig. 8.2. Hysteretic model for single screw-fastened connection.

The next section illustrates the component-based simulation framework applied to the analysis of full scale cold-formed sheathed shear walls and explores the possible limit states pertaining to the framing members. Simulations are compared to responses from full scale tested wood-sheathed shear walls tested at the University of North Texas [12,13].

8.2 Component-based modeling of CFS shear walls [7]

A finite element model for a sheathed CFS shear wall was implemented in OpenSees following the framework depicted in Fig. 8.1. The base model corresponds to a full scale on side wood sheathed CFS shear wall design employed in the CFS-NEES building [19,20] and tested as a single unit at the University of North Texas [12,13]. The wall unit is 2.74m high and 1.22m wide framed using back-to-back 600S162-54 CFS members fastened using two #10 fasteners every 305mm for the chord studs and a single 600S162-54 CFS member 610mm off center between the

[7] This section is a continuation of the work presented in the coauthored conference paper presented at the *2015 SSRC Annual Stability Conference* with the title **"OpenSees Modeling of Wood Sheathed Cold-Formed Steel Framed Shear Walls"** [84].

two chord studs (see Fig. 8.3). Two 600T162-54 CFS tracks at the top and bottom of the wall connect the vertical members together using #10 flat-head fasteners. A wood oriented-strand board (OSB) is fastened to one side of the steel frame using #8 flat-head fasteners spaced every 305mm as shown in Fig. 8.3. A steel strap 38mm wide and 1.438mm thick is used to fasten the OSB to the steel frame at the seam located 305mm from the top of the wall. A ledger 1200T200-97 track that serves to connect the wall to the floor diaphragm is fastened to the vertical members at the top of the wall and on the opposite side of the OSB panel. Vertical wall support is provided by two Simpson Strong-Tie S/HDU6 hold downs connected to the chord studs bottom inward face using #14 hex-head fasteners. Two 15.875mm (5/8in.) bolts connect the bottom track to the bottom of the testing frame.

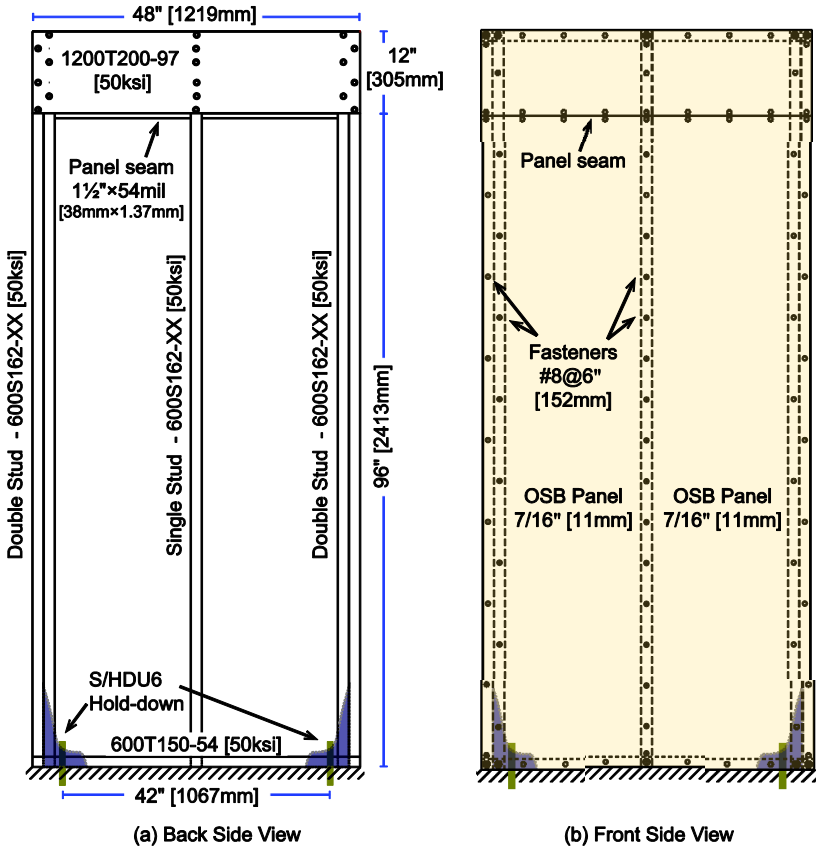

Fig. 8.3. Cold-formed shear wall front and back side detail [12].

8.3 Shear wall numerical model

The base numerical model of the shear wall is implemented herein using OpenSees [24] as illustrated in Fig. 8.4. The model uses *nonlinear beam-columns* elements with cross-section behavior simulated using *asymPinching* to model the steel framing members, shell elements to

model the sheathing panels and zero-length elements with hysteretic behavior using *Pinching4* to model all the screw-fastened connections. In OpenSees the nonlinear beam-columns are implemented using *dispBeamColumn* elements with the Gauss-Lobatto quadrature rule and at least five integration points, two at both ends of the member. A single element is used to model the built-up chord studs at both sides of the wall for simplicity, however the approach is the same if the built-up chord stud needed to be modeled. The fastener connections are implemented using *CoupledZeroLength* elements that allow defining the fastener force-deformation relationship on the plane parallel to the sheathing. The OSB panel is modeled using *ShellMITC4* elements to accommodate any deformations the sheathing can experience. The track-to-vertical framing members connection are modeled for simplicity by constraining the translational degrees of freedom and assuming linear spring with rotational stiffness k =113kN-m/rad based on approximations from measured lateral stiffness of bare frame [12]. Similarly, the translational and rotational degrees of freedom at the ends of the ledger track were constrained to corresponding nodes in the vertical studs. The hold-downs were modeled using elastic *zeroLength* springs with stiffness k=56.7kN/mm in tension while stiffness in compression was set 1000 times larger to simulated the contact with the foundation. Additional springs with large stiffness in compression and close to zero stiffness in tension were provided along the bottom track to simulate contact with the foundation while allowing uplift of the track nodes. Shear anchors were modeled by fixing the horizontal degree of freedom at two of the track nodes next to the hold-downs.

The base model was modified to help illustrate the nonlinear behavior in the vertical framing members and the differences in the failure mechanism due to the development of local buckling on the chord studs. In the modified model the vertical framing members slenderness has been set to a specific value but the rest of the properties (i.e., thickness, area and inertia) have been kept unchanged from the base model. The intention with these modified models is to study the effects of the vertical member slenderness on the response. The influence of the gravity load is included as well as this will trigger the nonlinear behavior in the vertical members and it represents more realistic loading conditions. Table 8.1 and Table 8.2 summarize the modeling scenarios implemented and properties of the framing members used. Properties for single screw-fastened connection between the OSB panel and steel depicted in Fig. 8.4 are adopted from the work performed by Peterman et al. [83] and are also listed in Table 8.3.

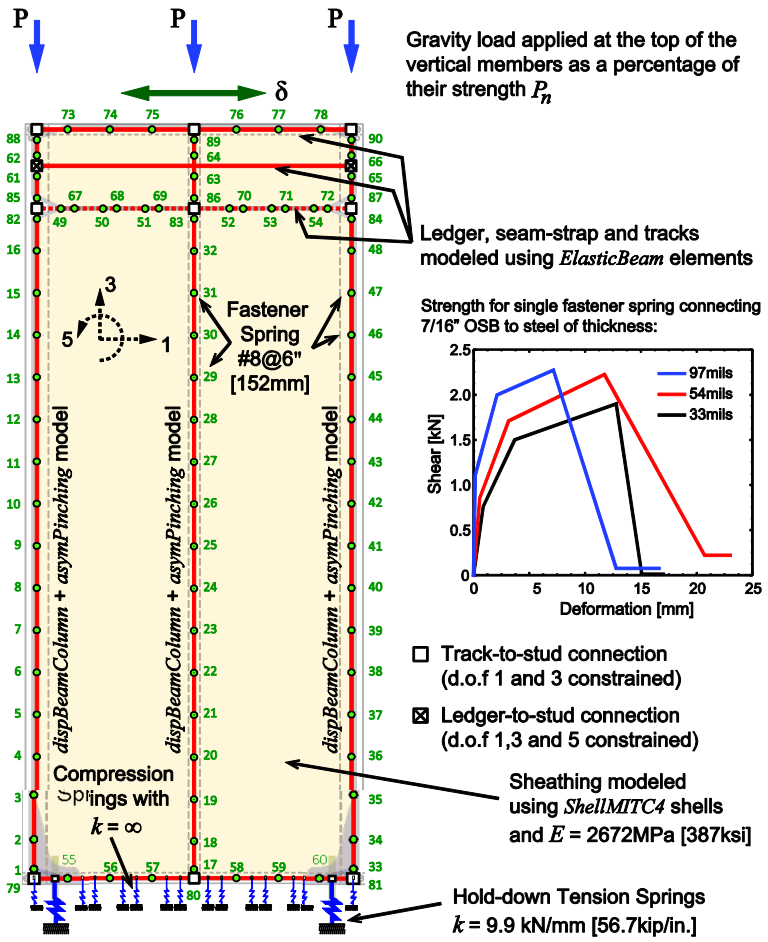

Fig. 8.4. Shear wall model and fastener properties.

Table 8.1. Shear wall model matrix.

Model	Gravity Load P [kN] (a)	Fastener Schedule	Chord Stud (a)	Infill Stud (a)	Stud λ_ℓ	Stud Type	Sheathing
SW1-a	$0.00P_n$= 0.0	#8 @ 152mm	2x54	1x54	1.89	*asymPinching*	7/16" OSB
SW1-b	$0.25P_n$= 16.9	#8 @ 152mm	2x54	1x54	1.89	*asymPinching*	7/16" OSB
SW1-c	$0.50P_n$= 33.8	#8 @ 152mm	2x54	1x54	1.89	*asymPinching*	7/16" OSB
SW1-d	$0.75P_n$= 50.7	#8 @ 152mm	2x54	1x54	1.89	*asymPinching*	7/16" OSB
SW2-a	$0.00P_n$= 0.0	#8 @ 152mm	2x33	1x33	2.51	*asymPinching*	7/16" OSB
SW2-b	$0.25P_n$= 5.6	#8 @ 152mm	2x33	1x33	2.51	*asymPinching*	7/16" OSB
SW2-c	$0.50P_n$= 11.2	#8 @ 152mm	2x33	1x33	2.51	*asymPinching*	7/16" OSB
SW2-d	$0.75P_n$= 16.8	#8 @ 152mm	2x33	1x33	2.51	*asymPinching*	7/16" OSB
SW3	$0.50P_n$= 11.2	#8 @ 152mm	2x33	1x33	2.51	*Elastic*	7/16" OSB
SW4	$0.50P_n$= 11.2	#8 @ 152mm	2x33	1x33	2.51	*Pinching4*	7/16" OSB
SW5-a	$0.50P_n$= 50.6	#8 @ 152mm	L1	L1	1.06	*asymPinching*	7/16" OSB
SW6-a	$0.50P_n$= 41.4	#8 @ 152mm	L2	L2	1.42	*asymPinching*	7/16" OSB
SW7-a	$0.50P_n$= 33.9	#8 @ 152mm	L3	L3	1.89	*asymPinching*	7/16" OSB
SW8-a	$0.50P_n$= 30.8	#8 @ 152mm	L4	L4	2.15	*asymPinching*	7/16" OSB
SW9-a	$0.50P_n$= 27.5	#8 @ 152mm	L5	L5	2.51	*asymPinching*	7/16" OSB
SW5-b	P= 27.5	#8 @ 152mm	L1	L1	1.06	*asymPinching*	7/16" OSB
SW6-b	P= 27.5	#8 @ 152mm	L2	L2	1.42	*asymPinching*	7/16" OSB
SW7-b	P= 27.5	#8 @ 152mm	L3	L3	1.89	*asymPinching*	7/16" OSB
SW8-b	P= 27.5	#8 @ 152mm	L4	L4	2.15	*asymPinching*	7/16" OSB
SW9-b	P= 27.5	#8 @ 152mm	L5	L5	2.51	*asymPinching*	7/16" OSB

(a) See Table 8.2.

Table 8.2. Framing element properties.

Name (a)	SSMA Section	P_y [kN]	A [cm^2]	I_y [cm^4]	I_x [cm^4]	Slenderness λ_ℓ	Predicted Strength [kN]
2x54	600S162-54	250.4	7.26	24.21	243.987	1.89	135.2
1x54	600S162-54	123.7	3.59	7.50	118.959	1.89	67.6
2x33	600S162-33	101.0	4.44	14.55	149.152	2.51	44.9
1x33	600S162-33	50.5	2.22	4.83	74.572	2.51	22.5
L1	-	-	3.59	7.50	118.959	1.06	101.1
L2	-	-	3.59	7.50	118.959	1.42	82.7
L3	-	-	3.59	7.50	118.959	1.89	67.7
L4	-	-	3.59	7.50	118.959	2.15	61.6
L5	-	-	3.59	7.50	118.959	2.51	55.0

(a) 2x indicates a built-up member and 1x indicates a single member

Table 8.3. Fastener backbone and *Pinching4* properties.

Connection	δ_1	δ_2	δ_3	δ_4	V_1	V_2	V_3	V_4	r_δ	r_f	u_f
7/16"OSB-to-97mils	0.152	2.101	7.165	12.789	1.108	1.998	2.274	0.077	0.410	0.010	0.001
7/16"OSB-to-54mils	0.559	3.145	11.740	20.711	0.855	1.710	2.224	0.220	0.420	0.010	0.001
7/16"OSB-to-33mils	0.871	3.701	12.779	15.080	0.760	1.500	1.900	0.012	0.410	0.010	0.001

See Fig. 8.2

8.4 Monotonic and cyclic response of the shear wall base model

The monotonic and cyclic responses of the base model (SW1) are shown in Fig. 8.5 and compared to the experimental response obtained from the full scale tests performed by Liu et.al [12]. Local buckling was included in the vertical members using the *asymPinching* model and properties from Table 8.3 for the 7/16”OSB-to-54mils fastened connection were selected. Gravity loads were not applied at the top of the load. The simulated monotonic and cyclic responses show reasonable agreement to the experimental response including the failure mechanism. The failure mechanism observed in the tests consisted of fastener failure along the bottom and bottom-side edges of the wall which resulted on the sudden drop in strength observed in the curves shown in Fig. 8.5. Some difference exists in the post-peak monotonic response due to the inclusion of the contact springs along the bottom track, however this difference is neglected for the purpose of the study presented in this chapter and the numerical model adopted is considered adequate.

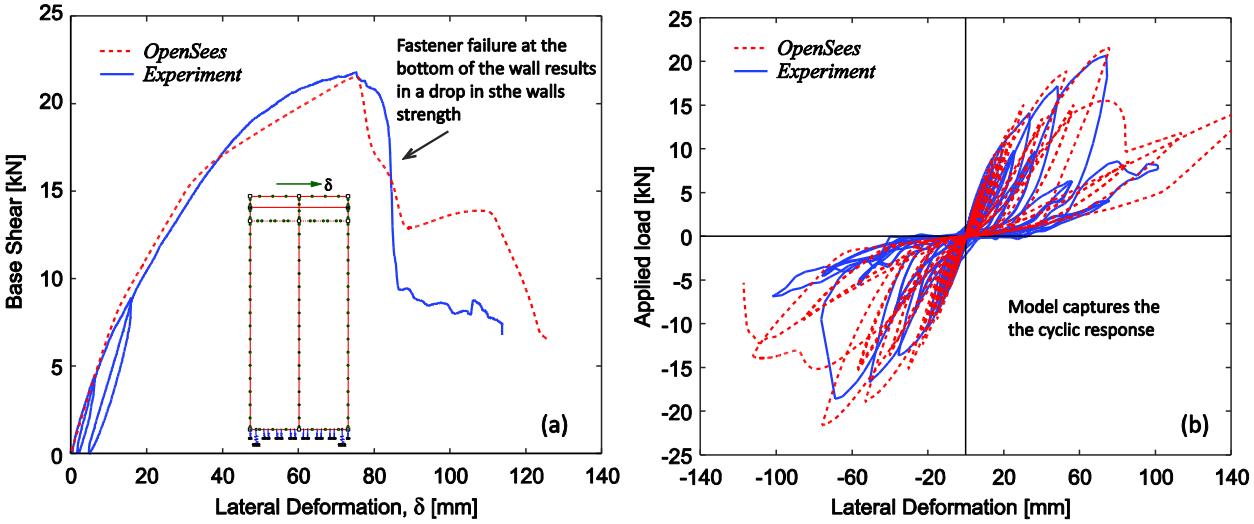

Fig. 8.5. Simulation to experiments comparison shows reasonable agreement between responses.

8.5 Nonlinear stud vs. linear stud behavior effects on the CFS shear wall response

Local buckling in the vertical framing members in walls is commonly addressed as a strength limit state only in design but rarely accounted explicitly during lateral load analysis and in CFS structures. Local buckling can affect greatly the shear wall response and failure mechanism observed in analysis. To illustrate this, responses of a modified version of the shear wall base model subjected to both gravity load and lateral pushover loading are compared. In the modified model the vertical members were replaced with thinner stud (600S162-33) which strength is governed by local buckling. Three approaches for modeling the studs were considered, in the first one (labeled SW3 in Table 8.1) the members are modeled as elastic beam-column elements with axial stiffness k_1 given in Table 7.3. For the second approach (SW2-c in Table 8.1), local buckling in the members was included using the *asymPinching* model. In the third approach (SW4 in Table 8.1) local buckling was included using the alternative equations given in Chapter 7 for the *Pinching4* model. Gravity loading is simulated as point loads applied at the top end of each vertical member and corresponding to 50% of the individual stud strength (i.e., $P = 0.5P_n$).

The pushover responses compared in Fig. 8.6 show clearly that the wall with elastic vertical members can reach higher strength at larger deformation than the wall that includes local buckling in the studs. From Fig. 8.7 and 8.9 the failure mechanism in the wall with elastic framing members is as expected driven by fastener failure along the edges. Moreover, in this wall the compression load developed in the stud to the right increases from an initial value of $0.5P_n$ to a value twice the predicted single stud strength P_n. This high compressive load occurs before the drop in strength

shown in the pushover curve in Fig. 8.6 after which the studs unload considerably (see Fig. 8.7b-g). Conversely, for the wall including local buckling in the studs, the failure mechanism is triggered by local buckling on the compression stud (right) as shown in Fig. 8.8. Most fasteners exhibit low force and deformation demands with most of them remaining on the ascending part of their load deformation response (Fig. 8.10). The axial load in the compression stud is capped at the predicted stud strength which occur slightly before the drop in strength shown in the corresponding pushover curve (Fig. 8.8).

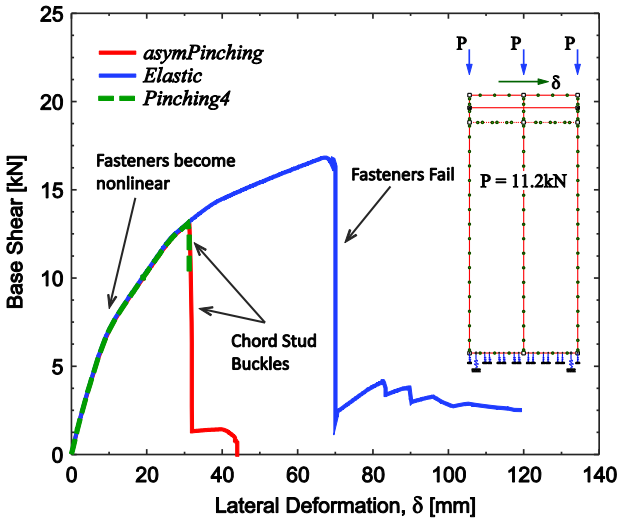

Fig. 8.6. Comparing shear wall with and without including local buckling (SW2-c and SW4). Modeling the chord studs elastic results in overestimation of the wall strength and maximum top displacement.

The main conclusion drawn from this comparison relates to the need to include local buckling when analyzing structural systems with thin walled members such that all possible design limit states are considered. Recalling the response for the base model (no gravity load) in Fig. 8.5, the vertical members were modeled including local buckling but they remained elastic with loads below their predicted strength, and the failure mechanism was fastener controlled like in the test. Using elastic beam column in the base model would yield the same response as if local buckling in the studs is considered. However, a small but significant modification such as changing the thickness of the vertical members can trigger a different failure mechanism, and reduce the wall strength and ductility. This difference can go unnoticed if the nonlinear behavior is not included.

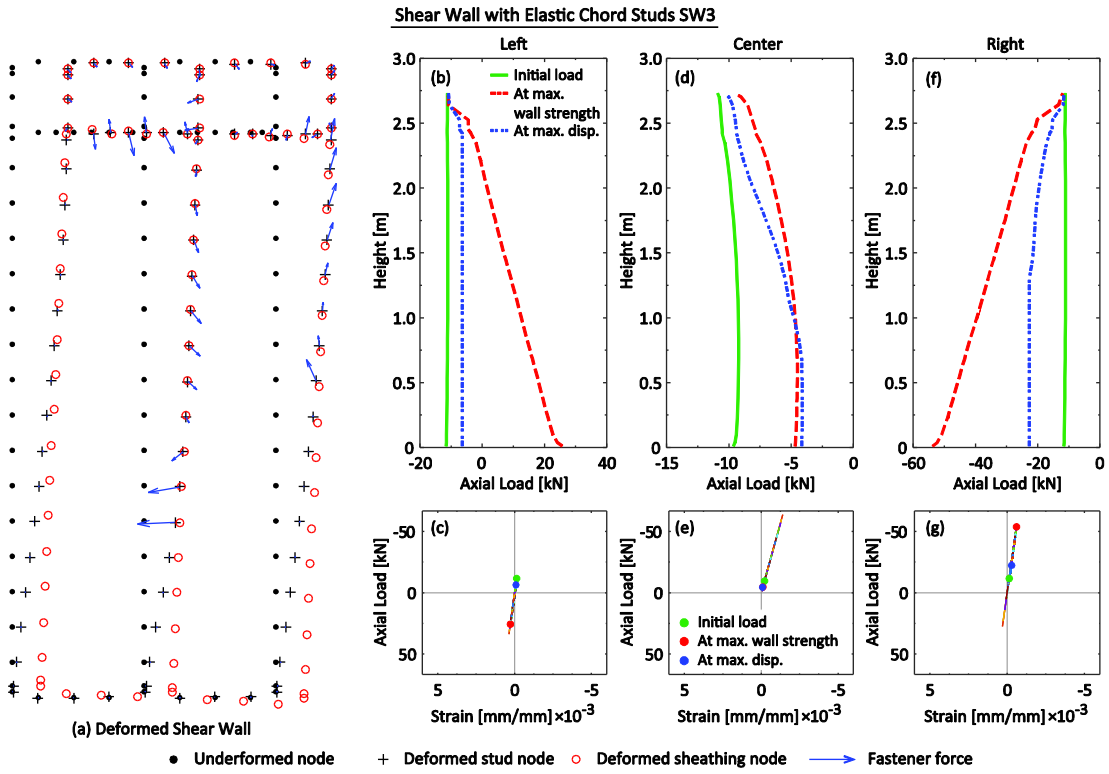

Fig. 8.7. Shear wall (SW3) deformed shape (a) showing the wall failure mechanism triggered by failure of the bottom fasteners, while the studs remain elastic even though $P > P_n$ on the right chord stud (f, g).

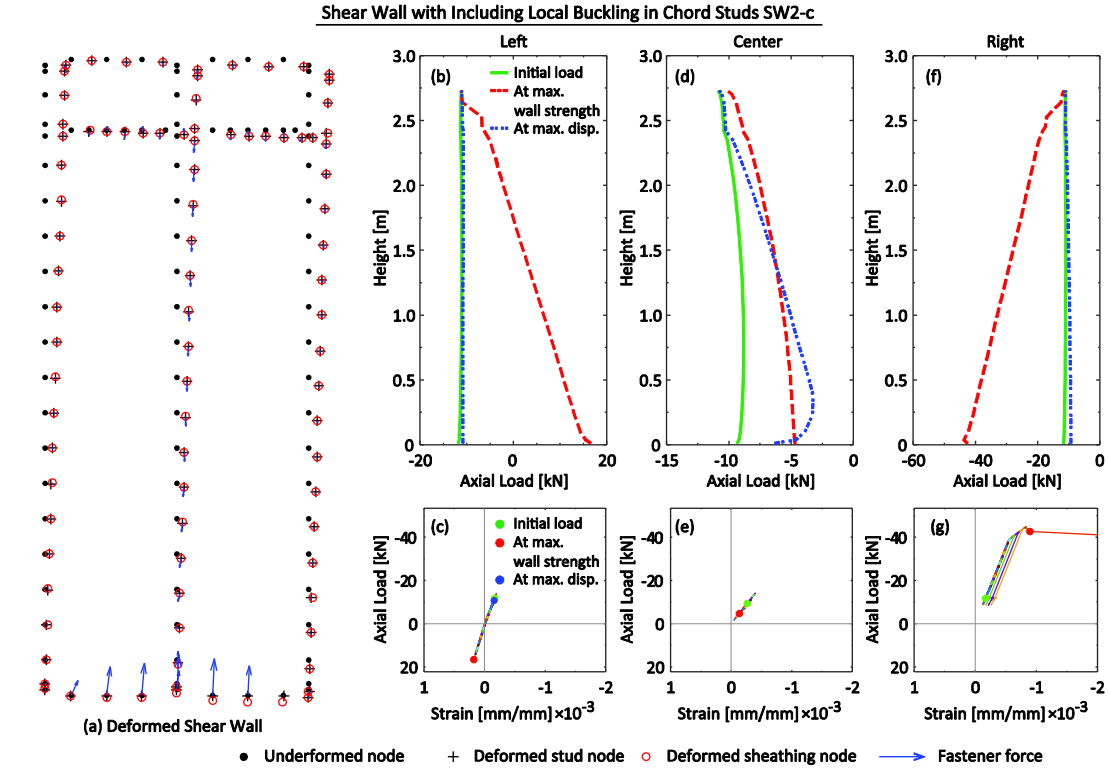

Fig. 8.8. Shear wall (SW2-c) deformed shape (a) showing the wall failure mechanism triggered by buckling of the compression chord stud, while fasteners exhibit low load and deformation demands.

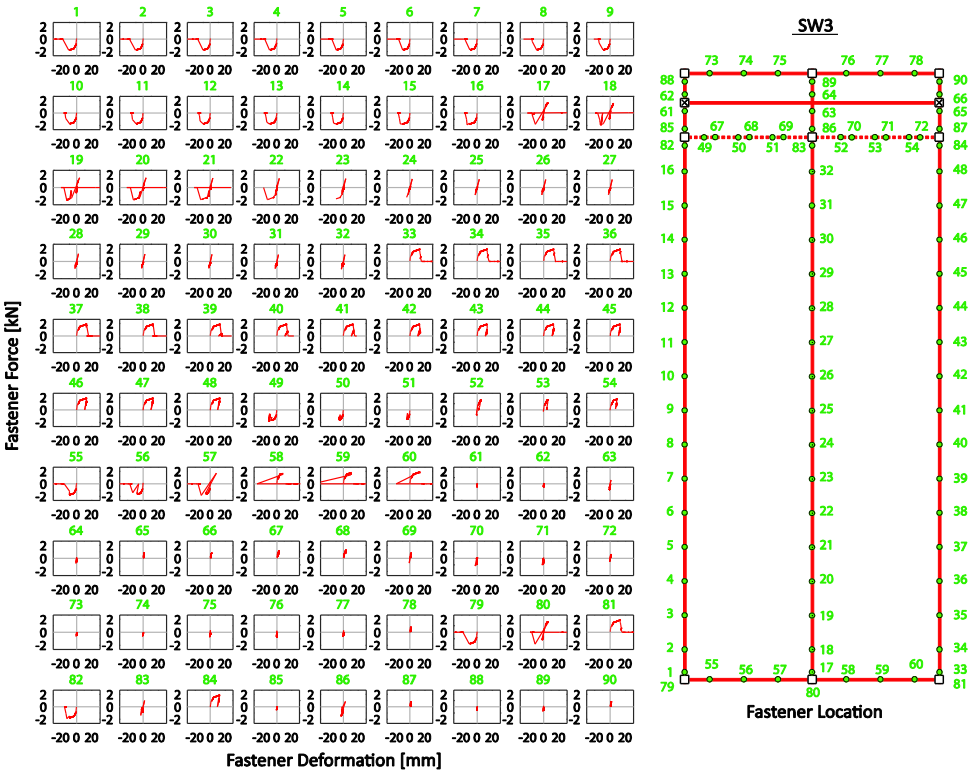

Fig. 8.9. Fastener load-deformation responses in shear wall with elastic chord studs (SW3) show the bottom fasteners along the sides failing that results on the wall's loss of strength.

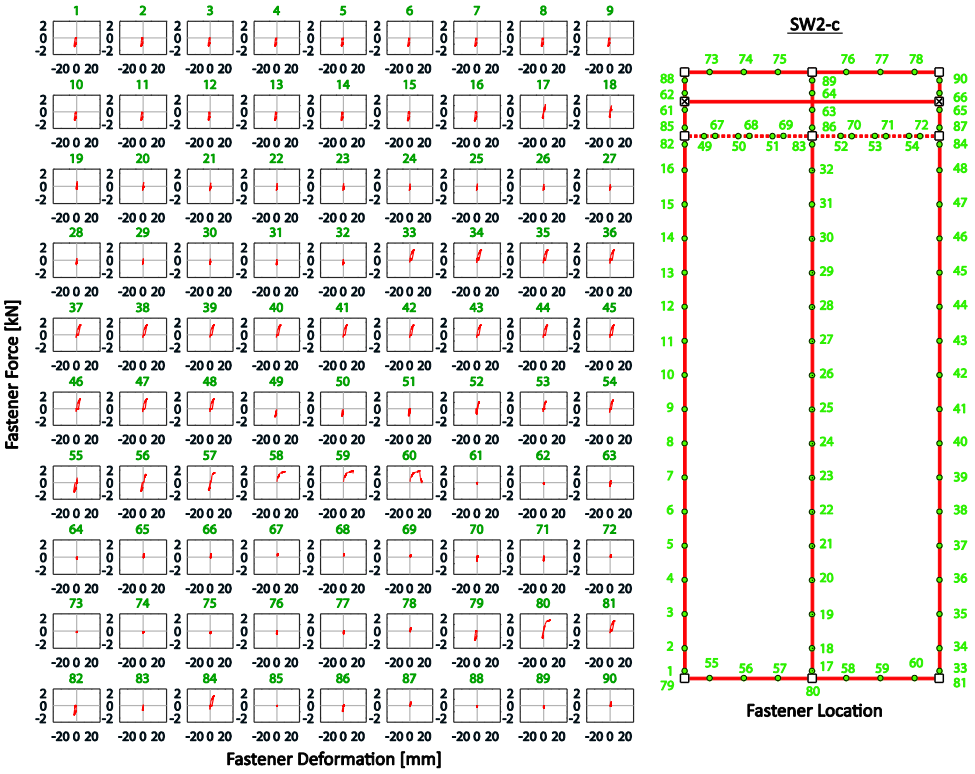

Fig. 8.10. Fastener load-deformation responses in shear wall with nonlinear studs (SW2-c) where fastener exhibit force and deformations below their prescribed strength.

8.6 Gravity load effects on the CFS shear wall response

Gravity load effects on the shear wall monotonic response were explored for two different shear wall configurations listed in Table 8.1 as SW1 and SW2. The first wall model corresponds to the base model and the second is the modified version of the base model with thinner vertical studs (600S162-33). Gravity loading was simulated as point loads applied at the top end of each vertical member and corresponding to a percentage of the individual stud strength (i.e., $P = 0.25P_n$, $0.5P_n$ and $0.75P_n$).

The gravity load influence on the shear wall response is of interest since its effects added to the vertical forces developed in the studs due to lateral loads can trigger sooner local buckling and change the failure mechanism. For instance, in the case of the shear wall base model (SW1) when the gravity load is increased, an expected reduction on the maximum strength is observed as well as decrement on the wall deformation at which point softening of the response occurs (see Fig. 8.11a). However, for the higher gravity load values (0.5 and 0.75) the failure mechanism involves some amount of local buckling developed in the infill stud after the fasteners on the compression side edge had failed. The influence of local buckling in the described case is small and plays a roll only after the fasteners have failed and for gravity loads close to the strength of the vertical members.

In the case of the shear wall with thinner studs (SW2), the effects of the gravity load is more pronounced. Local buckling affects the failure mechanism even for the low gravity load case ($0.25P_n$) where the fastener failure along the right edge and buckling at the bottom of the right stud happens almost simultaneously (see Fig. 8.12 and 8.13). Because the stud can still carry load the wall response shows a lower plateau (see Fig. 8.11b) where more fasteners fails until either buckling of the stud happens (e.g., case of $0.5P_n$) or all fastener have failed. As the gravity load applied is increased local buckling governs the failure mechanism and fasteners remain at low deformations and force demands and the post-peak plateau is not developed.

An additional effect observed of the gravity loads on the shear wall lateral response is an increase of the initial stiffness of the wall. For instance, in shear walls where the failure mechanism is mainly driven by fastener failure like in the base model case (SW1), the initial lateral stiffness of the wall increases about 50% as shown in Fig. 8.11a. There is a similar increase on the initial stiffness as well (25% to 48%) in the case of the shear wall SW2 where local buckling is driving the failure mechanism (Fig. 8.11b). This increase of the initial stiffness for example was not

captured in the shear wall test described in [12] as gravity load was not applied. While other few studies (e.g., [3]) have considered gravity load effects on the lateral response of CFS shear walls, the amount of testing needed to evaluate the effects of gravity load in a reliable way would be expensive. In this case, having the capability offered by the proposed analysis framework including the nonlinear behavior of the framing members would be of benefit.

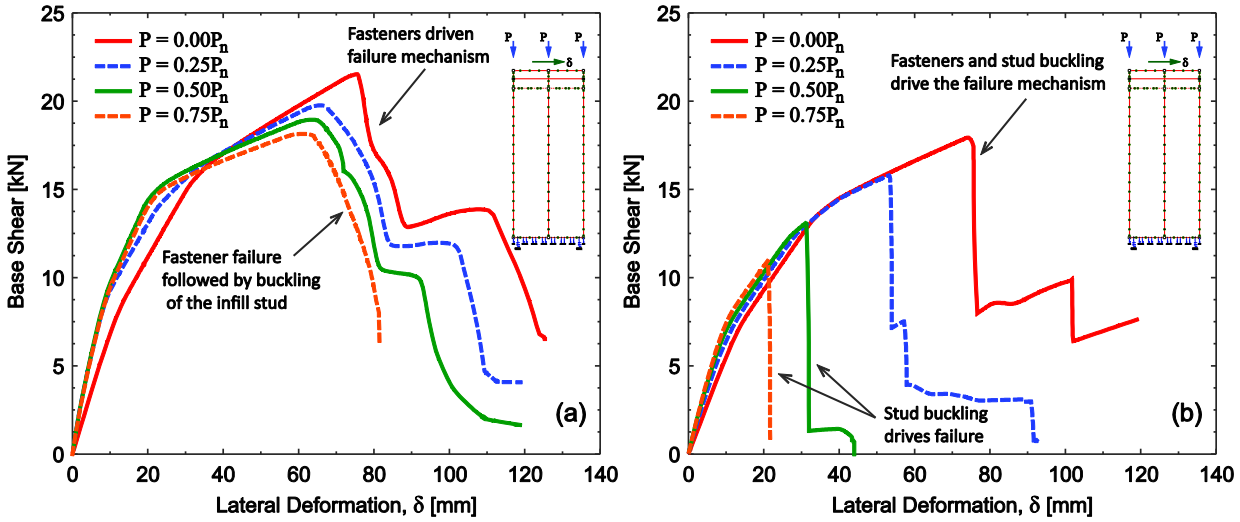

Fig. 8.11. Effects of gravity load on the shear wall lateral force-deformation response for (a) the base model SW1, and (b) the modified shear wall with thinner vertical members SW2.

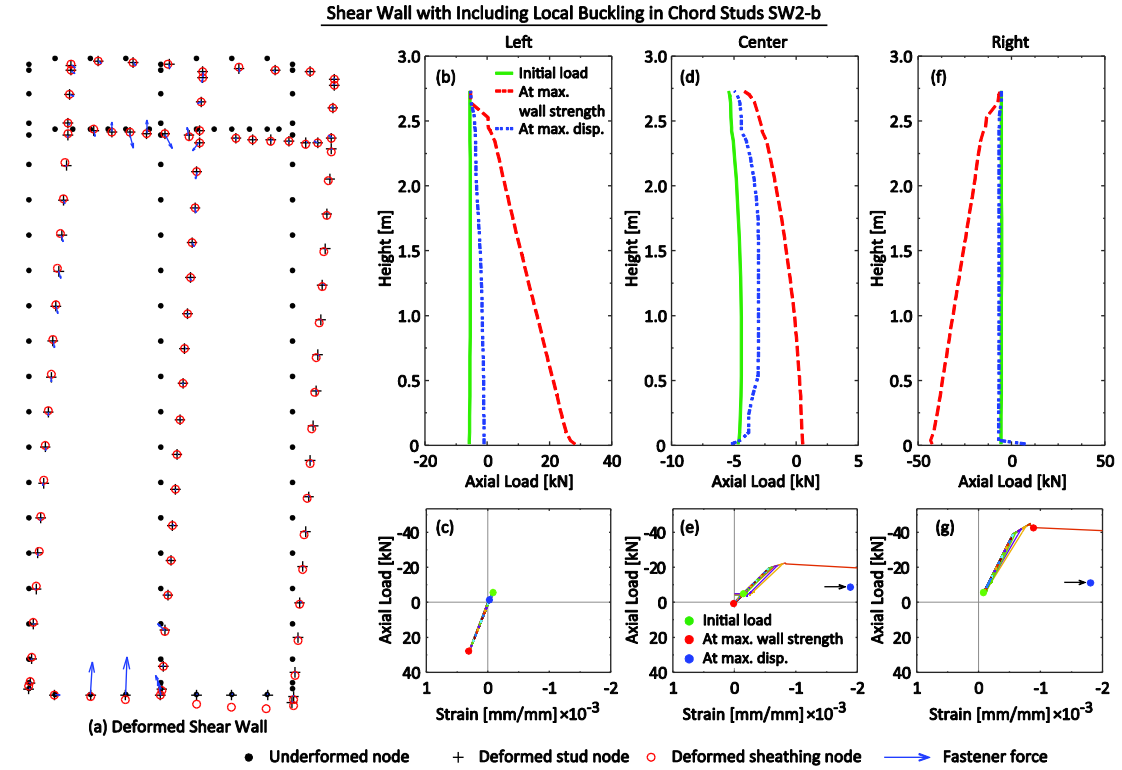

Fig. 8.12. Shear wall (SW2-b) deformed shape (a) showing fastener failure and local buckling and in the compression chord stud happening almost simultaneously when the wall reaching its maximum strength.

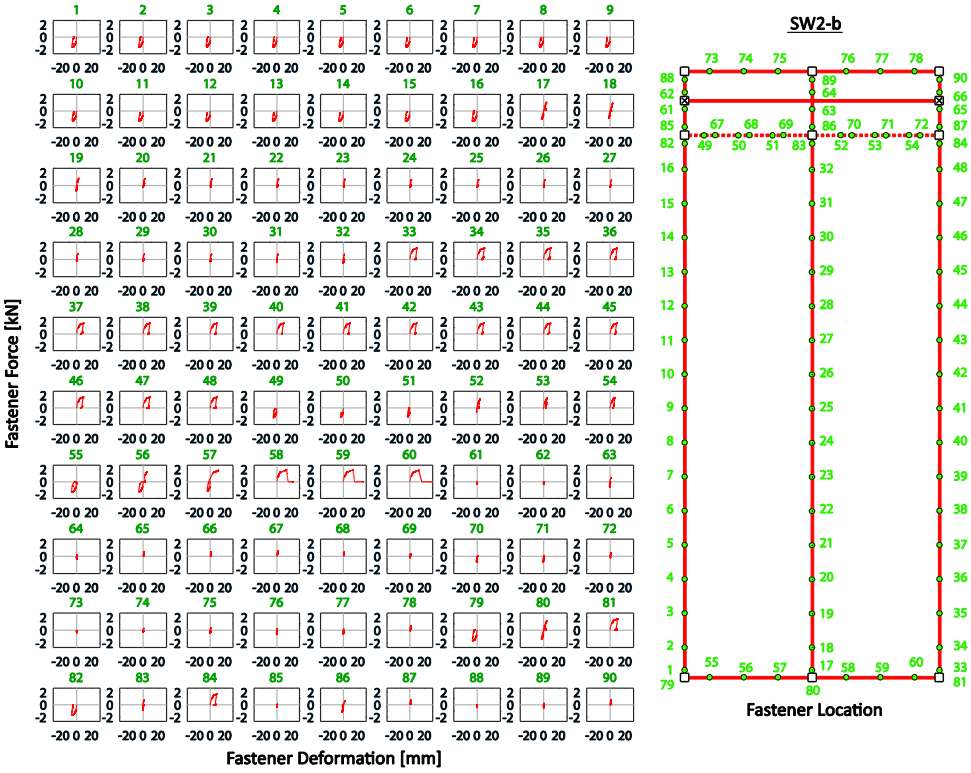

Fig. 8.13. Fastener load-deformation responses in shear wall SW2-b where fasteners failure and local buckling of the compression chord stud happen almost simultaneously.

8.7 Member slenderness effects on the CFS shear wall response

To evaluate the sensitivity of the shear wall response to the vertical member cross-section slenderness λ_ℓ. The vertical member cross-section slenderness is set to five different values in the interval 1.0 to 2.5 while keeping the remaining properties (i.e., thickness, area and inertia) unchanged from the base model SW1. The *asymPinching* model is used to model the cross-section behavior including local buckling. Because the thickness of the members is kept constant the properties for the fastened connection are the same as those in the base model SW1. Two gravity loading scenarios are considered, in the first one (SW5-a to SW9-a) the applied load corresponds to a 50% of the predicted stud strength P_n, while in the second scenario (SW5-b to SW8-b) the applied load is the same, P = 27.5kN, for all shear walls modeled. This last value of axial load corresponds to the 50% of the predicted strength P_n of the more slender stud considered in this example, i.e., members in wall SW9-a (see Table 8.1).

The monotonic responses for the first gravity load scenario (P =0.5P_n) in Fig. 8.14a show that the failure mechanism is triggered by local buckling of the compression chord stud except in

wall SW5-a. For this wall failure is fastener driven where the studs remain practically elastic (see Fig. 8.15) resulting in smooth softening branch of the response. The axial load developed in the studs from lateral loading added to the $0.5P_n$ initial load takes the studs beyond the deformation corresponding to the peak strength, e.g., see Fig. 8.16 and 8.17. This reflects as discussed previously in the abrupt drop in wall strength of the wall shown in the pushover curves in Fig. 8.13a. Development of a plateau after the peak strength for the first gravity loading scenario is not possible for walls SW6-a to SW9-a because of the buckled compression chord.

In the second gravity loading scenario, the pushover responses of the walls show similar behavior to the previous case where buckling of the compression chord stud leads to an abrupt drop in the wall strength (see Fig. 8.14b). However, because the initial load in this scenario is set to be the same for all walls and smaller than $0.5P_n$, each wall can sustain much larger deformations compared to the first gravity loading scenario. For example, the deformation at peak load for the SW7-b wall is 40mm, 70% more than the deformation at peak (24mm) experienced by wall SW7-a. Failure of the wall is triggered when the total axial load acting compression chord stud reaches P_n and buckling occurs. In the case of walls SW5-b and SW6-b, the response is almost identical because the initial gravity load is small enough that the studs in both cases remain practically elastic and wall failure is fastener driven. In two of the wall analyzed (SW7-b and SW8-b) a post-peak increase in strength is observed that corresponds to fasteners reloading after they first unloaded when buckling of the stud occurred.

Summarizing, the effects of slenderness are more noticeable as the initial gravity load acting on the wall increases such that added to the axial loads developed from lateral loading get closer to the vertical member strength. In this case the failure mechanism changes from the smooth fastener driven mechanism to a more abrupt failure mechanism triggered by local buckling of the studs.

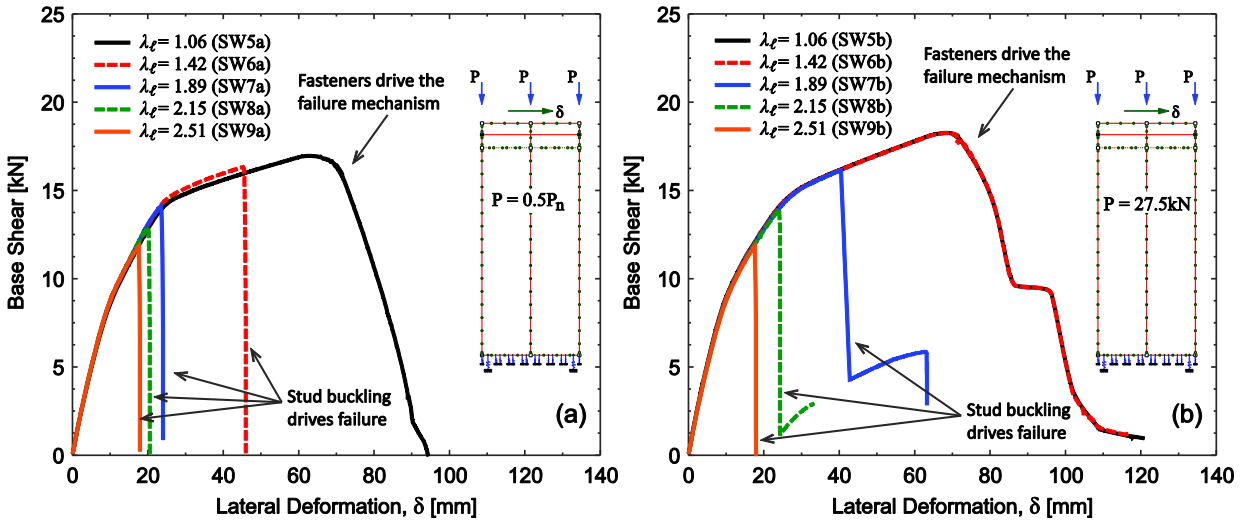

Fig. 8.14. Shear wall response sensitivity to the vertical member cross-section slenderness.

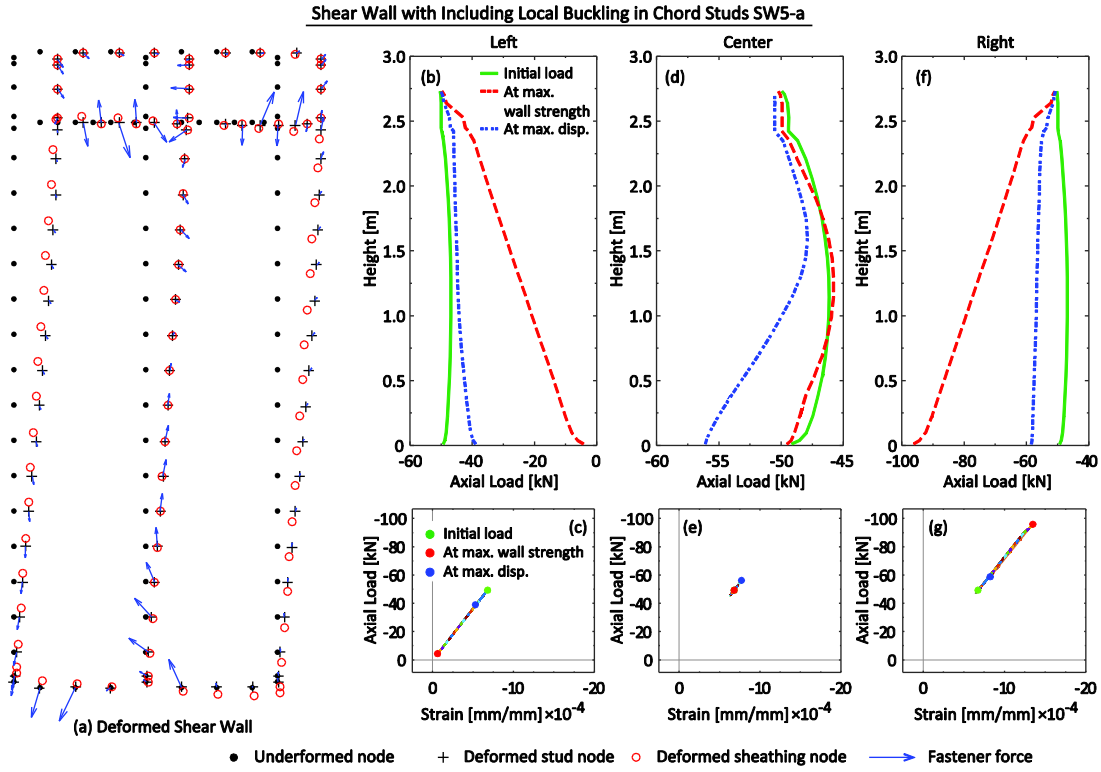

Fig. 8.15. Shear wall (SW5-a) deformed shape (a) showing fastener failure along the edges and studs remain elastic and always in compression.

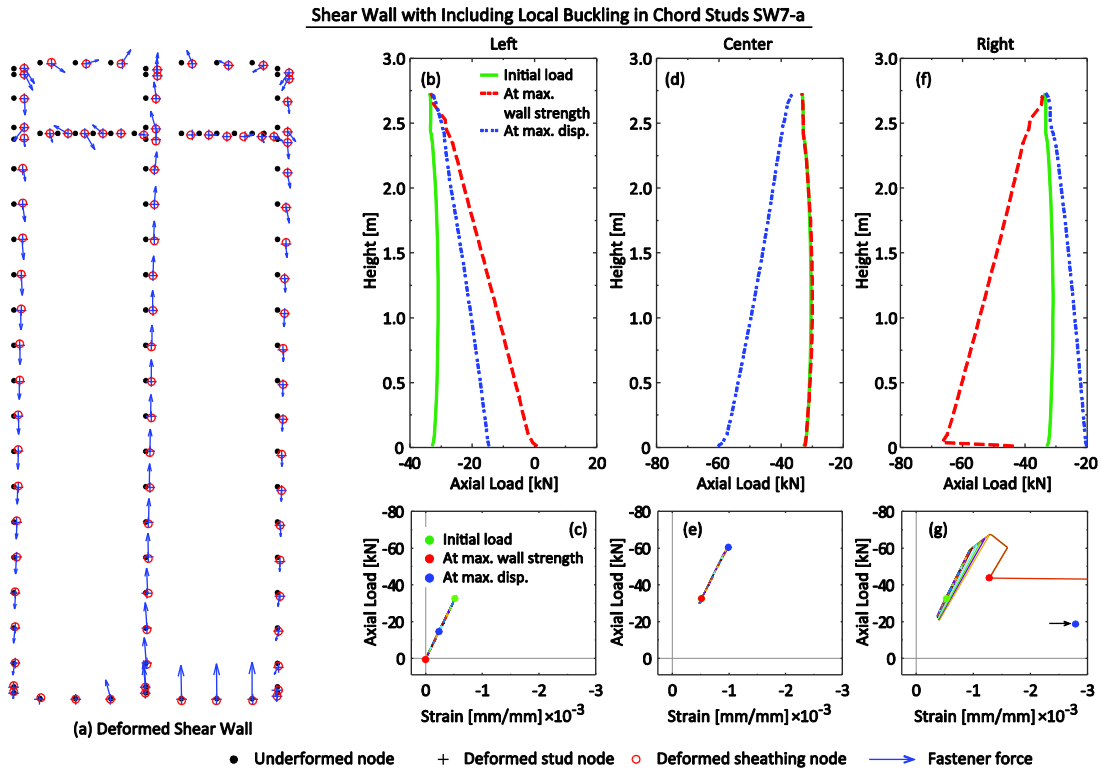

Fig. 8.16. Shear wall (SW7-a) deformed shape (a) showing the wall failure mechanism triggered by local buckling of the compression chord stud, while fasteners have low load and deformation demands.

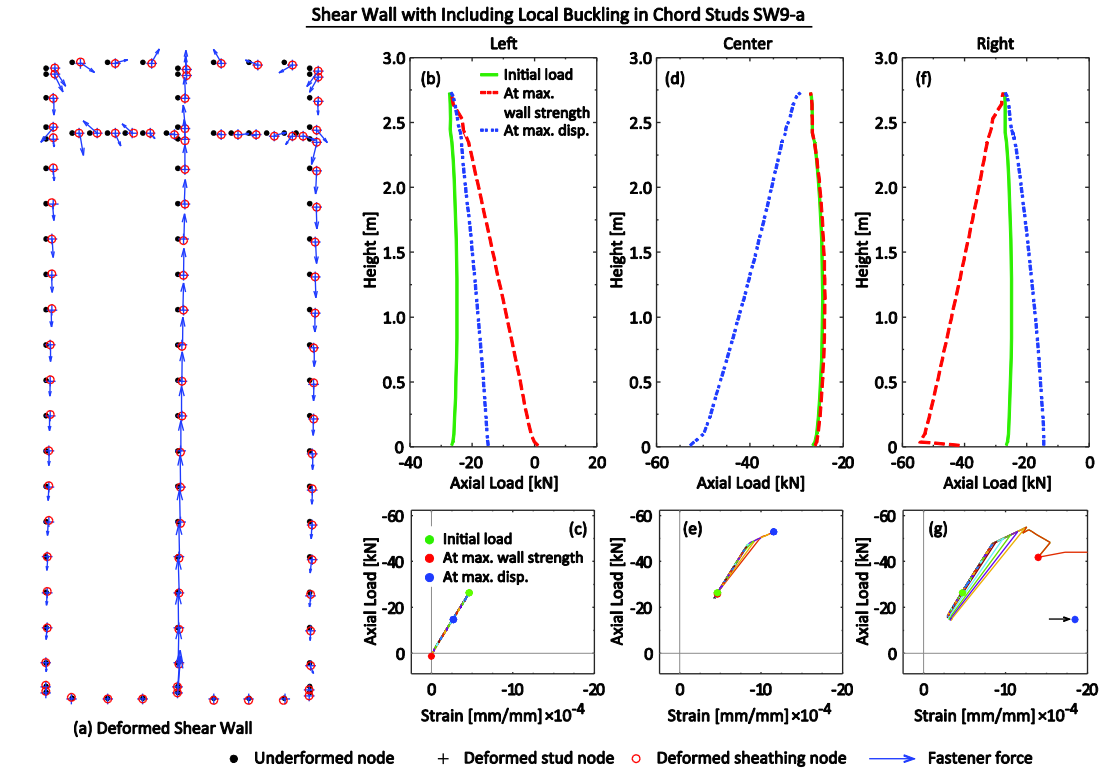

Fig. 8.17. Shear wall (SW9-a) deformed shape (a) showing the wall failure mechanism triggered by local buckling of the compression chord stud followed by buckling in the infill stud.

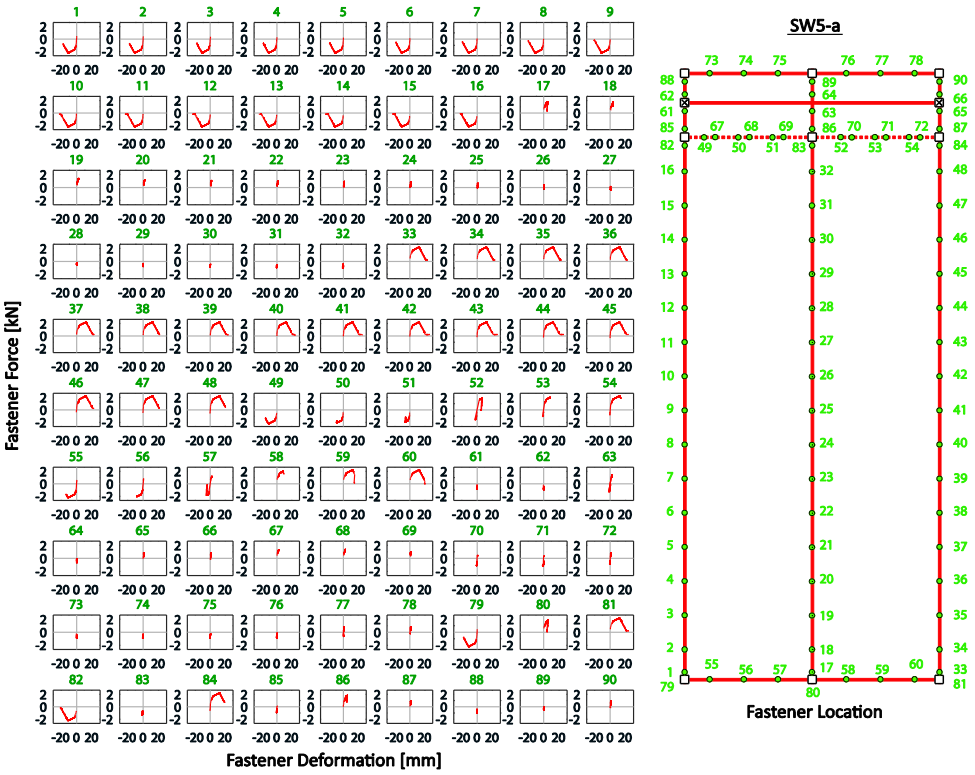

Fig. 8.18. Fastener load-deformation responses in shear wall with less slender studs (SW5-a) where bottom fasteners along the sides fail, while the studs remain elastic.

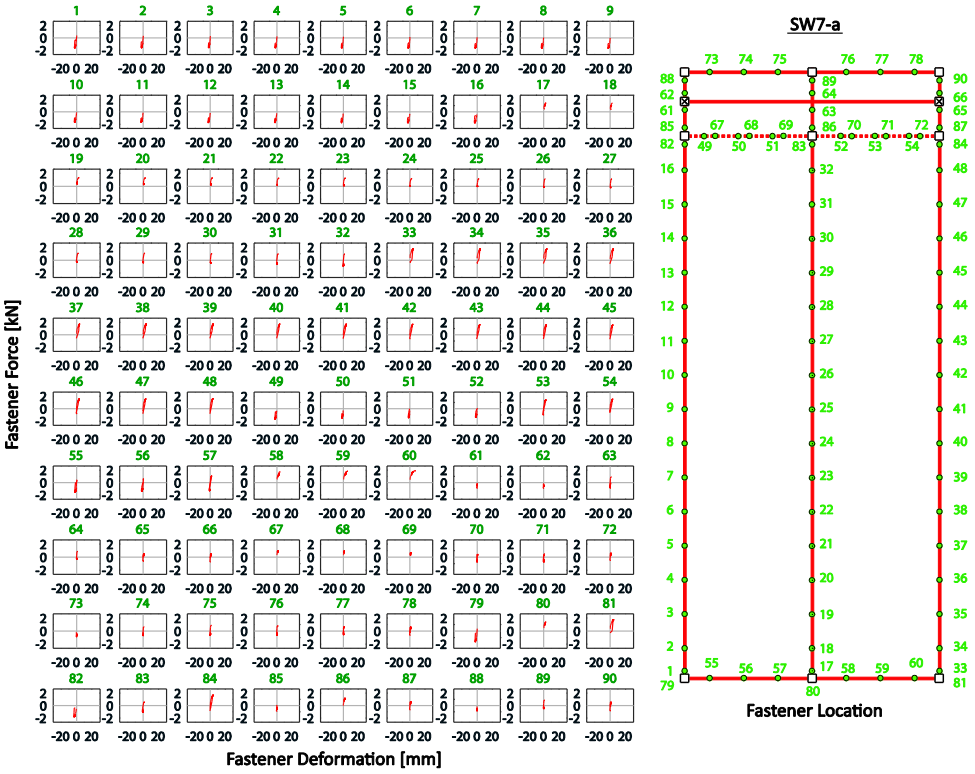

Fig. 8.19. Fastener load-deformation responses in shear wall (SW7-a) where failure is triggered by buckling in the compression chord stud while the other vertical members remain elastic.

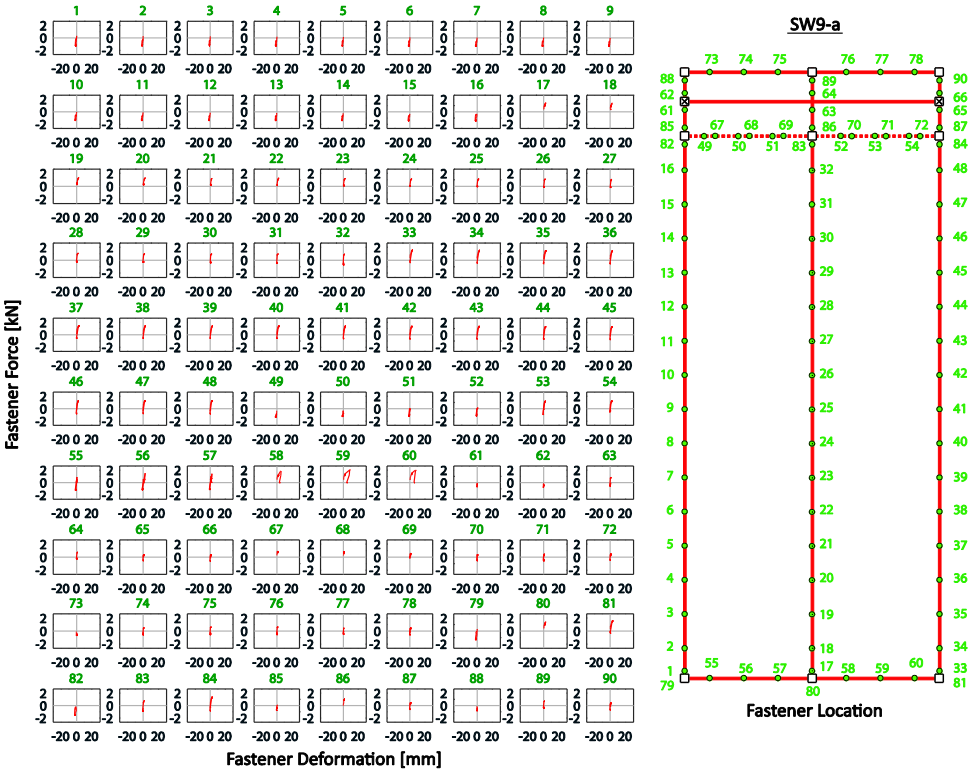

Fig. 8.20. Fastener load-deformation responses in shear wall with slender studs (SW9-a) where failure is triggered by buckling in the compression stud and infill stud reaches loads close to its strength P_n.

8.8 Shear wall cyclic response

Shear wall cyclic responses were obtained to investigate the influence of gravity load and sensitivity to the vertical member cross-section slenderness λ_ℓ. The resulting responses exhibit similar characteristics to the pushover responses previously described. Thus, increasing initial gravity loading acting on the wall reflects in a decrement of the cyclic envelope and increase of the initial lateral stiffness similar to that observed from the pushover responses, see Fig. 8.21a. The failure mechanism exhibited depends as well on the slenderness and magnitude of the applied initial gravity loads. Fig. 8.22 shows the typical response for a wall (SW1-c) where the failure mechanism is fastener driven, and the forces in the vertical studs remain elastic. Fig. 8.23 shows each fastener force-deformation response for the same wall (SW1-c) where it is seen the edge fasteners are the first ones to fail.

For the case of changing the vertical member cross-section slenderness effects, the responses also exhibit the same type of behavior than the corresponding pushover responses, see Fig. 8.21b. The failure mechanism is as well similar to the one observed for the pushover analysis,

and it varies from fastener driven to chord stud buckling triggered depending on the vertical members slenderness. For example Fig. 8.24 shows the response for wall SW7-b, where akin its monotonic response shows buckling in the chord studs. In this case most fasteners connecting the lower OSB panel experience force demands close to the fastener maximum strength, see Fig. 8.25.

In all cyclic responses obtained, vertical members do not experience large nonlinear cycles and therefore cyclic strength and stiffness degradation in this members and their effect on the overall shear wall response is minimal. This result is a consequence of the specific nature of the structural system analyzed where chord stud buckling immediately renders instability. If the analysis were included for example in the context of a whole building analysis where the wall were connected to other elements and redistribution is possible, then more dissipation from the chord studs could be expected. Additionally, the parameters used in this study to define the fastener behavior model do not include strength and/or stiffness cyclic degradation. It is expected that including these two phenomena would result in additional degradation especially for those walls where the failure mechanism is fastener driven.

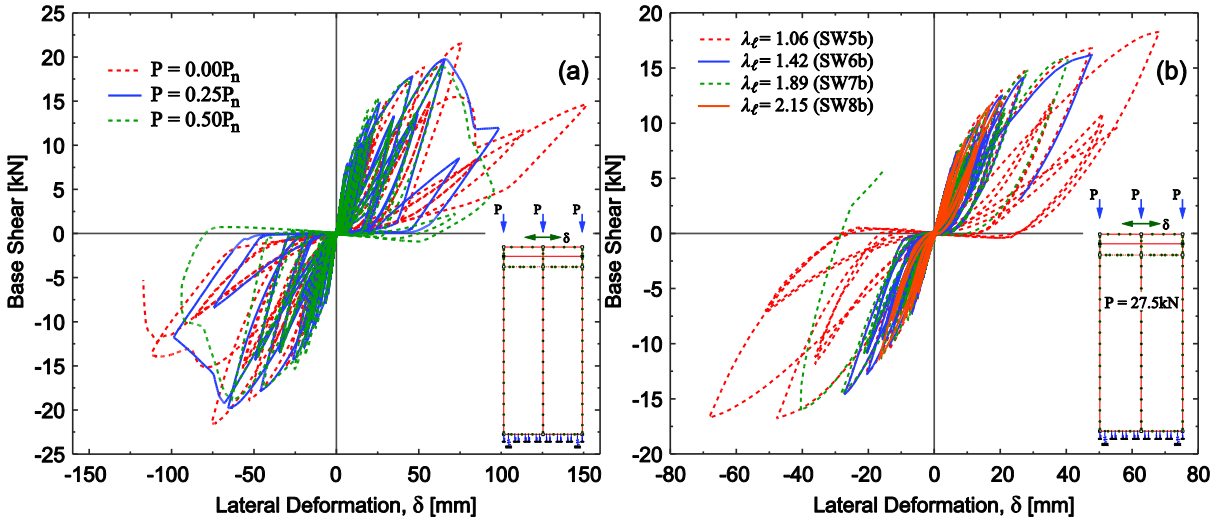

Fig. 8.21. Cyclic response for the shear wall SW1 (a) shows the reduction on the strength envelope because of increasing initial gravity loads, and (b) shows the shear wall response sensitivity to the vertical member cross-section slenderness (SW5b-9b).

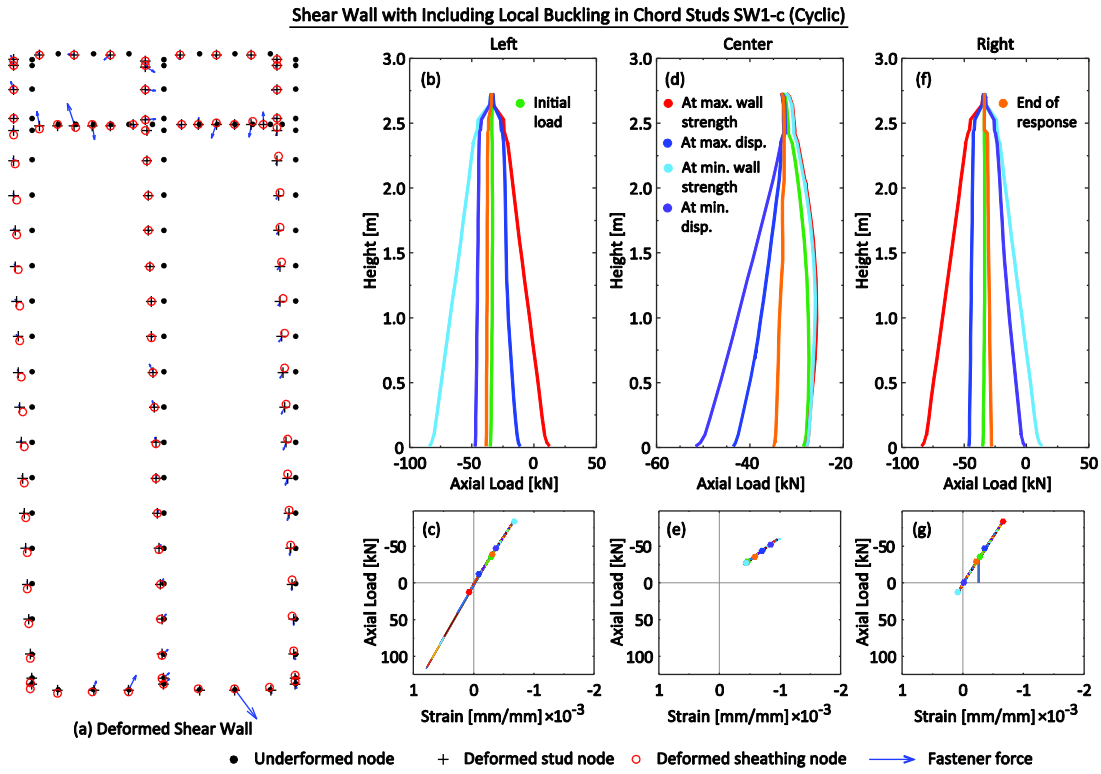

Fig. 8.22. Shear wall (SW1-c) deformed shape from cyclic loading (a) showing fastener failure along the edges and (b) studs remain elastic.

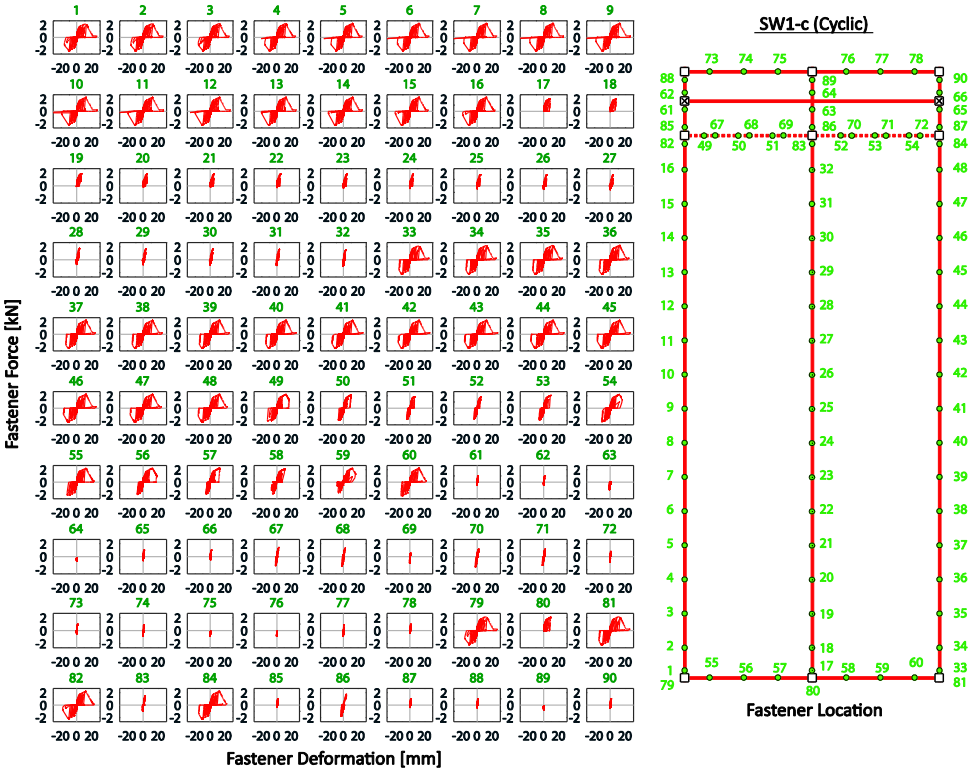

Fig. 8.23. Fastener cyclic responses in shear wall (SW7-b) where edge fasteners fail, while the studs remain elastic

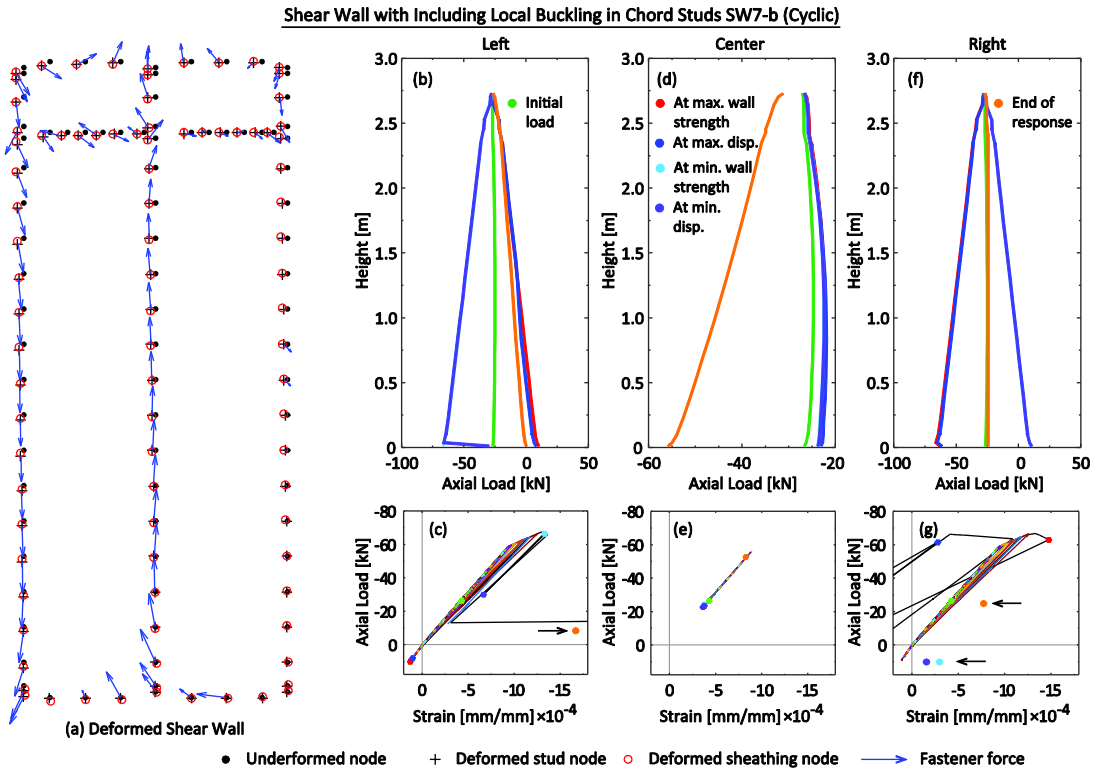

Fig. 8.24. Shear wall (SW7-b) deformed shape from cyclic loading (a) showing the wall failure mechanism triggered by local buckling of the chord studs.

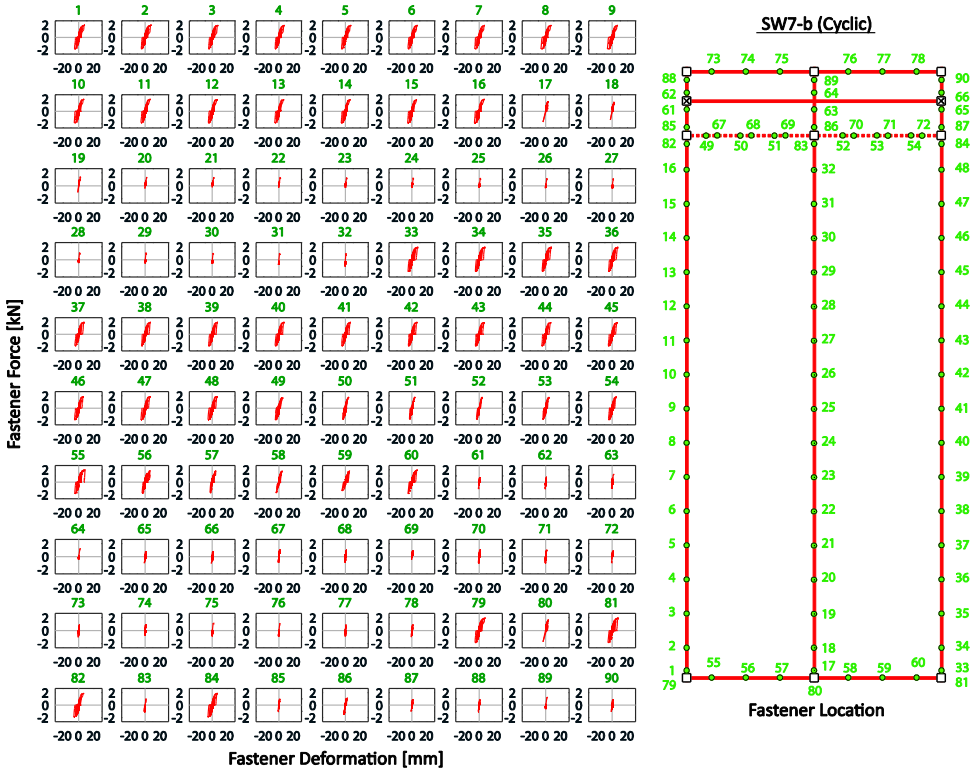

Fig. 8.25. Fastener load-deformation responses in shear wall (SW7-b) where failure is triggered by buckling in the chord studs.

8.9 Conclusions

In this chapter a computationally efficient component based simulation framework for cold-formed steel structures that captures the nonlinear behavior in all critical components was introduced. Cold-formed shear walls were simulated and discussed to illustrate the use of the framework and its advantages. Nonlinear behavior in critical components was included using the *asymPinching* model developed in Chapter 7 for framing members, and *Pinching4* for screw-fastened connections. The capability of the framework to easily modify the geometry or material properties allows exploring different loading scenarios as it was demonstrated by the small study on the shear wall behavior discussed. The results from the shear wall study highlighted the need to include local buckling behavior when analyzing structural systems with thin-walled members. Including local buckling and any other nonlinear behavior can reveal additional limit states and failure mechanisms that may go unnoticed if not included.

Chapter 9: Conclusions and Future Work

9.1 Conclusions

A computationally efficient component-based framework for the analysis of light-framed steel structures was introduced. The framework is supported by nonlinear hysteretic models that capture thin-walled behavior in framing members and nonlinear behavior in screw-fastened connections. To develop the models needed for the framework, the cyclic behavior of thin-walled steel members was investigated analytically and experimentally.

Finite element analyses using ABAQUS were performed to explore cyclic behavior and energy dissipation mechanisms in thin steel plates. Energy dissipation in thin-plates occurs through accumulation of plastic deformations at localized damaged zones that coincide with the leading buckling half-wave. The shape of the initial imperfections influenced where these damaged zones occurred. This study provided insight into the cyclic behavior and energy dissipation in thin-walled cross-section elements, such as webs and stiffened elements.

Cold-formed steel members can dissipate energy and provide post-buckling strength and stiffness during cyclic loading. Full scale experiments (48 total) were performed to investigate and characterize the cyclic behavior of axial and flexural thin-walled cold formed steel members. The test showed that energy dissipation within the leading buckled half-wave decreases as cross-section slenderness (λ_d and λ_ℓ) increases, and increases with cross-section area A (for axial members) and cross section elastic modulus S (for flexural members). Cyclic strength and stiffness degradation were characterized showing that in axial members, strength degradation is independent of cross-section slenderness while stiffness degradation in compression depends on λ_d and λ_ℓ. In flexural members, although not very clear, cyclic strength and stiffness degradation appear larger as the member governing slenderness increases.

A framework to include thin-walled behavior into the modeling of framing axial and flexural steel members was introduced. This framework consisted of a hysteretic model that captures the nonlinear behavior including thin-walled behavior attached to a nonlinear beam column or spring element. The results from the experimental program were used to develop the hysteretic model parameters including backbone curves, strength degradation, and stiffness degradation for each of the tests. This set of parameters were used to illustrate the approach to

model thin walled behavior in steel axial and flexural members using beam-column elements and hysteretic springs.

The framework for modeling thin-walled behavior in steel members was then specialized into the hysteretic model, *asymPinching* for simulating steel columns cyclic behavior including local buckling. General expressions were develop for backbones, total energy dissipation capability, strength degradation and stiffness degradation as a function of the member local slenderness λ_ℓ. These expressions were developed from monotonic and cyclic responses obtained through nonlinear finite element simulations in ABAQUS of cold-formed steel columns which strength predicted by AISI-S100-12 [22] is govern by local buckling. The set of columns simulated covered a wide interval of cross-section local slenderness from stocky to slender thin-walled cross-sections (λ_ℓ from 0.69 to 3.39). Initial imperfections simulated using a 1D spectral approach were included, as well as steel plasticity implemented using combined nonlinear isotropic-kinematic hardening. Steel damage initiation and evolution was also included to simulate the effects of material deterioration due to cold-bending and fracture. The nonlinear finite element modeling protocol was validated against the cyclic responses obtained experimentally.

Even though the proposed methodology is established for thin-walled cold-formed steel members, the *asymPinching* model parameters are presented generally as a function of local buckling slenderness λ_ℓ and could be extended to hot-rolled steel members and cross-sections with future validation. The same methodology could be applied to thin-walled cold-formed steel members that experience distortional and global buckling with further validation. Moreover, the *asymPinching* model can be applied to any material, component or subassembly that exhibits asymmetric pinched hysteretic behavior.

A computationally efficient component based simulation framework for cold-formed steel structures that captures the nonlinear behavior in all critical components was introduced. The framework includes the *asymPinching* to model thin-walled behavior in framing members and allows to consider different loading scenarios and changes in geometries in the analyzed structural system. An illustrative example highlighted the need to include local buckling behavior and any other nonlinear behavior in components when analyzing structural systems with thin walled members as it can reveal additional limit states and failure mechanisms that may go unnoticed if these are not included.

9.2 Future research topics

In the course of conducting the work described in this dissertation, some research needs and future research topics were identified and are summarized below.

Components (member and connections) behavior characterization:

Experimental and analytical investigations on the monotonic and cyclic behavior of CFS members and connections would help to expand the amount of data available needed for validation of the hysteretic models needed for the framework. The following are some the main topics identified as a need for future research on this area:

- Non-uniform loading conditions: Because members in a structure are loaded many different ways, consideration of different loading condition such as moment gradients, varying axial load, and distributed transverse loads is warranted.
- P-M interaction: A study of the effects of axial load bending moment interaction on the behavior of thin-walled beam-columns is needed as most systems that resist lateral loading in cold-formed steel buildings are also supporting gravity loads, e.g., columns in CFS portal frames, chord studs in sheathed shear walls and others.
- Effect of boundary conditions: The effect of different boundary conditions different than the ones used in this research is warranted (e.g., such as pinned warping free end conditions or elements supported only through the web or flanges).
- Screw-fastened Connections: Characterization of the of single screw-fastened steel to steel and sheathing to steel connections cyclic behavior is needed to develop connection models which are one of the main parts of the component-based analysis framework described in Chapter 8.
- Steel material characterization: A comprehensive steel material characterization is very important to accurately simulate the CFS members and connections response using advanced finite elements analysis as described in Chapter 7. The parameters that need characterization besides the tensile strength are hardening parameters based on half-cycle stress-strain data from coupons, and the fracture criteria parameters for cold-formed steel sheets, (i.e., the triaxiality vs. fracture strain locus).

Computationally efficient models for components and structures:

Efficient models to simulate the behavior of members and connections are needed to advance performance analysis based engineering of light-framed steel structures. Additional work to further advance the modeling approach described in this dissertation to include thin walled behavior in modeling members is warranted. Similarly, there is need for efficient models to simulate the typical connections in a light-framed steel structure. The following list summarizes ideas for future research needed on this topic:

- Complete the modeling framework for thin-walled axial members: The framework presented in Chapter 7 to simulate the cyclic behavior including local buckling in axial members needs to be expanded to include the other buckling limit states considered in AISI-S100-12 [22]. Plans are set to developed expressions as a function of slenderness for distortional and global buckling limit states to be used with the *asymPinching* model.
- Sensitivity analysis and validation of the modeling framework for thin-walled members: A sensitivity analysis and validation of the expressions in Chapter 7 is needed. The sensitivity analysis and validation should focus in checking the approach for different cold-formed steel cross-section shapes and possibly hot-rolled steel cross sections.
- Develop general expressions for CFS flexural member hysteretic models: To complete the framework it is necessary to develop expressions for CFS flexural members like the ones described in Chapter 7. The expressions can be set as functions of the member slenderness for local, distortional and global buckling.
- Screw-fastened connection models: General expressions to define the hysteretic model based on fastener and connected parts properties is needed. Currently research is underway to define this parameters.
- A comprehensive beam-column model for thin-walled members: The approach described in Chapter 6 to model cyclic response including thin-walled behavior presents some shortcomings the most relevant being interaction and localization. Axial load-moment interaction which is one important load case for members that are part of the lateral-load resisting system in CFS structures is not included. Localization of the damage as it was observed in the tests and finite element analysis is also not included because of the beam-column element used in this dissertation.

A comprehensive element model for thin-walled members that can model thin wall behavior is needed. In addition to interaction, the model should capture the buckling phenomena with localization of deformations for most member loading cases, as well as material plasticity and fracture. These element model should be computationally more efficient than a thin-shell finite element model of the member but comparatively accurate. Parameters in the form of those presented in Chapter 7 can be developed.

- Validation of the analysis framework through high-end finite element analysis or experiments: The analysis framework described in Chapter 8 needs further validation by comparing simulated responses using the framework to experimental responses of shear walls or other CFS systems. In addition to experimental responses, high-end finite simulations (e.g., thin-shell finite element analysis in ABAQUS) can be used for validation.

Assessment and performance factor quantification for CFS structures:

As mentioned in the introduction of this dissertation, there is an ongoing effort to advance performance based analysis and design of cold-formed steel structures. The simulation framework and models introduced in this dissertation can be used to quantify seismic performance factors R, Ω_0 and C_d for cold-formed steel structures and assemblies following the FEMA P695 approach [2]. Also the framework can be used in seismic performance assessment of CFS buildings using the FEMA P58 methodology [86].

References

[1] AISI S213-07. *North American Standard for Cold-Formed Steel Framing: Lateral Design*, American Iron and Steel Institute, Washington, D.C. ANSI/AISI-S213-07, 2007.

[2] FEMA, *FEMA P695-Quantification of Building Seismic Performance Factors*, Federal Emergency Management Agency (FEMA), Document No. FEMA 965, Washington, D.C., 2009.

[3] DaBreo J, Balh N, Ong-Tone C, Rogers CA. Steel sheathed cold-formed steel framed shear walls subjected to lateral and gravity loading. Thin-Walled Structures 2014;74:232–245.

[4] Balh N, DaBreo J, Ong-Tone C, El-Saloussy K, Yu C, Rogers CA. Design of steel sheathed cold-formed steel framed shear walls. Thin-Walled Structures 2014;75:76–86.

[5] Zeynalian M, Ronagh H. Experimental Study on Seismic Performance of Strap-Braced Cold-Formed Steel Shear Walls. Advances in Structural Engineering 2013;16:245–257.

[6] Shamim, I., and Rogers, C. A., "Steel sheathed/CFS framed shear walls under dynamic loading: Numerical modelling and calibration." Thin-Walled Structures, 71, 57 - 71, 2013.

[7] Shamim I, DaBreo J, Rogers C. Dynamic Testing of Single- and Double-Story Steel-Sheathed Cold-Formed Steel-Framed Shear Walls. Journal of Structural Engineering 2013;139:807–17.

[8] Yu C, Li C. Behavior and strength of cold-formed steel framed shear walls sheathed with composite panels. 21st International Specialty Conference on Cold-Formed Steel Structures, October 24, 2012 - October 25, 2012, Center for Cold-Formed Steel Structures; 2012, p. 637 – 651.

[9] Yu C, Li C. Experimental investigation of cold-formed steel shear walls sheathed with steel-gypsum composite panels. Structural Stability Research Council Annual Stability Conference 2012, April 18, 2012 - April 21, 2012, Structural Stability Research Council (SSRC); 2012, p. 298 – 309.

[10] Nithyadharan M, Kalyanaraman V. Behaviour of cold-formed steel shear wall panels under monotonic and reversed cyclic loading. Thin-Walled Structures 2012;60:12–23.

[11] Peck Q, Rogers N, Serrette R. Cold-Formed Steel Framed Gypsum Shear Walls: In-Plane Response. Journal of Structural Engineering 2012;138:932 – 941.

[12] Liu P, Peterman KD, Yu C, Schafer BW. Cold-formed steel shear walls in ledger-framed buildings. Structural Stability Research Council Annual Stability Conference 2012, April 18, 2012 - April 21, 2012, Structural Stability Research Council (SSRC); 2012, p. 310 – 323.

[13] Liu P, Peterman KD, Yu C, Schafer BW. Characterization of cold-formed steel shear wall behavior under cyclic loading for the CFS-NEES building. 21st International Specialty Conference on Cold-Formed Steel Structures, October 24-25, 2012, Center for Cold-Formed Steel Structures; 2012, p. 703 – 722.

[14] Dastjerdi MZ, Ronagh HR. Seismic performance of steel sheathed cold-formed steel shear walls. 21st International Specialty Conference on Cold-Formed Steel Structures, October 24, 2012 - October 25, 2012, Center for Cold-Formed Steel Structures; 2012, p. 671 – 685.

[15] B. W. Schafer, D. Ayhan, J. Leng, P. Liu, D. A. Padilla-Llano, K. D. Peterman, M. Stehman, S. G. Buonopane, M. R. Eatherton, R. L. Madsen, B. Manley, C. D. Moen, N. Nakata, C. A. Rogers, and C. Yu, "The CFS-NEES Effort: Advancing Cold-Formed Steel Earthquake Engineering," presented at the 10th U.S. National Conference on Earthquake Engineering, Anchorage, AK, 2014.

[16] Peterman K, Nakata N, Schafer B. Cyclic Behavior of Cold-Formed Steel Stud-to-Sheathing Connections. 15th World Conference on Earthquake Engineering, Lisbon, Portugal: 2012.
[17] Okasha A. Performance of steel frame/wood sheathing screw connections subjected to monotonic and cyclic loading. M.Sc. Thesis. University of McGill, 2004.
[18] Ayhan D.and Schafer B.W., Characterization of moment-rotation response of cold-formed steel beams. Proceedings of the Annual Stability conference, SSRC, April 18-21, 2012, Grapevine, Texas.
[19] Madsen, R.L., Nakata, N., and Schafer, B.W., "CFS-NEES Building Structural Design Narrative", Research Report, RR01, access at www.ce.jhu.edu/cfsness, October 2011, revised RR01c May 2012.
[20] K. D. Peterman, M. Stehman, S. G. Buonopane, N. Nakata, R. L. Madsen, and B. W. Schafer, "Stability behavior of full-scale cold-formed steel buildings under seismic excitations," in Structural Stability Research Council Annual Stability Conference 2014, SSRC 2014, March 25-28, 2014.
[21] Lowes, L., Mitra, N., Altoontash, A., *A Beam-Column Joint Model for Simulating the Earthquake Response of Reinforced Concrete Frames*, PEER Report 2003/10, Pacific Earthquake Engineering Research Center., 2004.
[22] AISI-S100-12, North American Specification for the Design of Cold-Formed Steel Structural Members. American Iron and Steel Institute, Washington, D.C. ANSI/AISI-S100-07. 2007.
[23] ABAQUS. ABAQUS Documentation v6.13, Dassault Systèmes Simulia Corp., Providence, RI, USA, 2013.
[24] Mazzoni, S., McKenna, F., Scott, M.H., Fenves, G.L. *Open System for Earthquake Engineering Simulation User Command-Language Manua*l, *OpenSees Version 2.0*, Berkeley, California, 2009.
[25] MATLAB, Version 7.12.0.635. The Mathworks, Inc., www.mathworks.com, 2011.
[26] L.E. McAnallen, D.A. Padilla-Llano, X. Zhao, C.D. Moen, B.W. Schafer, M.R. Eatherton, "Initial Geometric Imperfection Measurement and Characterization of Cold-Formed Steel C-Section Structural Members with 3D Non-Contact Measurement Techniques". Proceedings of the Annual Stability conference, SSRC 2014, March 25-28, 2014, Toronto, Canada.
[27] A. Filiatrault, P. Léger, and R. Tinawi, "On the computation of seismic energy in inelastic structures," Engineering Structures, vol. 16, no. 6, pp. 425–436, 1994.
[28] Zeinoddini VM, Schafer BW. Simulation of geometric imperfections in cold-formed steel members using spectral representation approach. Thin-Walled Structures 2012;60:105–17.
[29] Schafer BW, Pekoz T. Computational modeling of cold-formed steel: characterizing geometric imperfections and residual stresses. Journal of Constructional Steel Research 1998; 47(3):193–210.
[30] FEMA, FEMA 461 - Interim protocols for determining seismic performance characteristics of structural and nonstructural components through laboratory testing, Federal Emergency Management Agency (FEMA), Document No. FEMA 461. 2007.
[31] Higginbotham, A. B., and Hanson, R. D., Axial Hysteretic Behavior of Steel Members. Journal of the Structural Division, 1976; 102(7), 1365-1381.
[32] Ikeda, K., and Mahin, S. A., Cyclic Response of Steel Braces. Journal of Structural Engineering, 1986; 112(2), 342.

[33] Tang, X., and Goel, S. C., Seismic Analysis and Design Considerations of Concentrically Braced Steel Structures. Report No UMCE 87-4, Department of Civil Engineering, The University of Michigan, Ann Arbor, MI. 1987.
[34] Papadrakakis, M., and Loukakis, K., Elastic-plastic hysteretic behaviour of struts with imperfections. Engineering Structures, 1987; 9(3), 162-170.
[35] Nonaka, T., An elastic-plastic analysis of a bar under repeated axial loading." International Journal of Solids and Structures, 1973; 9(5), 569-580.
[36] Sohal, I. S., and Chen, W. F., Local buckling and inelastic cyclic behavior of tubular sections. Thin-Walled Structures, 1988; 6(1), 63-80.
[37] Goel, S. C., Cyclic Post-Buckling Behavior of Steel Bracing Members. Stability and Ductility of Steel Structures Under Cyclic Loading. pp75-84 CRC Press, 1992.
[38] Goggins, J. M., Broderick, B. M., Elghazouli, A. Y., and Lucas, A. S., Behaviour of tubular steel members under cyclic axial loading. Journal of Constructional Steel Research, 2006; 62(1–2), 121-131.
[39] Popov, E. P., and Black, R. G., Steel Struts under Severe Cyclic Loadings. Journal of the Structural Division, 1981; 107(9), 1857-1881.
[40] Jain, A. K., Hanson, R. D., and Goel, S. C., Hysteretic Cycles of Axially Loaded Steel Members. Journal of the Structural Division, 1980; 106(8), 1777-1795.
[41] Popov, E. P., Mahin, Stephen A, and Zayas, V. A., Cyclic Inelastic Buckling of Thin Tubular Columns. Journal of the Structural Division, 1979; 105(11), 2261-2277.
[42] Yao, T., and Nikolov, P. I., Numerical Experiment on Buckling/Plastic Collapse Behavior of Plates under Cyclic Loading. Stability and Ductility of Steel Structures Under Cyclic Loading. pp203-214 CRC Press. 1992.
[43] Usami, T., and Ge, H. B., Cyclic behavior of thin-walled steel structures–numerical analysis. Thin-Walled Structures, 1998; 32(1–3), 41-80.
[44] Watanabe, E., Sugiura, K., Mori, T., and Suzuki, I., Modeling of Hysteretic Behavior of Thin-Walled Box Members. Stability and Ductility of Steel Structures Under Cyclic Loading. pp225-235 CRC Press. 1992.
[45] Calderoni, B., De Martino, A., Formisano, A., and Fiorino, L., Cold formed steel beams under monotonic and cyclic loading: Experimental investigation. Journal of Constructional Steel Research, 2009; 65(1), 219–227.
[46] SSMA Steel Stud Manufacturers Association, Product Technical Information, ICBO ER-4943P, <http://www.ssma.com>, December 15, 2011.
[47] Moen, C. D., Direct strength design for cold-formed steel members with perforations. Ph.D. dissertation, Johns Hopkins University, Baltimore. 2008.
[48] Schafer BW, Adany S. Buckling analysis of cold-formed steel members using CUFSM: conventional and constrained finite strip methods. In: Proceedings of the 18th international specialty conference on cold-formed steel structures. Orlando, FL, United states: University of Missouri-Rolla; 2006.
[49] ASTM. E8M-13, Standard Test Methods for Tension Testing of Metallic Materials (Metric). ASTM International, West Conshohocken, PA. 2004.
[50] Moncarz, P.D., and Krawinkler H., Theory and Application of Experimental Model Analysis in Earthquake Engineering. The John A. Blume Earthquake Engineering Center Report No. 50. 1981.

[51] AISI-S910-08, Test Method for Distortional Buckling of Cold-Formed Steel Hat Shaped Compression Members. American Iron and Steel Institute, Washington, D.C. ANSI/AISI-S910-08. 2008.
[52] Moen CD, Schafer BW. Experiments on cold-formed steel columns with holes. Thin-Walled Structures 2008; 46(10):1164–1182.
[53] Zeinoddini, V. M., Geometric imperfections in cold-formed steel members. Ph.D. dissertation, Johns Hopkins University, Baltimore. 2011.
[54] Padilla-Llano, D.A., Moen, C.D., and Eatherton, M.R., *Energy Dissipation of Thin-Walled Cold-Formed Steel Members*. Virginia Polytechnic Institute and State University Research Report No. CE/VPI-ST-13/06, Blacksburg, VA. 2013.
[55] ASTM-C955, Standard Specification for Load-Bearing (Transverse and Axial) Steel Studs, Runners (Tracks), and Bracing or Bridging for Screw Application of Gypsum Panel Products and Metal Plaster Bases. West Conshohocken, PA. 2009.
[56] Moen, C.D., Igusa, T., and Schafer, B.W., "Prediction of Residual Stresses and Strains in Cold-Formed Steel Members." Thin-Walled Structures, 46(11), 1274-1289, 2008.
[57] VTechWorks, <http://hdl.handle.net/10919/18721> (May, 2012).
[58] M. Wong and K. Chung, "Structural behaviour of bolted moment connections in cold-formed steel beam-column sub-frames," *Journal of Constructional Steel Research*, vol. 58, no. 2, pp. 253–274, Feb. 2002.
[59] C.-M. Uang, A. Sato, J.-K. Hong, and K. Wood, "Cyclic testing and modeling of cold-formed steel special bolted moment frame connections," Journal of Structural Engineering, vol. 136, no. 8, pp. 953–960, 2010.
[60] A. Bagheri Sabbagh, M. Petkovski, K. Pilakoutas, and R. Mirghaderi, "Experimental work on cold-formed steel elements for earthquake resilient moment frame buildings," *Engineering Structures*, vol. 42, pp. 371–386, Sep. 2012.
[61] S. Yin, E. Corona, and M. Ellison, "Degradation and Buckling of I-Beams under Cyclic Pure Bending," *Journal of Engineering Mechanics*, vol. 130, no. 7, pp. 809–817, 2004.
[62] G. C. Lee and E. T. Lee, "Local buckling of steel sections under cyclic loading," *Journal of Constructional Steel Research*, vol. 29, no. 1–3, pp. 55–70, 1994.
[63] H.-L. Hsu and P.-S. Chi, "Flexural performance of symmetrical cold-formed thin-walled members under monotonic and cyclic loading," *Thin-Walled Structures*, vol. 41, no. 1, pp. 47–67, Jan. 2003.
[64] M. Elchalakani, X. Zhao, and R. Grzebieta, "Cyclic Bending Tests to Determine Fully Ductile Section Slenderness Limits for Cold-Formed Circular Hollow Sections," *Journal of Structural Engineering*, vol. 130, no. 7, pp. 1001–1010, 2004.
[65] P. K. Shaw and S. Kyriakides, "Inelastic analysis of thin-walled tubes under cyclic bending," *International Journal of Solids and Structures*, vol. 21, no. 11, pp. 1073–1100, 1985.
[66] S. Kyriakides and P. K. Shaw, "Inelastic Buckling of Tubes Under Cyclic Bending," *J. Pressure Vessel Technol.*, vol. 109, no. 2, pp. 169–178, May 1987.
[67] E. Corona and S. Kyriakides, "An experimental investigation of the degradation and buckling of circular tubes under cyclic bending and external pressure," *Thin-Walled Structures*, vol. 12, no. 3, pp. 229–263, 1991.
[68] S. P. Vaze and E. Corona, "Degradation and collapse of square tubes under cyclic bending," *Thin-Walled Structures*, vol. 31, no. 4, pp. 325–341, Aug. 1998.

[69] B. Calderoni, A. De Martino, A. Formisano, and L. Fiorino, “Cold formed steel beams under monotonic and cyclic loading: Experimental investigation,” *Journal of Constructional Steel Research*, vol. 65, no. 1, pp. 219–227, 2009.
[70] B. Calderoni, C. Giubileo, and A. De Martino, “Assessment of hysteretic cyclic behaviour of plastic hinge in cold-formed steel beams,” in *5th International Conference on Behaviour of Steel Structures in Seismic Areas - Stessa 2006, August 14, 2006 - August 17, 2006*, 2006, pp. 185–190.
[71] A. De Martino, A. Formisano, and B. Calderoni, “Flexural cyclic behaviour and low-cycle fatigue of cold-formed steel members,” in *Improvement of Buildings’ Structural Quality by New Technologies*, H. Koukkari, L. Bragança, H. Trumpf, G. de Matteis, F. Mazzolani, C. Schaur, J.-P. Jaspart, and G. Huber, Eds. Taylor & Francis, 2005, pp. 301–309.
[72] EN-1993. Eurocode 3: design of steel structures. European Committee for Standardization. Brussels, Belgium; 2006.
[73] Schafer B.W., Ayham, D., Leng, J., Liu, P., Padilla-Llano, D., Peterman, K., Stehman, M., Buonopane, S.G., Eatherton, M., Madsen, R., Manley, B., Moen, C.D., Nakata, N., Rogers, C., and Yu, C. “The CFS-NEES Effort: Advanced Cold-Formed Steel Earthquake Engineering” Submitted for the Proceedings of the 10th National Conference on Earthquake Engineering, July 21-25 2014, Anchorage Alaska.
[74] AISI-S911-08, Method for Testing Cold-Formed Steel Hat Shaped Beams. American Iron and Steel Institute, Washington, D.C. ANSI/AISI-S911-08. 2008.
[75] VTechWorks, <http://hdl.handle.net/10919/18721> (May, 2012).
[76] B. Put, Y. Pi, and N. Trahair, “Lateral Buckling Tests on Cold-Formed Channel Beams,” *Journal of Structural Engineering*, vol. 125, no. 5, pp. 532–539, 1999.
[77] D. A. Padilla-Llano, C. D. Moen, and M. R. Eatherton, “Cyclic axial response and energy dissipation of cold-formed steel framing members,” *Thin-Walled Structures*, vol. 78, pp. 95–107, 2014.
[78] Ibarra, L.F., Krawinkler H., 2005. *Global collapse of frame structures under seismic excitations*, Report No. 152, The John A. Blume Earthquake Engineering Center.
[79] Lemaitre, Jean and Jean-Louis Chaboche. Mechanics of Solid Materials. 1st ed. Cambridge: Cambridge University Press, 1990. Cambridge Books Online. Web. 22 April 2015. http://dx.doi.org/10.1017/CBO9781139167970.
[80] Y. Bao and T. Wierzbicki, “On fracture locus in the equivalent strain and stress triaxiality space,” *International Journal of Mechanical Sciences*, vol. 46, no. 1, pp. 81–98, Jan. 2004.
[81] Lee, Y.W., Wierzbicki, T., “Quick Fracture Calibration for Industrial Use,” Massachusetts Institute of Technology, Impact & Crashworthiness Laboratory Report No. 115, 2004.
[82] S.G., Buonopane, T.H., Tun, B. W. Schafer, “Fastener-Based Computational Models for Prediction of Seismic Behavior of CFS Shear Walls.” 10th U.S. National Conference on Earthquake Engineering, Anchorage, AK, 2014.
[83] K. D. Peterman, N. Nakata, and B. W. Schafer, “Hysteretic characterization of cold-formed steel stud-to-sheathing connections,” *Journal of Constructional Steel Research*, vol. 101, pp. 254 – 264, Oct. 2014.
[84] Bian, G., Padilla-Llano, D.A., Buonopane, S.G., Moen, C.D., Schafer, B.W., OpenSees modeling of wood sheathed cold-formed steel framed shear walls. Structural Stability Research Council Annual Stability Conference. Nashville, TN, March 24-27, 2015.

[85] Padilla-Llano, D.A., Moen, C.D., Eatherton, M.R., OpenSees simulation of steel column axial cyclic response including local buckling. Structural Stability Research Council Annual Stability Conference. Nashville, TN, March 24-27, 2015.
[86] FEMA, *FEMA P58-Seismic Performance Assessment of Buildings*, Federal Emergency Management Agency (FEMA), Document No. FEMA 58, Washington, D.C., 2012.

Appendix A Displacement-Controlled Protocol for Cyclic Testing of Cold-Formed Steel Members

Cyclic loading protocols attempt to experimentally simulate deformation demands, cumulative deformation, and the number of inelastic cycles a system (or component) might endure during a design level seismic event [A.1]. The peak axial displacement demand, cumulative displacement demand, and number of inelastic cycles in a particular cold-formed steel member depends on many factors such as the location of the member in the building (e.g., chord studs in a shear wall experience larger axial deformation demands than studs in a typical partition wall), end fixity/constraints (i.e., connections may not fully transfer tension, compression, or moments to the member), bracing conditions, the building's dynamic properties (elastic and nonlinear), and ground motion properties (which can vary depending source characteristics, distance to fault, site characteristics, etc.). Because of the inherent challenges associated with predicting demands on specific CFS members, the displacement-controlled testing protocol adopted here instead focuses on the progression of damage limit states in the member rather than reproducing seismic demands for a specific member configuration.

The loading protocol in Fig. A.1 was adapted from the FEMA 461 quasi-static cyclic deformation-controlled testing protocol. The FEMA 461 protocol was developed to obtain fragility data and hysteretic response characteristics of building components for which damage is best predicted by imposed deformations [A.2]. Cold-formed steel members can experience symmetrical or asymmetrical loading depending on the end connections (e.g., screwed or welded connection), bracing conditions, and location within a building system (e.g., floor joist compared to a stud in a shear wall). The adapted protocol is fully reversed with symmetric deformation amplitudes in both loading directions. Hysteretic models built based on the responses obtained from this protocol are expected to be capable of capturing the behavior under different loading patterns such as one-sided loading.

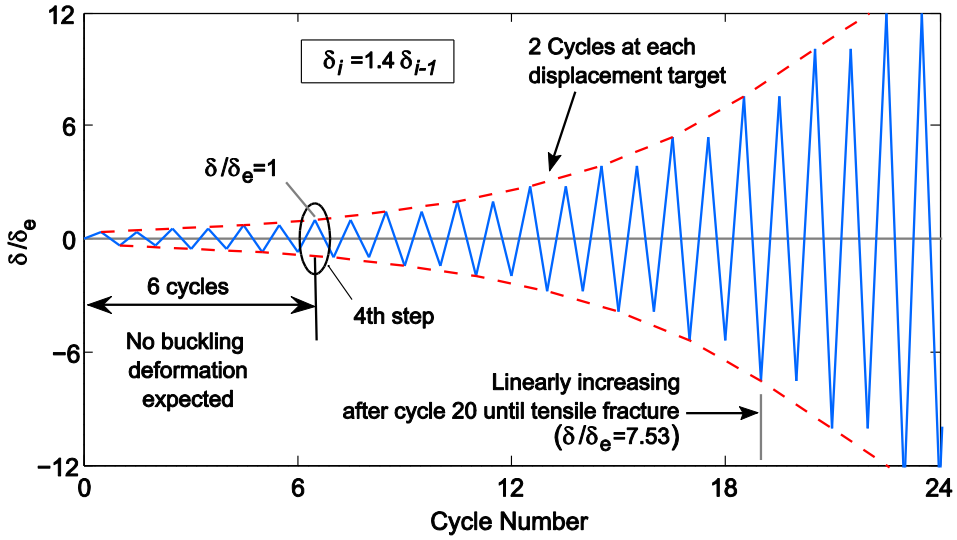

Fig. A.1. Displacement-controlled testing protocol for cold-formed steel members.

The FEMA 461 protocol is defined to reach a deformation associated with the most severe damage state at a preset point in the loading protocol, such as the 20th cycle. It is also suggested that at least six cycles should be completed prior to reaching the lowest damage state [A.2]. For cold-formed steel members the lowest damage state is assumed to occur when the member stiffness decreases due to buckling deformations. Hence, linear elastic behavior is expected before the corresponding deformation that leads to a reduction of the member initial stiffness. In the adapted protocol this linear behavior is expected to be comprised within the first six cycles (see Fig. A.1).

The protocol comprises steps of increasing amplitude with two cycles per step. The loading protocol comprises steps of increasing amplitude with two cycles per step. Each step's displacement amplitude is 40% larger than the previous, i.e., $\delta_i = 1.4\delta_{i-1}$, see Fig. A.1. The loading protocol is anchored to the elastic deformation δ_e at the fourth step (i.e., 7th and 8th cycles). The deformation δ_e is the deformation corresponding to the axial load P_e (axial members) or bending moment M_e associated to with stiffness deterioration due to buckling deformations. The values for P_e and M_e are estimated using slenderness limits defined in the AISI Direct Strength Method (DSM) [A.3].

For CFS axial members, the DSM approach predicts that local buckling deformation initiates at λ_ℓ=0.776 and the distortional buckling deformation initiates at λ_d=0.561. Calculating the slenderness $\lambda=(P_e/P_{cr})^{0.5}$, then P_e=0.60$P_{cr\ell}$ and P_e=0.31P_{crd}. The load where global buckling deformation influences load-deformation response is assumed to be P_e=0.50P_{cre}. In the axial tests

described in Chapter 3, the load P_e associated with stiffness deterioration from buckling deformations is given by Eq. A.1.

For CFS flexural members, the DSM approach predicts that local buckling initiates at λ_ℓ=0.776 and distortional buckling initiates at λ_d=0.673. Calculating the slenderness $\lambda=(M_e/M_{cr})^{0.5}$, the moments associated with stiffness degradation from buckling deformations are M_e=0.60$M_{cr\ell}$ and M_e=0.45M_{crd} for local and distortional buckling respectively. The DSM approach estimates that global buckling deformations initiate at M_e=0.36M_{cre}. In the flexural test described in Chapter 4, the bending moment M_e associated with stiffness deterioration from buckling deformations is given by Eq. A.2.

$$\delta_e = P_e L / AE \quad \text{A.1}$$

$$\delta_e = aM_e(3L_u + 2a)/6EI \quad \text{A.2}$$

where E is the elastic modulus; A and I are respectively the member area and strong axis moment of inertia; L_u the constant moment span length; a is the shear span.

References

[A.1] Krawinkler, H., "Loading histories for cyclic tests in support of performance assessment of structural components" *The 3rd International Conference on Advances in Experimental Structural Engineering*, October 15-16, 2009, San Francisco, CA. 2009.

[A.2] FEMA, FEMA 461 - Interim protocols for determining seismic performance characteristics of structural and nonstructural components through laboratory testing, Federal Emergency Management Agency (FEMA), Document No. FEMA 461. 2007.

[A.3] AISI-S100-07, North American Specification for the Design of Cold-Formed Steel Structural Members. American Iron and Steel Institute, Washington, D.C. ANSI/AISI-S100-07. 2007.

Appendix B Test Setup Drawings

Three-dimensional CAD models for both axial and flexural tests setups with the exact dimensions used are available at http://edcfs.blogspot.com/p/drawings.html. Additional drawings with details are shown below:

B.1. Axial test setup drawings

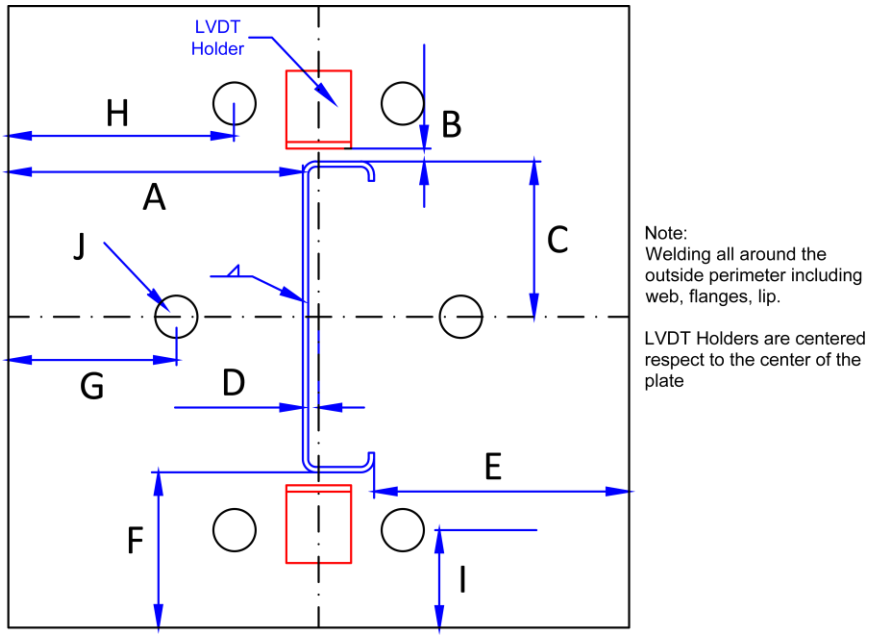

Fig. B.1. End plate and specimen location detail.

Table B.1. Dimensions for specimen location on the end plates.

SSMA Stud	*A*	*B*	*C*	*D*	*E*	*F*	*G*	*H*	*I*	*J*
					[in.]					
600S137-97	5-11/16	1/4	3	5/16	4-15/16	3	3-1/4	4-3/8	1-7/8	13/16
362S137-68	5-19/32	1/4	1-13/16	13/32	5-1/32	4-3/16	3-1/4	4-3/8	3-1/8	13/16
600S137-68	5-11/16	1/4	3	5/16	4-15/16	3	3-1/4	4-3/8	1-7/8	13/16
600S162-33	5-19/32	1/4	3	13/32	4-25/32	3	3-1/4	4-3/8	1-7/8	13/16
362S162-54	5-15/32	1/4	1-13/16	17/32	4-29/32	4-3/16	3-1/4	4-3/8	3-1/8	13/16

B.2. Flexural test setup

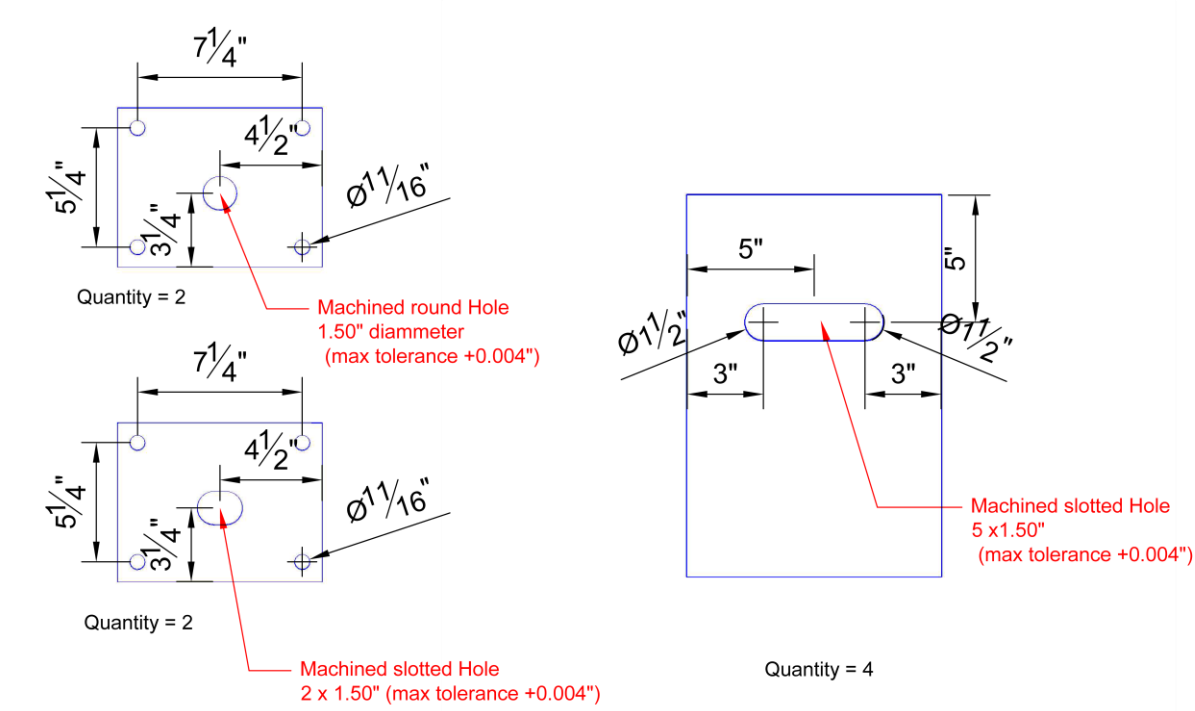

Fig. B.2. Plates for loading point and end support detail.

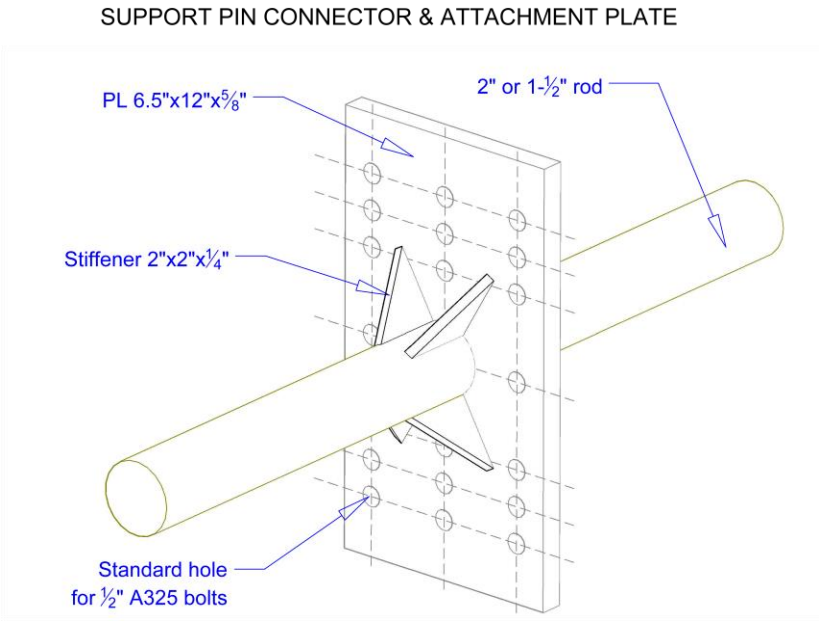

Fig. B.3. Detail for the Pin use at end supports and loading points (see Fig. B.4).

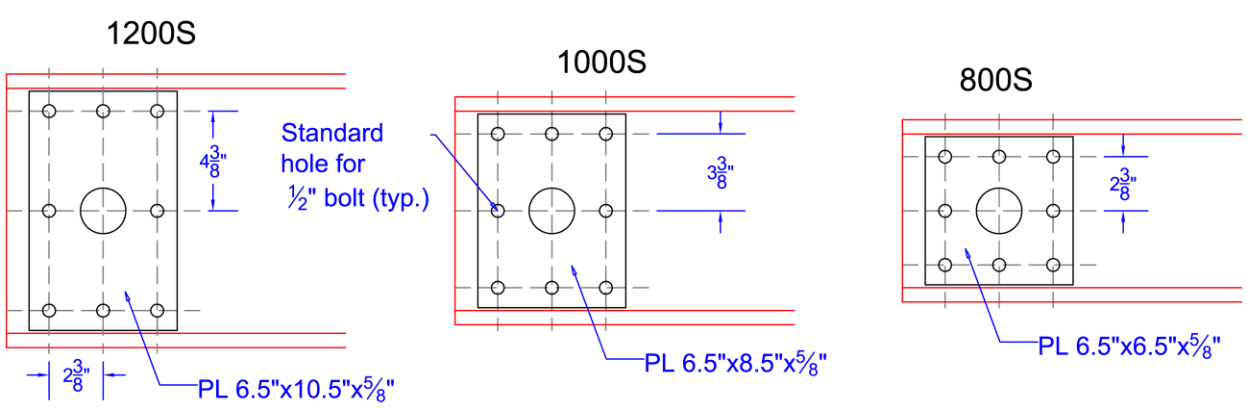

Fig. B.4. Specimen attachment plates.

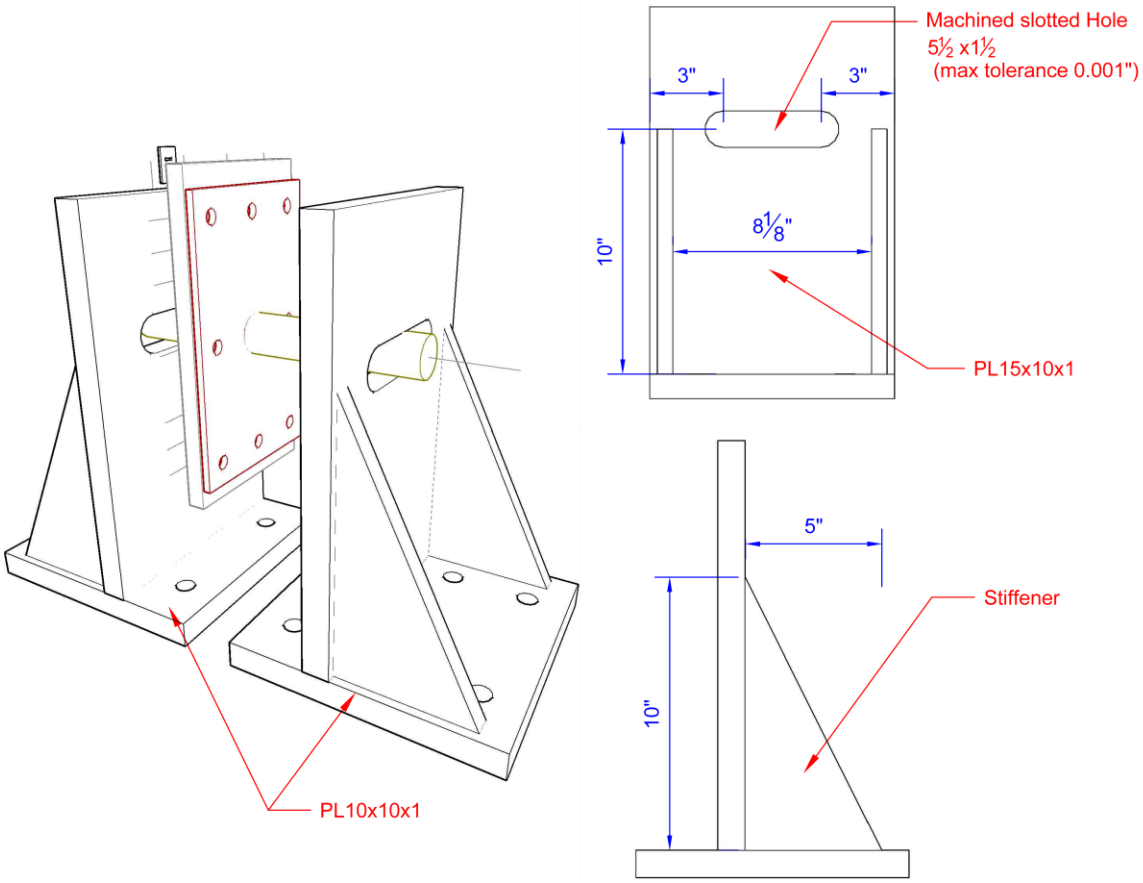

Fig. B.5. End supports detail.

Appendix C Axial Experiment Results

This appendix includes the load-deformation experimental curves for all tests in Chapter 3 accompanied by the coupon tests curves and the cross-section deformations measured with the string potentiometers (see Fig. C.1). Data measured from string potentiometers is processed according to Fig. C.2 to Fig. C.5 where P_k indicates the 4 points tracked and P_{ij} indicates the vector from point i to j.

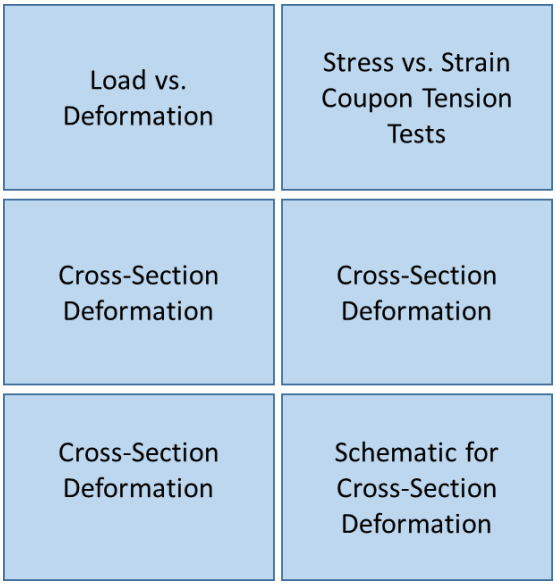

Fig. C.1. How to read each specimen results sheet below

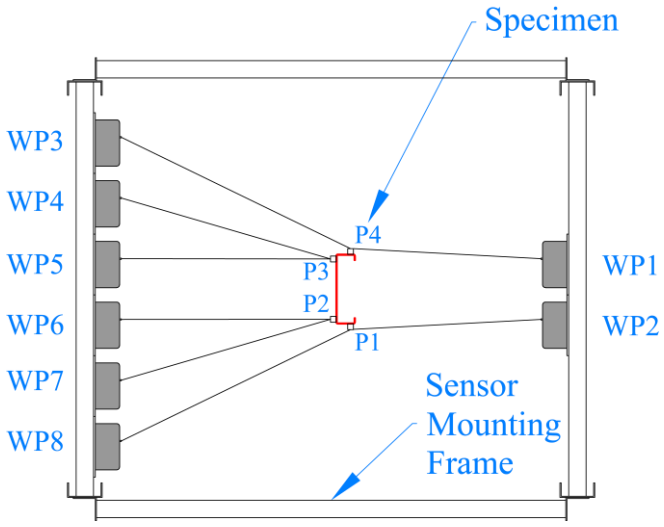

Fig. C.2. String potentiometers map at the middle cross-section for global and distortional buckling specimens.

Solve θ from:

$$\sin(\theta/2) = \left\|\overrightarrow{P_{23}}\right\| \left(\frac{\theta}{2S \pm \theta}\right)$$

$$d_1 = (S/\theta)[1 - \sqrt{1 - \sin^2(\theta/2)}]$$

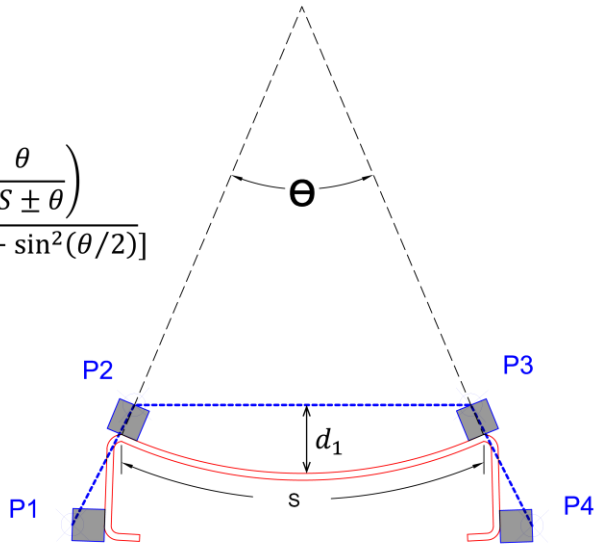

Fig. C.3. Calculating the web deformation d_1 based on string potentiometer reading s for global and distortional specimens.

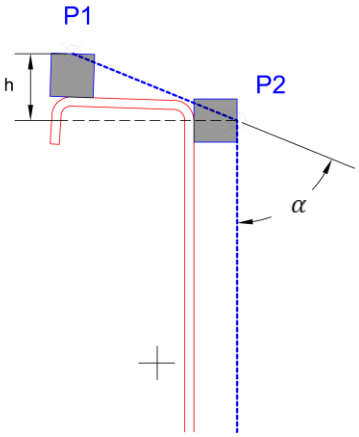

$$h = \left\|\overrightarrow{P_{12}}\right\| \cos\alpha$$

$$\cos\alpha = \frac{\overrightarrow{P_{12}} \cdot \overrightarrow{P_{23}}}{\left\|\overrightarrow{P_{12}}\right\| \left\|\overrightarrow{P_{23}}\right\|}$$

$$d_2 = h - h_0$$

Fig. C.4. Calculating the flange imperfection d_2 based on the string potentiometer readings for global and distortional specimens.

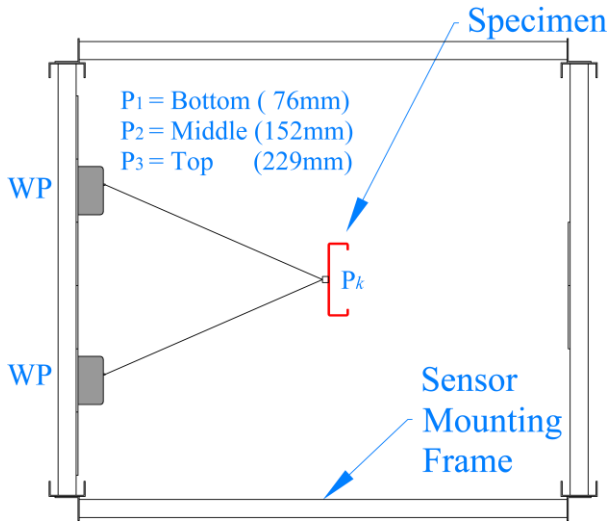

Fig. C.5. String potentiometers map for local buckling specimens.

600S137-97-GAM-1

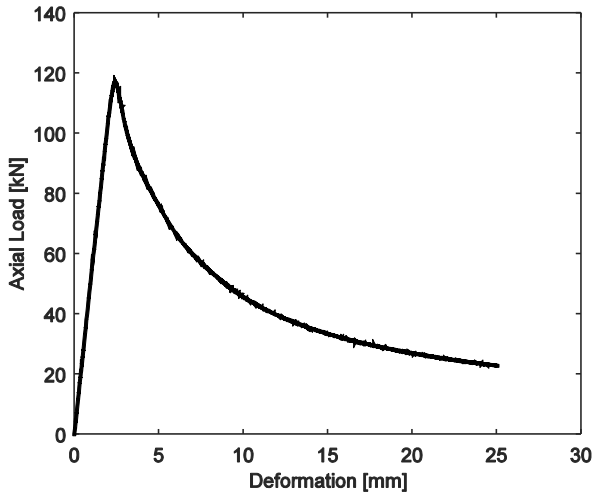

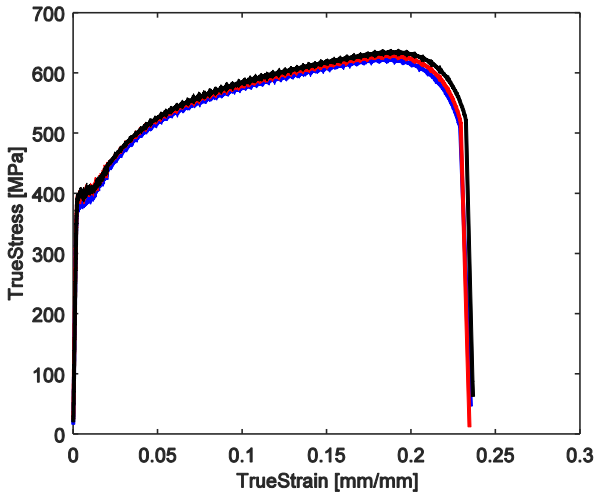

600S137-97-GAM-2

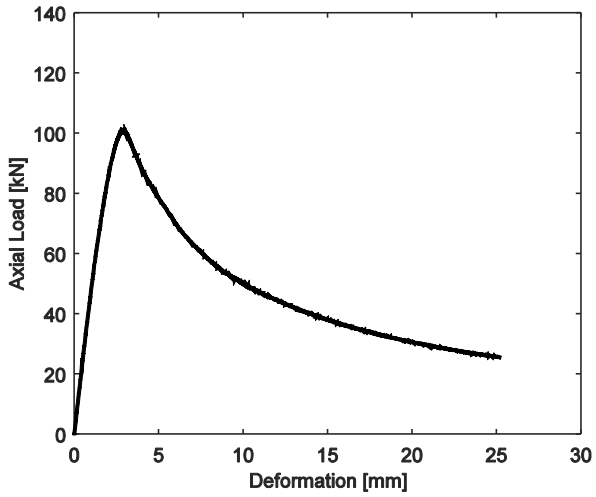

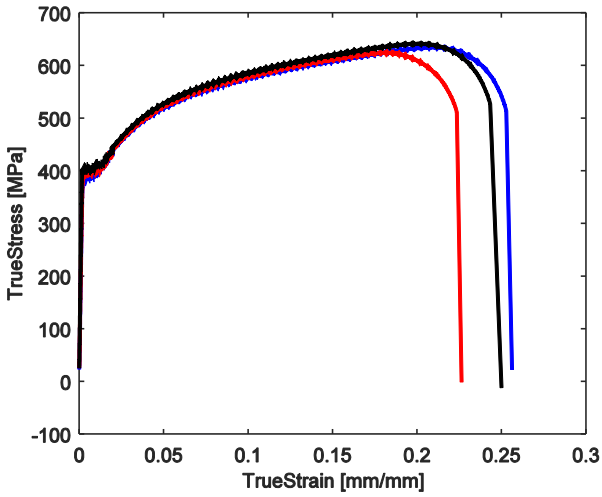

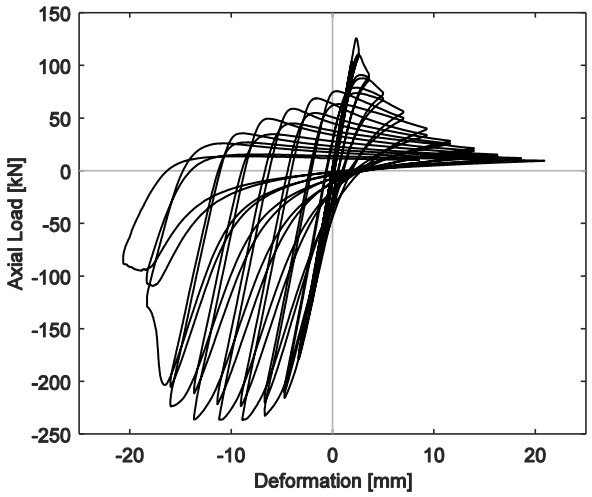
Axial Load [kN]
Deformation [mm]

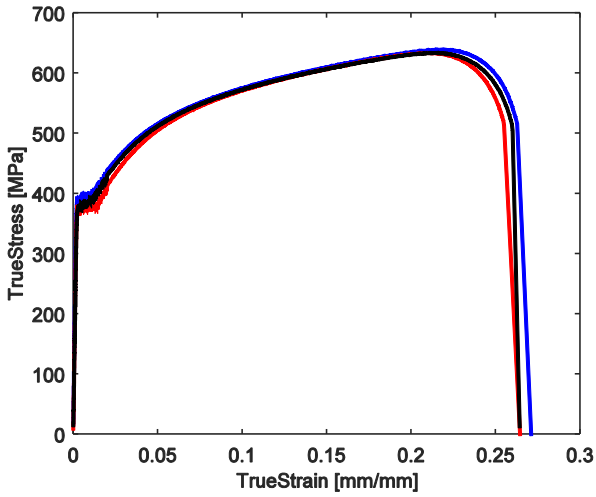
TrueStress [MPa]
TrueStrain [mm/mm]

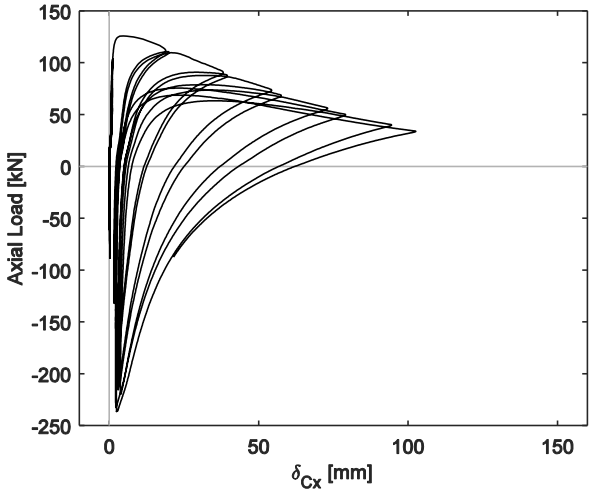
Axial Load [kN]
δCx [mm]

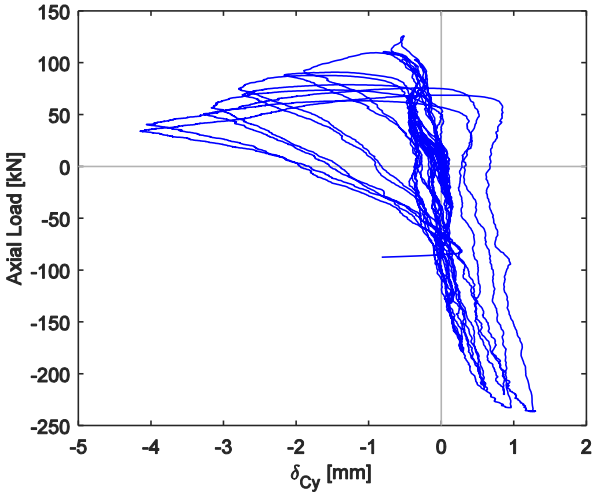
Axial Load [kN]
δCy [mm]

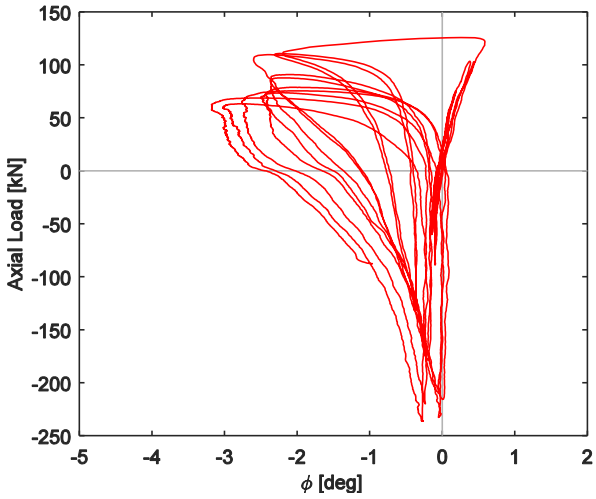
Axial Load [kN]
ϕ [deg]

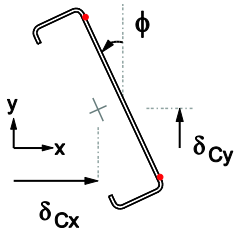
ϕ
y
x
δCy
δCx

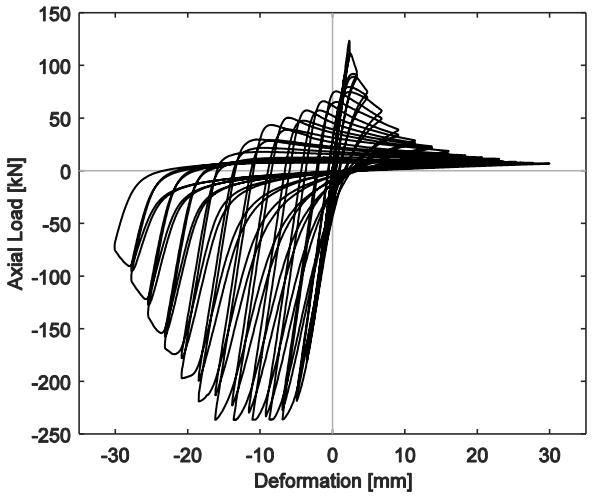
Axial Load [kN]
Deformation [mm]

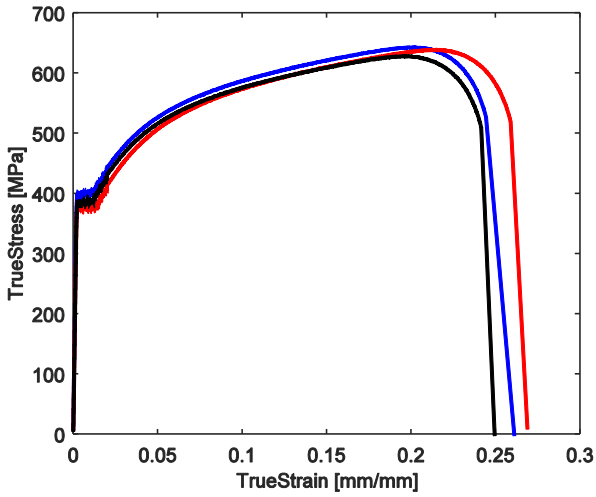
TrueStress [MPa]
TrueStrain [mm/mm]

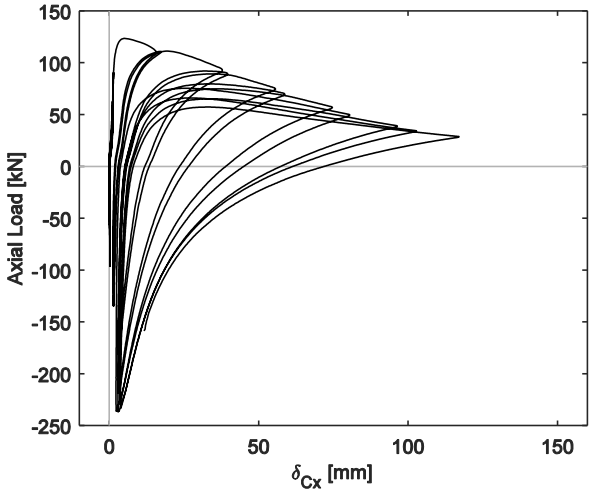
Axial Load [kN]
δCx [mm]

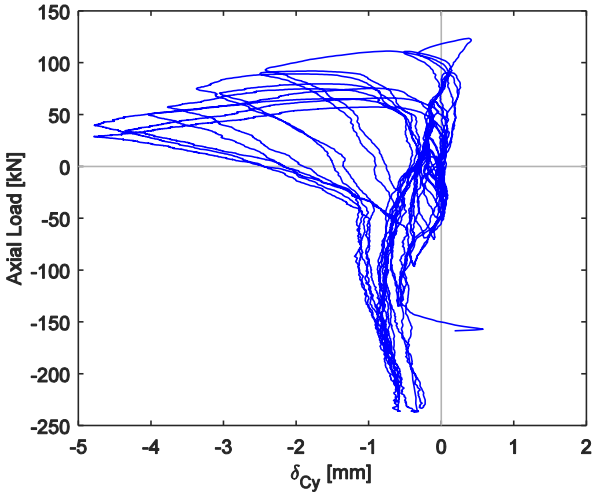
Axial Load [kN]
δCy [mm]

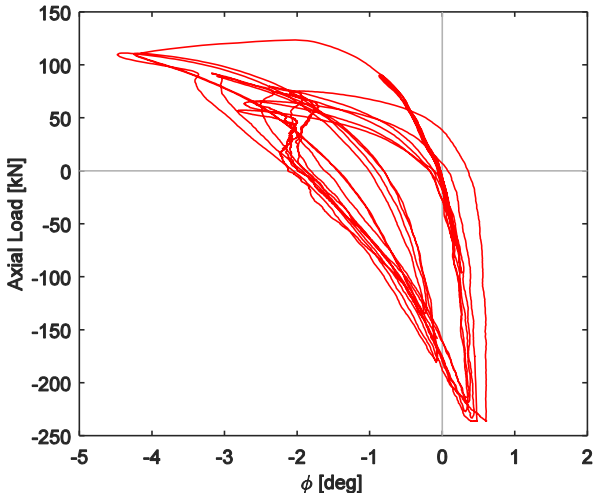
Axial Load [kN]
ϕ [deg]

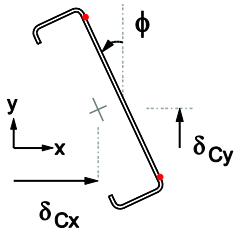
ϕ
y
x
δCy
δCx

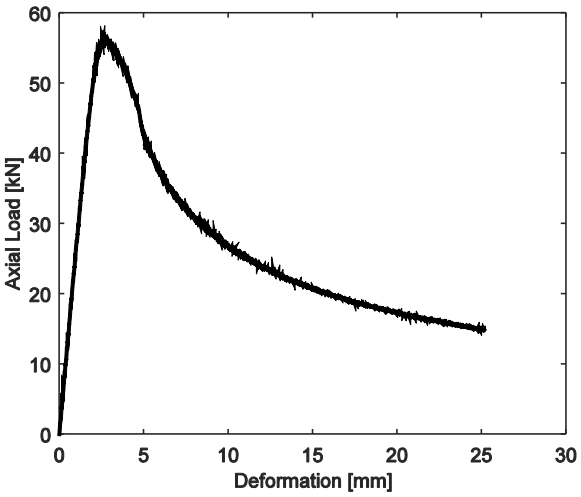
Axial Load [kN]
Deformation [mm]
0
10
20
30
40
50
60
0
5
10
15
20
25
30

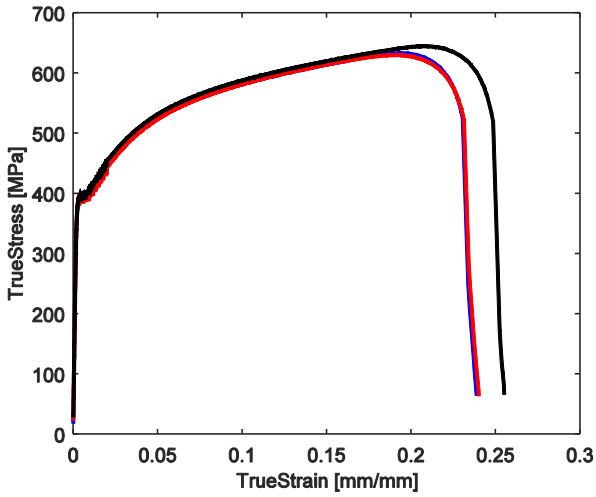
TrueStress [MPa]
TrueStrain [mm/mm]
0
100
200
300
400
500
600
700
0
0.05
0.1
0.15
0.2
0.25
0.3

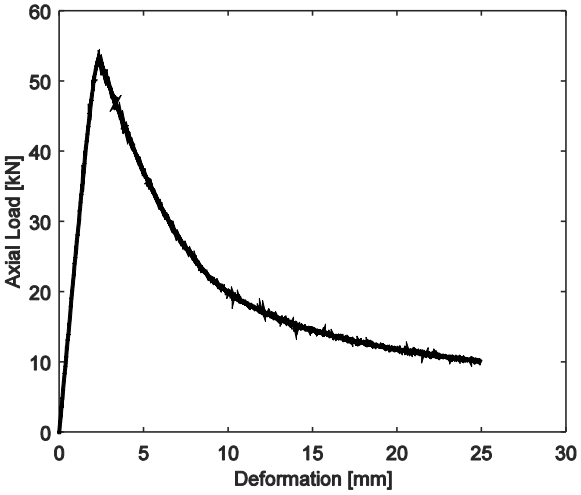
Axial Load [kN]
Deformation [mm]

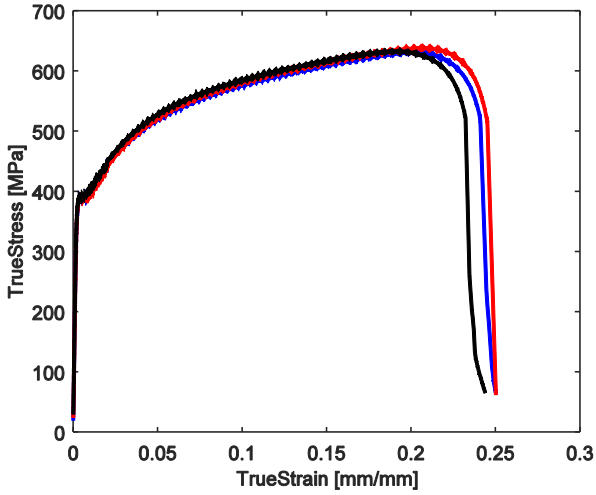
TrueStress [MPa]
TrueStrain [mm/mm]

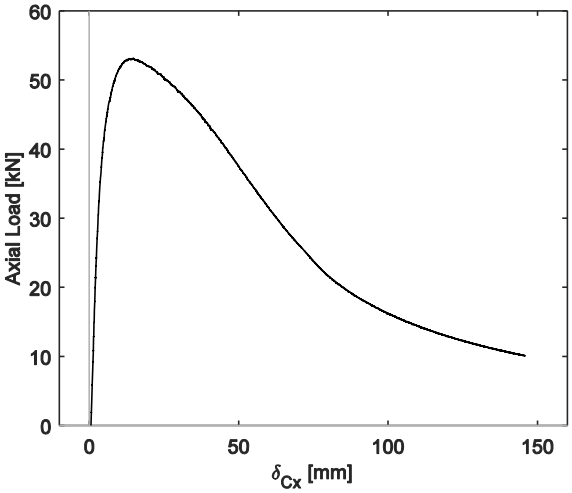
Axial Load [kN]
δCx [mm]

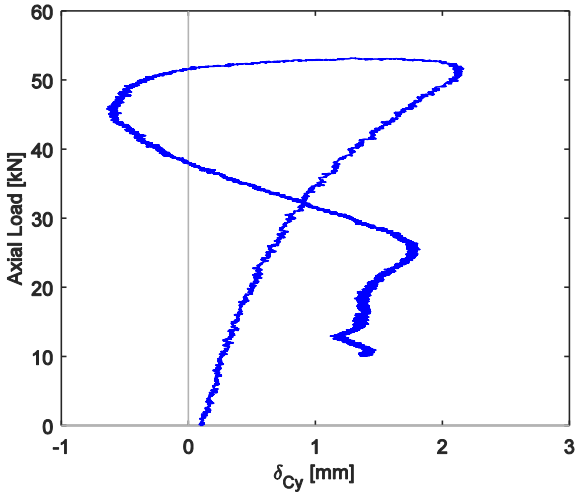
Axial Load [kN]
δCy [mm]

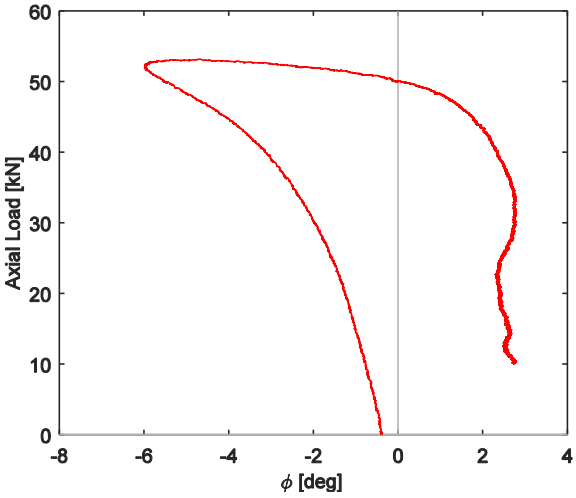
Axial Load [kN]
ϕ [deg]

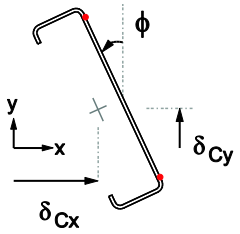
ϕ
y
x
δCy
δCx

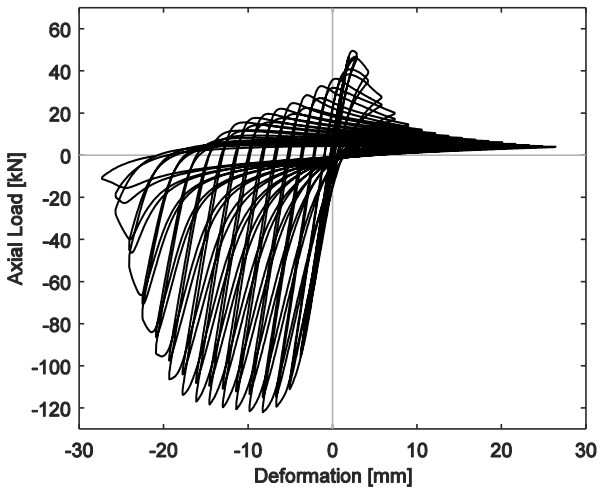
Axial Load [kN]
Deformation [mm]

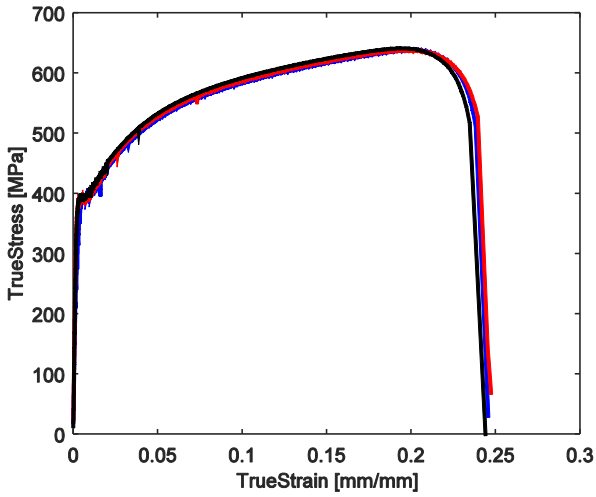
TrueStress [MPa]
TrueStrain [mm/mm]

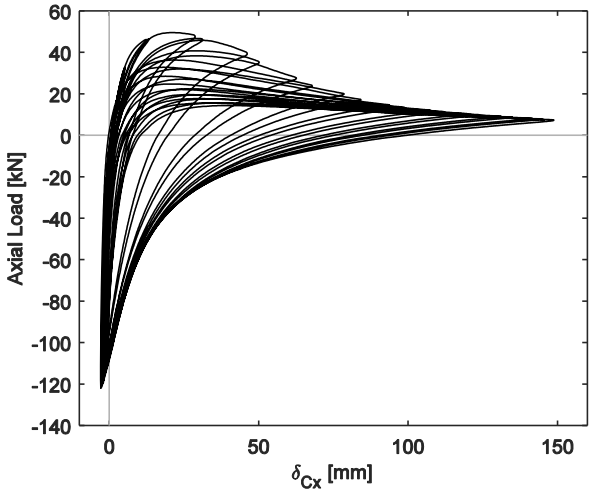
Axial Load [kN]
δCx [mm]

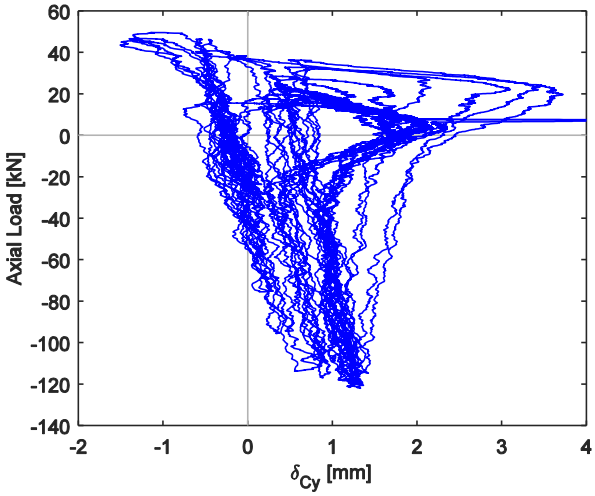
Axial Load [kN]
δCy [mm]

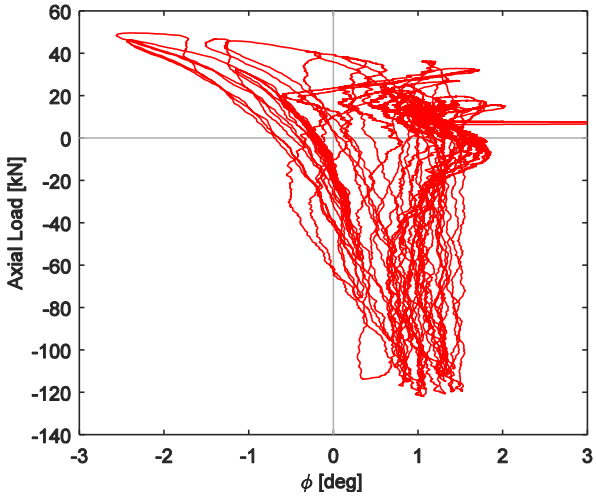
Axial Load [kN]
ϕ [deg]

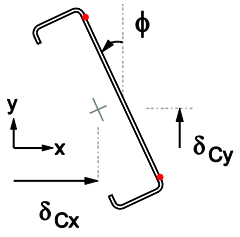
ϕ
y
x
δCy
δCx

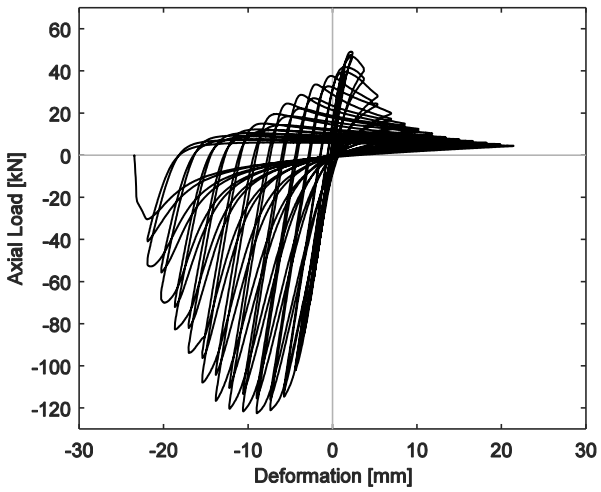
Axial Load [kN]
Deformation [mm]
60
40
20
0
-20
-40
-60
-80
-100
-120
-30
-20
-10
0
10
20
30

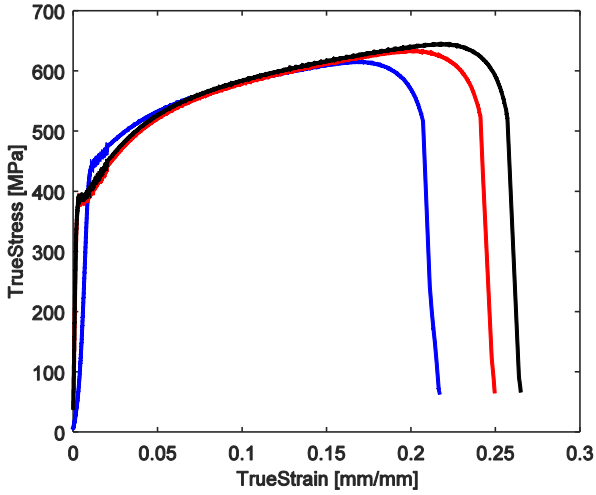
TrueStress [MPa]
TrueStrain [mm/mm]
700
600
500
400
300
200
100
0
0
0.05
0.1
0.15
0.2
0.25
0.3

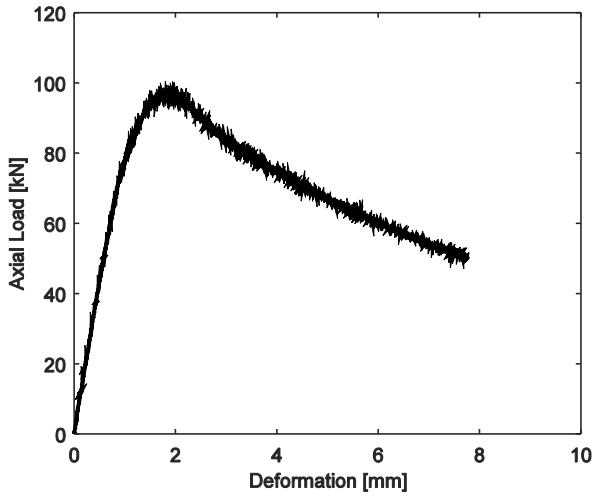
Axial Load [kN]
Deformation [mm]

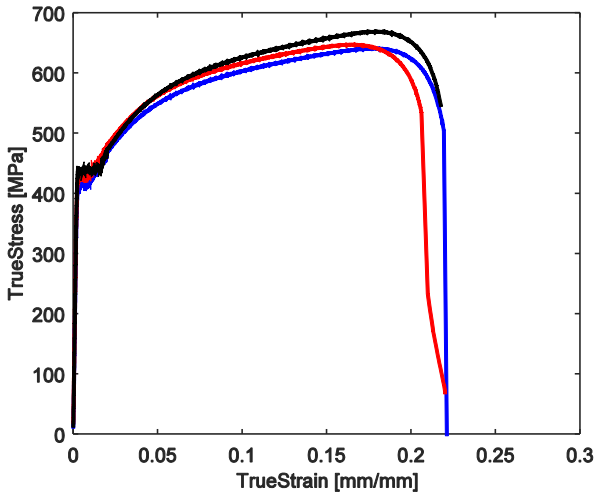
TrueStress [MPa]
TrueStrain [mm/mm]

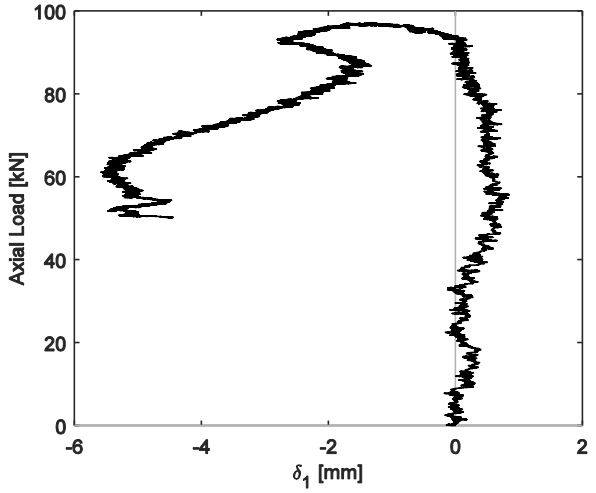
Axial Load [kN]
δ1 [mm]

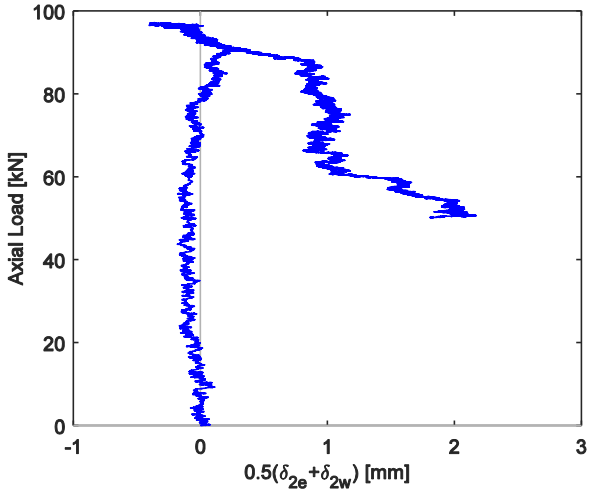
Axial Load [kN]
0.5(δ2e+δ2w) [mm]

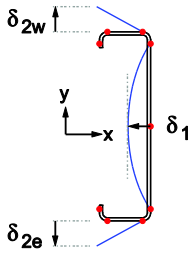
δ2w
y
x
δ1
δ2e

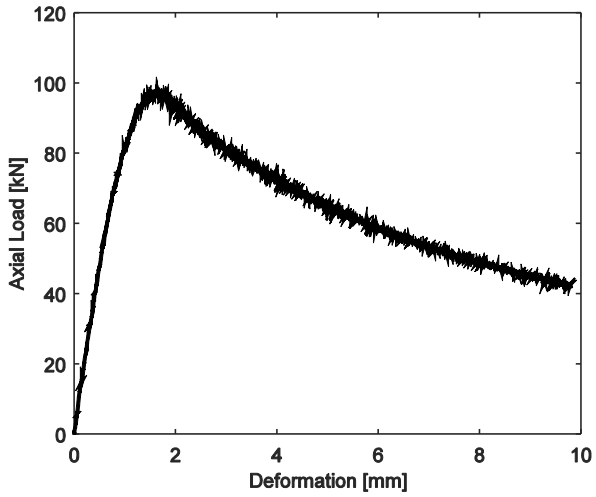
Axial Load [kN]
Deformation [mm]

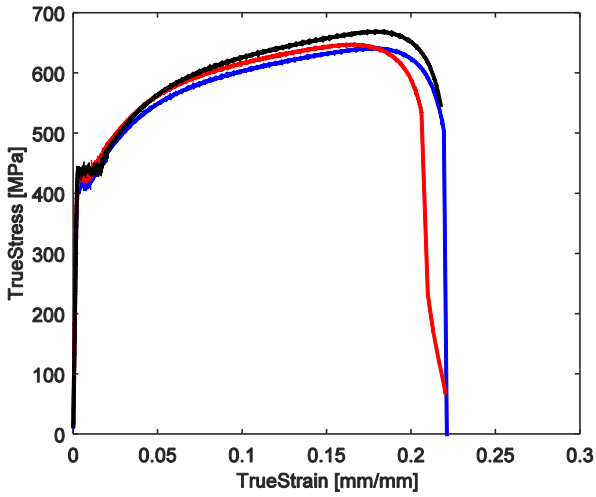
TrueStress [MPa]
TrueStrain [mm/mm]

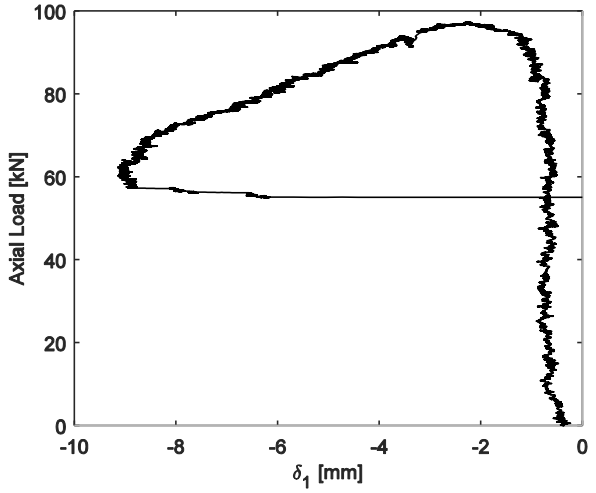
Axial Load [kN]
δ1 [mm]

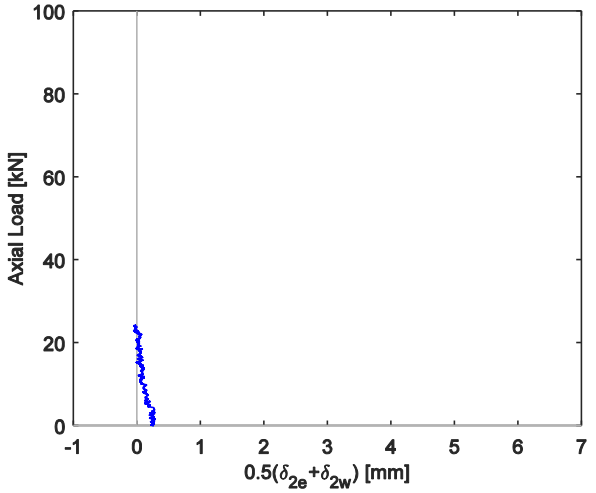
Axial Load [kN]
0.5(δ2e+δ2w) [mm]

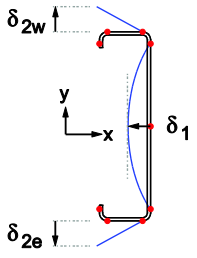
δ2w
y
x
δ1
δ2e

600S137-68-DAC-1

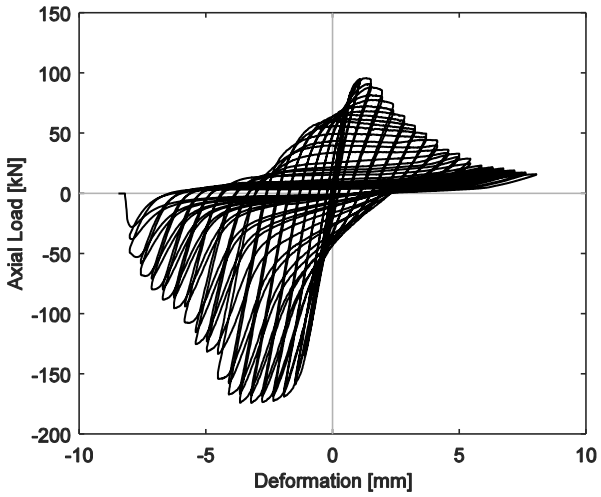

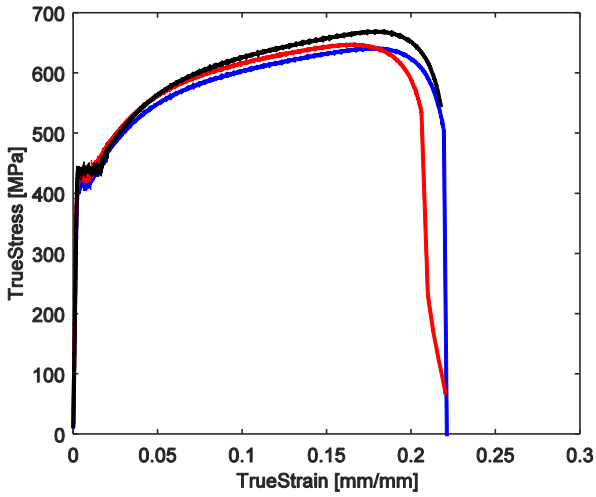

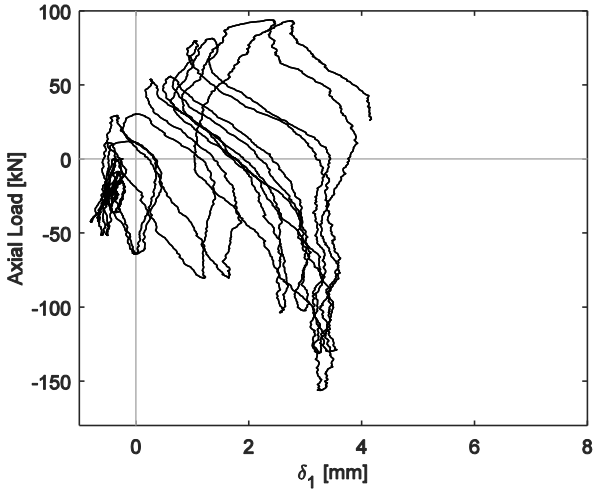

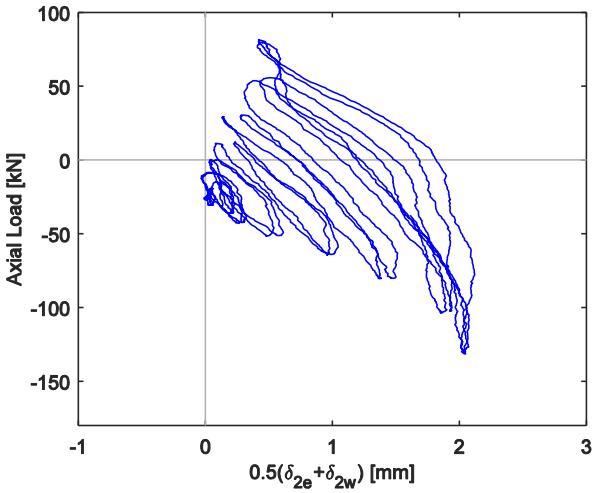

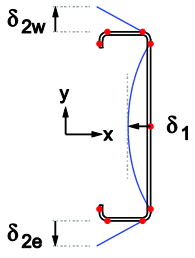

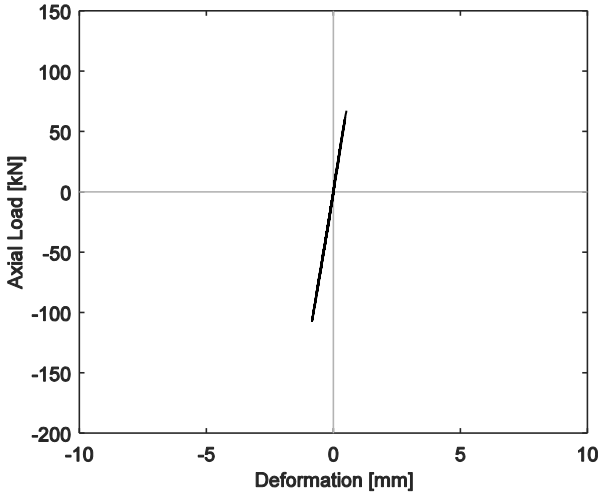
Axial Load [kN]
Deformation [mm]

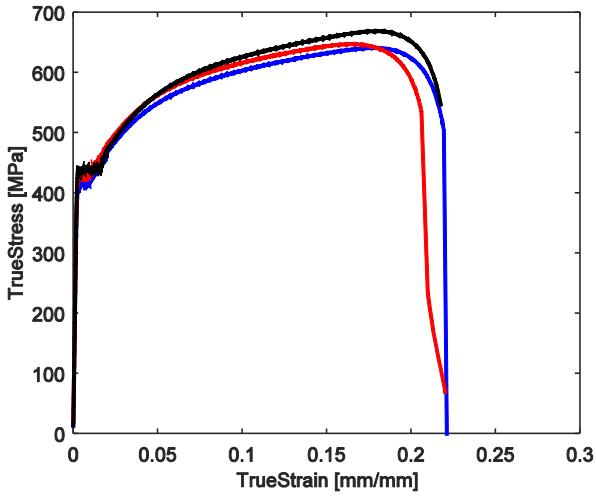
TrueStress [MPa]
TrueStrain [mm/mm]

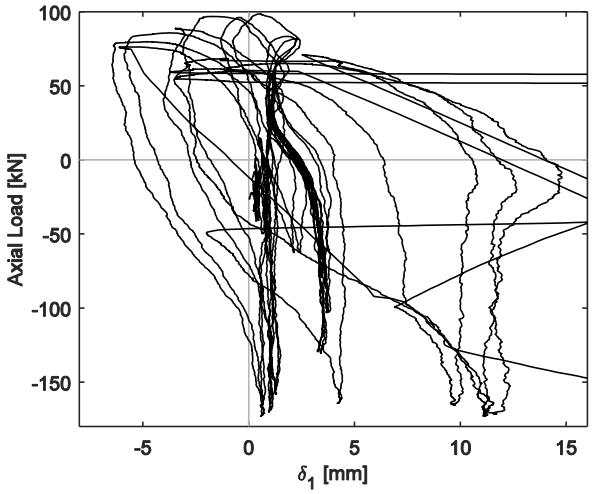
Axial Load [kN]
δ1 [mm]

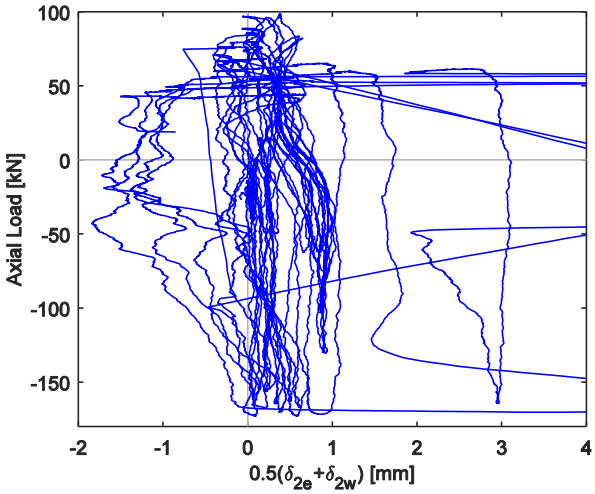
Axial Load [kN]
0.5(δ2e+δ2w) [mm]

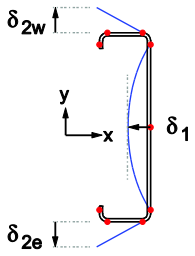
δ2w
y
x
δ1
δ2e

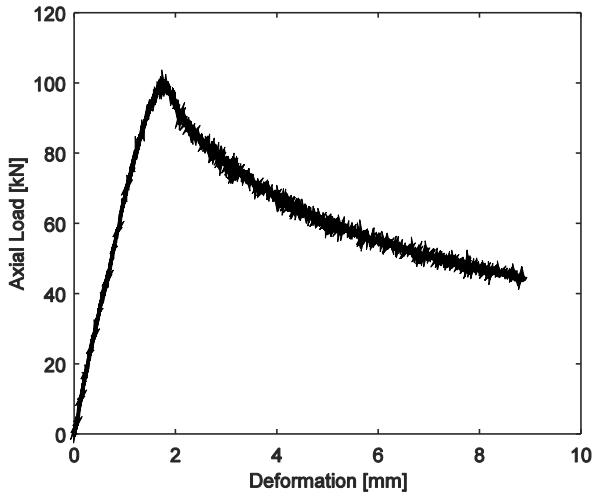
Axial Load [kN]
Deformation [mm]

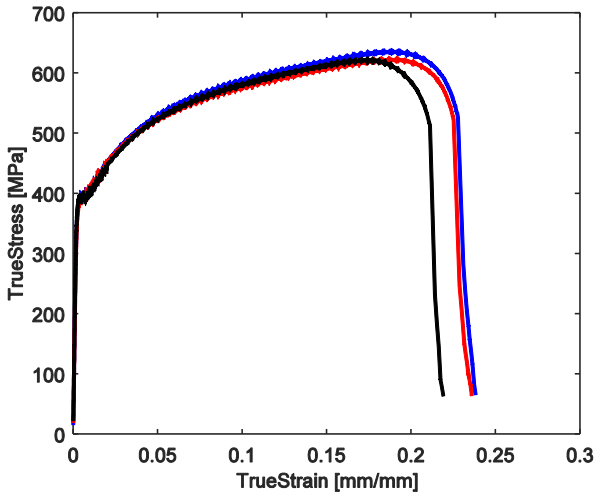
TrueStress [MPa]
TrueStrain [mm/mm]

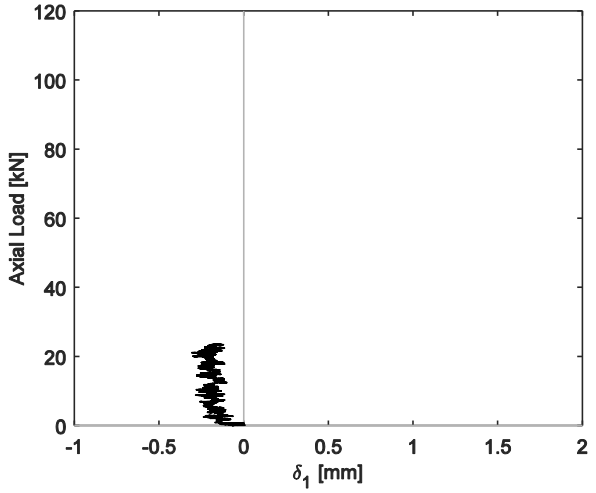
Axial Load [kN]
δ1 [mm]

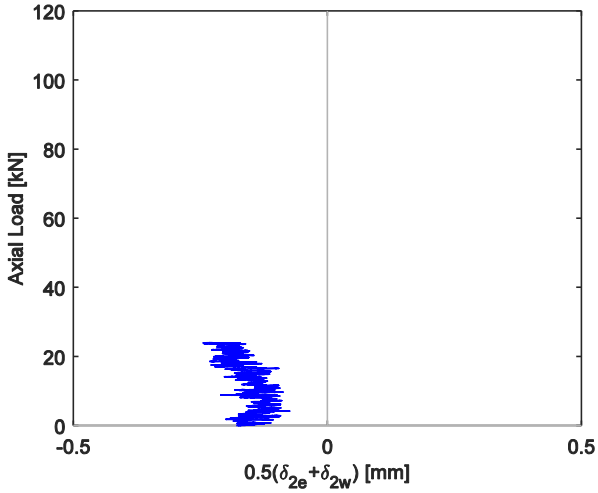
Axial Load [kN]
0.5(δ2e+δ2w) [mm]

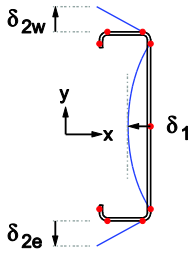
δ2w
y
x
δ1
δ2e

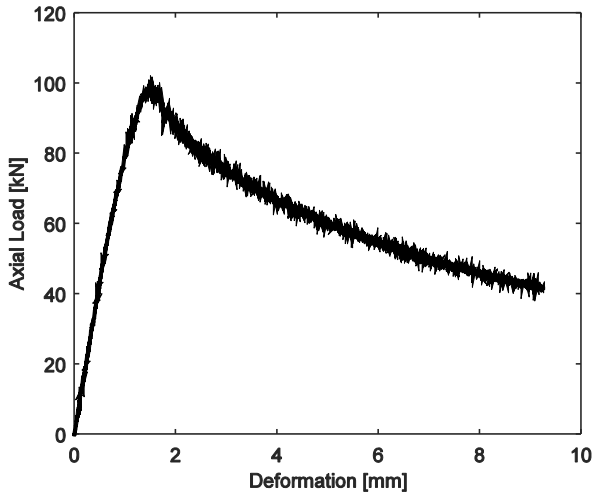
Axial Load [kN]
Deformation [mm]

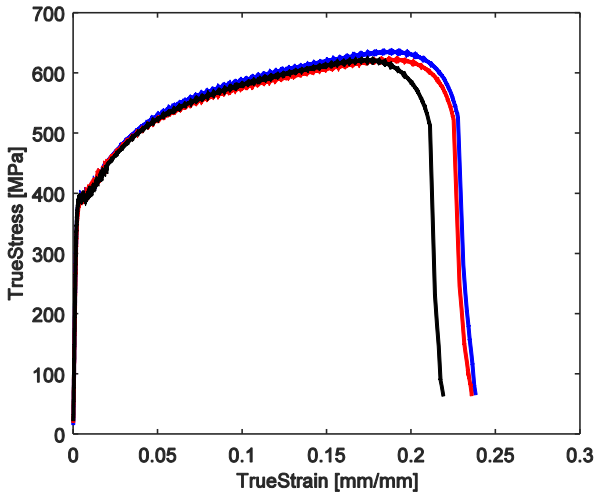
TrueStress [MPa]
TrueStrain [mm/mm]

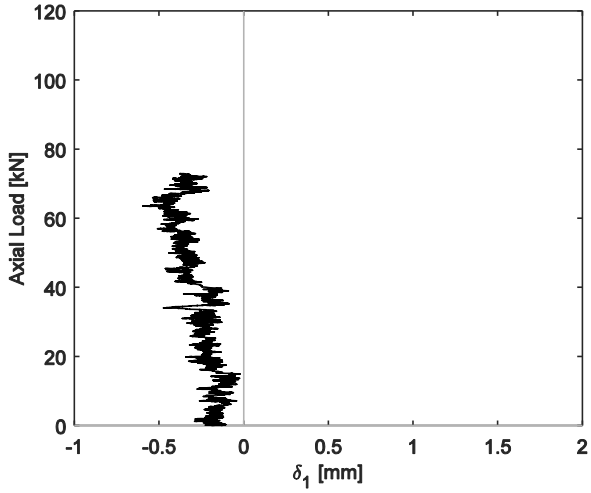
Axial Load [kN]
δ1 [mm]

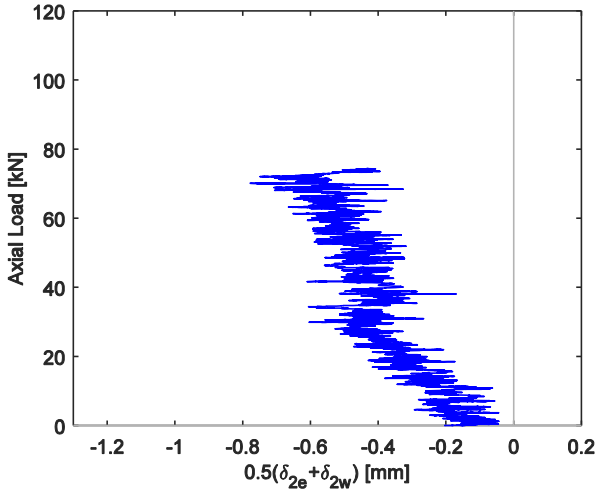
Axial Load [kN]
0.5(δ2e+δ2w) [mm]

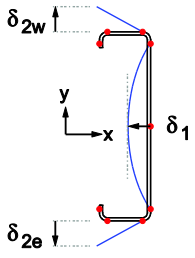
δ2w
y
x
δ1
δ2e

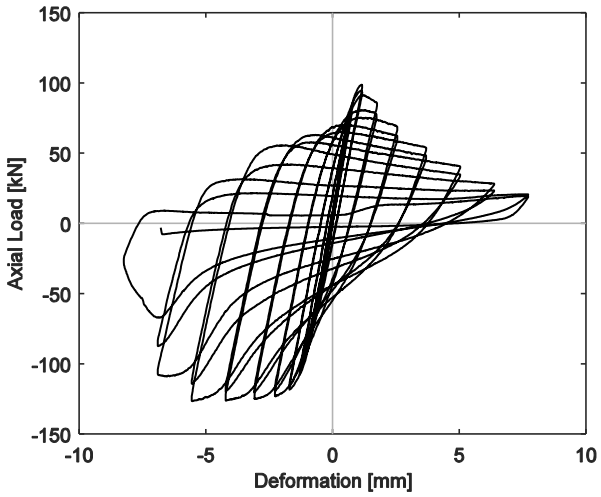
Axial Load [kN]
Deformation [mm]

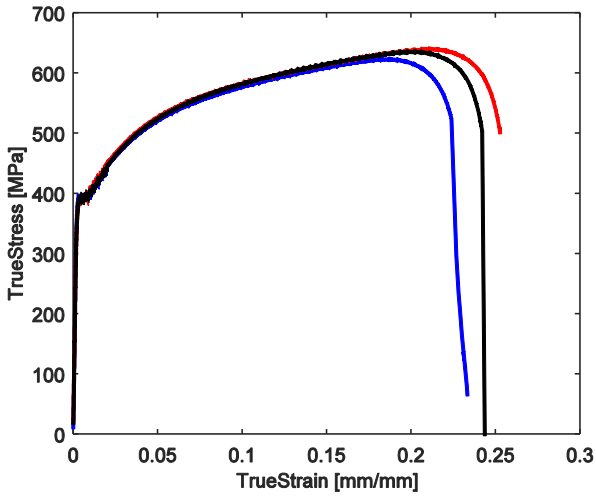
TrueStress [MPa]
TrueStrain [mm/mm]

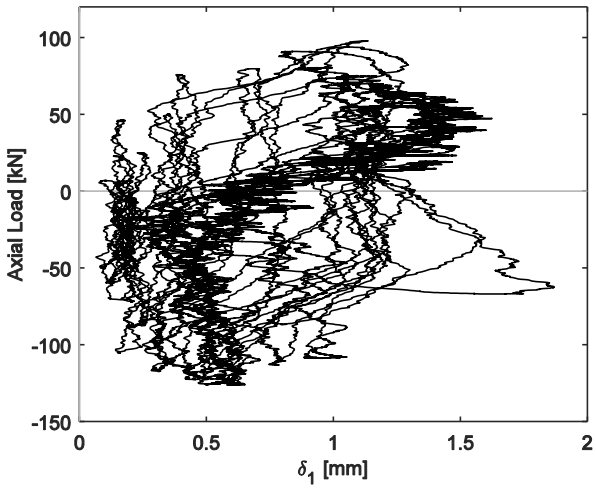
Axial Load [kN]
δ1 [mm]

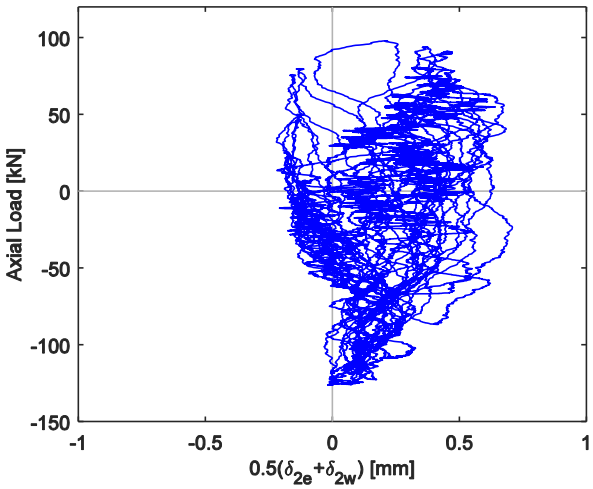
Axial Load [kN]
0.5(δ2e+δ2w) [mm]

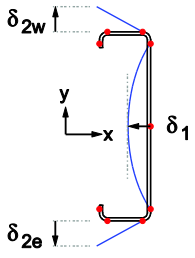
δ2w
y
x
δ1
δ2e

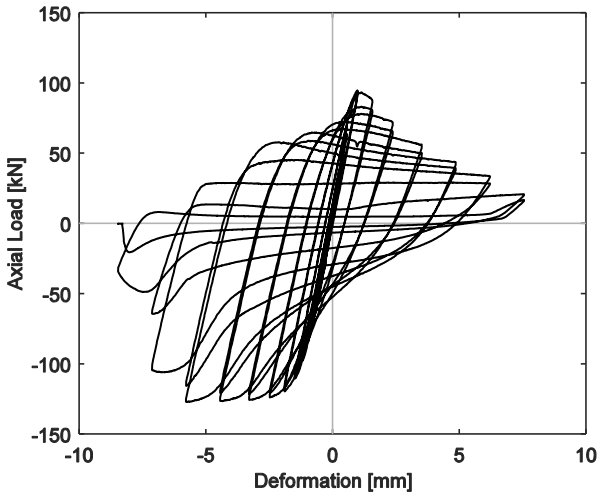
Axial Load [kN]
Deformation [mm]

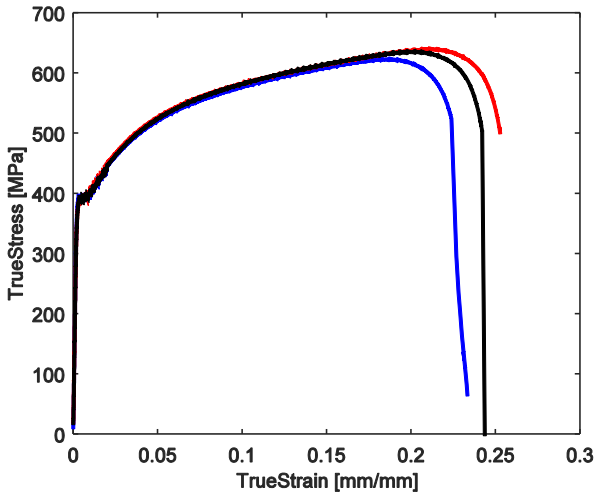
TrueStress [MPa]
TrueStrain [mm/mm]

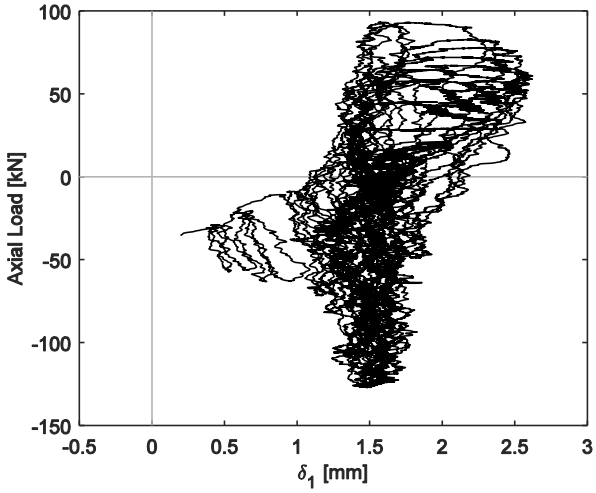
Axial Load [kN]
δ1 [mm]

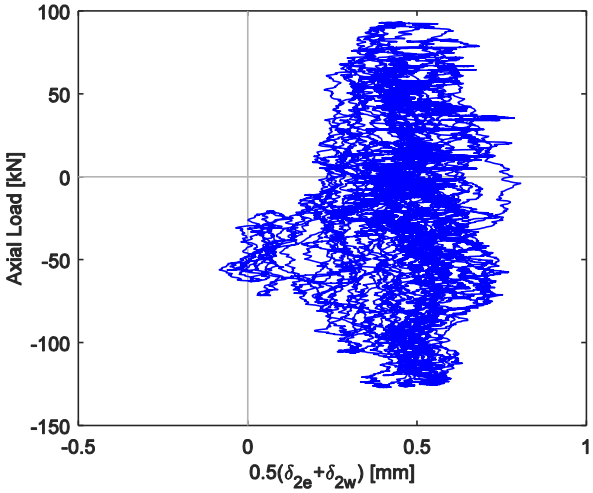
Axial Load [kN]
0.5(δ2e+δ2w) [mm]

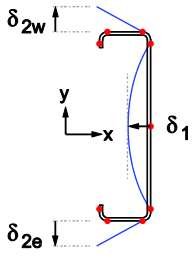
δ2w
y
x
δ1
δ2e

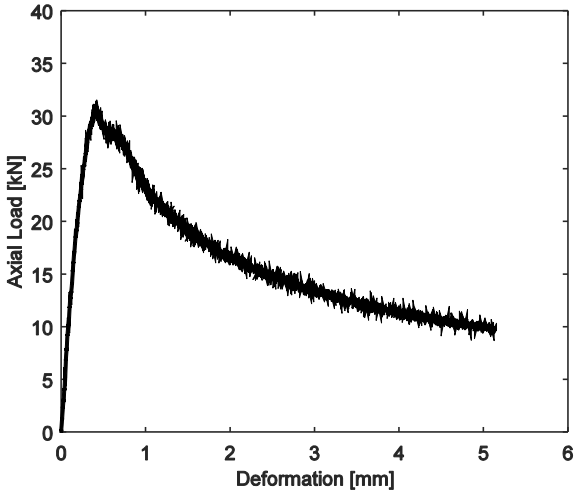
Axial Load [kN]
Deformation [mm]

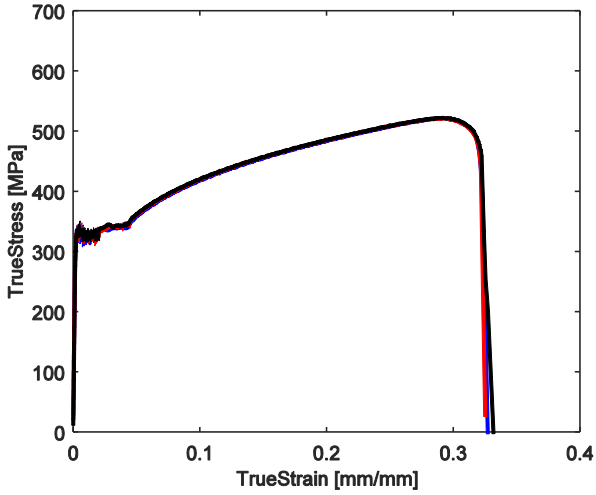
TrueStress [MPa]
TrueStrain [mm/mm]

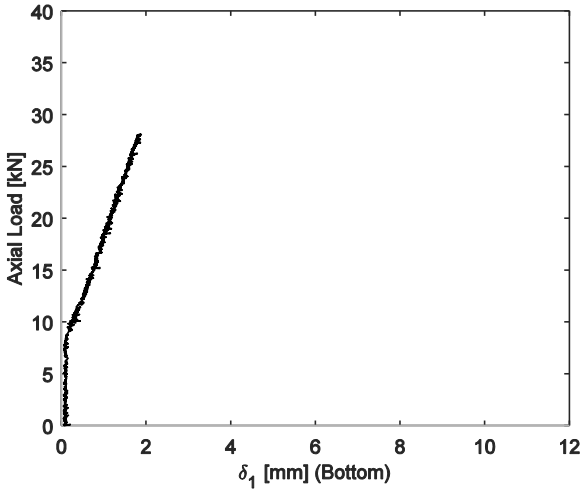
Axial Load [kN]
δ1 [mm] (Bottom)

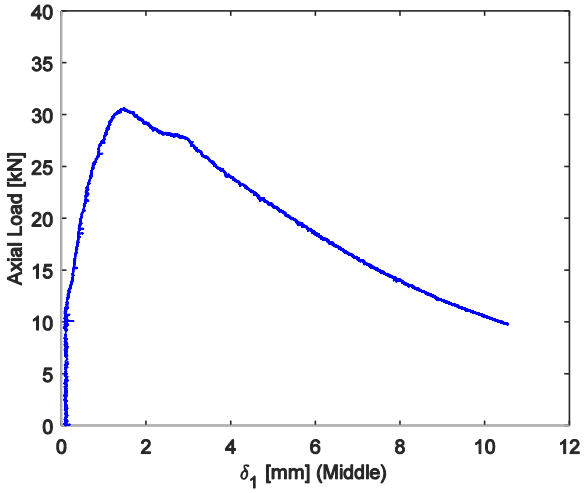
Axial Load [kN]
δ1 [mm] (Middle)

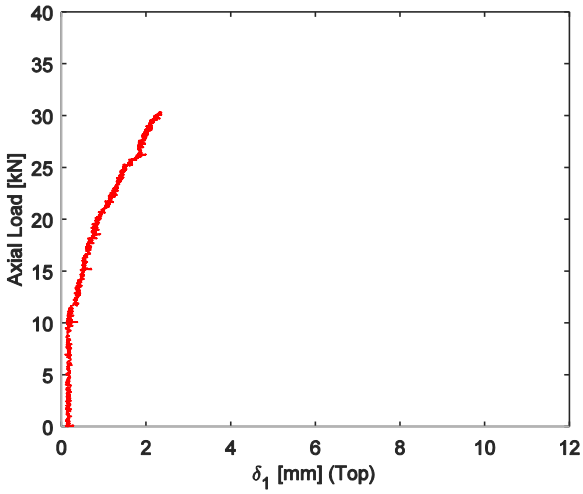
Axial Load [kN]
δ1 [mm] (Top)

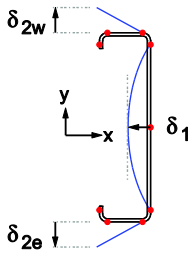
δ2w
y
x
δ1
δ2e

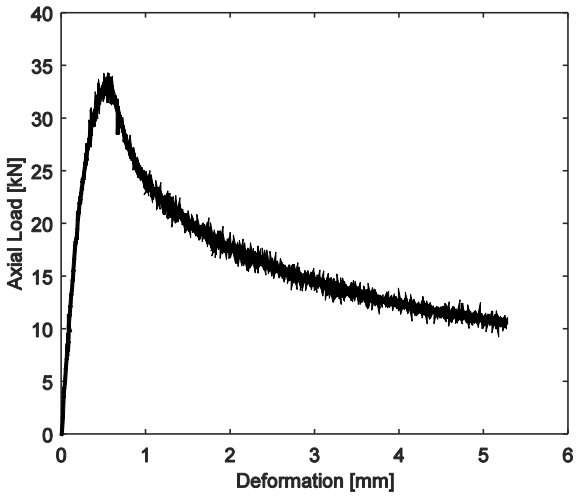
Axial Load [kN]
Deformation [mm]

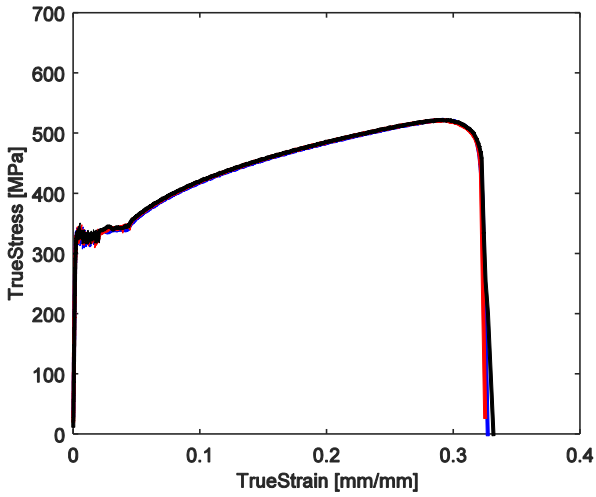
TrueStress [MPa]
TrueStrain [mm/mm]

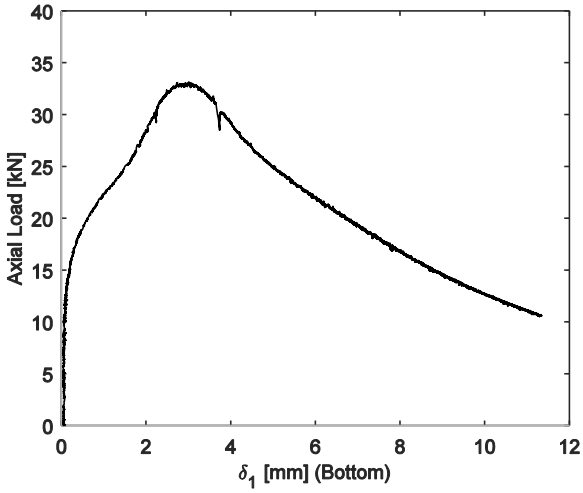
Axial Load [kN]
δ1 [mm] (Bottom)

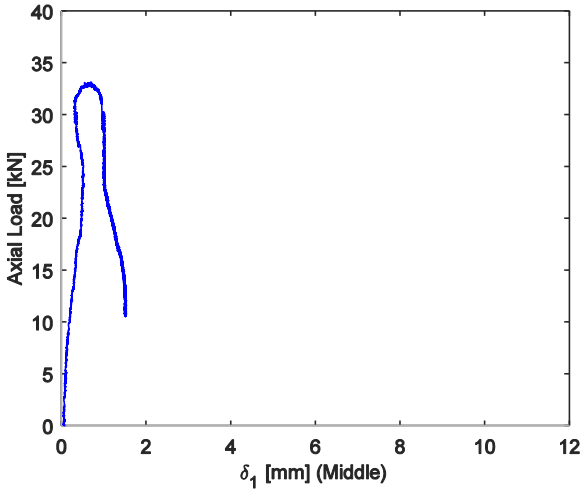
Axial Load [kN]
δ1 [mm] (Middle)

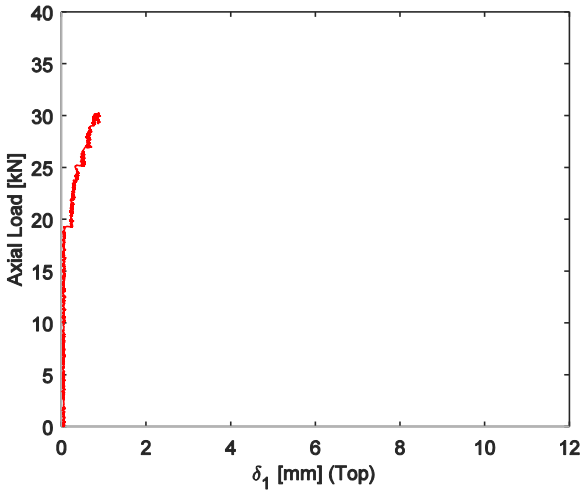
Axial Load [kN]
δ1 [mm] (Top)

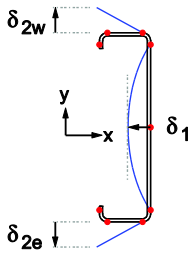
δ2w
y
x
δ1
δ2e

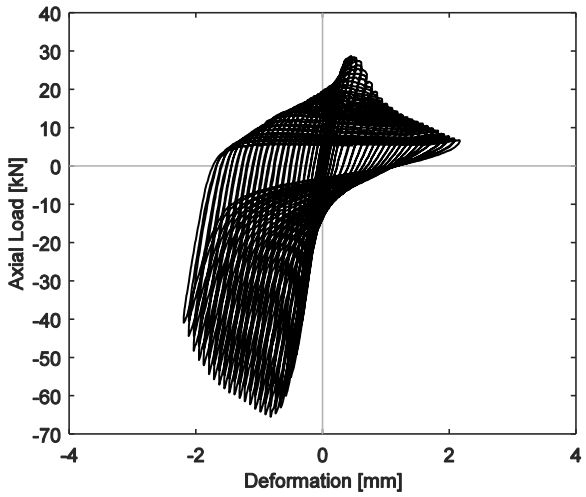
Axial Load [kN]
Deformation [mm]

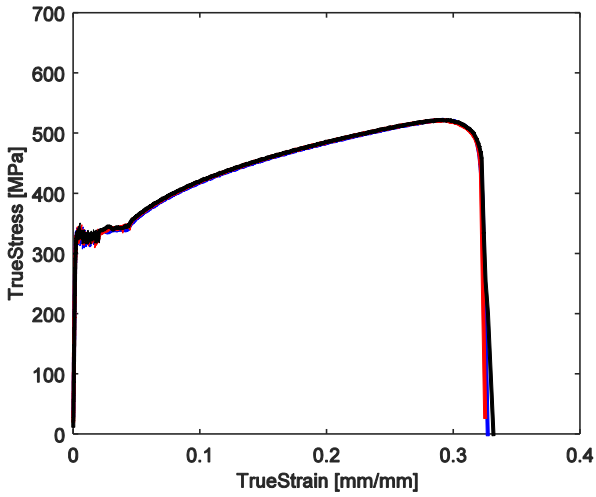
TrueStress [MPa]
TrueStrain [mm/mm]

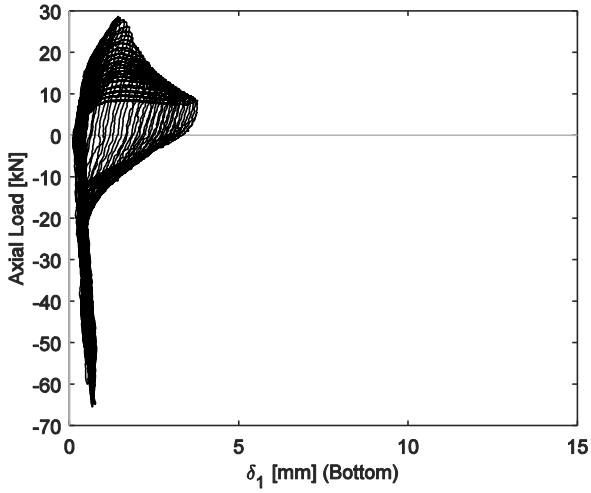
Axial Load [kN]
δ1 [mm] (Bottom)

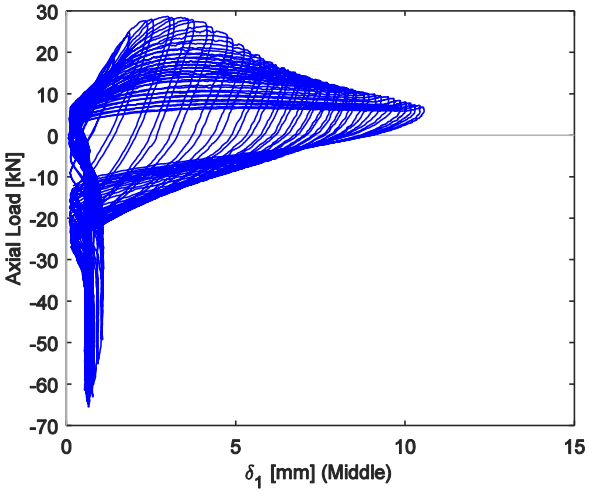
Axial Load [kN]
δ1 [mm] (Middle)

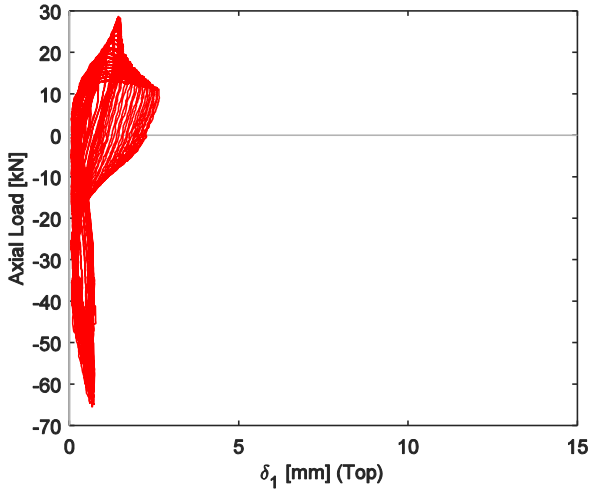
Axial Load [kN]
δ1 [mm] (Top)

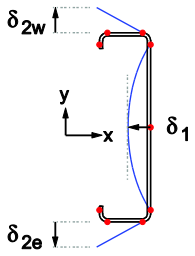
δ2w
y
x
δ1
δ2e

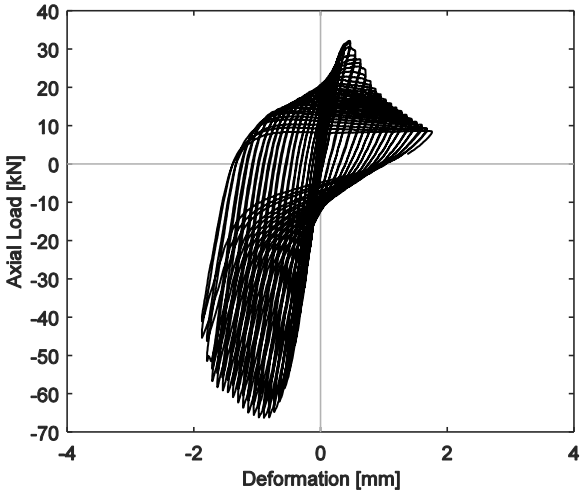
Axial Load [kN]
Deformation [mm]

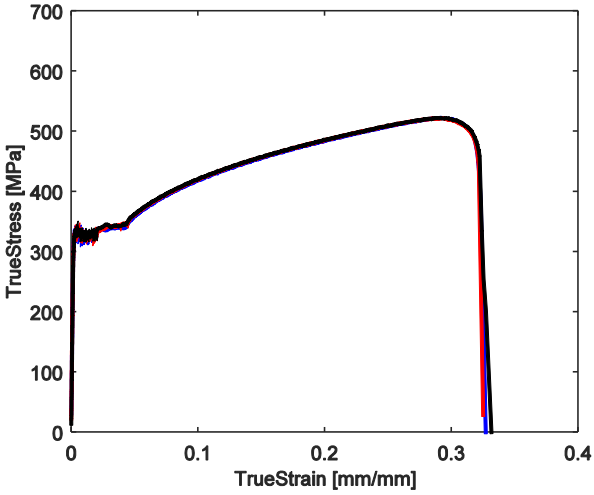
TrueStress [MPa]
TrueStrain [mm/mm]

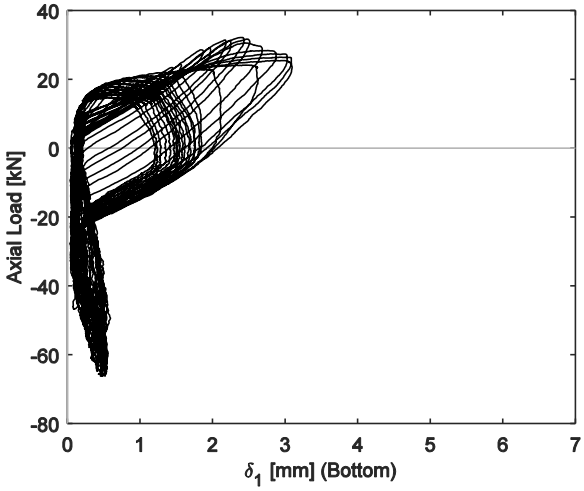
Axial Load [kN]
δ1 [mm] (Bottom)

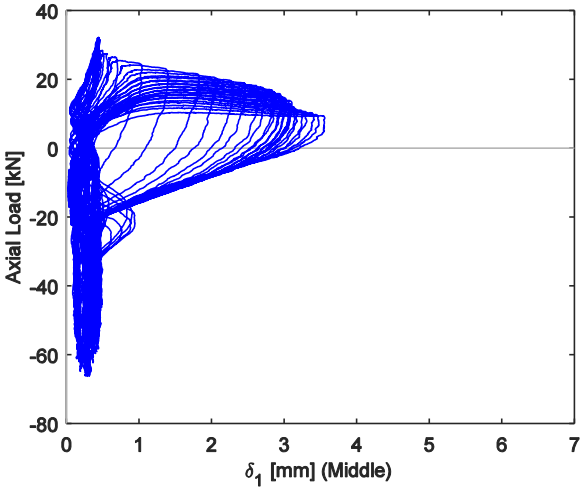
Axial Load [kN]
δ1 [mm] (Middle)

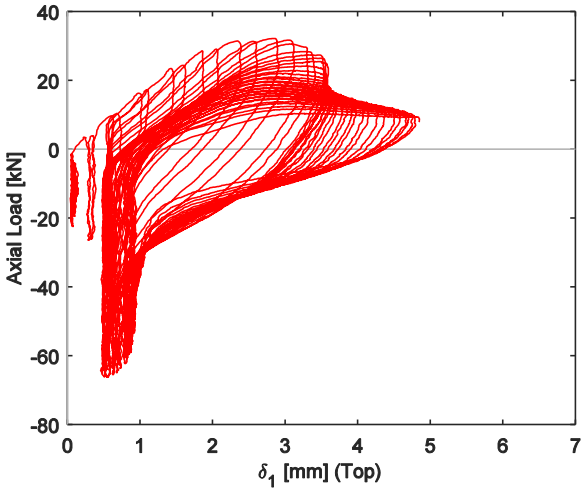
Axial Load [kN]
δ1 [mm] (Top)

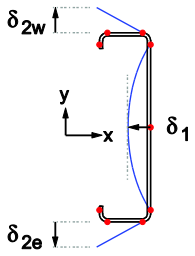
δ2w
y
x
δ1
δ2e

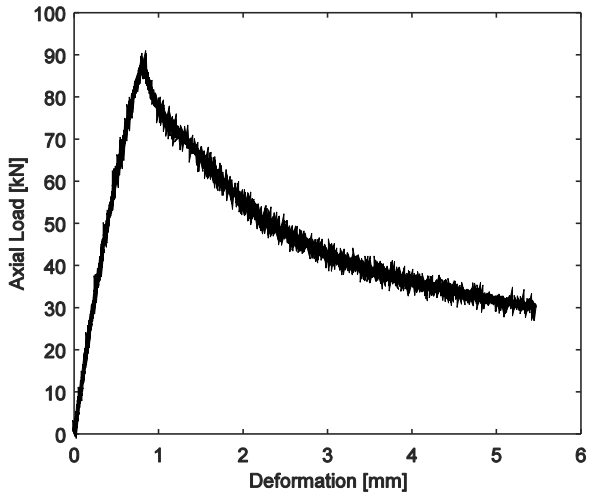
Axial Load [kN]
Deformation [mm]

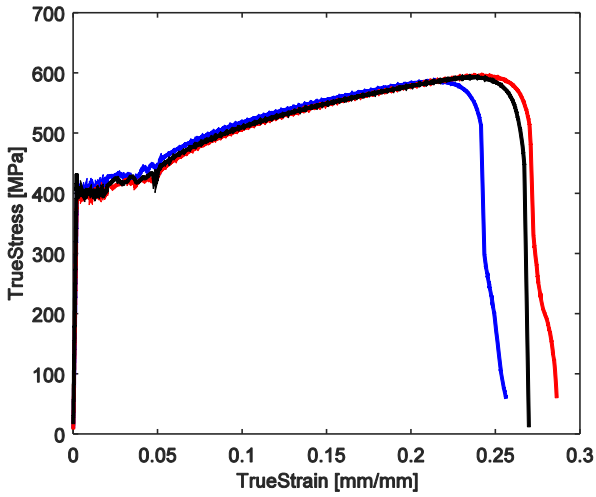
TrueStress [MPa]
TrueStrain [mm/mm]

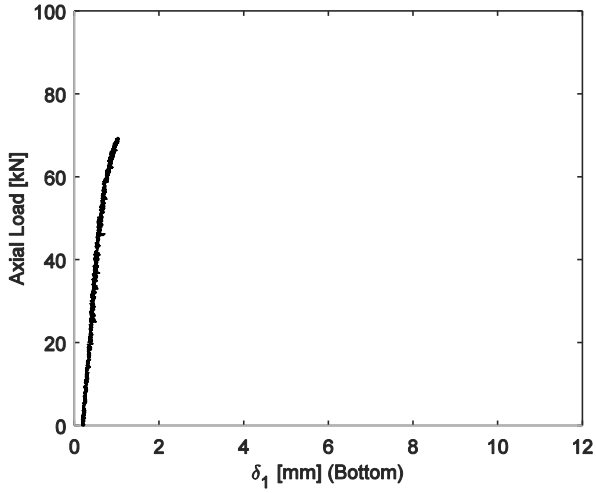
Axial Load [kN]
δ1 [mm] (Bottom)

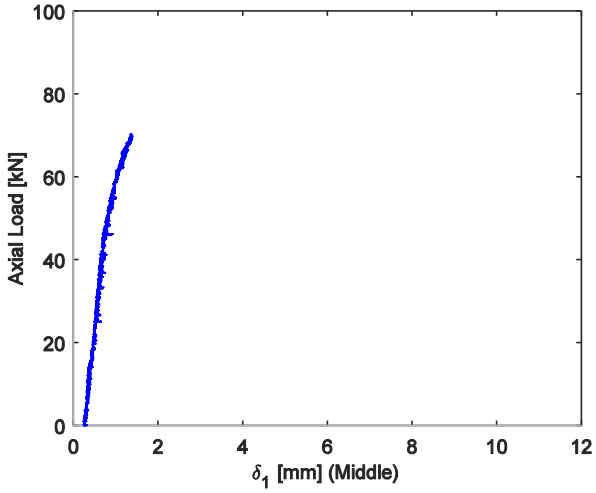
Axial Load [kN]
δ1 [mm] (Middle)

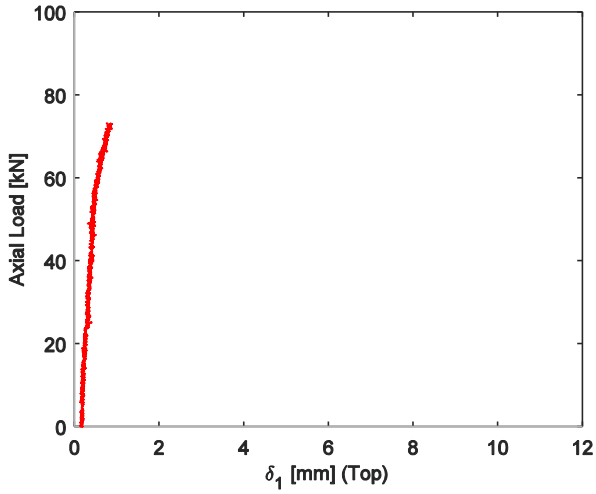
Axial Load [kN]
δ1 [mm] (Top)

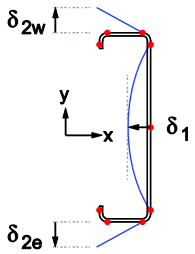
δ2w
y
x
δ1
δ2e

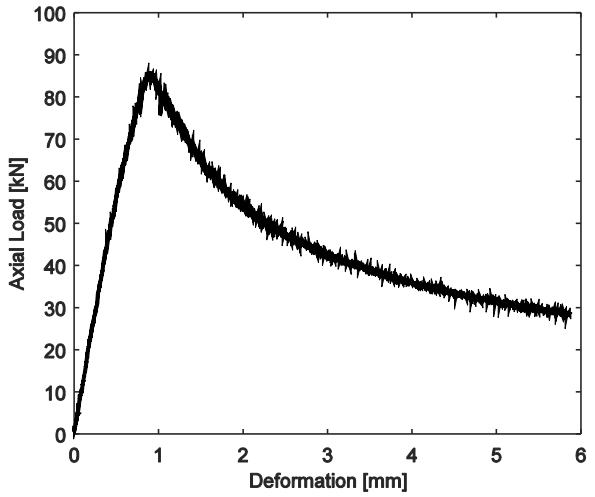
Axial Load [kN]
Deformation [mm]

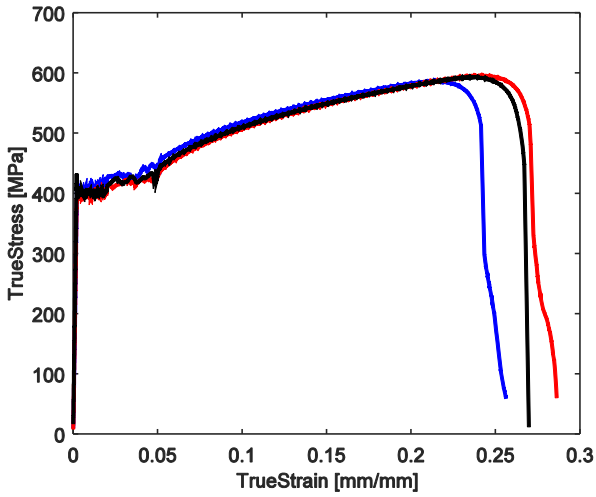
TrueStress [MPa]
TrueStrain [mm/mm]

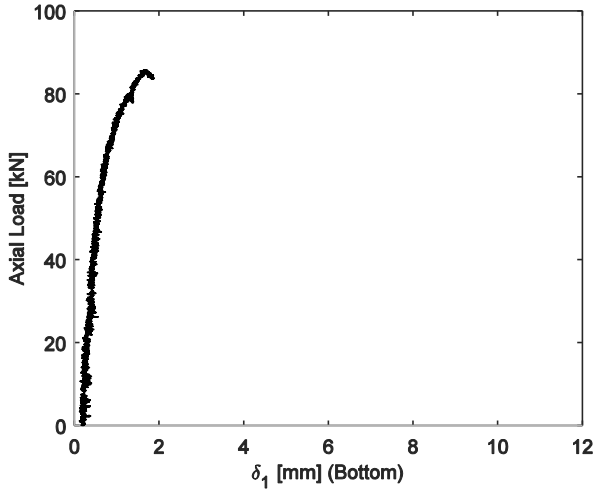
Axial Load [kN]
δ1 [mm] (Bottom)

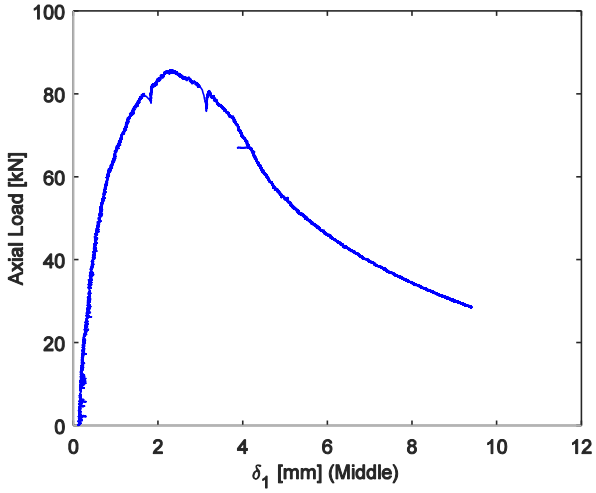
Axial Load [kN]
δ1 [mm] (Middle)

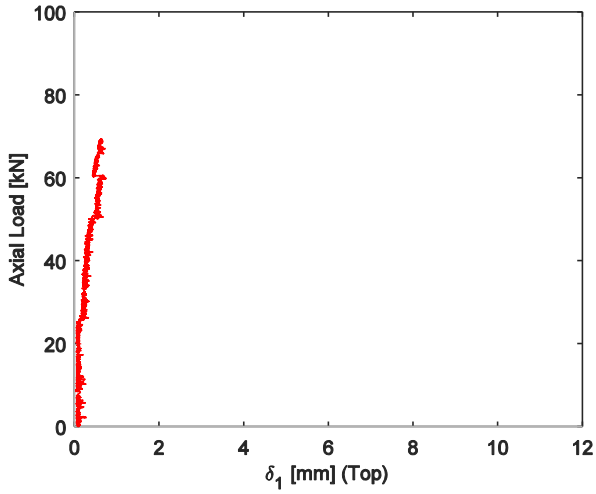
Axial Load [kN]
δ1 [mm] (Top)

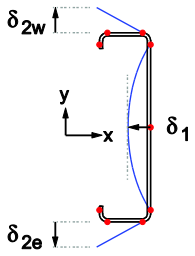
δ2w
y
x
δ1
δ2e

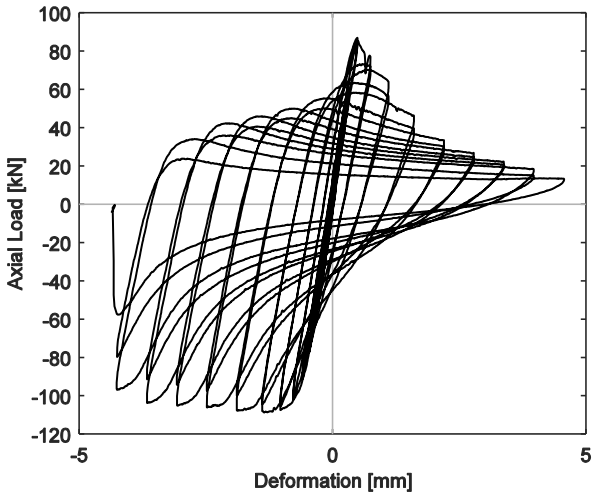
Axial Load [kN]
Deformation [mm]

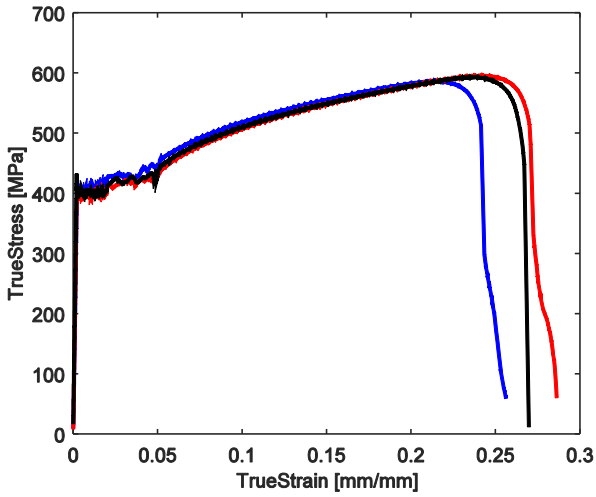
TrueStress [MPa]
TrueStrain [mm/mm]

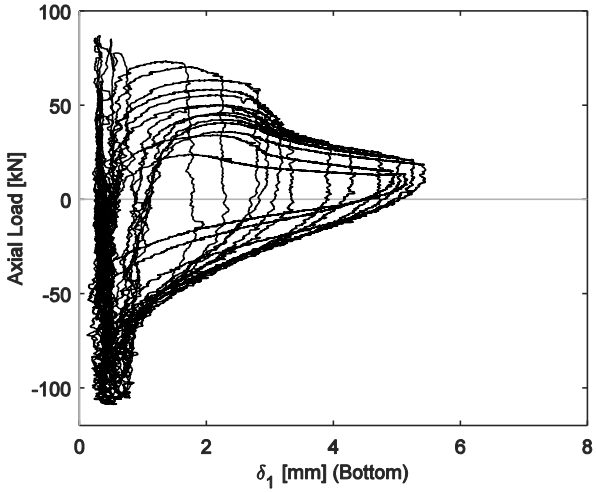
Axial Load [kN]
δ1 [mm] (Bottom)

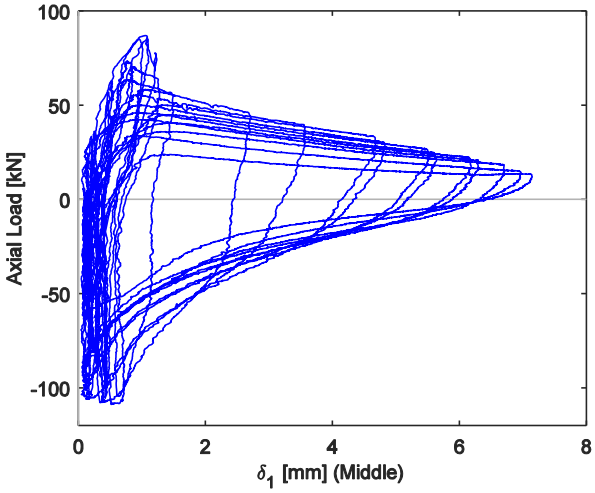
Axial Load [kN]
δ1 [mm] (Middle)

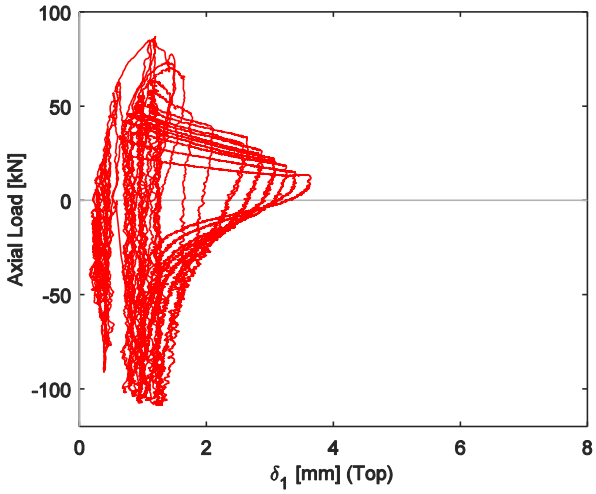
Axial Load [kN]
δ1 [mm] (Top)

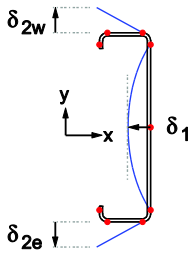
δ2w
y
x
δ1
δ2e

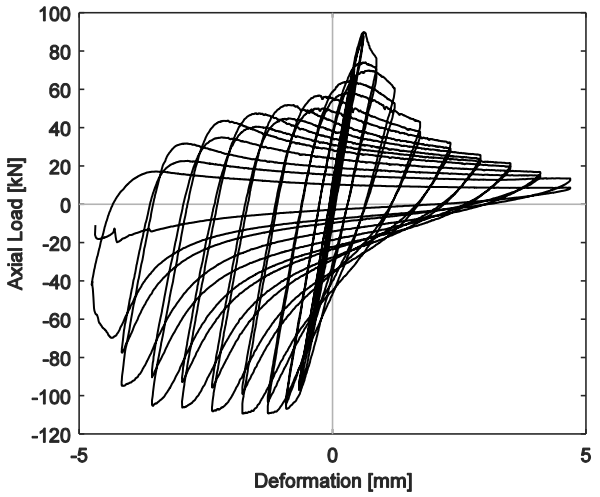
Axial Load [kN]
Deformation [mm]

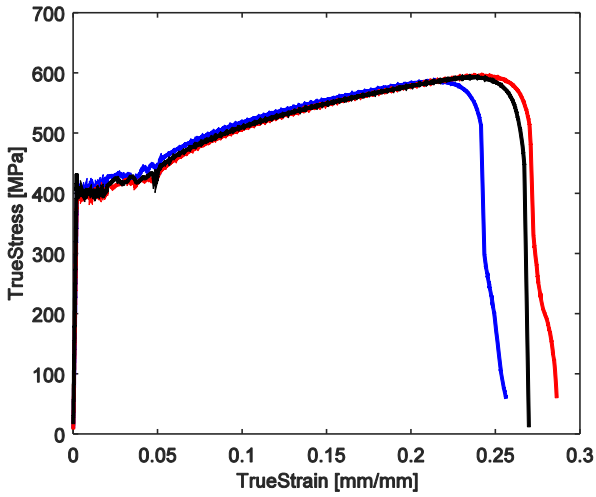
TrueStress [MPa]
TrueStrain [mm/mm]

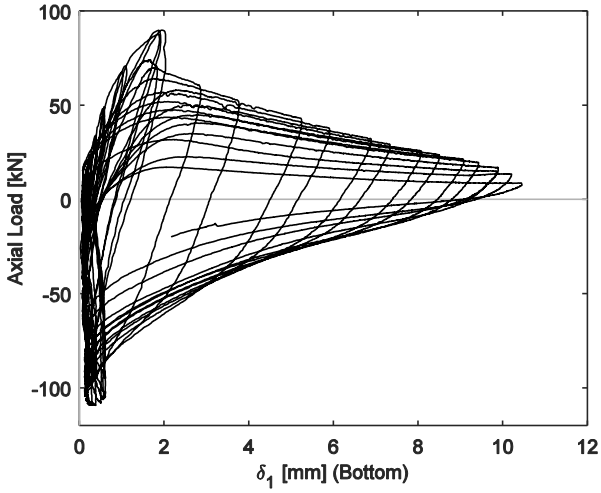
Axial Load [kN]
δ1 [mm] (Bottom)

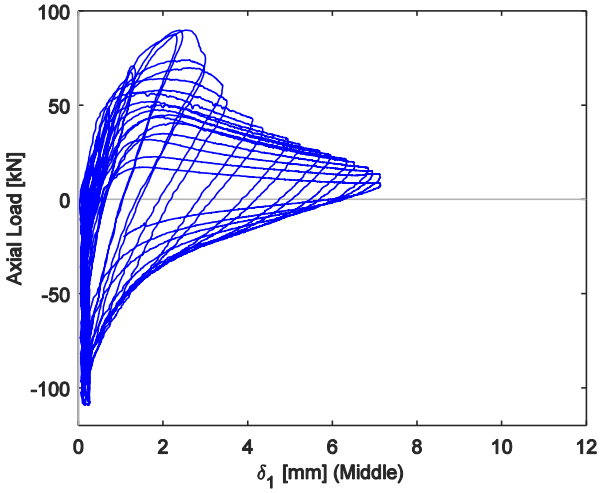
Axial Load [kN]
δ1 [mm] (Middle)

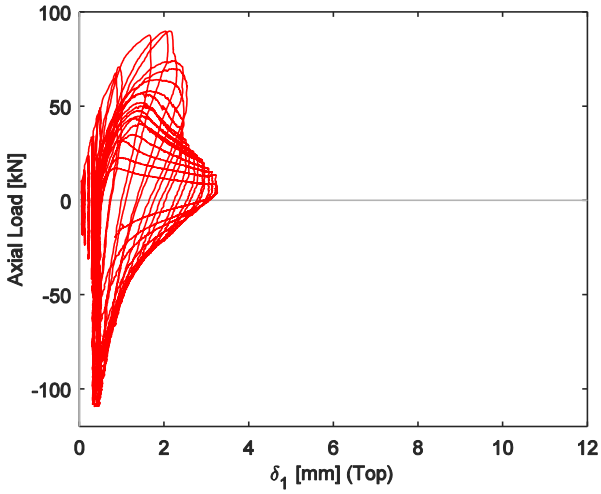
Axial Load [kN]
δ1 [mm] (Top)

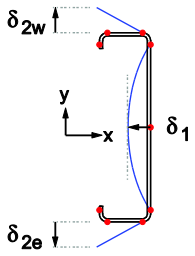
δ2w
y
x
δ1
δ2e

Appendix D Flexural Experiment Results

This appendix includes moment-rotation experimental curves for all tests in Chapter 4 accompanied by the specimen coupon tests curves, the mid-span deflection and the horizontal displacement at the supports measured with the a string potentiometer (see Fig. D.1).

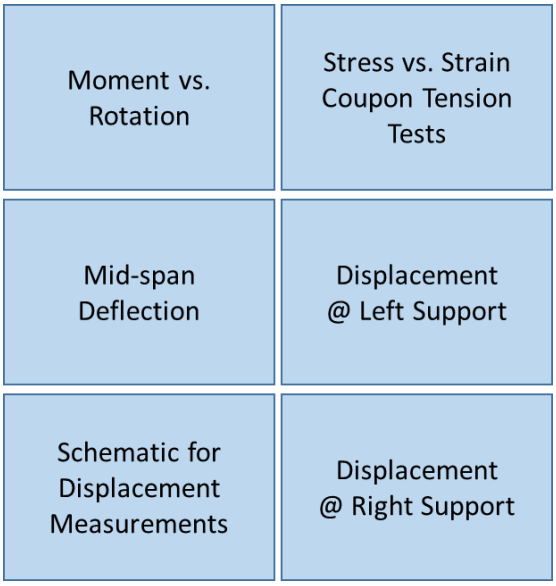

Fig. D.1. How to read each specimen results sheet below

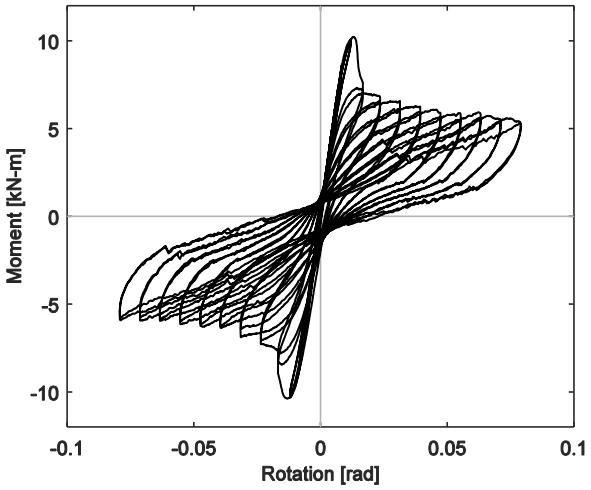
Moment [kN-m]
Rotation [rad]

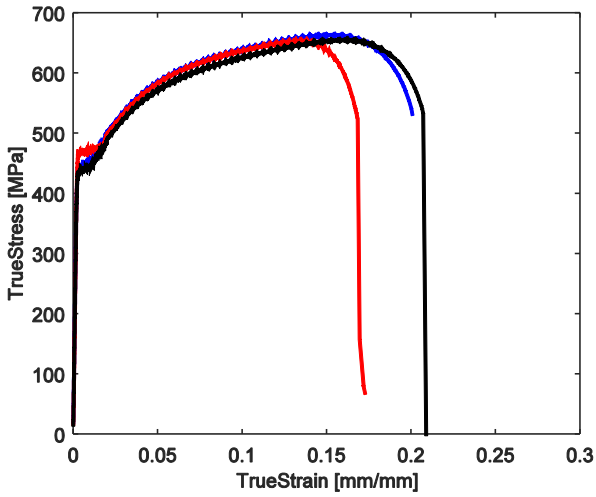
TrueStress [MPa]
TrueStrain [mm/mm]

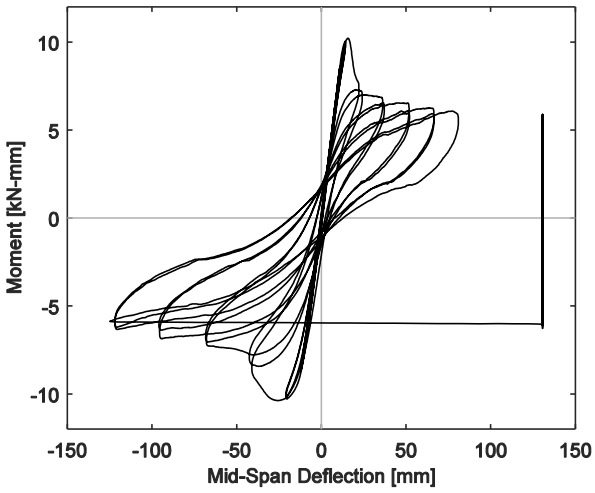
Moment [kN-mm]
Mid-Span Deflection [mm]

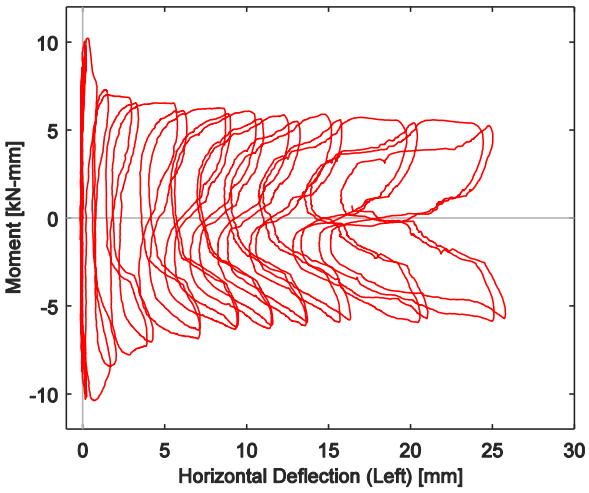
Moment [kN-mm]
Horizontal Deflection (Left) [mm]

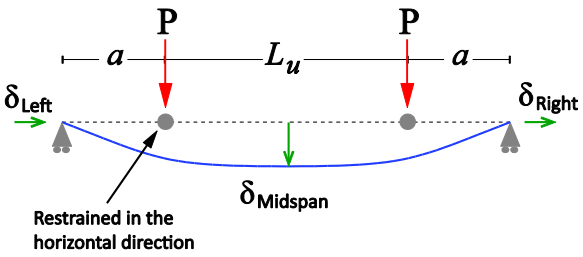
P
P
a
L_u
a
δ_{Left}
δ_{Right}
$\delta_{Midspan}$
Restrained in the horizontal direction

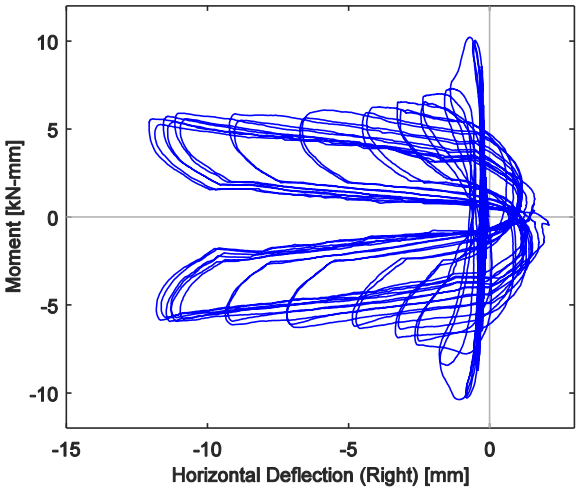
Moment [kN-mm]
Horizontal Deflection (Right) [mm]

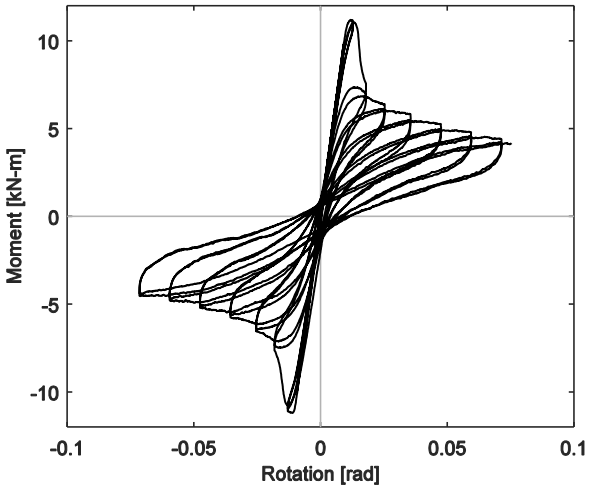
Moment [kN-m]
Rotation [rad]

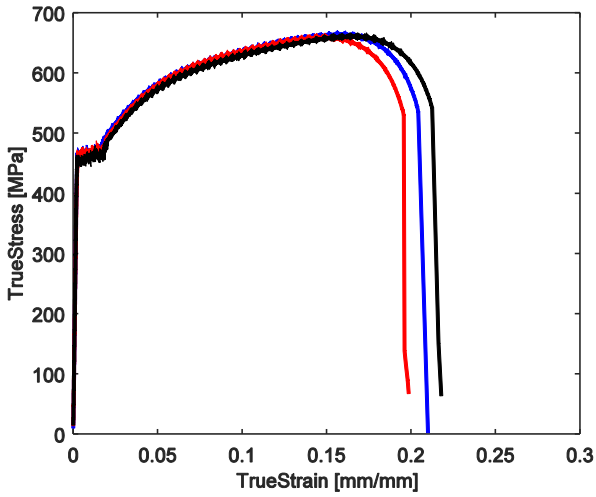
TrueStress [MPa]
TrueStrain [mm/mm]

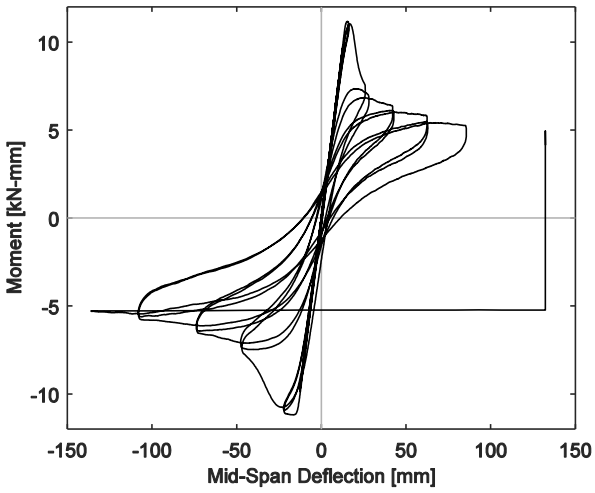
Moment [kN-mm]
Mid-Span Deflection [mm]

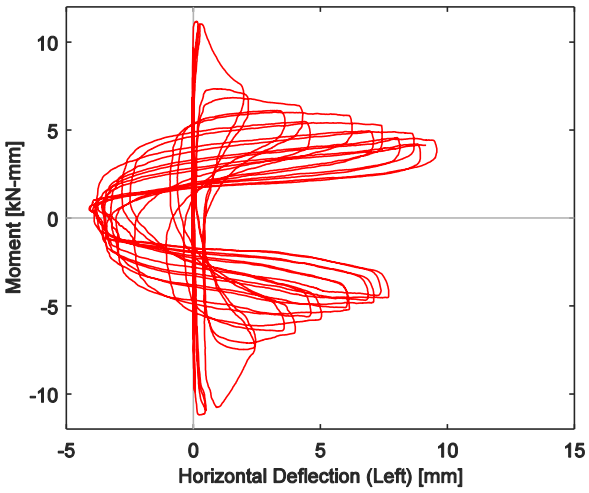
Moment [kN-mm]
Horizontal Deflection (Left) [mm]

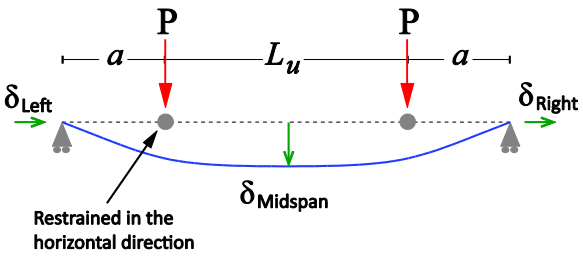
P
P
a
L_u
a
δ_{Left}
δ_{Right}
$\delta_{Midspan}$
Restrained in the horizontal direction

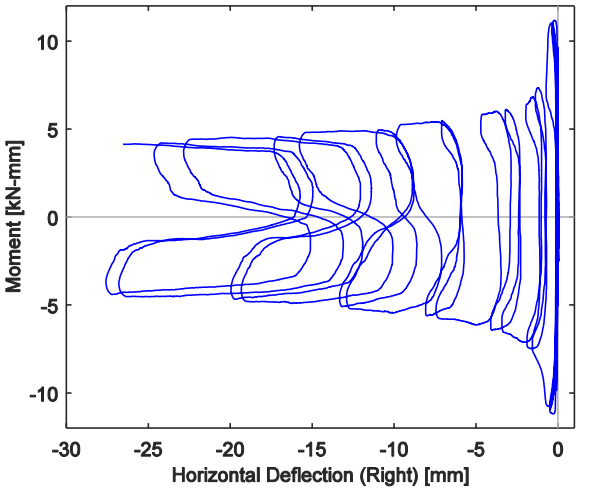
Moment [kN-mm]
Horizontal Deflection (Right) [mm]

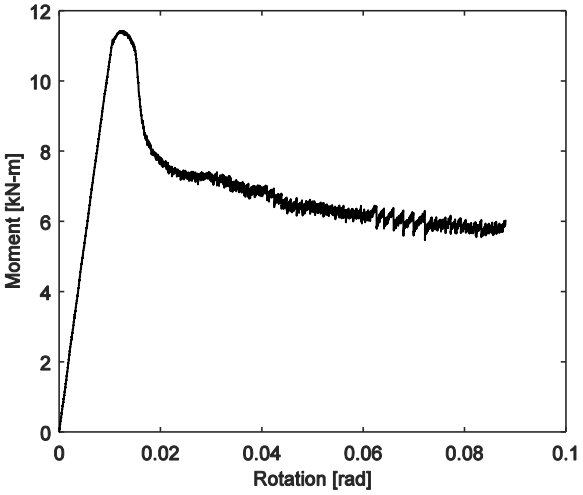
Moment [kN-m]
Rotation [rad]

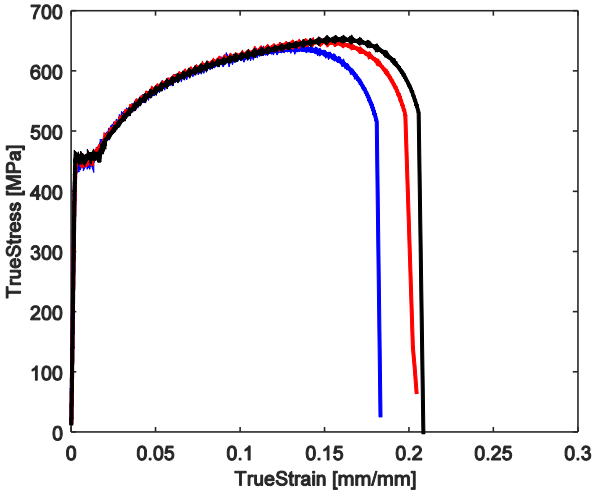
TrueStress [MPa]
TrueStrain [mm/mm]

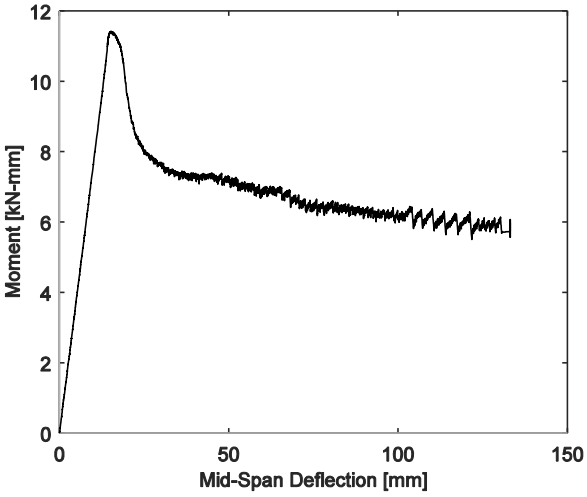
Moment [kN-mm]
Mid-Span Deflection [mm]

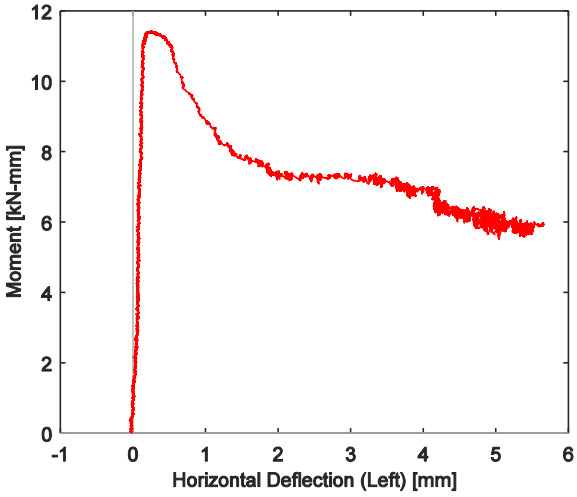
Moment [kN-mm]
Horizontal Deflection (Left) [mm]

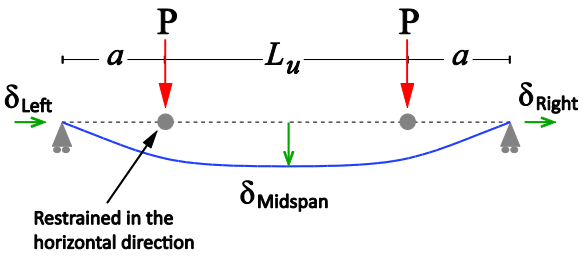
P
P
a
L_u
a
δ_{Left}
δ_{Right}
$\delta_{Midspan}$
Restrained in the horizontal direction

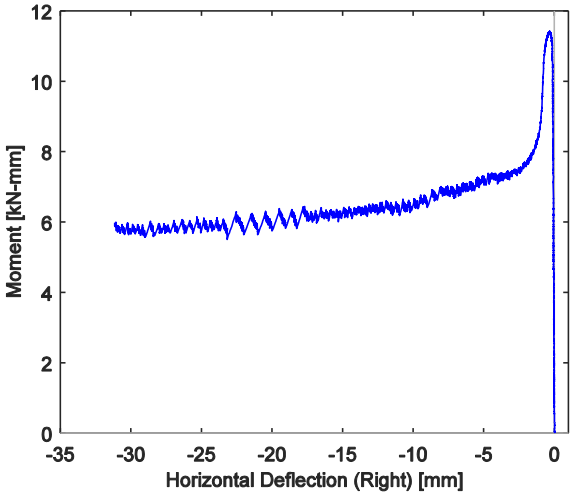
Moment [kN-mm]
Horizontal Deflection (Right) [mm]

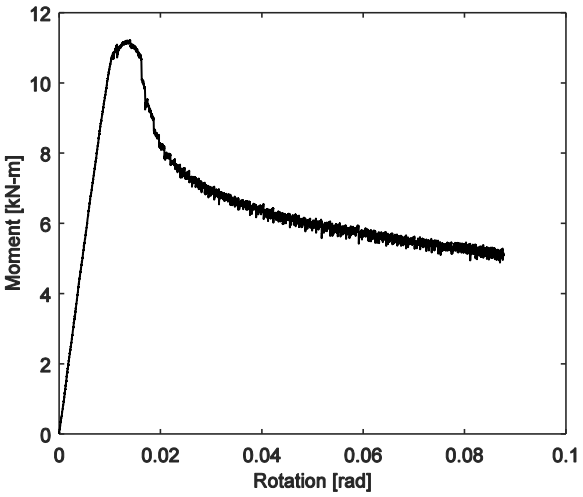
Moment [kN-m]
Rotation [rad]

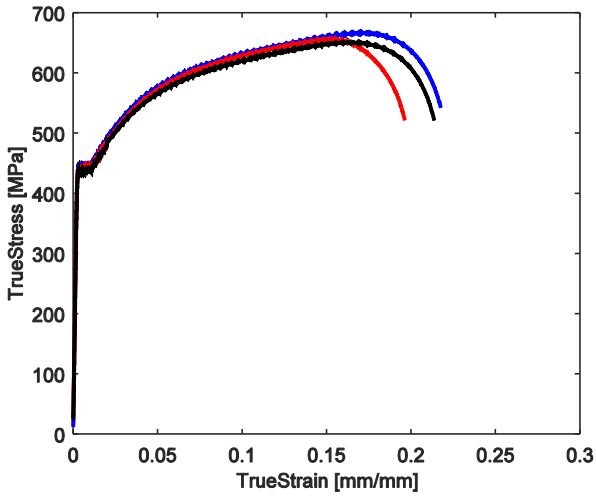
TrueStress [MPa]
TrueStrain [mm/mm]

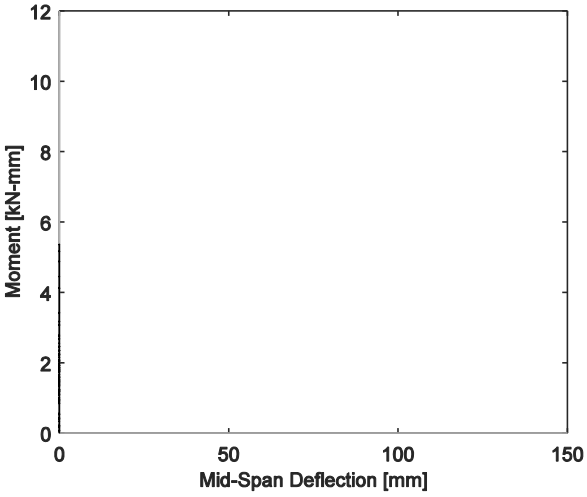
Moment [kN-mm]
Mid-Span Deflection [mm]

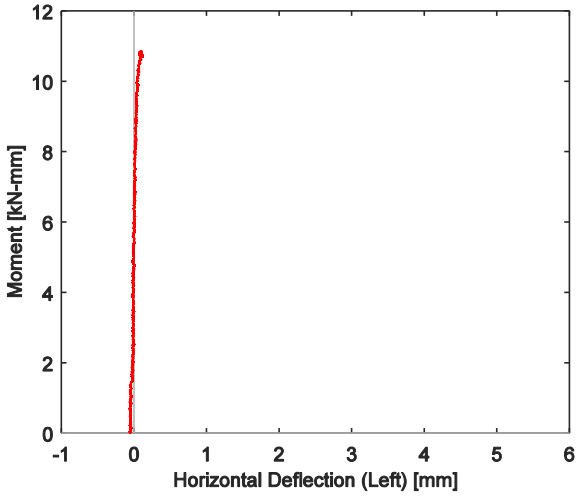
Moment [kN-mm]
Horizontal Deflection (Left) [mm]

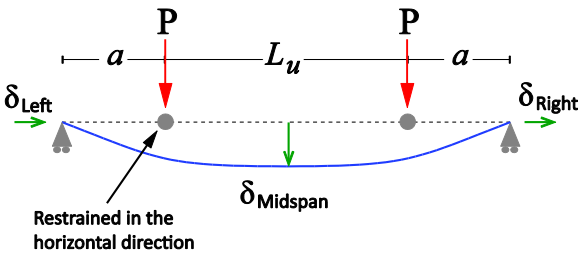
P
P
a
L_u
a
δ_{Left}
δ_{Right}
$\delta_{Midspan}$
Restrained in the horizontal direction

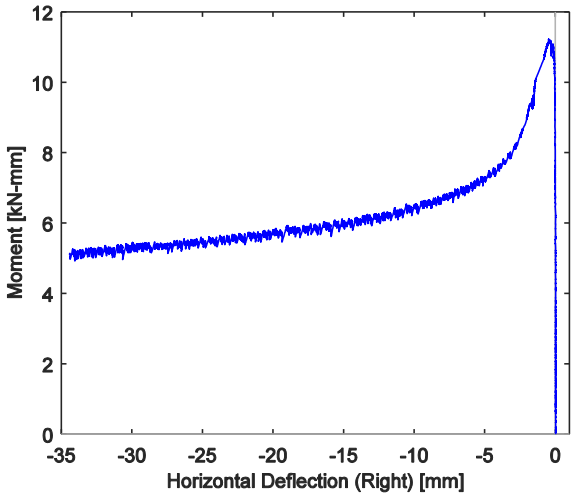
Moment [kN-mm]
Horizontal Deflection (Right) [mm]

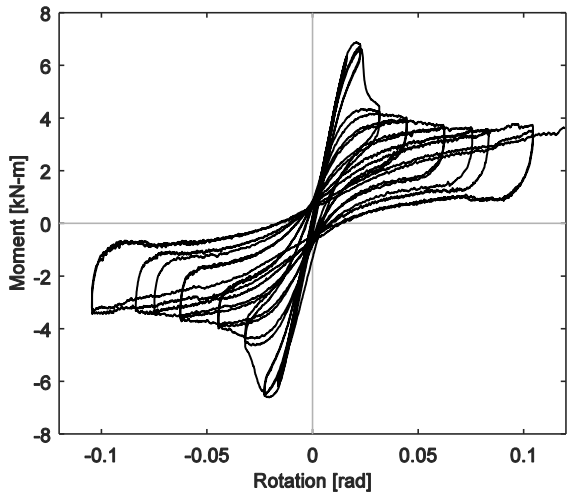
Moment [kN-m]
Rotation [rad]

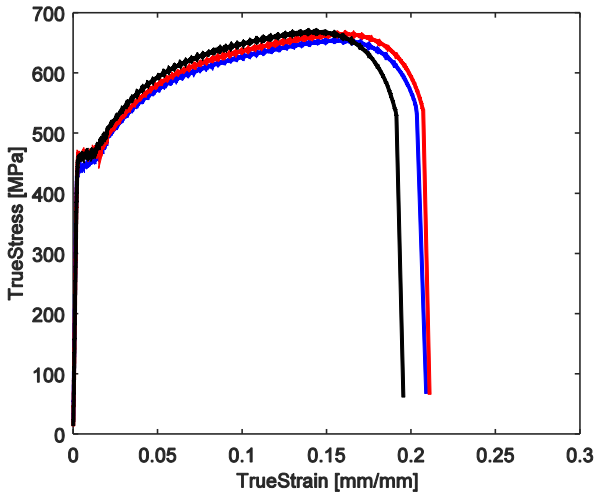
TrueStress [MPa]
TrueStrain [mm/mm]

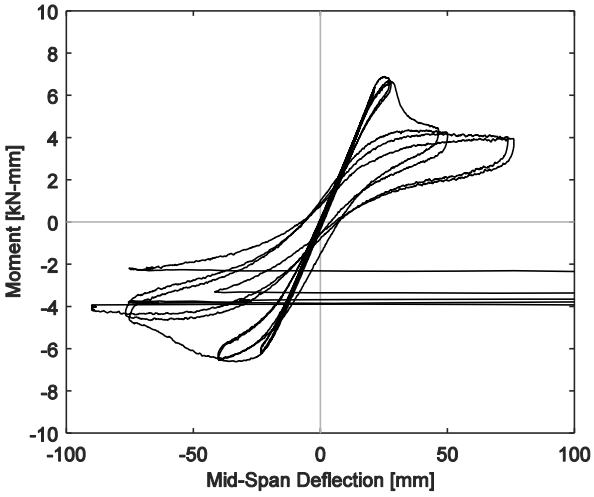
Moment [kN-mm]
Mid-Span Deflection [mm]

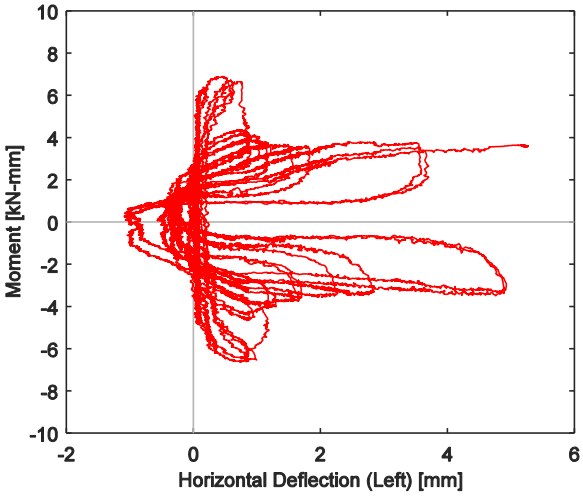
Moment [kN-mm]
Horizontal Deflection (Left) [mm]

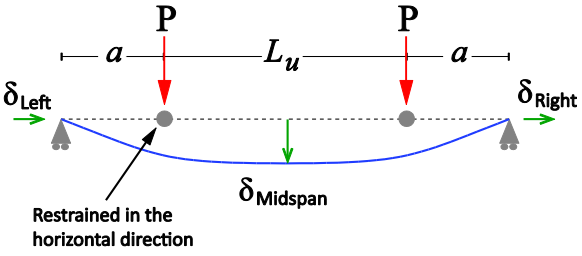
P
P
a
L_u
a
δ_{Left}
δ_{Right}
$\delta_{Midspan}$
Restrained in the horizontal direction

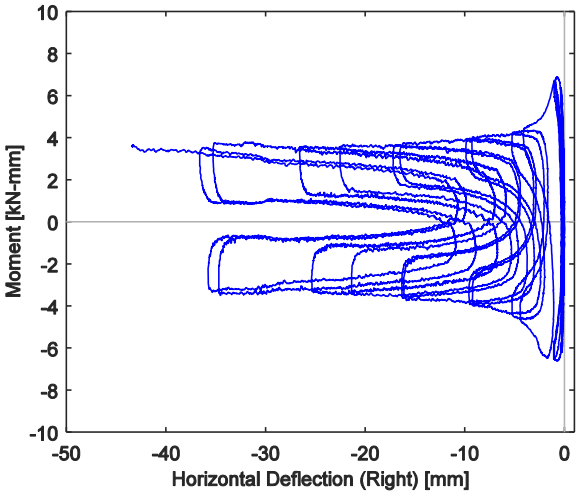
Moment [kN-mm]
Horizontal Deflection (Right) [mm]

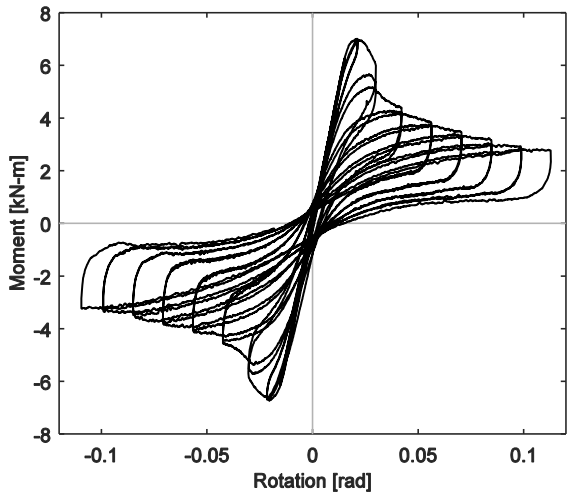
Moment [kN-m]
Rotation [rad]

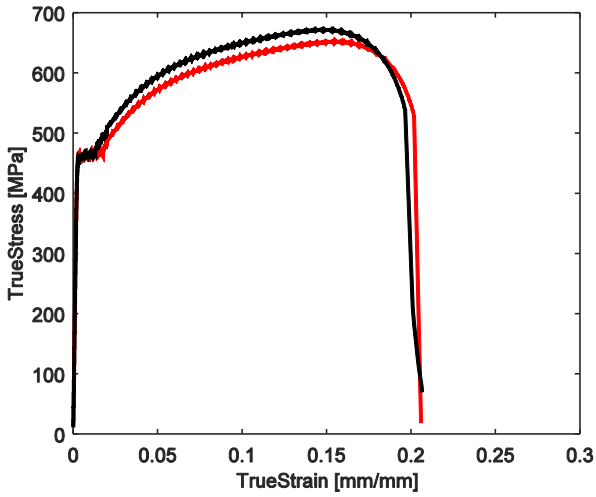
TrueStress [MPa]
TrueStrain [mm/mm]

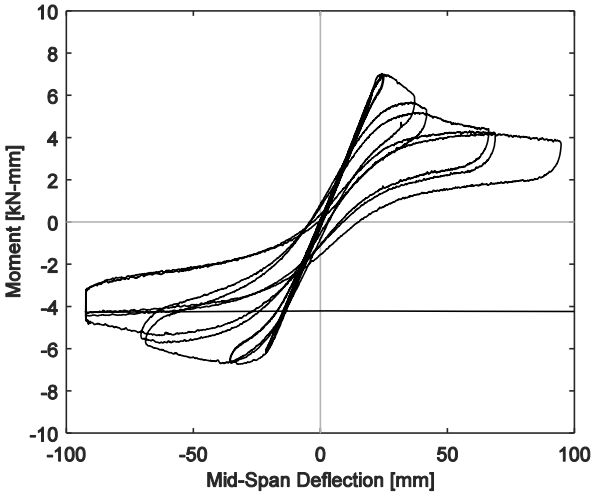
Moment [kN-mm]
Mid-Span Deflection [mm]

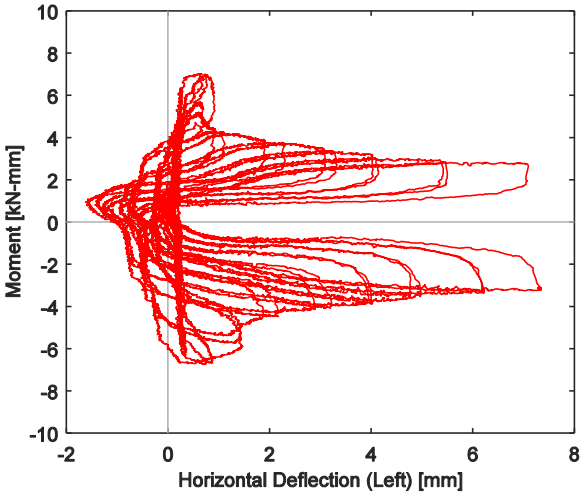
Moment [kN-mm]
Horizontal Deflection (Left) [mm]

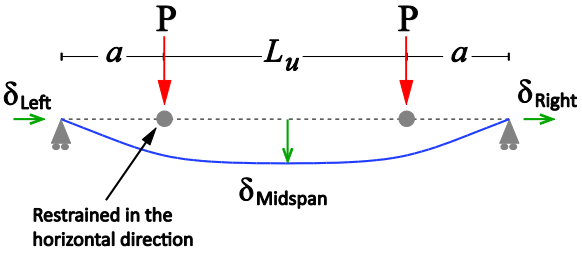
P
P
a
L_u
a
δ_{Left}
δ_{Right}
$\delta_{Midspan}$
Restrained in the horizontal direction

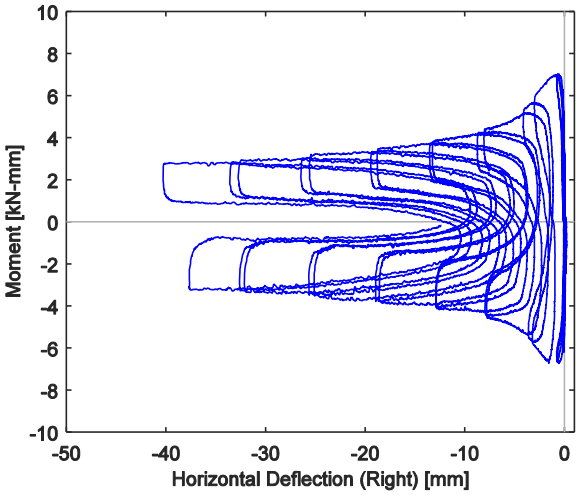
Moment [kN-mm]
Horizontal Deflection (Right) [mm]

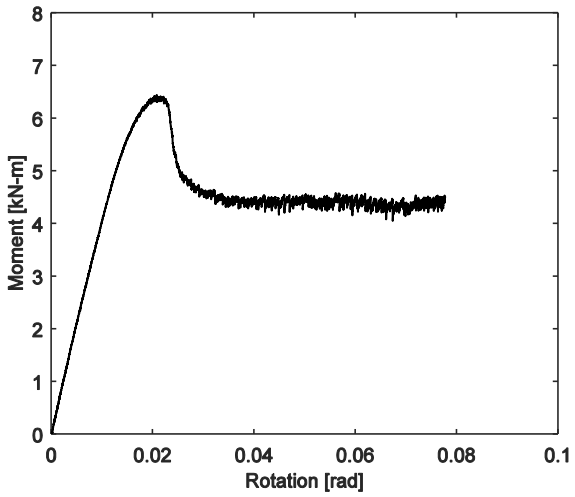
Moment [kN-m]
Rotation [rad]

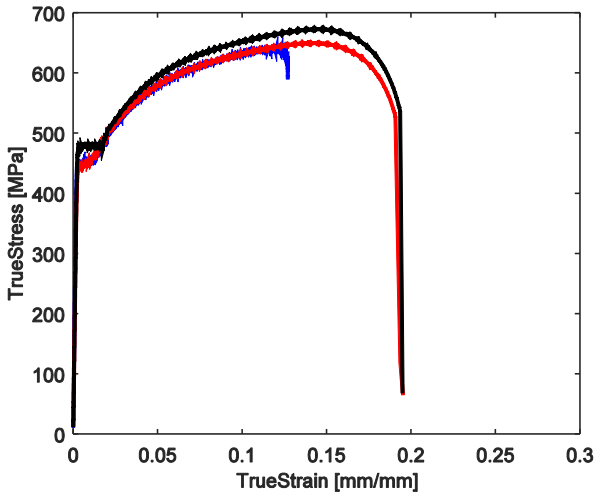
TrueStress [MPa]
TrueStrain [mm/mm]

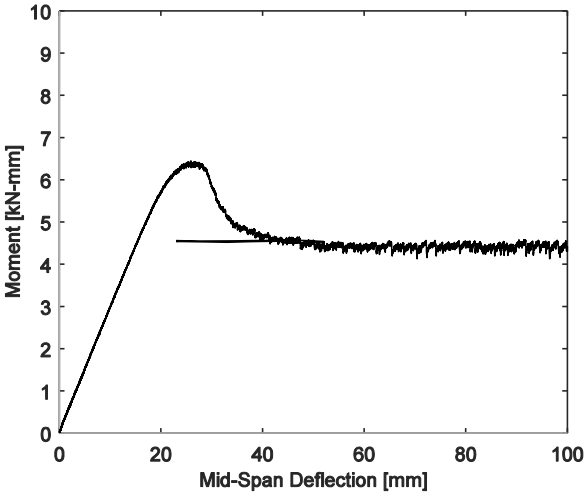
Moment [kN-mm]
Mid-Span Deflection [mm]

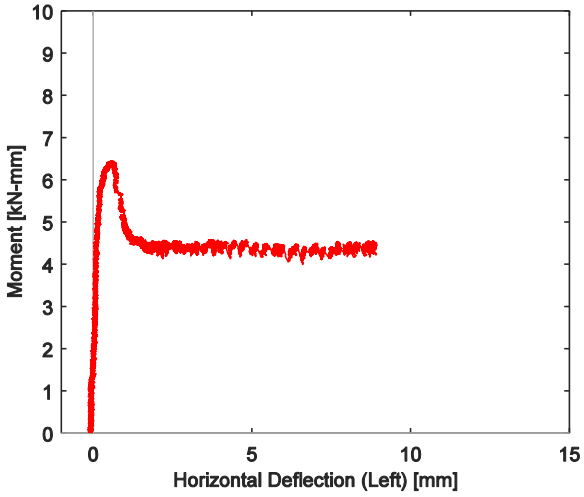
Moment [kN-mm]
Horizontal Deflection (Left) [mm]

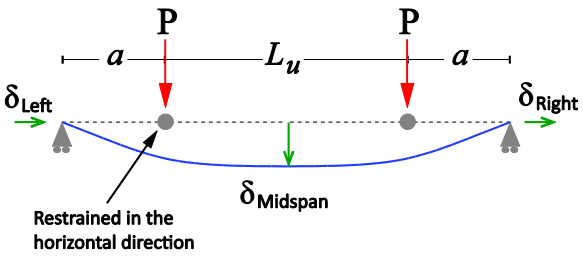
P
P
a
L_u
a
δ_{Left}
δ_{Right}
$\delta_{Midspan}$
Restrained in the horizontal direction

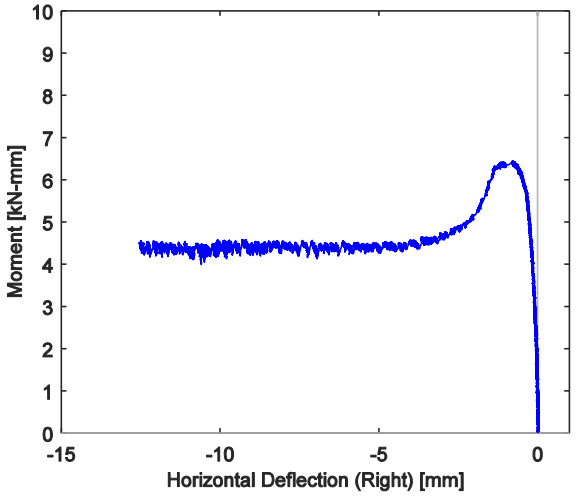
Moment [kN-mm]
Horizontal Deflection (Right) [mm]

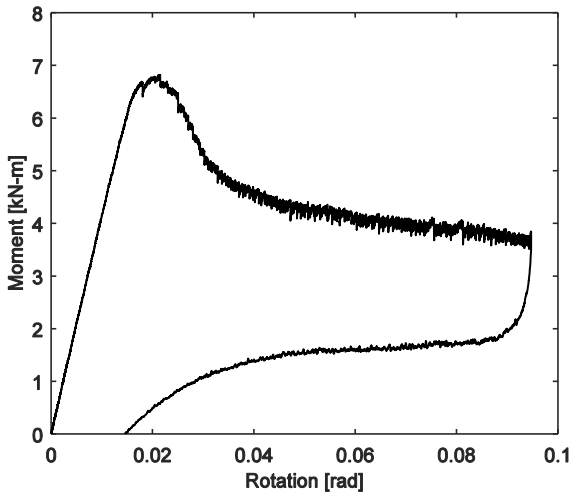
Moment [kN-m]
Rotation [rad]

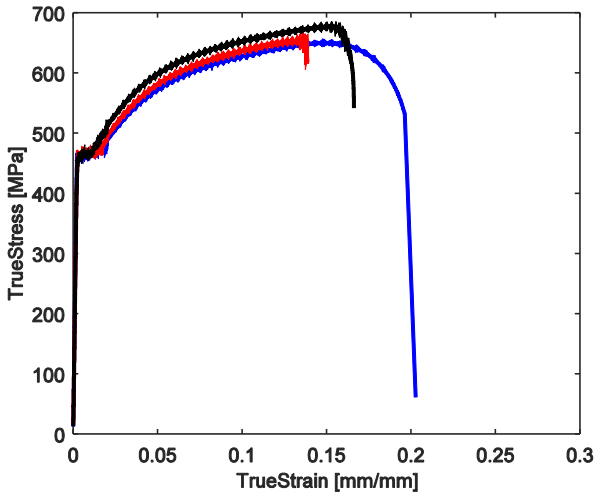
TrueStress [MPa]
TrueStrain [mm/mm]

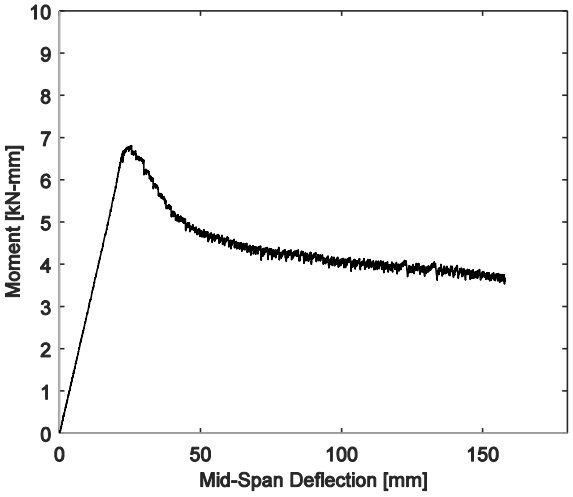
Moment [kN-mm]
Mid-Span Deflection [mm]

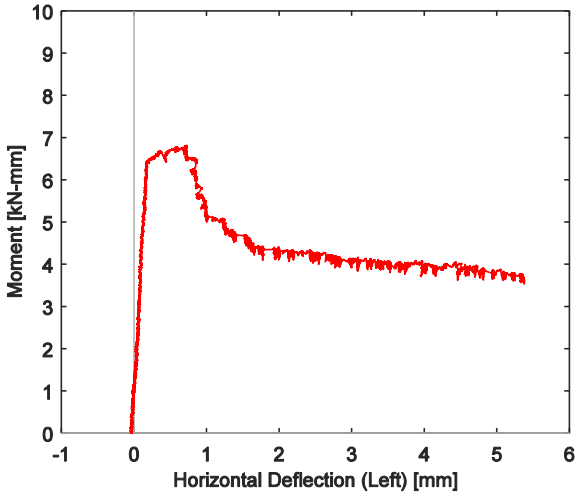
Moment [kN-mm]
Horizontal Deflection (Left) [mm]

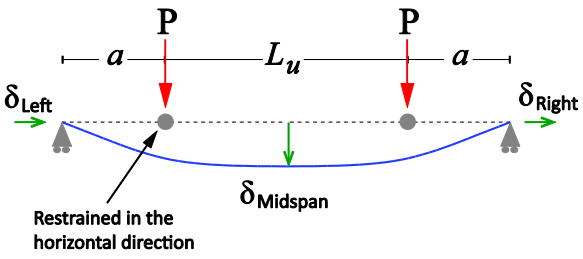
P
P
a
L_u
a
δ_{Left}
δ_{Right}
$\delta_{Midspan}$
Restrained in the horizontal direction

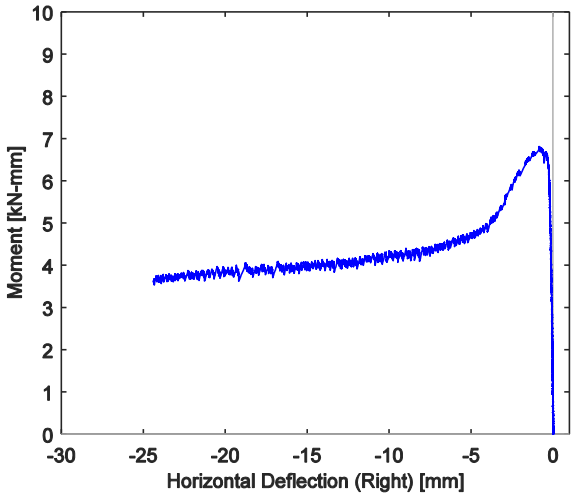
Moment [kN-mm]
Horizontal Deflection (Right) [mm]

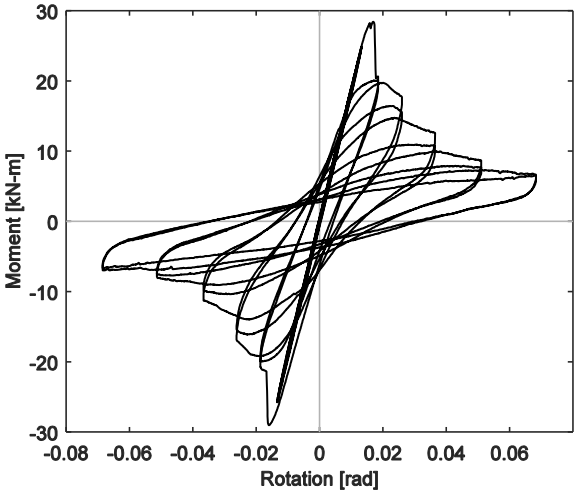
Moment [kN-m]
Rotation [rad]

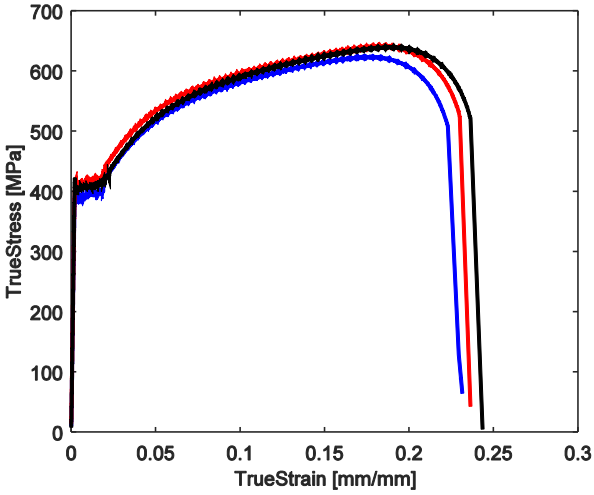
TrueStress [MPa]
TrueStrain [mm/mm]

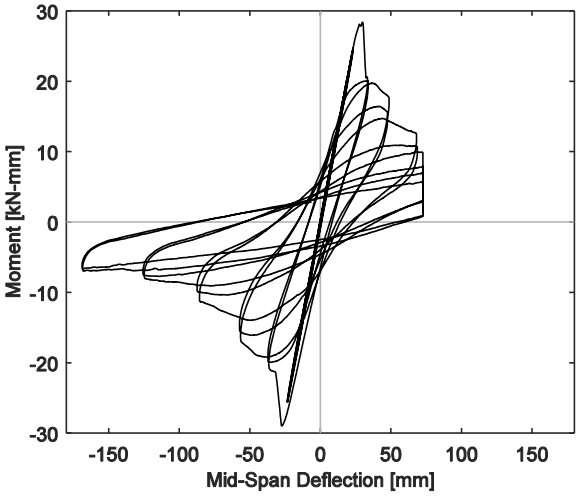
Moment [kN-mm]
Mid-Span Deflection [mm]

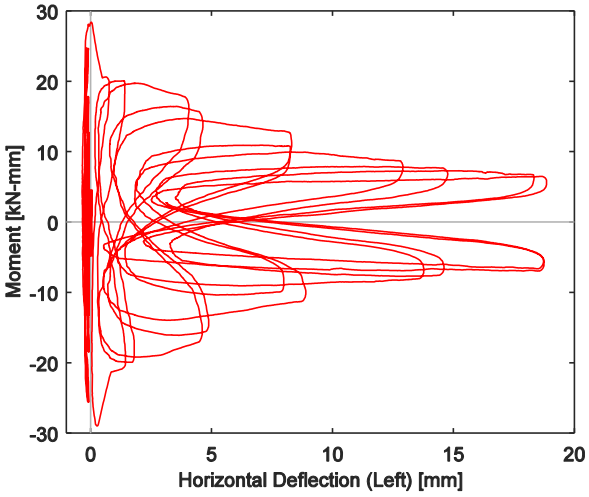
Moment [kN-mm]
Horizontal Deflection (Left) [mm]

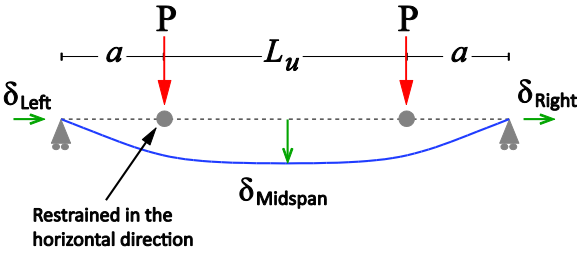
P
P
a
L_u
a
δ_{Left}
δ_{Right}
$\delta_{Midspan}$
Restrained in the horizontal direction

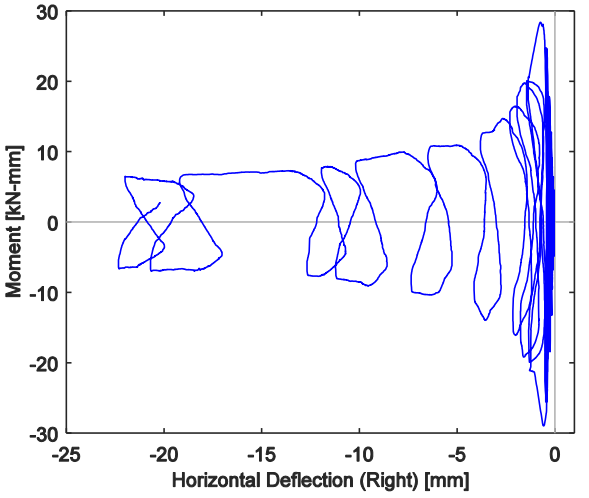
Moment [kN-mm]
Horizontal Deflection (Right) [mm]

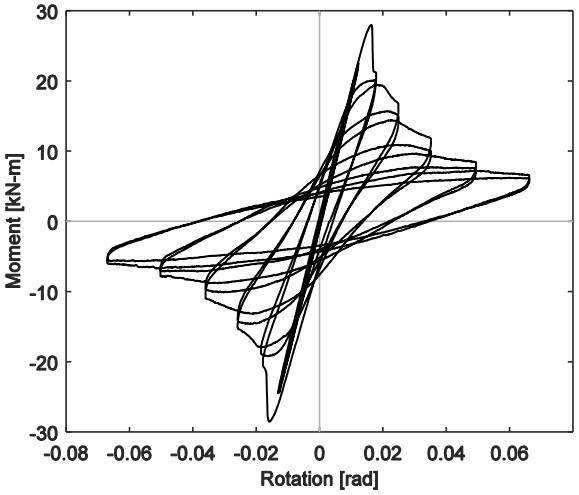
Moment [kN-m]
Rotation [rad]

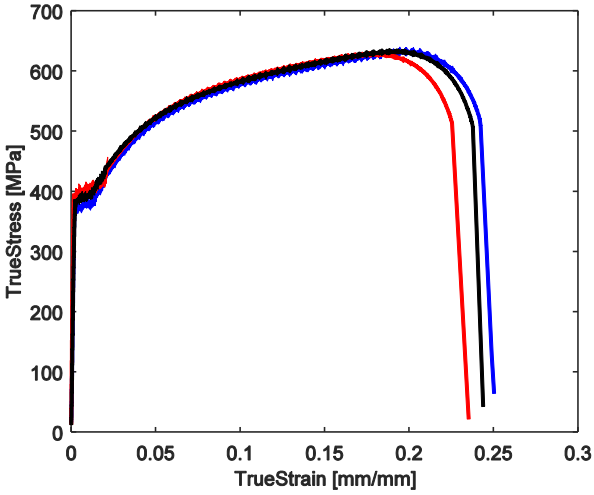
TrueStress [MPa]
TrueStrain [mm/mm]

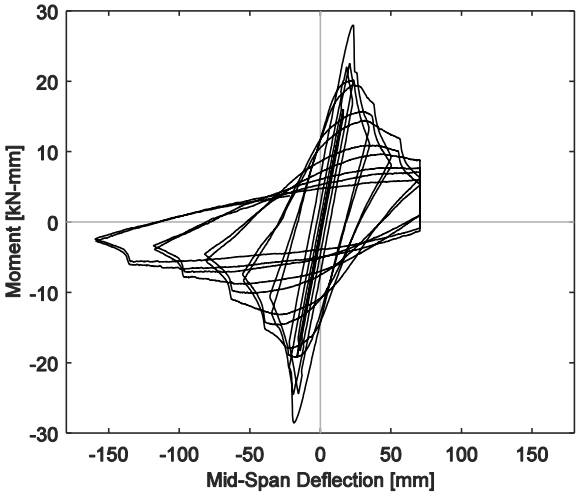
Moment [kN-mm]
Mid-Span Deflection [mm]

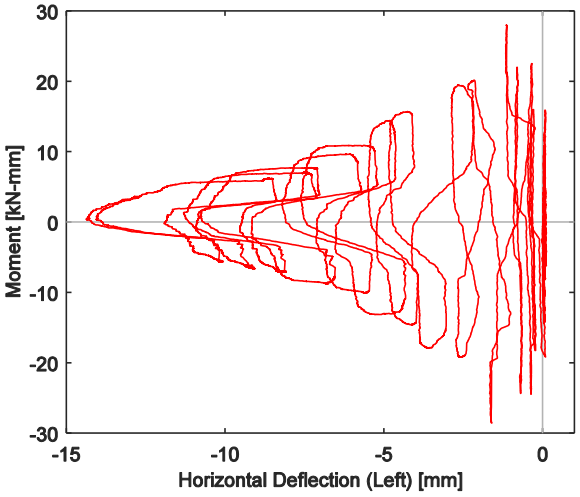
Moment [kN-mm]
Horizontal Deflection (Left) [mm]

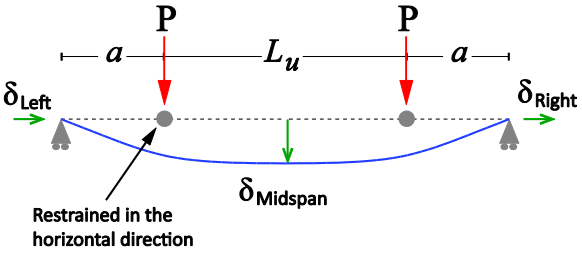
P
P
a
L_u
a
δ_{Left}
δ_{Right}
$\delta_{Midspan}$
Restrained in the horizontal direction

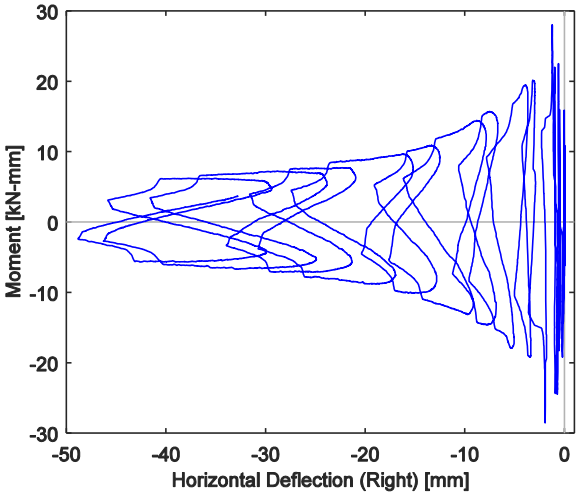
Moment [kN-mm]
Horizontal Deflection (Right) [mm]

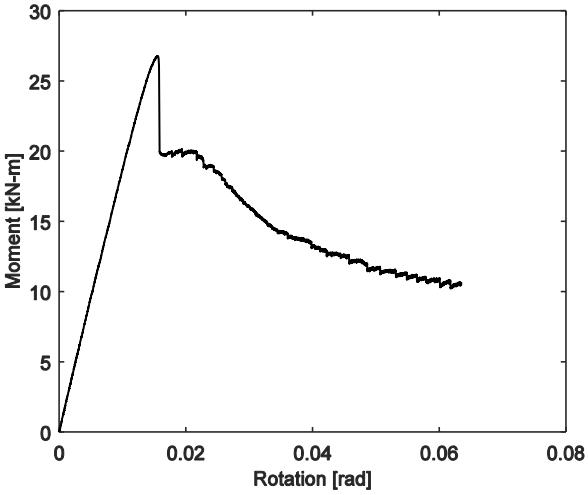
Moment [kN-m]
Rotation [rad]

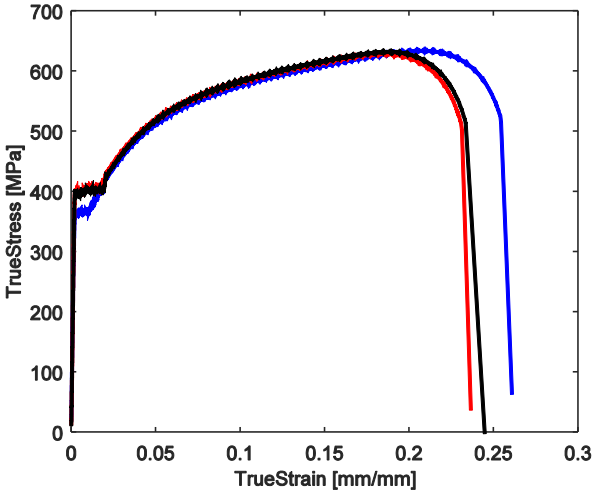
TrueStress [MPa]
TrueStrain [mm/mm]

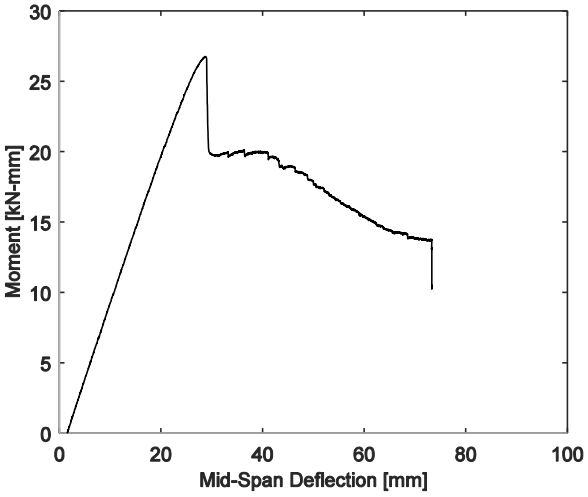
Moment [kN-mm]
Mid-Span Deflection [mm]

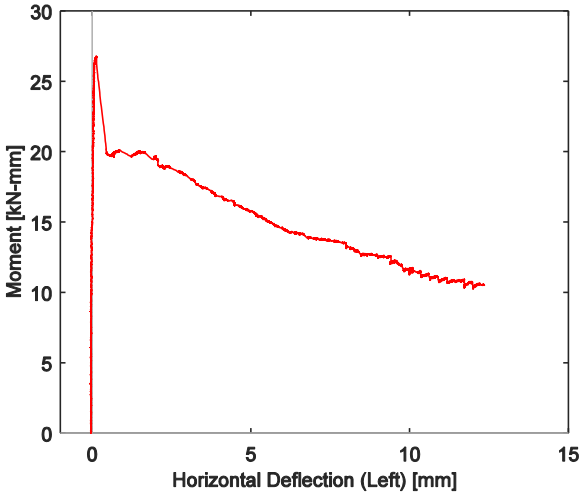
Moment [kN-mm]
Horizontal Deflection (Left) [mm]

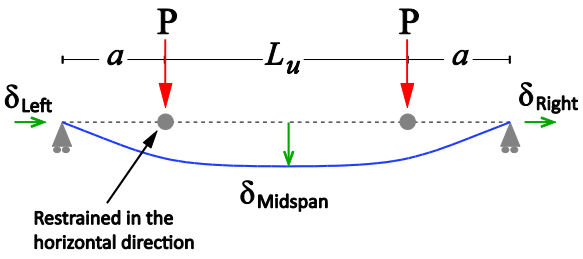
P
P
a
L_u
a
δ_{Left}
δ_{Right}
$\delta_{Midspan}$
Restrained in the horizontal direction

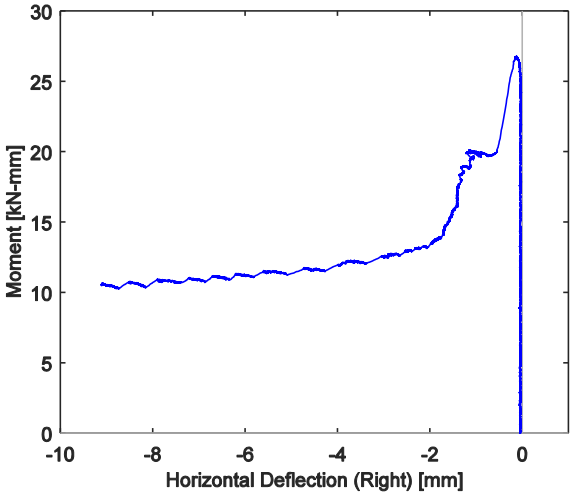
Moment [kN-mm]
Horizontal Deflection (Right) [mm]

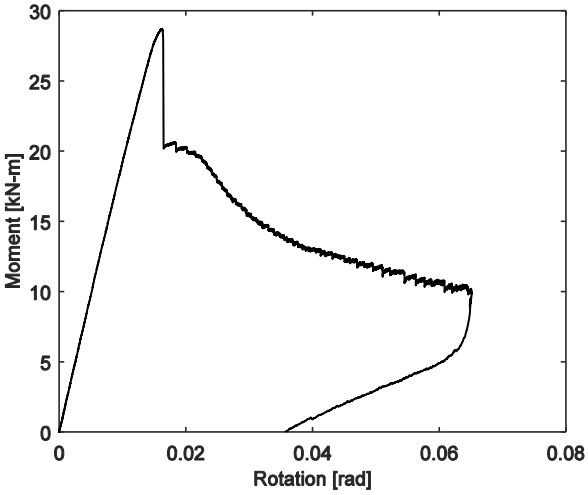
Moment [kN-m]
Rotation [rad]
0
5
10
15
20
25
30
0
0.02
0.04
0.06
0.08

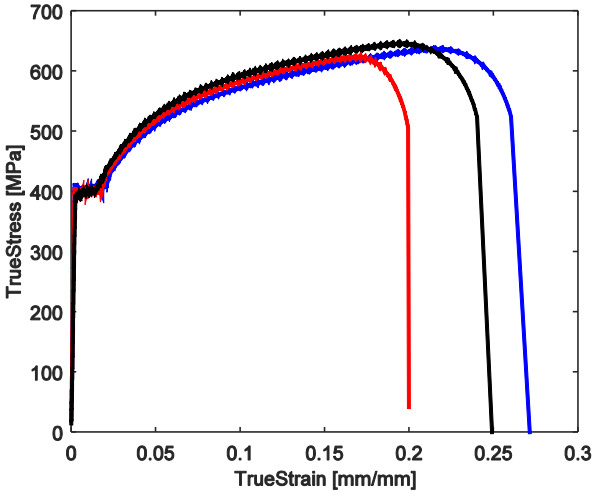
TrueStress [MPa]
TrueStrain [mm/mm]
0
100
200
300
400
500
600
700
0
0.05
0.1
0.15
0.2
0.25
0.3

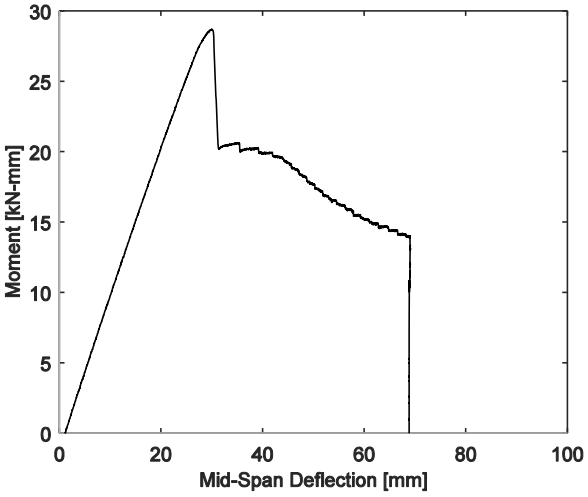
Moment [kN-mm]
Mid-Span Deflection [mm]
0
5
10
15
20
25
30
0
20
40
60
80
100

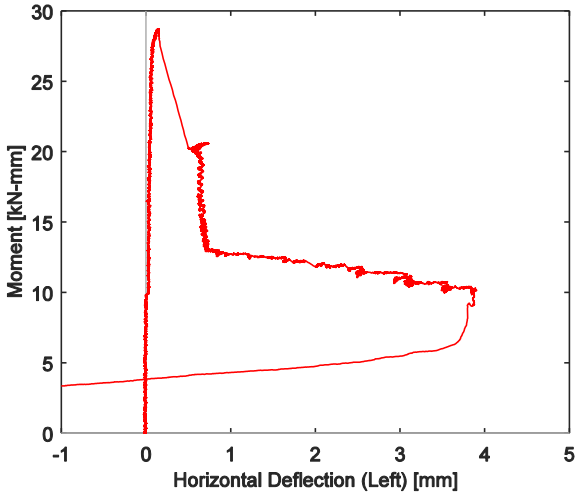
Moment [kN-mm]
Horizontal Deflection (Left) [mm]
0
5
10
15
20
25
30
-1
0
1
2
3
4
5

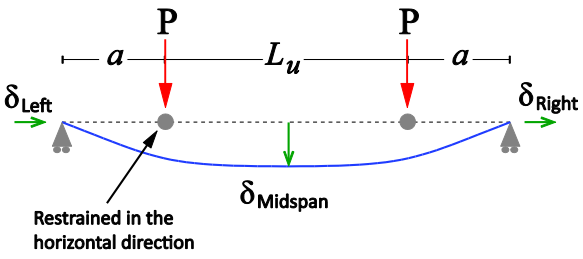
P
P
a
L_u
a
δ_{Left}
δ_{Right}
$\delta_{Midspan}$
Restrained in the
horizontal direction

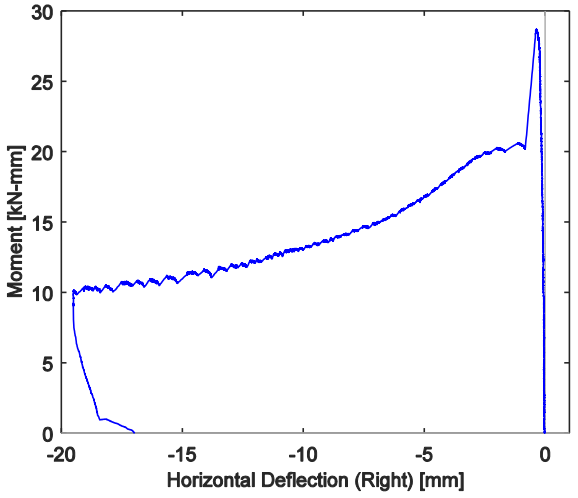
Moment [kN-mm]
Horizontal Deflection (Right) [mm]
0
5
10
15
20
25
30
-20
-15
-10
-5
0

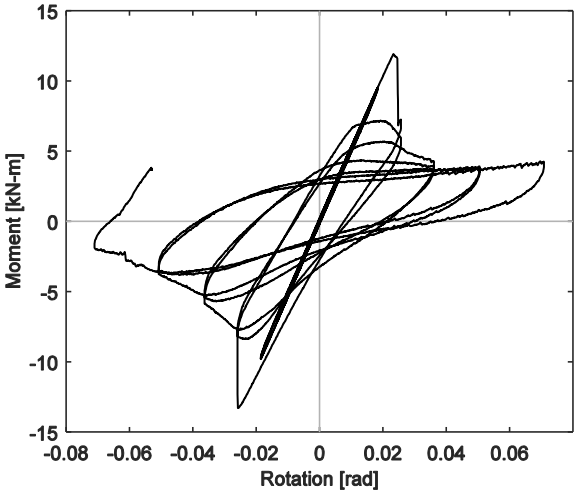
Moment [kN-m]
Rotation [rad]

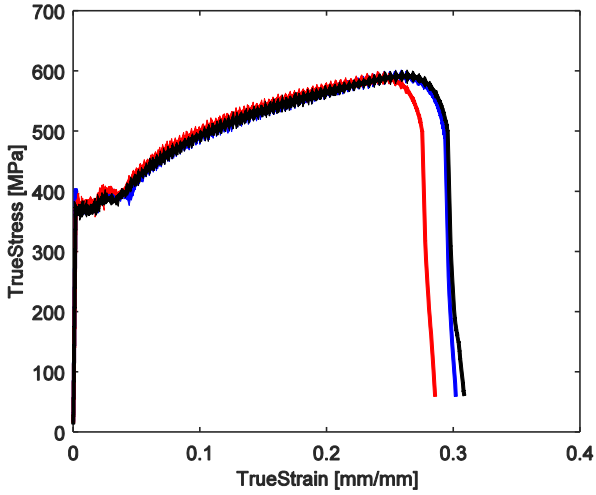
TrueStress [MPa]
TrueStrain [mm/mm]

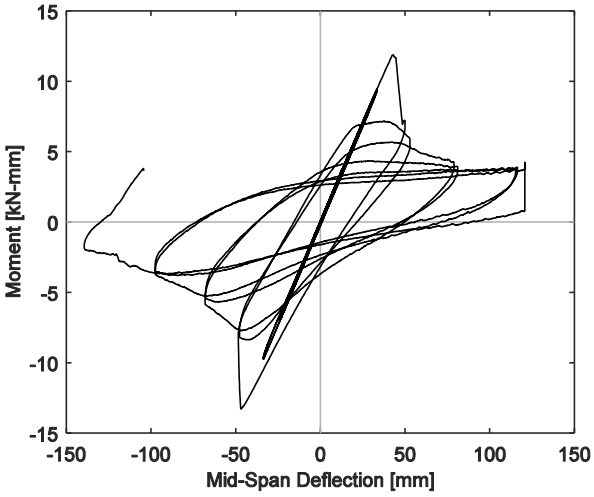
Moment [kN-mm]
Mid-Span Deflection [mm]

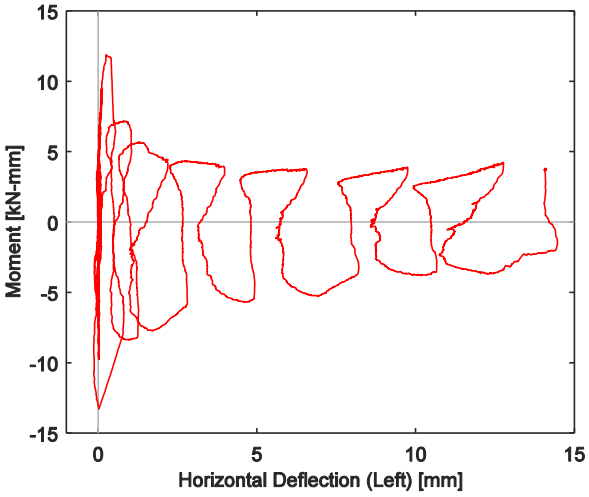
Moment [kN-mm]
Horizontal Deflection (Left) [mm]

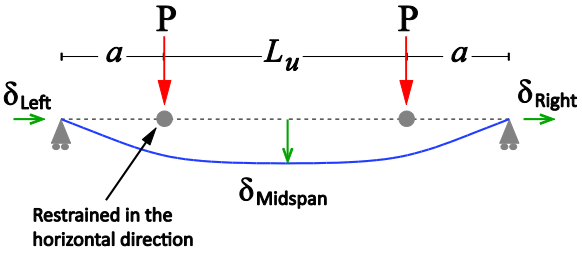
P
P
a
L_u
a
δ_{Left}
δ_{Right}
$\delta_{Midspan}$
Restrained in the horizontal direction

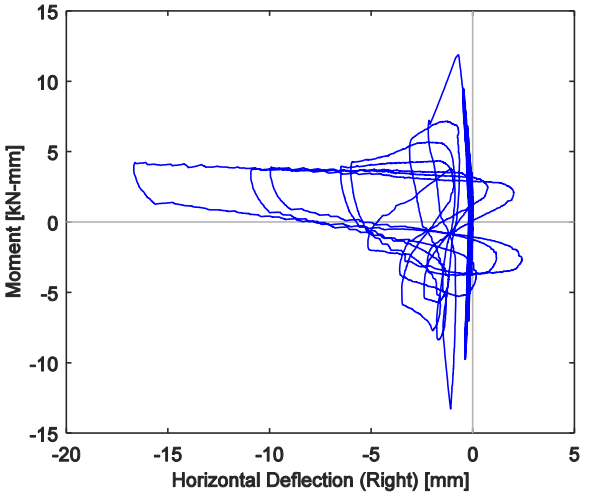
Moment [kN-mm]
Horizontal Deflection (Right) [mm]

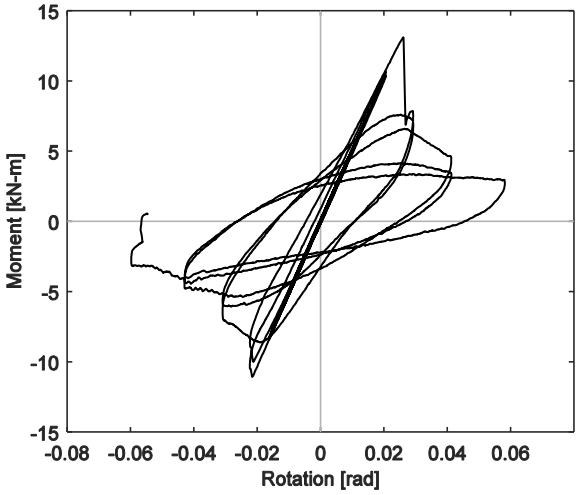
Moment [kN-m]
Rotation [rad]

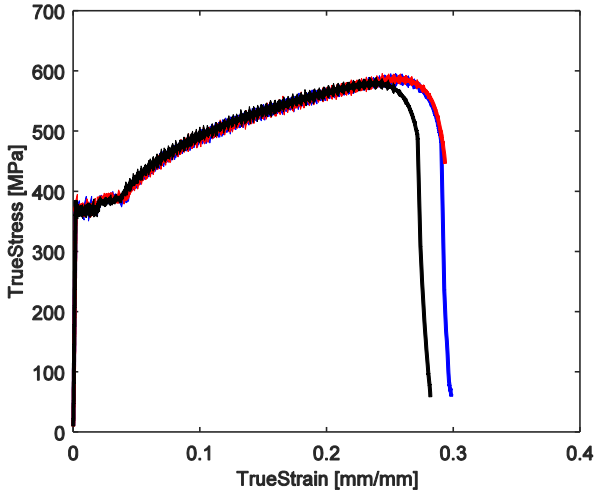
TrueStress [MPa]
TrueStrain [mm/mm]

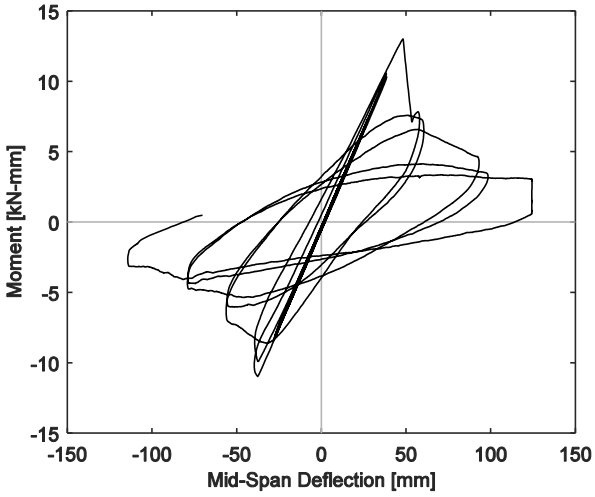
Moment [kN-mm]
Mid-Span Deflection [mm]

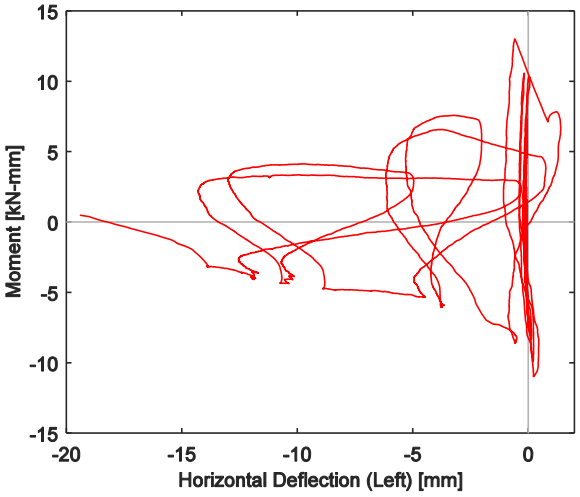
Moment [kN-mm]
Horizontal Deflection (Left) [mm]

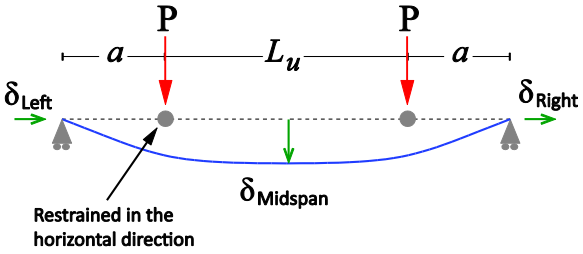
P
P
a
L_u
a
δ_{Left}
δ_{Right}
$\delta_{Midspan}$
Restrained in the horizontal direction

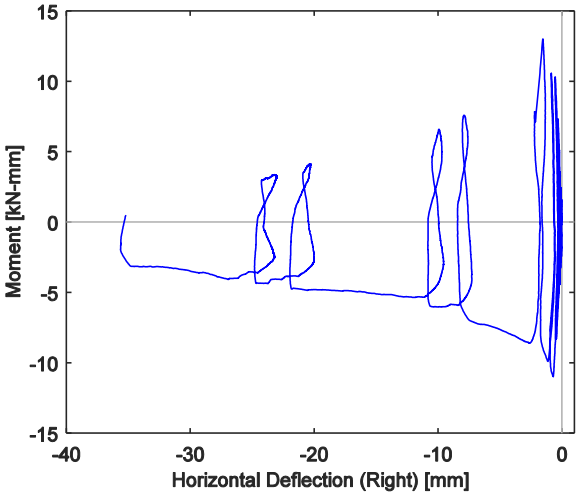
Moment [kN-mm]
Horizontal Deflection (Right) [mm]

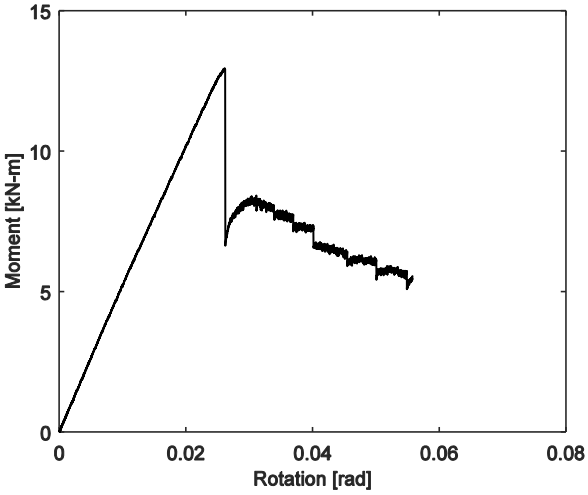
Moment [kN-m]
Rotation [rad]

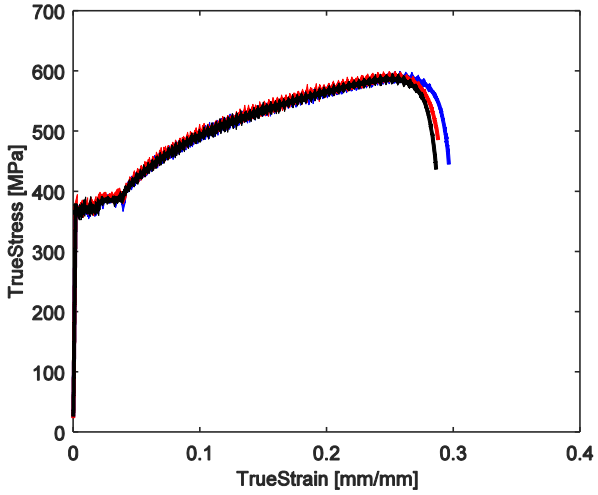
TrueStress [MPa]
TrueStrain [mm/mm]

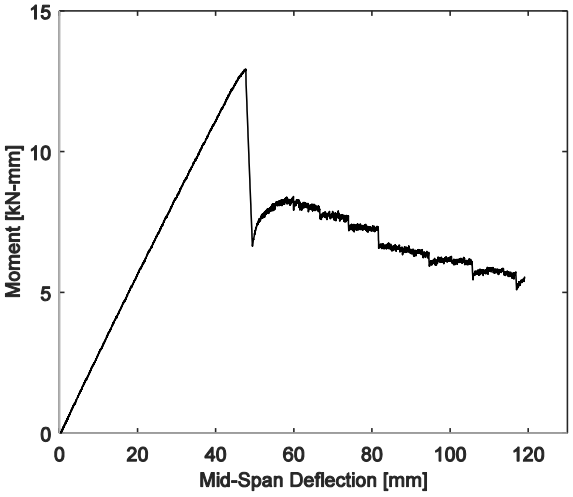
Moment [kN-mm]
Mid-Span Deflection [mm]

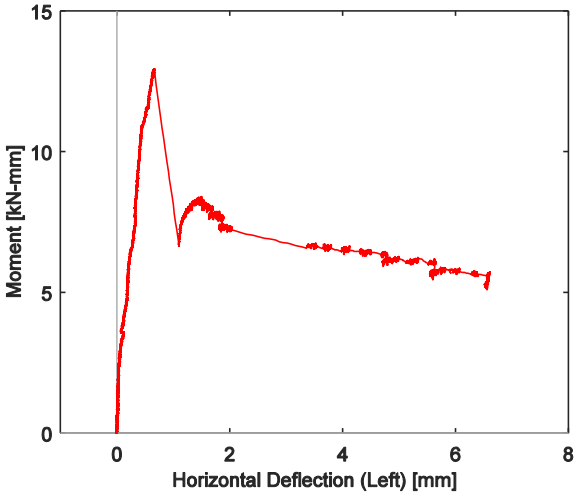
Moment [kN-mm]
Horizontal Deflection (Left) [mm]

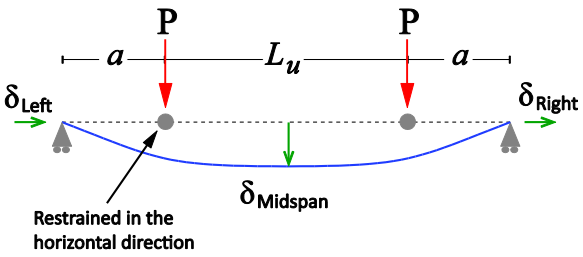
P
P
a
L_u
a
δ_{Left}
δ_{Right}
$\delta_{Midspan}$
Restrained in the horizontal direction

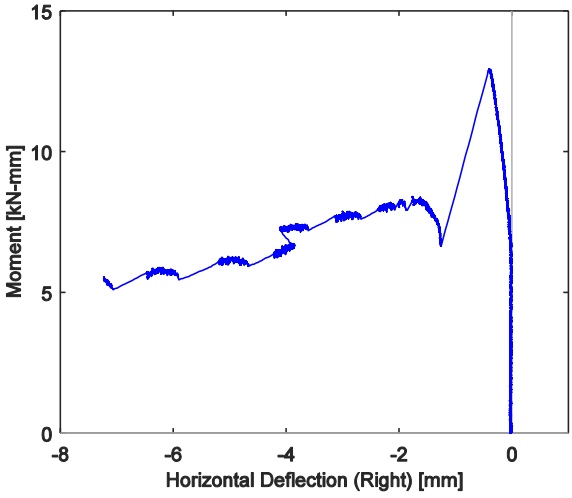
Moment [kN-mm]
Horizontal Deflection (Right) [mm]

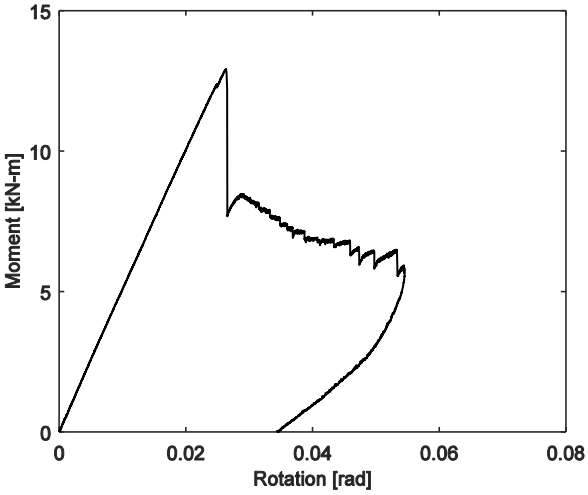
Moment [kN-m]
Rotation [rad]
0
5
10
15
0
0.02
0.04
0.06
0.08

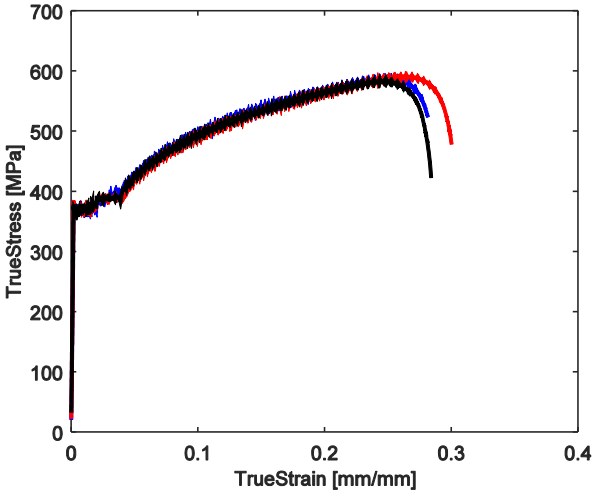
TrueStress [MPa]
TrueStrain [mm/mm]
0
100
200
300
400
500
600
700
0
0.1
0.2
0.3
0.4

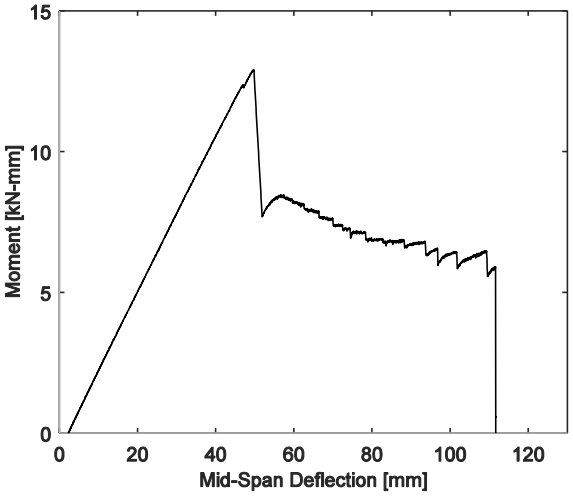
Moment [kN-mm]
Mid-Span Deflection [mm]
0
5
10
15
0
20
40
60
80
100
120

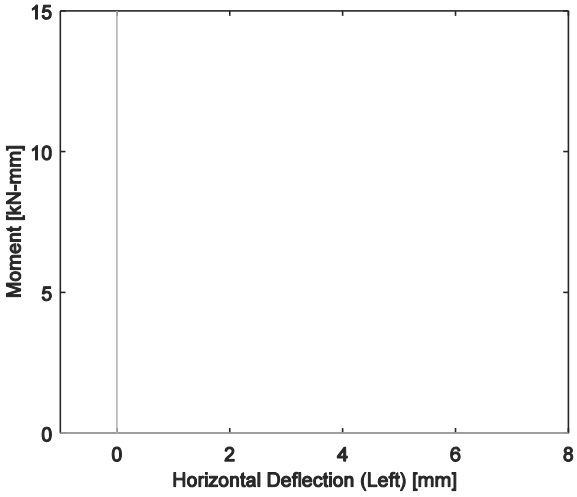
Moment [kN-mm]
Horizontal Deflection (Left) [mm]
0
5
10
15
0
2
4
6
8

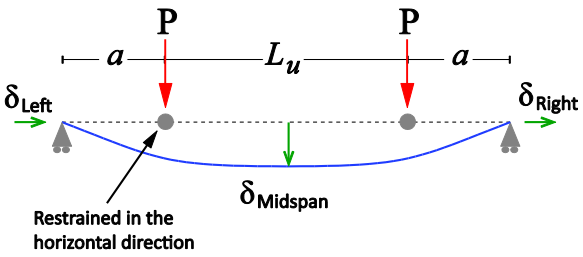
P
P
a
L_u
a
δ_{Left}
δ_{Right}
$\delta_{Midspan}$
Restrained in the horizontal direction

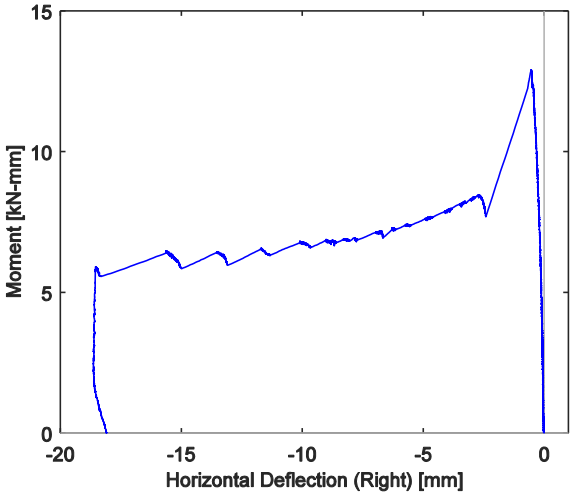
Moment [kN-mm]
Horizontal Deflection (Right) [mm]
0
5
10
15
-20
-15
-10
-5
0

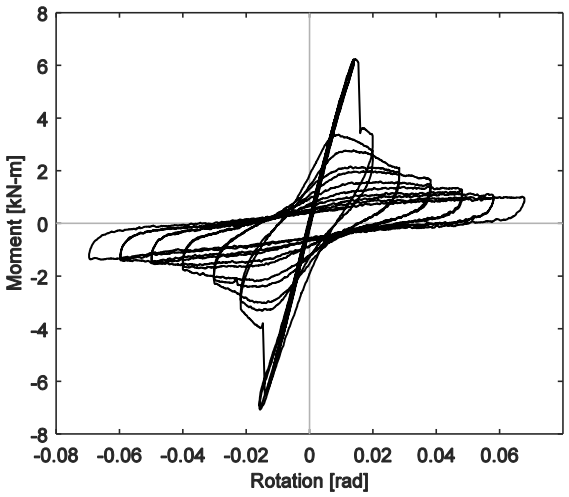
Moment [kN-m]
Rotation [rad]

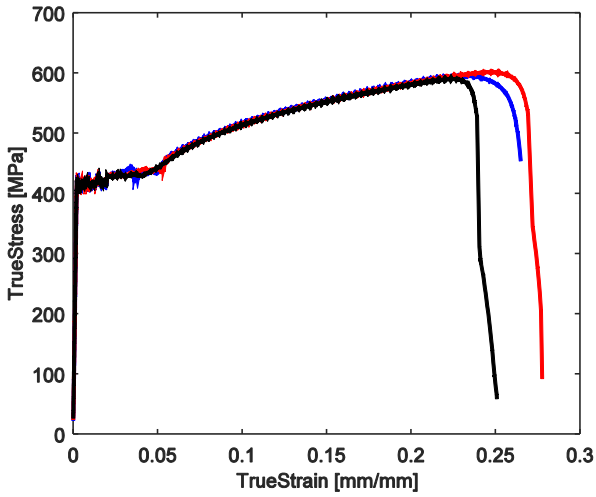
TrueStress [MPa]
TrueStrain [mm/mm]

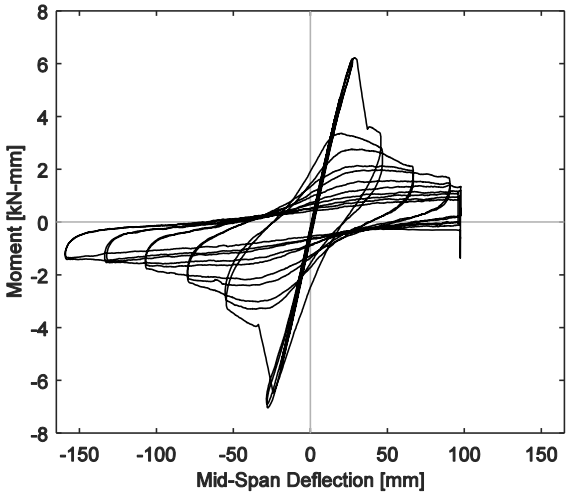
Moment [kN-mm]
Mid-Span Deflection [mm]

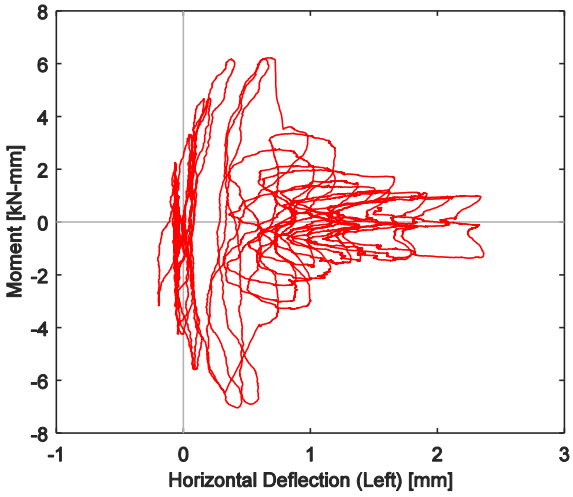
Moment [kN-mm]
Horizontal Deflection (Left) [mm]

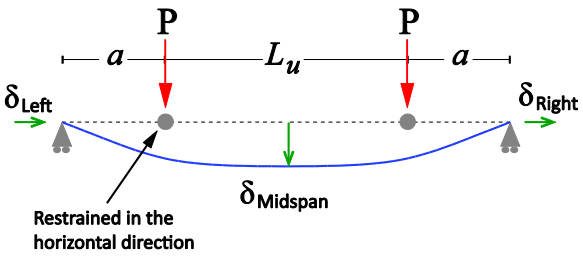
P
P
a
L_u
a
δ_{Left}
δ_{Right}
$\delta_{Midspan}$
Restrained in the horizontal direction

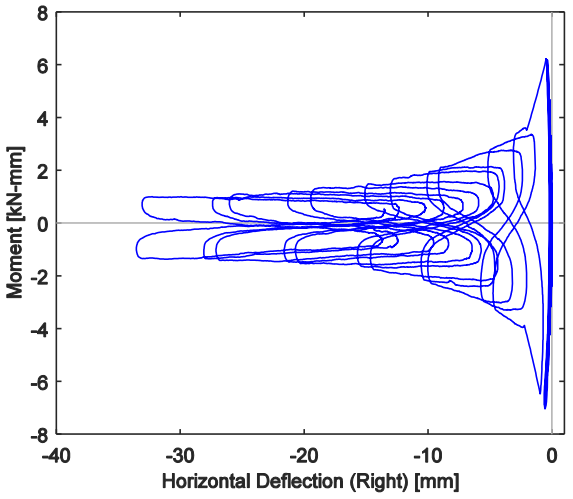
Moment [kN-mm]
Horizontal Deflection (Right) [mm]

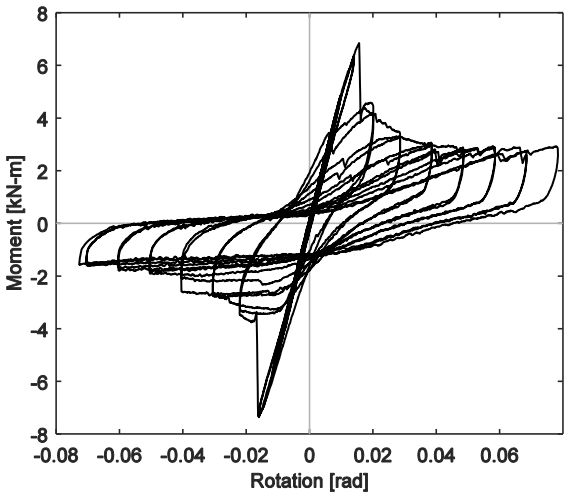
Moment [kN-m]
Rotation [rad]

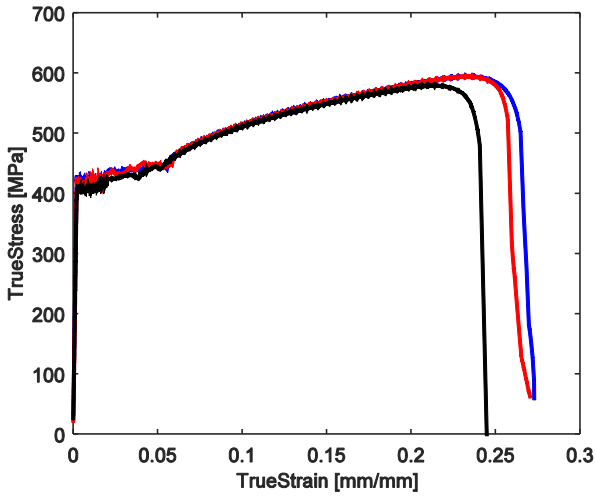
TrueStress [MPa]
TrueStrain [mm/mm]

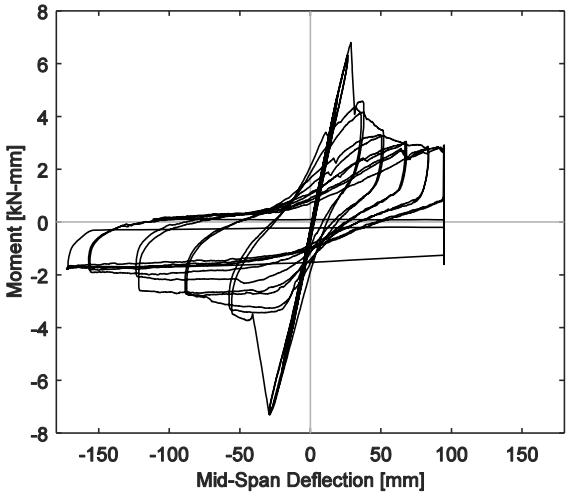
Moment [kN-mm]
Mid-Span Deflection [mm]

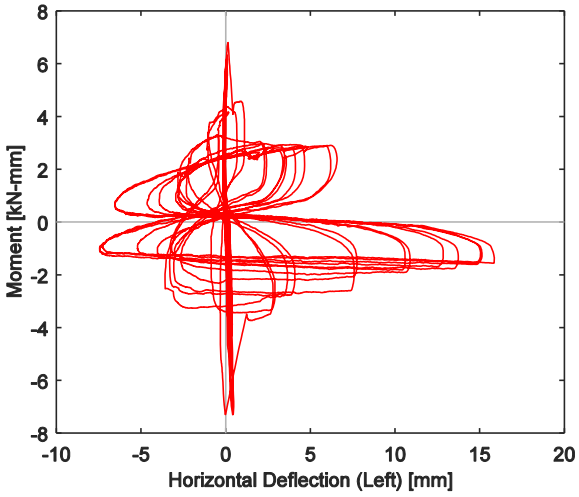
Moment [kN-mm]
Horizontal Deflection (Left) [mm]

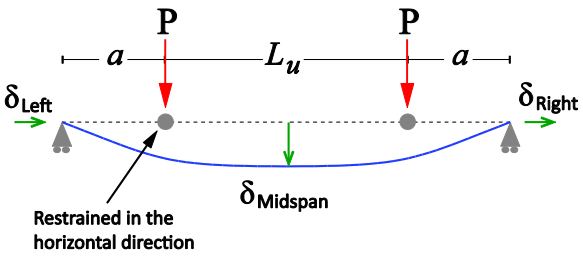
P
P
a
L_u
a
δ_{Left}
δ_{Right}
$\delta_{Midspan}$
Restrained in the horizontal direction

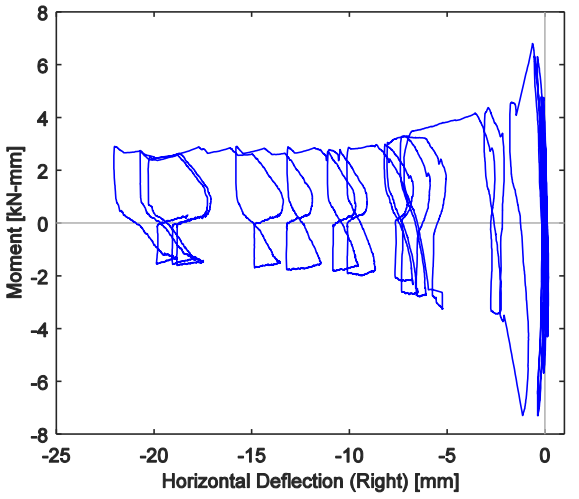
Moment [kN-mm]
Horizontal Deflection (Right) [mm]

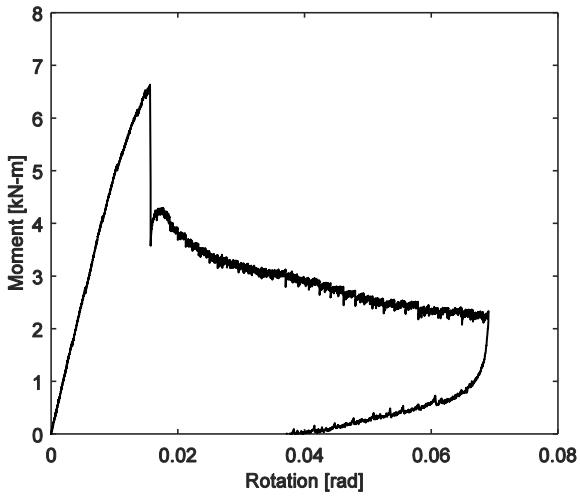
Moment [kN-m]
Rotation [rad]

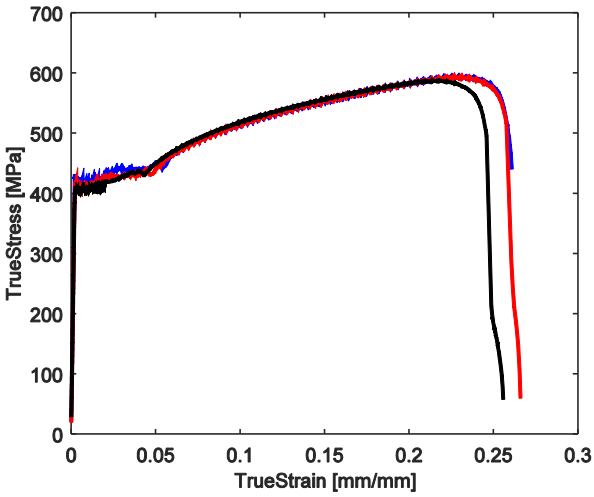
TrueStress [MPa]
TrueStrain [mm/mm]

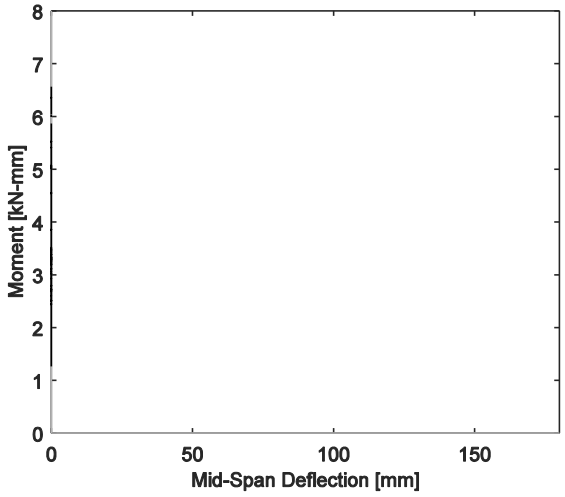
Moment [kN-mm]
Mid-Span Deflection [mm]

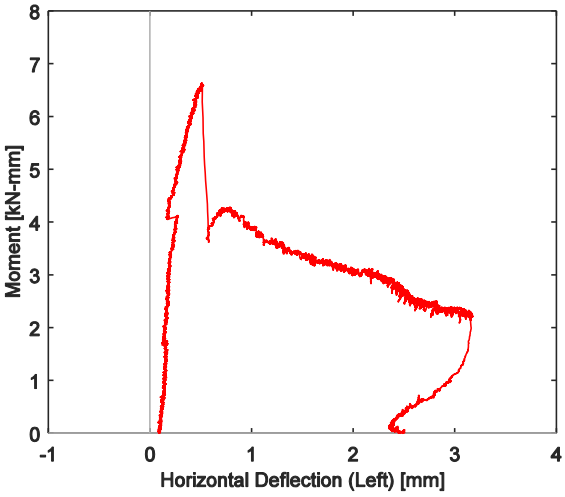
Moment [kN-mm]
Horizontal Deflection (Left) [mm]

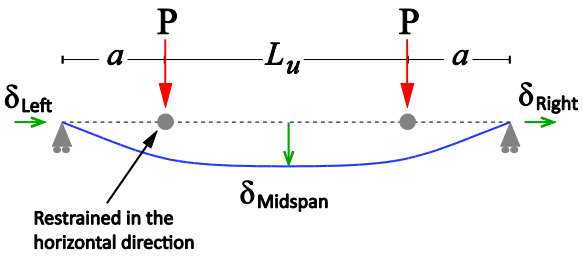
P
P
a
L_u
a
δ_{Left}
δ_{Right}
$\delta_{Midspan}$
Restrained in the horizontal direction

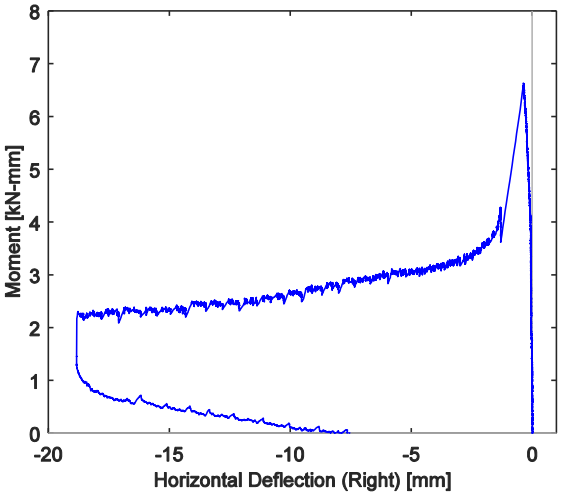
Moment [kN-mm]
Horizontal Deflection (Right) [mm]

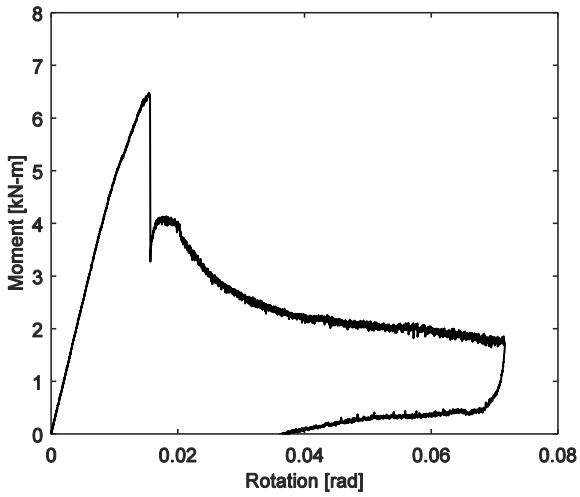
Moment [kN-m]
Rotation [rad]

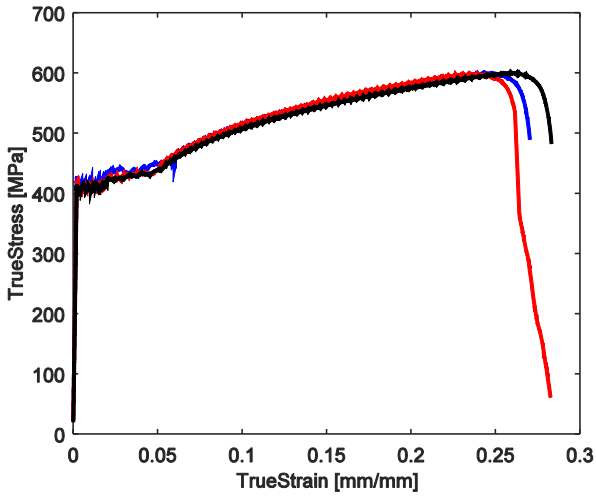
TrueStress [MPa]
TrueStrain [mm/mm]

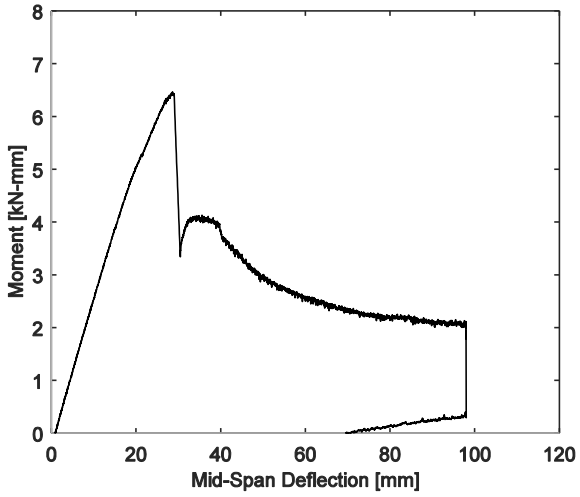
Moment [kN-mm]
Mid-Span Deflection [mm]

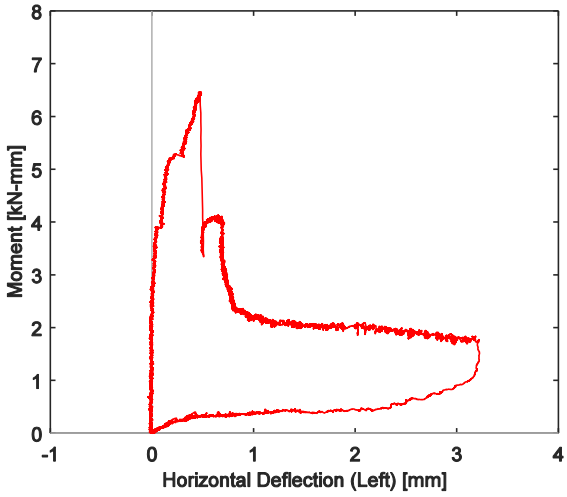
Moment [kN-mm]
Horizontal Deflection (Left) [mm]

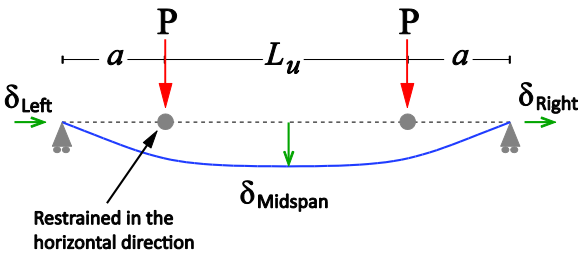
P
P
a
L_u
a
δ_{Left}
δ_{Right}
$\delta_{Midspan}$
Restrained in the horizontal direction

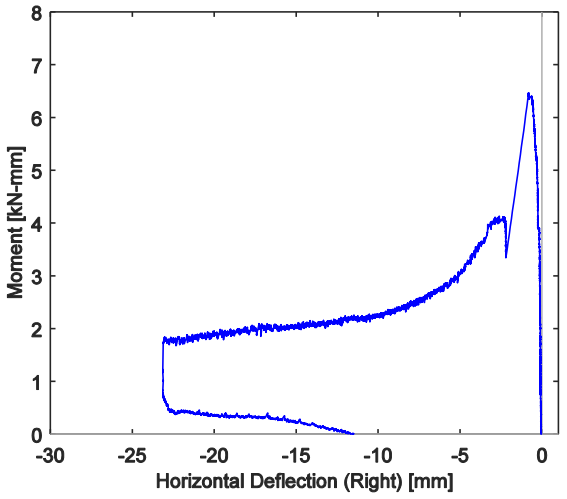
Moment [kN-mm]
Horizontal Deflection (Right) [mm]

800S200-33-LFC-1

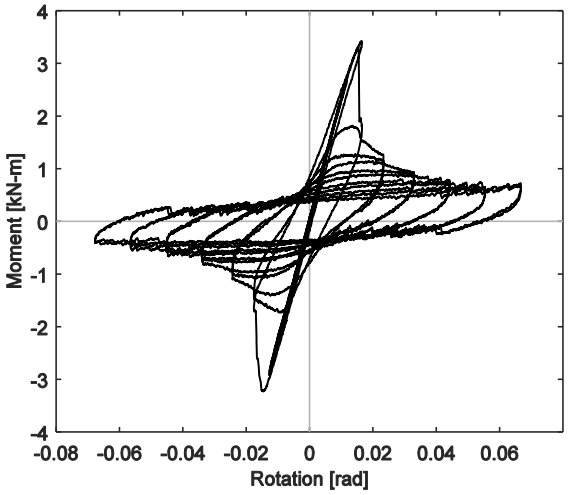

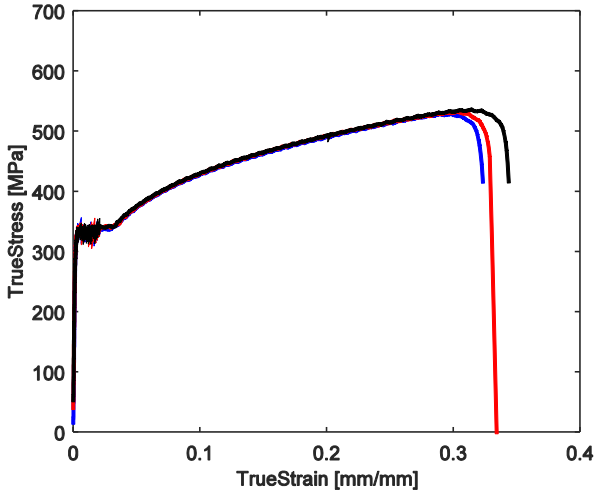

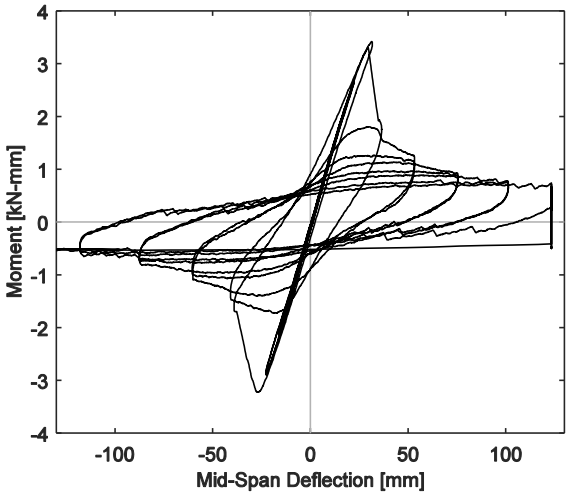

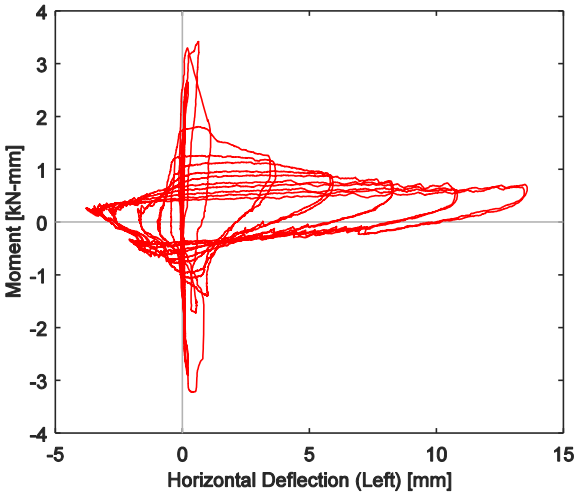

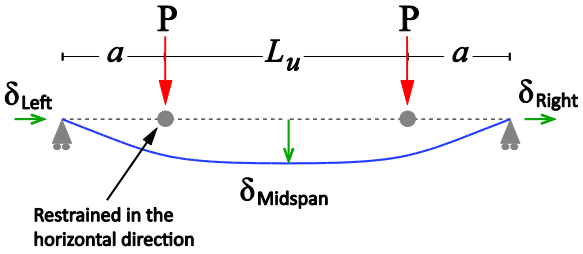

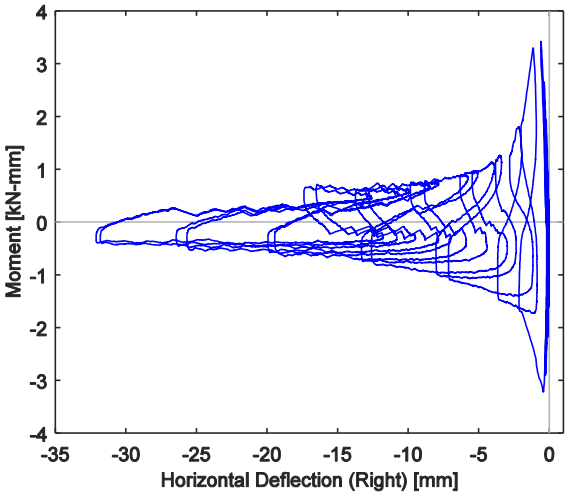

800S200-33-LFC-2

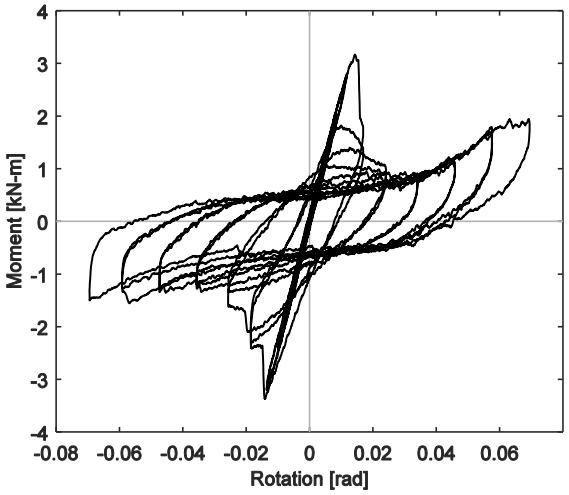

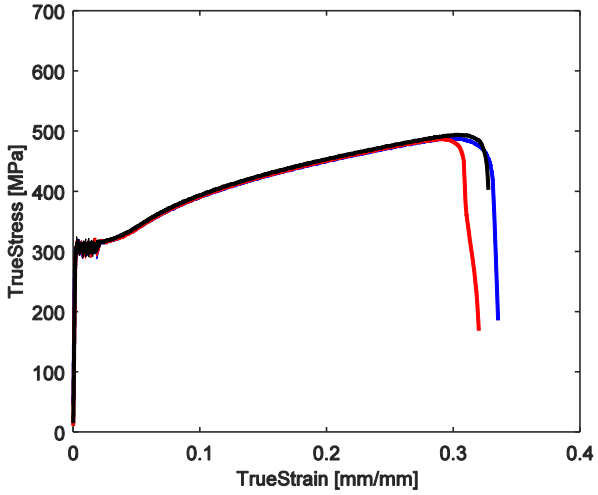

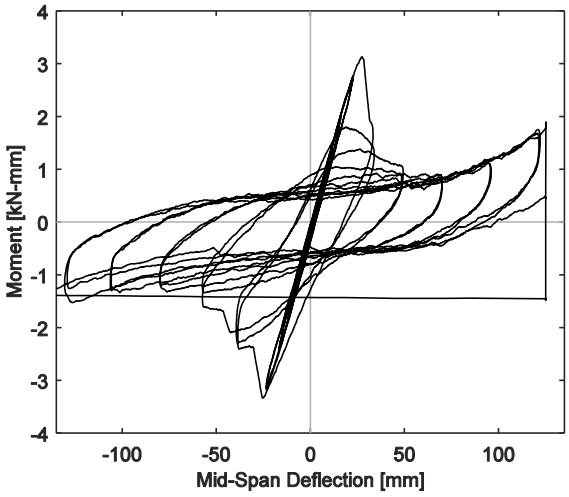

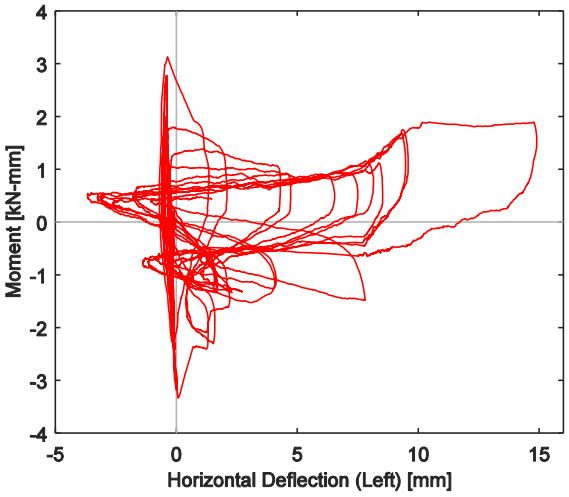

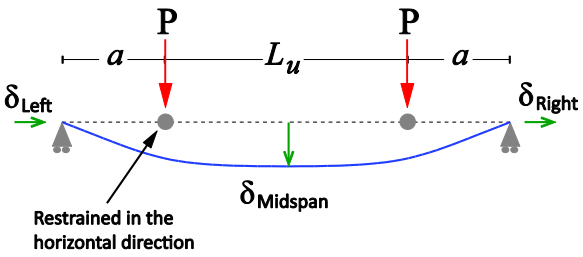

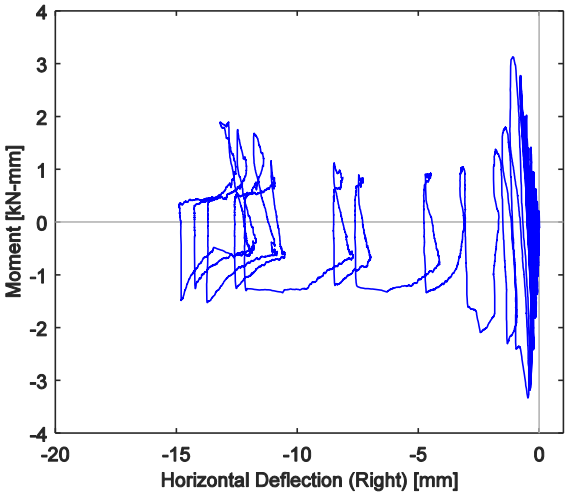

800S200-33-LFM-1

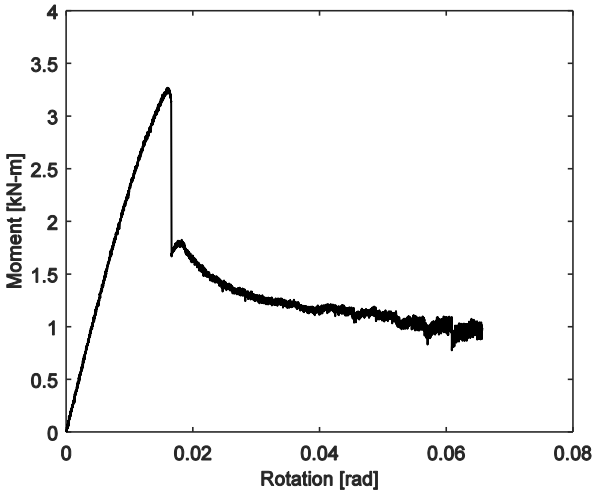

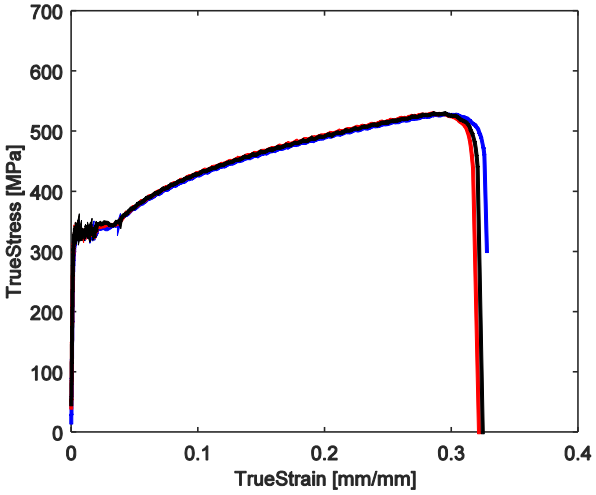

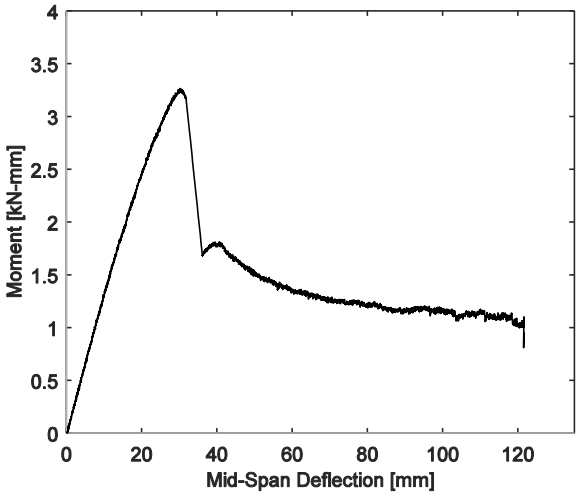

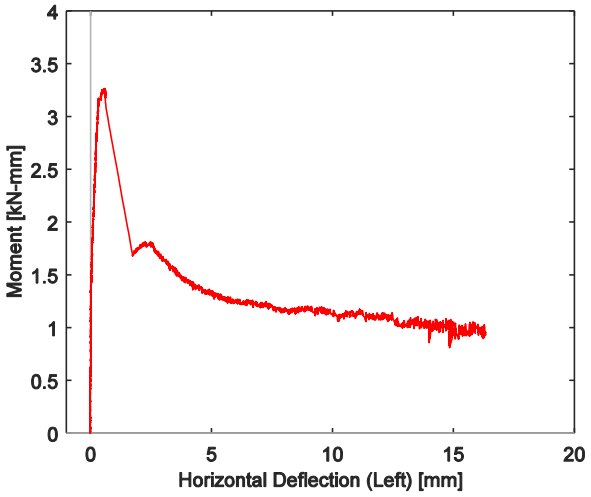

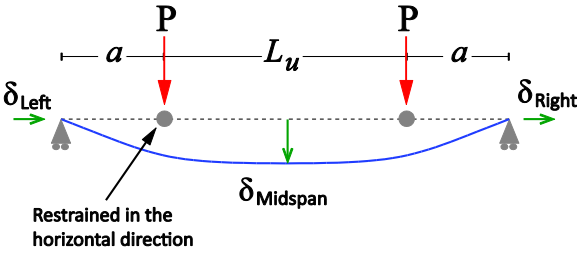

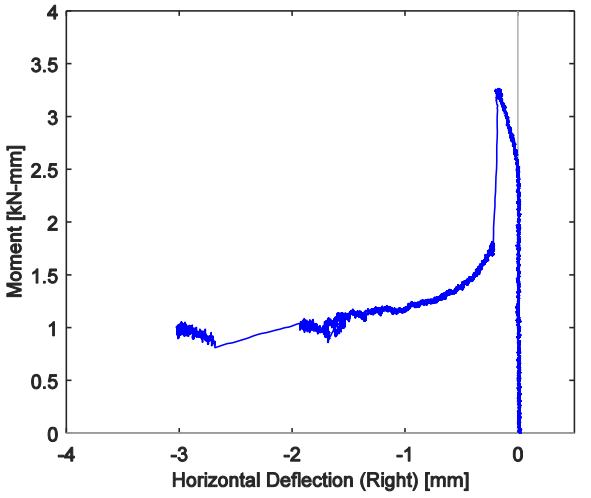

800S200-33-LFM-2

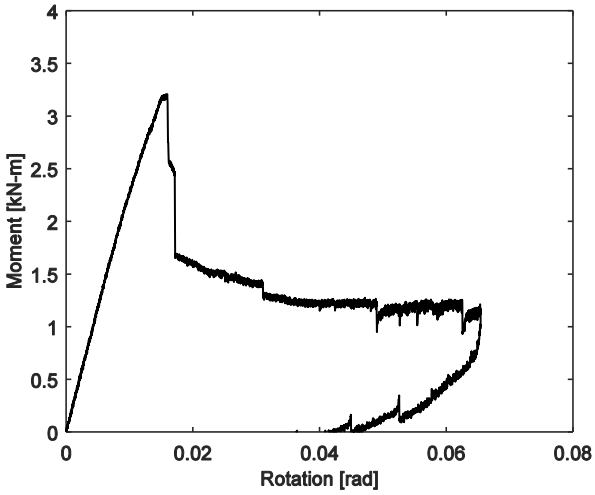

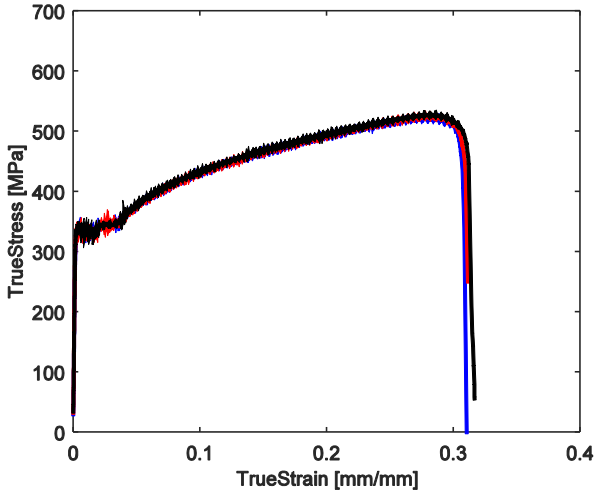

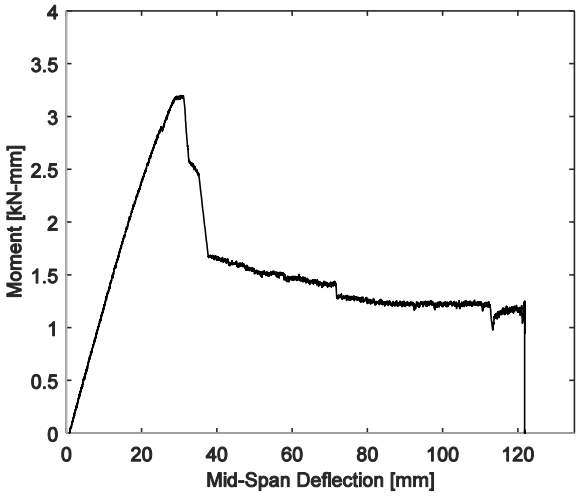

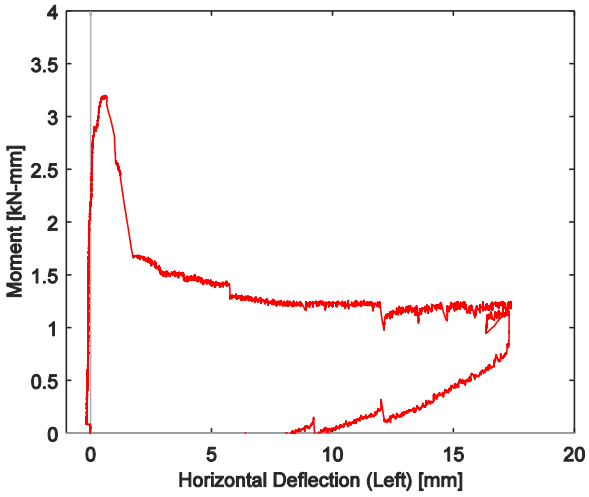

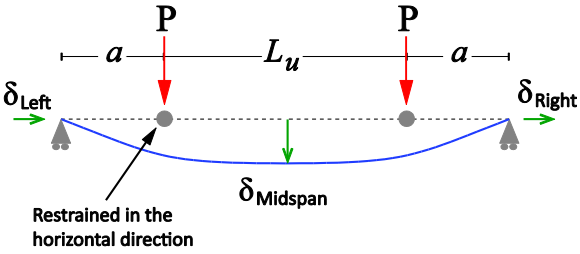

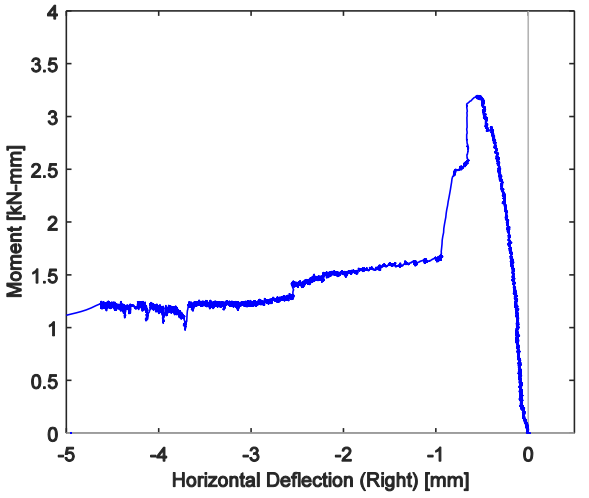

Appendix E Member Imperfections Measurements and Characterization [8]

This appendix describes program that uses a 3D non-contact method for measuring initial geometric imperfection fields in cold-formed steel (CFS) lipped channels. Tables and figures of measured cross-section and global imperfections and imperfections profiles are provided for 20 of the tested specimens from Chapter 3 and 4. The work described in this appendix has been presented as part of a co-authored conference paper at the Annual Stability Conference, SSRC 2014 Stability Conference [E.1].

Thin-walled CFS structural member cross-sectional dimensions are much larger than their base metal thickness, which makes their load-deformation response sensitive to initial geometric imperfections. Stiffness and ultimate strength tend to decrease when imperfections are present [E.2, E.3] either as local imperfections caused by shipping and handling or global imperfections along the length, e.g., sweep caused from sheet coiling [E.4, E.5, E.6]. A first step, and the focus of this paper, is to define and validate a procedural framework for accurately measuring, characterizing, and organizing 3D imperfection fields.

The most frequently used method to characterize global imperfections considers a maximum imperfection amplitude (e.g., $L/960$ for sweep in [E.7]). The method typically used to characterize cross-sectional imperfections considers two types: local web (δ_w) and local flange (δ_f) imperfections, as shown in Fig. E.1 (e.g., [E.8]). This method uses probability density functions of occurrence for a specific imperfection magnitude to set as the maximum imperfection amplitude (proportional to member thickness) and using cross-sectional buckling modes to distribute it along the member. The probability density functions were derived from single point hand measurements of imperfections along a member length. This probabilistic approach is still applicable for 3D imperfection fields. However, updated methods for using imperfection shapes and magnitudes in computational simulations are needed as 3D data fields are collected.

Recent work is beginning to hash out these new recommendations, starting with a comprehensive U.S. imperfection measurement study of 210 CFS specimens [E.9] that also

---

[8] This appendix is part of a co-authored paper presented at the *Annual Stability Conference SSRC 2014*, with the title **"Initial Geometric Imperfection Measurement and Characterization of Cold-Formed Steel C-Section Structural Members with 3D Non-Contact Measurement Techniques"**.

collected and summarized existing imperfection measurements from previous studies, including full-field measurements on channel sections [E.10, E.11, E.12]. Spectral approaches for representing imperfections now exist for combinations of buckling modes [E.9]. The work presented in this appendix expands on these ideas with a simple procedure that uses a generalized sum of sine-waves δ to describe magnitude imperfection variations along the length and that are imposed by directly modifying the member cross section geometry through simple transformations.

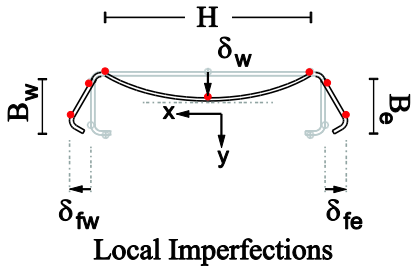

Fig. E.1. Imperfections defined by Schafer and Peköz [E.8].

E.1. Imperfection measurements using photogrammetry

In the photogrammetry method, a CFS member is covered with unique, recognizable targets strategically placed to capture its geometry. Sets of photos are taken from multiple viewpoints around the specimen, and processed using commercial software PhotoModeler [E.13], to identify all the targets. A gradient based optimization algorithm built into PhotoModeler finds the spatial coordinates of each target based on the oriented projections from each picture. The result is a 3D point cloud with the *x*-*y*-*z* coordinates of each target.

Ringed automatically detected (RAD) targets and plain dot targets were used in this study (Fig. E.2a-b). RAD targets are unique markers, each with a different pattern that allows automated photo processing with PhotoModeler. Unlike RAD targets, all dot targets are identical. Both targets can be scaled to fit within member dimensions.

On each member, RAD targets were affixed along the web and flanges at equal spacing, and dot targets were placed along longitudinal lines 2 through 8 in Fig. E.2c. Photo sets of the specimen were taken from different angles and positions along the member's length. The following parameters were used to obtain optimum accuracy in PhotoModeler: each photo set contained (i) photos with at least 50% point coverage, (ii) at least 50% point overlap between photos, (iii) at least 10 RAD targets in each photo, and (iv) a camera station angle separation between 30° and

90° for most photos. The 3D point cloud obtained is used to obtain local and global imperfection shapes and magnitudes relative to a perfect reference specimen as described after next section.

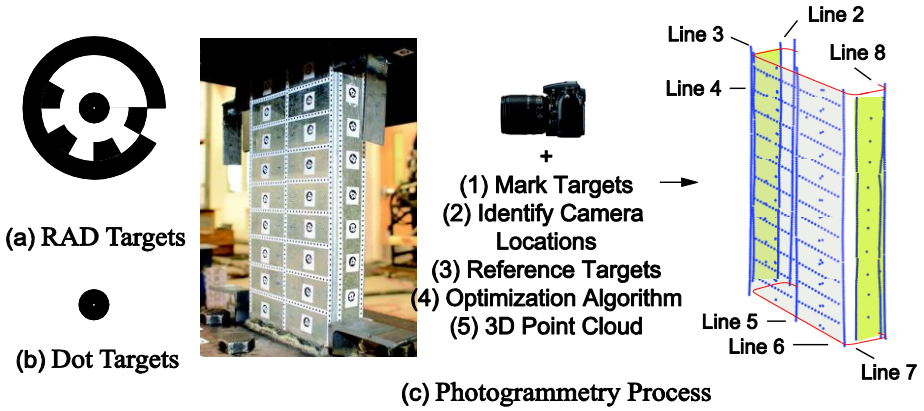

Fig. E.2. (a) RAD targets and (b) dot targets are used to (c) complete the photogrammetry process of marking targets, identifying camera locations, referencing targets, and using an optimization algorithm to process a 3D point cloud.

E.2. Imperfection measurements using dial gages mounted on precision rail

Manual measurements from three dial gages mounted to a carriage riding on a high-precision aluminum rail along the member's length as depicted in Fig. E.3. Imperfections are manually measured at three locations across the web, corresponding to lines 4, 5, and 6 in Fig. E.3, at 25 mm, 51 mm, or 152 mm longitudinal increments, for member lengths of L=305mm, 610mm and $L \geq$ 2286mm respectively. Dial gauge measurements were used to obtain global and local web imperfection shapes and magnitudes. Flange imperfections in the manual measurement method were derived from measured cross-section dimensions.

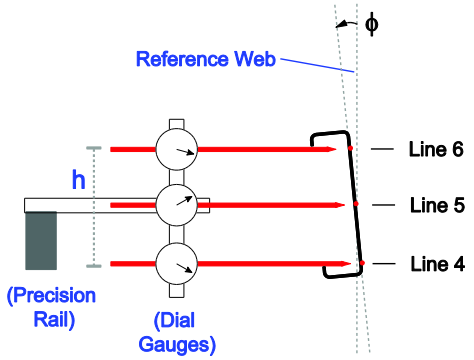

Fig. E.3. Dial gage and precision rail setup for manual measurements.

Although the procedures to obtain a 3D point cloud to represent the geometry of a CFS member are different for manual and photogrammetry methods, the definitions and notations described in the following section apply to both.

E.3. Measurement definitions and notation

Initial geometric imperfections are defined as the measured geometry deviations from a perfect reference member. A perfect member is straight and has a perfect C-shaped cross-section. The *perfect C-shaped cross-section* has a flat web surface, flat flanges perpendicular to the web, and dimensions corresponding to measured values at each member mid-length as shown Fig. E.4a. Five imperfection quantities named: out-of-straightness in the weak axis (δ_B), out-of-straightness in the strong axis (δ_C), twist (ϕ), web local buckling (δ_W), and flange imperfections (δ_{FE} and δ_{FW}) are characterized herein, see Fig. E.4. Longitudinal lines extending the length of the measured member and located as shown in Fig. E.4a are used in this study to compute local imperfections pertinent to CFS channel sections. Lines 2-4 and 6-8 are located at the edges of the corresponding flat portions of the cross-section, such that points on these lines do not fall on the cross-section's rounded corners. Line 5 is located at the center of the measured web height. Dot targets (Fig. E.2b) were placed along these lines making sure they laid flat to directly obtain the needed coordinates.

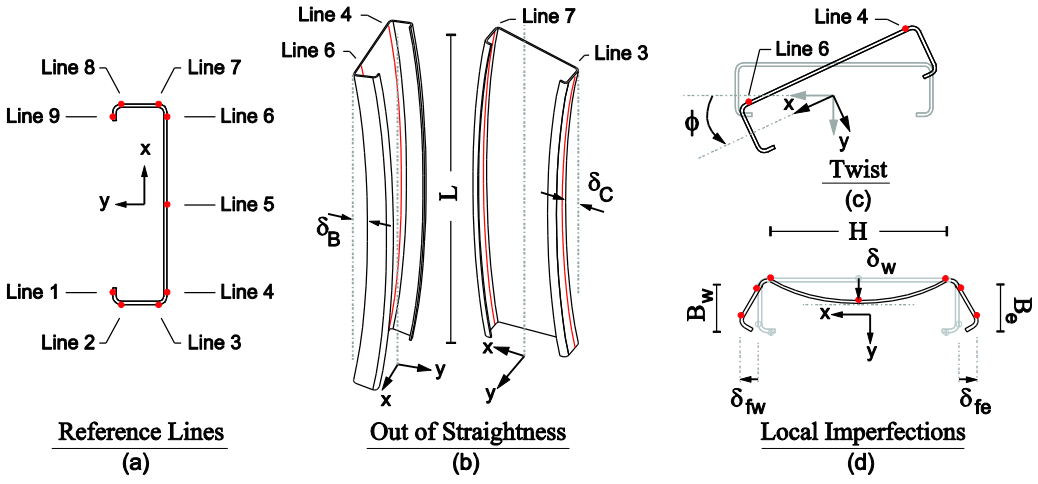

Fig. E.4. Global and local imperfection definitions.

The orientation of the measured 3D point cloud is defined by first finding the principal axes of the point cloud. To find the principal axes an orthogonal least squared approach is used to determine the 3D line that best fits the point cloud and two orthogonal vectors that will complete

the reference coordinate system. The principal component analysis, PCA [E.14] was used in this study to find these principal axes, however, more complex procedures could also be used (e.g. [E.15]. For a prismatic member without imperfections (e.g., channel) the PCA procedure gives the direction vector of the 3D line aligned with the longitudinal axis, the direction of the major cross-section axis and the direction of the minor cross-section axis. In a member with imperfections, the 3D line that best fits the point cloud should align with the longer dimension, thus the length L of the member, and it will be regarded herein as the *reference axis*. The 3D point cloud is the rotated such that the *reference axis* is vertical, aligning with the z-axis and the two orthogonal vectors align with the x- and y- axes respectively.

E.3.1. Global imperfections

Global imperfections, i.e., out-of-straightness and twist, are defined, after orienting the member, respect to a *centroidal axis* of the member that is determined as follows. Cross sections are sampled for different z-coordinates along the *reference axis*, their centroid is found as well as the cross-section principal axes (using the PCA for example). The centroid of all sampled cross sections defines the *centroidal axis* and the centroid of this centroidal axis defines the *center point* needed to derive global sweep imperfections. The principal axes are used to obtain initial twist imperfections. Out-of-straightness in the weak axis direction, δ_B, (see Fig. E.4b), at a specific z-coordinate along the length, is the distance parallel to the y- axis between points in the *centroidal axis* to the *center point*. Similarly, out-of-straightness in the strong axis direction, δ_C, at a certain z-coordinate along the length is the distance parallel to the x- axis between points in the *centroidal axis* to the *center point* (see Fig. E.4b). The cross-section initial twist, ϕ at a specific z-coordinate along the length is the angle between the major principal axes (found using PCA or other methods), and the x-axis, as shown in Fig. E.4c.

E.3.2. Cross-sectional imperfections

Local imperfections, i.e., local web and flange imperfections, are defined respect to a *perfect C-shaped cross-section* that rides along the member that has global imperfections. Such *perfect C-shaped cross-section* is defined using measured dimensions. The web imperfection magnitude, δ_W, at any $\boldsymbol{z}$-coordinate along the member is the perpendicular distance from a point in line 5 to the web of the *perfect C-shaped cross-section*, i.e., the line connecting points in lines 4 and 6 (see Fig. E.4d). The flange east and west imperfections, δ_{FE} and δ_{FW}, are computed as the

perpendicular distances of points in lines 2 and 8 to the corresponding flanges of the *perfect C-shaped cross-section*, as shown in Fig. E.4d.

E.4. Imperfection study using photogrammetry

The imperfection reference system and notation described in the previous section were employed in this section to characterize imperfections for 20 of the tested CFS specimens from Chapter 3 and 4. The measured cross-section dimensions are summarized in Table E.1.

Table E.1. Measured specimen dimensions (photogrammetry and manual methods).

Specimen	L (mm)	D_E (mm)	D_W (mm)	B_E (mm)	B_W (mm)	H (mm)	RT_E (mm)	RT_W (mm)	RB_E (mm)	RB_W (mm)	F_E (°)	F_W (°)	S_E (°)	S_W (°)	t (mm)
362S137-68-GAC-2	2286	11.8	13.3	34.4	33.4	93.3	4.0	4.0	4.4	4.4	88.5	88.2	-2.5	4.1	1.82
800S162-97-GFC-2	3048	12.0	13.4	40.4	40.3	203.9	4.8	5.2	5.4	5.2	90.1	88.6	0.3	2.2	2.50
800S162-97-GFM-2	3048	12.2	13.6	40.2	40.0	203.8	4.8	5.2	5.4	5.2	88.6	87.8	0.1	2.0	2.51
1200S162-97-GFC-1	3048	9.8	11.2	42.7	43.2	305.6	4.8	5.2	5.5	5.5	91.4	87.7	-3.4	0.4	2.52
362S162-54-LAM-2	305	11.7	12.2	42.3	41.6	92.7	4.2	4.4	3.6	4.4	89.2	89.2	3.2	2.2	1.44
362S162-54-LAC-1	305	11.7	11.8	42.0	41.6	92.7	4.0	4.4	3.6	4.4	88.9	89.5	1.0	2.0	1.44
600S162-33-LAM-2	305	13.0	13.5	42.0	41.5	150.3	3.6	4.0	3.6	4.4	88.1	91.9	2.0	-0.2	0.86
600S162-33-LAC-2	305	12.7	13.6	41.9	41.5	150.3	3.6	4.0	3.2	4.4	86.6	89.1	3.1	3.6	0.86
800S200-33-LFM-2	1626	14.6	14.7	50.1	49.8	204.6	3.6	3.6	3.1	3.2	91.3	89.4	-0.6	0.8	0.88
800S200-33-LFC-2	1626	13.9	14.3	52.8	50.3	203.7	3.6	4.4	3.2	3.2	89.7	90.7	-0.8	0.9	0.95
1000S200-43-LFC-2	1626	10.3	12.0	49.1	50.0	254.4	3.6	3.6	3.2	3.6	90.4	87.0	0.5	1.5	1.15
1000S200-43-LFM-2	1626	10.2	12.0	49.2	50.3	254.5	3.6	3.6	3.2	3.6	90.3	87.2	0.8	1.6	1.16
362S137-68-DAM-2	610	12.0	12.9	34.5	33.9	93.3	4.0	4.0	4.4	4.4	89.8	86.4	-2.0	4.2	1.82
362S137-68-DAC-2	610	11.6	13.4	34.4	33.9	93.2	4.0	4.0	4.4	4.4	89.7	86.2	-2.1	4.0	1.81
600S137-68-DAM-2	610	10.7	11.5	34.8	33.8	152.7	4.0	4.0	4.4	4.0	90.5	89.5	-1.4	-0.7	1.80
600S137-68-DAC-2	610	10.5	11.9	34.9	33.8	152.5	4.0	4.0	4.4	4.2	89.9	89.6	-1.1	-0.1	1.80
800S250-68-DFC-2	1626	14.5	11.9	64.3	63.2	204.1	8.7	4.1	6.1	4.0	90.6	90.6	-4.1	-3.9	1.80
800S250-68-DFM-2	1626	14.4	12.1	64.4	63.6	204.2	4.4	4.0	4.4	4.0	90.8	90.6	-4.8	-4.2	1.84
1200S250-97-DFC-1	1626	12.8	14.4	65.7	65.7	306.5	5.2	5.6	5.6	5.6	92.1	89.7	-4.6	-3.6	2.57
1200S250-97-DFM-1	1626	12.7	14.6	65.1	65.9	306.7	5.2	5.6	5.6	5.6	92.5	89.6	-5.1	-2.7	2.58

E.4.1. Maximum imperfection magnitudes

Maximum imperfection magnitudes were determined for all 20 members. Maximum imperfection magnitudes do not reflect the variation of imperfections along the length of the member and are provided here as reference measurements for comparison to commonly accepted limits, including those defined in ASTM C955-09 standard [E.7]. The tolerance in ASTM C955 for out-of-straightness imperfections is $L/960$, for local web and flange imperfections is 1.59mm; and for twist $L/384$ (max 12.7mm). Measurement statistics are summarized in Table E.2 for each imperfection type, measurement method, and targeted buckling mode. The average maximum measured imperfections were generally smaller than these tolerances (see *mean* values in Table E.2).

Maximum imperfections are compared to ASTM C955-09 tolerances in Fig. E.5. Results show that most maximum imperfections fall below the ASTM C955-09 limits, and that out-of-straightness imperfections generally increase with length (Fig. E.5a-b). Global imperfections magnitudes increase with sheet thickness because of the plastic strains caused by coiling of the sheet for transportation and manufacturing. Initial twist in longer members was less than the ASTM limits while for short members with narrow webs twist tended to have imperfections greater than the ASTM tolerance. Fig. E.5d shows that local web imperfections typically increase with web slenderness (H/t), and Fig. E.5e shows that flange imperfections generally decrease with flange slenderness (B/t). These trends are associated to through-thickness nonlinear residual stresses and elastic spring-back from the cold formed bending of the flanges [E.5].

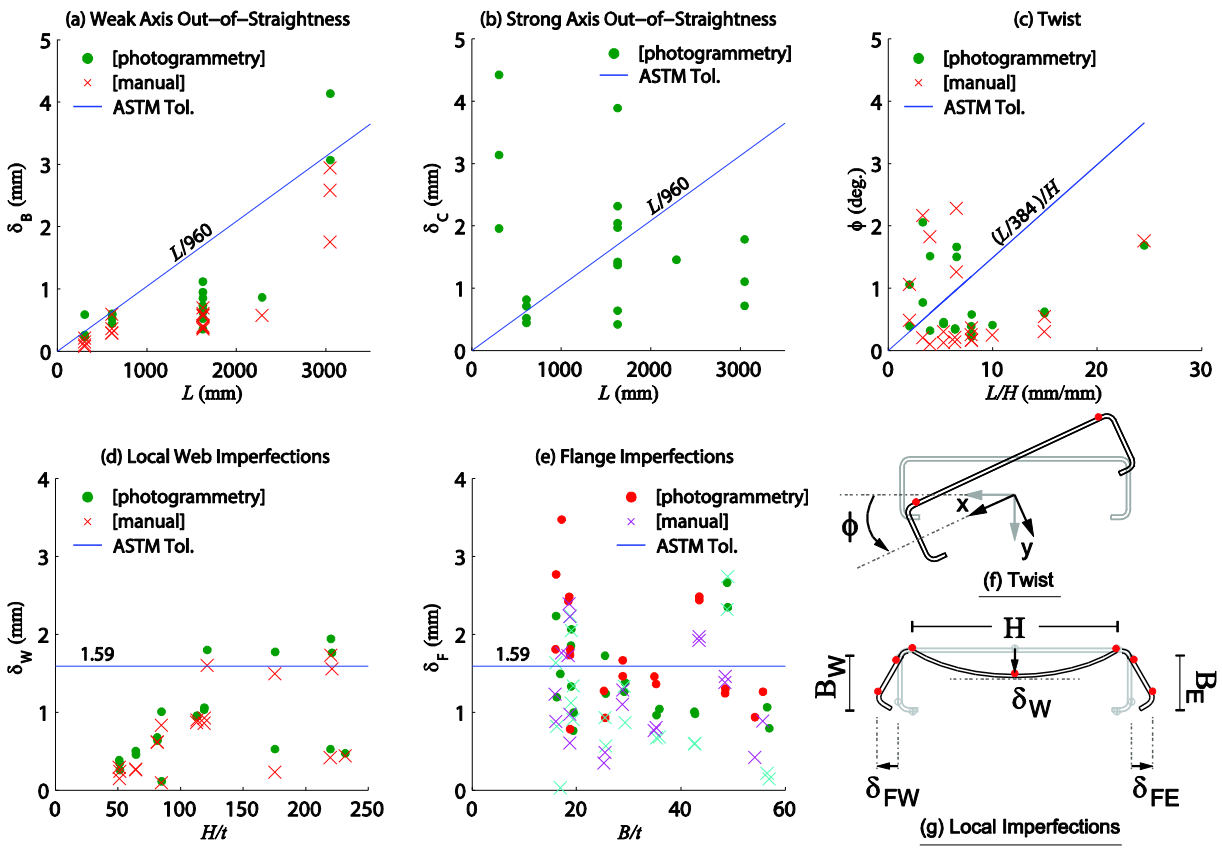

Fig. E.5. Maximum imperfection magnitudes and ASTM C955-09 tolerance limits.

Table E.2. Maximum imperfection magnitudes (photogrammetry and manual methods).

			Weak Axis Out-of-Straightness	Strong Axis Out-of Straightness	Twist	Local Web	Local Flange (East)	Local Flange (West)
			δ_B/L (x10^{-3})	δ_C/L (x10^{-3})	ϕ (°)	δ_W/H (x10^{-3})	δ_{FE}/B_E (x10^{-3})	δ_{FW}/B_W (x10^{-3})
Manual	Global	Mean	0.55 (L/1813)	-	0.99	2.79 (H/359)	25.88 (B/39)	40.36 (B/25)
		Max.	0.97 (L/1035)	-	1.76	5.24 (H/191)	40.52 (B/25)	51.57 (B/19)
		Min.	0.25 (L/3970)	-	0.25	1.59 (H/628)	0.65 (B/1527)	21.92 (B/46)
		St.Dev.	0.11	-	0.09	0.70	10.96	5.20
		COV	0.14	-	0.24	0.19	0.54	0.17
	Local	Mean	0.37 (L/2740)	-	0.55	4.29 (H/233)	23.76 (B/42)	28.42 (B/35)
		Max.	0.68 (L/1465)	-	2.16	9.93 (H/101)	65.36 (B/15)	39.14 (B/26)
		Min.	0.24 (L/4226)	-	0.14	1.53 (H/653)	2.73 (B/367)	8.36 (B/120)
		St.Dev.	0.13	-	0.42	3.11	12.07	10.11
		COV	0.33	-	0.54	0.73	0.57	0.38
	Distortional	Mean	0.46 (L/2193)	-	0.75	3.32 (H/301)	27.24 (B/37)	25.72 (B/39)
		Max.	0.97 (L/1028)	-	2.28	5.45 (H/183)	64.82 (B/15)	70.55 (B/14)
		Min.	0.22 (L/4513)	-	0.10	0.63 (H/1597)	8.59 (B/116)	5.35 (B/187)
		St.Dev.	0.16	-	0.48	1.35	9.46	13.81
		COV	0.33	-	0.57	0.43	0.29	0.47
Photogrammetry	Global	Mean	0.92 (L/1090)	0.50 (L/1987)	1.06	3.95 (H/253)	39.42 (B/25)	68.38 (B/15)
		Max.	1.71 (L/586)	0.64 (L/1572)	1.69	5.89 (H/170)	55.48 (B/18)	80.53 (B/12)
		Min.	0.38 (L/2636)	0.24 (L/4246)	0.41	3.14 (H/319)	29.42 (B/34)	45.33 (B/22)
		St.Dev.	0.19	0.10	0.06	0.84	7.53	9.86
		COV	0.14	0.25	0.12	0.21	0.19	0.15
	Local	Mean	0.76 (L/1312)	6.28 (L/159)	0.71	5.57 (H/179)	31.10 (B/32)	34.96 (B/29)
		Max.	1.94 (L/516)	18.33 (L/55)	2.06	11.81 (H/85)	63.67 (B/16)	49.69 (B/20)
		Min.	0.32 (L/3087)	0.39 (L/2548)	0.34	2.32 (H/432)	15.06 (B/66)	18.69 (B/54)
		St.Dev.	0.35	2.79	0.38	3.20	9.09	10.72
		COV	0.42	0.56	0.45	0.57	0.25	0.30
	Distortional	Mean	0.62 (L/1613)	0.95 (L/1052)	0.75	3.83 (H/261)	28.98 (B/35)	33.41 (B/30)
		Max.	0.99 (L/1009)	1.34 (L/746)	1.66	6.61 (H/151)	60.08 (B/17)	73.25 (B/14)
		Min.	0.22 (L/4543)	0.26 (L/3880)	0.22	0.75 (H/1339)	15.09 (B/66)	14.12 (B/71)
		St.Dev.	0.12	0.38	0.34	1.50	11.21	11.41
		COV	0.24	0.41	0.41	0.41	0.35	0.29

L= specimen length; H = web widht; B_E = east flange width; B_W = west flange width;
n = number of specimens in the group.

E.4.2. Imperfection shapes

Global and local imperfection shapes for specimen 362S137-68-DAM-2 (L=609.6mm) are plotted in Fig. E.6 and Fig. E.7. Local imperfections shapes (δ_W, δ_{FE}, and δ_{FW},) vary along the length because of residual stresses induced by the cold forming process and elastic spring-back [E.5]. The spring-back is greater at the ends of the members due to the decreased cross-sectional restraint yielding greater cross-sectional imperfections, as shown in Fig. E.7, and resulting in opening of the cross-section. Additional imperfections can be induced in the members during transportation and/or installation specially when connecting them to other members/pieces. The specimens in this study had 15.9mm end plates welded at both ends that could increase the cross-sectional imperfections magnitudes towards the ends due to the thermal expansion during welding,

see Fig. E.7. The imperfection shapes obtained using the photogrammetry and manual measurement methods for all 20 specimens are qualitatively consistent (see Fig. E.6 and Fig. E.7). Imperfection shapes of the remaining specimens are shown at the end of this appendix.

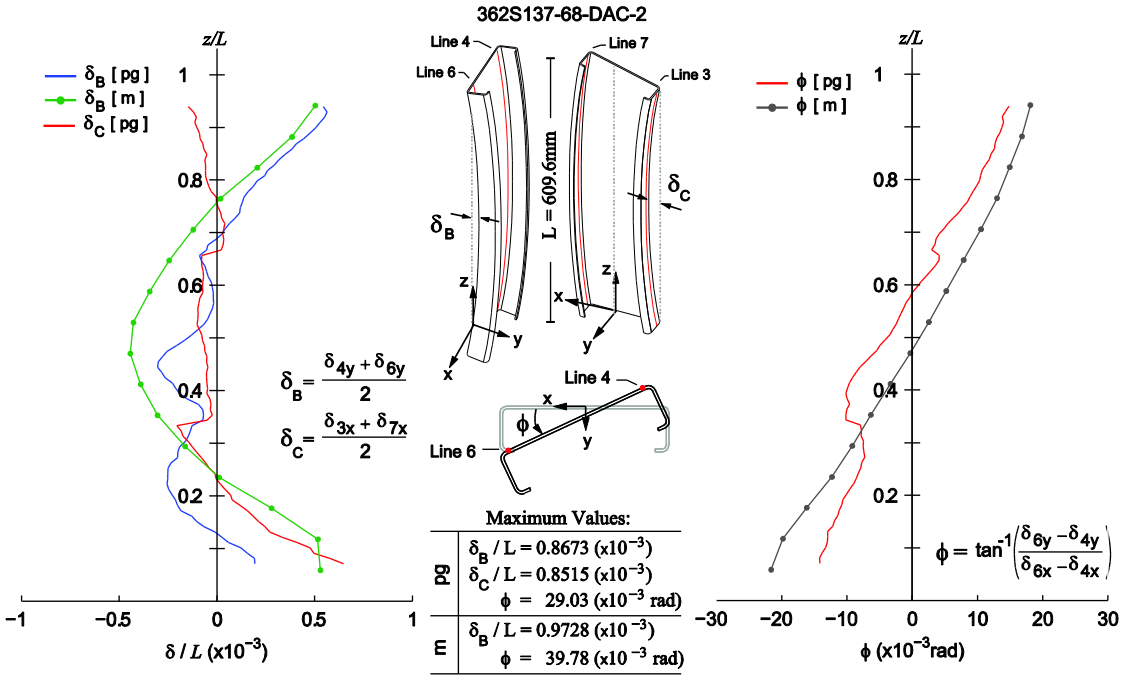

Fig. E.6. Global imperfections for specimen 362S137-68-DAM-2 (pg = photogrammetry, m = manual).

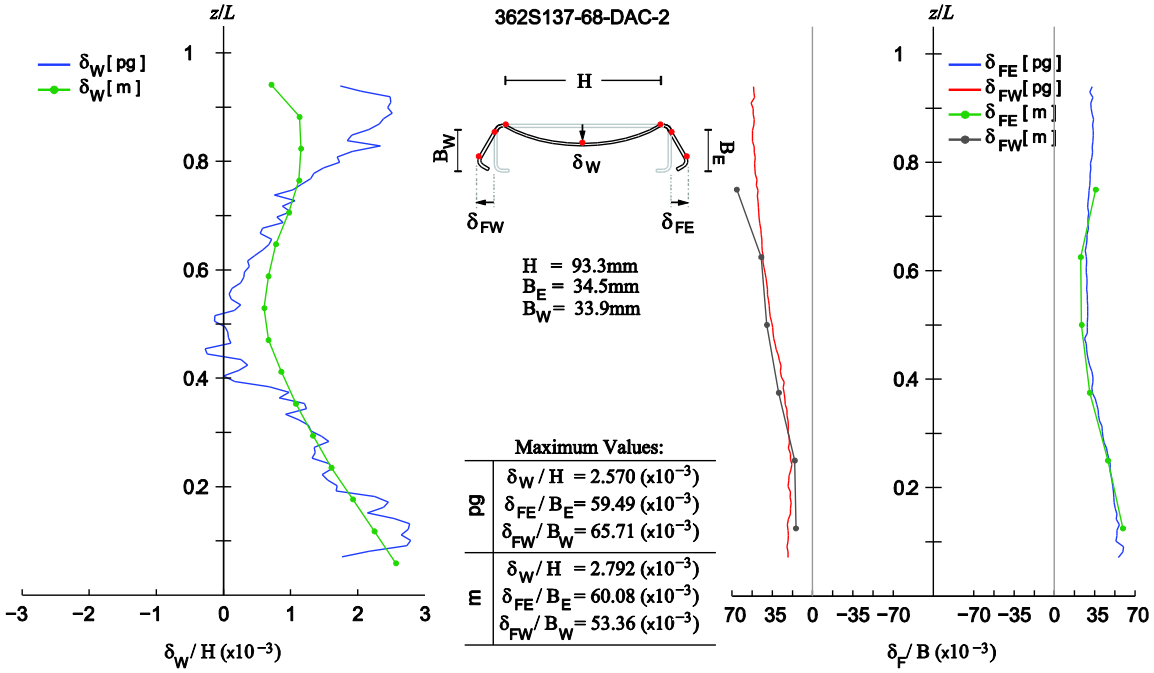

Fig. E.7. Local imperfections for Specimen 362S137-68-DAM-2 (pg = photogrammetry, m = manual).

E.5. Imperfection Characterization Method

Imperfections measurements from the photogrammetry method were used to characterize specimen imperfect geometry as trigonometric series to describe imperfection magnitudes that are superposed to the geometry of a perfect cross-section. This type of characterization makes it possible to represent the initial geometry with a limited set of variables as opposed to use a large 3D point cloud. The initial geometry including imperfections can be reconstructed by modifying the geometry of the perfect cross-section in Fig. E.8a such that the coordinates of points 2 to 8 match the shapes of the imperfections δ_B, δ_C, ϕ, δ_W, δ_{FE}, and δ_{FW}. For local web imperfections for example, the geometry is modified such that the out-of-plane deformation at any point along line 5 (i.e., P5 in Fig. E.8a) is equal to δ_W. The first step for this characterization requires a continuum representation of the imperfection magnitudes along the length. A sine-wave consisting of four terms plus a linear term was fit using a least-squares-approach to the measured imperfection shapes of the 20 specimens listed in Table E.1 as shown in Eq. E.1

$$\delta_i(z) = (mz + b) + \sum_{k=1}^{4} C_k \sin\left(\frac{\pi}{L_k} z + \varphi_k\right) \qquad \text{E.1}$$

where $mz+b$ is the linear fit of the member, C_k ,L_k and φ_k respectively are the amplitude, the half-wavelength, and the phase angle of each sine-wave term. The linear term '$mz + b$' was subtracted from the data before fitting the sine-wave series in Eq. E.1. The fitted parameters are provided in Table E.3 to Table E.5.

The procedure to impose initial imperfections on the perfect geometry of a member by modifying the geometry of a *perfect C-shaped cross-section* is depicted in Fig. E.8. For each cross-section along the length of the member, the geometry of the imperfect geometry is derived by first applying the local deformations, δ_W, δ_{FE}, and δ_{FW}, to the *perfect C-shaped cross-section,* as depicted in Fig. E.8b. The resulting geometry is then further modified by applying the global imperfections, ϕ, δ_B, δ_C, as illustrated in Fig. E.8c. The procedure demonstrated in Fig. E.8 is repeated to impose imperfections for any cross-section along the member.

The procedure to impose imperfections described above allows to consistently apply imperfections on a perfect member by directly modifying the geometry of the cross section to match the imperfections magnitude profiles $\delta(z)$. This differs from the traditional modal and modal spectral approaches, where imperfections are imposed as a linear combination of buckling modes (e.g., [E.9]). Buckling mode calculations are not needed in the proposed procedure (Fig. E.8) to

impose imperfections, only systematic geometry transformations. Imperfection profiles $\delta(z)$ can be of the form described by Eq. E.1 or any other that can properly represent the corresponding imperfection magnitude profile. The geometric transformations depend on the cross-sections and the imperfection definitions; however, they only need to be set up once for a cross-section type, as it is shown in Fig. E.8 for a channel section.

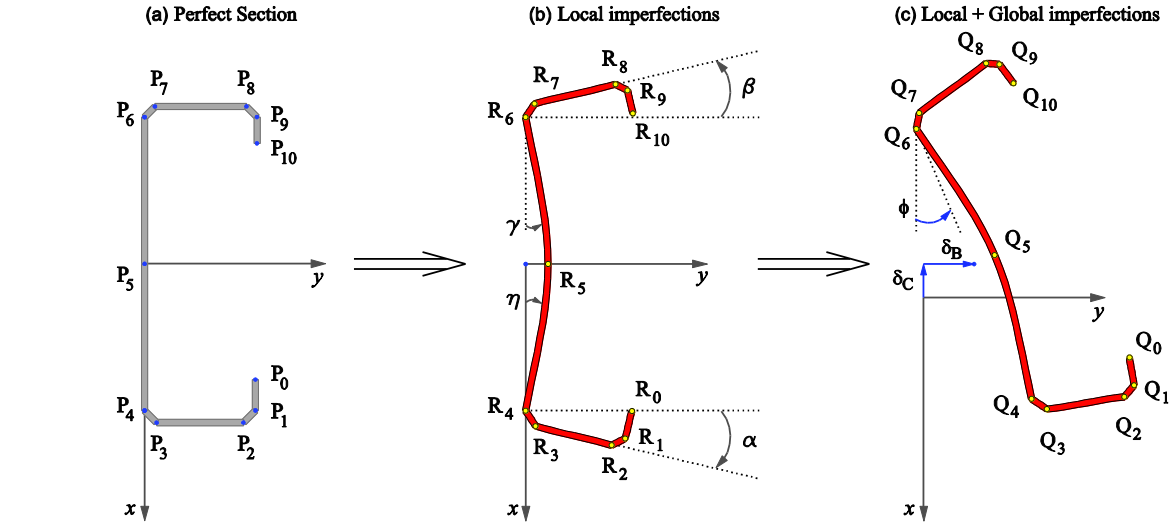

Step 1: Use Eq. (1) and Table 6 to obtain values of $\delta_B,\delta_C,\phi,\delta_w,\delta_{fe},\delta_{fw}$ for any cross section located at the z-coordinate along the member.

Step 2: Use values in Table 2 to obtain the perfect section geometry:

$$P_4=[(0.5H-RB_2)\ \ 0]^T \quad P_6=[-(0.5H-RB_1)\ \ 0]^T$$
$$P_3=[0.5H\ \ RB_2]^T \quad P_7=[-0.5H\ \ RB_1]^T$$
$$P_2=[0.5H\ \ (B_2-RT_2)]^T \quad P_8=[-0.5H\ \ (B_2-RT_1)]^T$$
$$P_1=P_2+[-RT_2\ \ RT_2]^T \quad P_9=P_8+[RT_1\ \ RT_1]^T$$
$$P_0=P_2+[-D_2\ \ RT_2]^T \quad P_{10}=P_8+[D_1\ \ RT_1]^T$$
$$P_5=[0\ \ 0]^T$$

Step 3: Apply local imperfections $\delta_w,\delta_{fe},\delta_{fw}$ from step 1

$$R_i=T_\alpha(P_i-Z)+Z,\ i=0...3$$
$$R_j=T_\beta(P_j+Z)-Z,\ j=7...10$$
$$R_4=P_4,\ R_6=P_6,\ R_5=[0\ \ \delta_w]^T$$
$$T_\alpha=\begin{bmatrix}\cos\alpha & -\sin\alpha\\ \sin\alpha & \cos\alpha\end{bmatrix},\ T_\beta=\begin{bmatrix}\cos\beta & -\sin\beta\\ \sin\beta & \cos\beta\end{bmatrix}$$
$$Z=[0.5H\ \ 0]^T$$
$$\alpha=-\sin^{-1}(\delta_{fw}/(B_2-RT_2)),\beta=\sin^{-1}(\delta_{fe}/(B_1-RT_1))$$
$$\gamma=\tan^{-1}(3\delta_w/(H-2RB_1)),\eta=-\tan^{-1}(3\delta_w/(H-2RB_2))$$

Step 4: Apply global imperfections δ_B,δ_C,ϕ from step 1

$$Q_k=T_\phi R_k+[\delta_C\ \ \delta_B]^T,\ k=0...10$$
$$T_\phi=\begin{bmatrix}\cos\phi & -\sin\phi\\ \sin\phi & \cos\phi\end{bmatrix}$$

Fig. E.8. Imperfection reconstruction procedure.

Table E.3. Imperfection fitted coefficients - global specimens.

		L_1	L_2	L_3	L_4	C_1	C_2	C_3	C_4	φ_1	φ_2	φ_3	φ_4	m	b	R^2	SSE	$RMSE$
		(mm)				(mm) or (°)				(rad)				(mm/mm) or (°/mm)	(mm) or (°)			
362S137-68-	δ_B	988.1	540.6	179.9	348.7	0.210	0.174	0.032	0.009	0.571	3.142	3.091	-0.435	1.36E-04	-0.170	0.995	3.92E-02	1.64E-02
	δ_C	757.7	533.5	419.6	252.8	0.349	0.254	0.143	0.034	-0.547	0.527	1.482	-0.013	-7.53E-04	0.940	0.997	1.30E-02	9.50E-03
	ϕ	863.5	484.6	300.9	140.9	0.619	0.293	0.114	0.023	0.066	-0.252	-0.743	1.862	1.82E-04	-0.264	0.999	1.86E-02	1.13E-02
	δ_w	837.0	314.3	413.5	261.9	0.060	0.060	0.048	0.029	-3.140	1.981	1.621	3.131	-6.19E-05	-0.002	0.979	1.07E-02	8.60E-03
	δ_{FE}	916.1	435.8	245.7	38.0	0.225	0.118	0.087	0.003	0.557	-3.142	-0.432	3.142	2.90E-04	-1.188	0.995	2.69E-02	1.36E-02
	δ_{FW}	686.1	315.6	480.5	254.6	0.078	0.078	0.042	0.041	1.556	1.992	-3.142	1.789	-3.85E-05	1.447	0.961	2.57E-02	1.32E-02
800S162-97-	δ_B	1410.3	844.2	577.9	461.6	1.729	0.681	0.254	0.085	1.358	1.941	2.350	3.141	4.70E-06	-0.007	0.999	8.45E-01	4.19E-02
	δ_C	1542.0	466.7	532.6	338.9	0.311	0.152	0.106	0.040	-1.537	-1.475	-3.142	-0.281	3.78E-04	-0.579	0.997	7.96E-02	1.29E-02
	ϕ	1347.4	608.8	336.7	545.1	0.085	0.059	0.015	0.001	1.112	-2.831	2.519	3.142	-1.52E-04	0.292	0.996	8.20E-03	4.10E-03
	δ_w	1448.0	687.5	513.3	418.3	0.056	0.056	0.056	0.039	-1.569	-2.472	-1.714	-0.856	2.42E-05	0.508	0.976	4.49E-02	9.60E-03
	δ_{FE}	490.7	406.5	599.0	1631.6	0.111	0.093	0.086	0.039	2.059	3.142	0.942	0.750	5.66E-05	-0.906	0.958	7.76E-02	1.27E-02
	δ_{FW}	628.3	1843.9	443.2	312.2	0.071	0.057	0.049	0.044	-3.142	-1.010	1.527	1.633	-3.87E-05	0.939	0.951	1.89E-01	1.98E-02
800S162-97-	δ_B	1336.4	838.5	584.6	406.5	1.508	0.694	0.159	0.065	1.266	2.414	3.142	2.757	-1.28E-04	0.188	1.000	1.16E-01	1.55E-02
	δ_C	508.0	687.7	930.9	417.7	0.099	0.099	0.097	0.039	-1.247	-1.290	-2.222	-0.365	-1.54E-04	0.225	0.955	1.29E-01	1.63E-02
	ϕ	1499.4	588.9	390.3	341.0	0.102	0.040	0.028	0.020	1.679	0.944	-3.142	-0.816	1.05E-04	0.016	0.984	5.25E-02	1.04E-02
	δ_w	1435.4	499.5	664.4	392.3	0.058	0.058	0.057	0.018	-1.528	-1.459	-2.186	-0.811	1.98E-05	0.517	0.972	6.46E-02	1.15E-02
	δ_{FE}	440.6	498.6	266.2	685.5	0.116	0.063	0.032	0.022	2.462	-0.198	1.916	-3.142	-3.23E-05	-1.585	0.895	3.47E-01	2.67E-02
	δ_{FW}	1352.7	541.8	859.8	303.7	0.177	0.108	0.068	0.020	-1.947	0.796	-0.963	-0.326	-5.91E-05	1.304	0.994	5.50E-02	1.07E-02
1200S162-97-	δ_B	1107.1	815.6	576.6	336.2	2.987	1.699	0.298	0.096	0.646	2.326	3.142	-0.116	-2.87E-04	0.412	0.999	4.92E-01	3.46E-02
	δ_C	622.8	1275.1	451.2	272.2	0.194	0.156	0.116	0.044	-2.824	-1.949	-1.431	0.187	-6.73E-05	0.097	0.990	1.58E-01	1.97E-02
	ϕ	498.8	1072.1	303.2	259.3	0.045	0.030	0.021	0.017	-3.142	0.219	-3.023	3.142	-8.86E-05	0.106	0.962	2.46E-02	7.70E-03
	δ_w	1192.9	613.2	487.6	337.1	0.090	0.090	0.057	0.020	-1.978	-2.938	-1.569	3.142	7.71E-05	1.387	0.980	5.09E-02	1.11E-02
	δ_{FE}	509.7	495.4	333.6	254.8	0.274	0.210	0.110	0.071	0.058	-3.142	-0.166	0.146	1.80E-04	-0.241	0.977	1.16E-01	1.68E-02
	δ_{FW}	326.0	711.2	231.3	1797.2	0.096	0.095	0.054	0.025	3.069	2.061	2.586	0.139	-7.44E-05	1.862	0.968	1.42E-01	1.86E-02

Table E.4. Imperfection fitted coefficients - local specimens.

		L_1	L_2	L_3	L_4	C_1	C_2	C_3	C_4	φ_1	φ_2	φ_3	φ_4	m	b	R^2	SSE	$RMSE$
		(mm)				(mm) or (°)				(rad)				(mm/mm) or (°/mm)	(mm) or (°)			
362S162-54-	δ_B	120.1	221.5	36.8	23.7	0.078	0.019	0.014	0.004	0.882	-0.475	-2.122	3.141	2.51E-04	-0.038	0.998	2.02E-04	2.90E-03
	δ_C	112.6	184.9	49.6	34.0	0.070	0.047	0.020	0.009	1.897	0.213	1.121	1.344	1.47E-02	-2.232	0.964	1.20E-03	7.10E-03
	ϕ	86.2	304.8	42.7	30.1	0.126	0.036	0.027	0.009	1.840	1.319	3.142	3.142	-2.70E-03	0.482	0.997	9.41E-04	6.00E-03
	δ_w	87.2	39.5	33.2	24.8	0.035	0.026	0.011	0.008	-0.371	-1.566	-1.278	3.141	3.70E-03	-0.454	0.993	2.08E-04	2.90E-03
	δ_{FE}	112.6	119.9	51.6	42.4	0.104	0.054	0.031	0.019	-3.027	-2.146	1.868	3.142	-7.00E-03	0.783	0.999	6.04E-04	5.00E-03
	δ_{FW}	95.2	67.0	51.7	37.7	0.334	0.231	0.072	0.010	-0.286	0.938	2.289	3.061	8.90E-03	-1.009	1.000	1.79E-04	2.70E-03
362S162-54-	δ_B	71.3	86.3	59.9	6.9	0.143	0.114	0.059	0.001	0.468	-0.911	1.959	-2.271	-2.21E-04	0.033	0.993	5.78E-04	4.80E-03
	δ_C	106.6	40.8	57.8	31.4	0.034	0.032	0.029	0.015	-2.596	1.910	-3.142	0.523	-2.55E-02	3.774	0.974	1.40E-03	7.40E-03
	ϕ	49.1	38.8	127.5	32.6	0.041	0.025	0.025	0.007	-2.299	-1.877	1.545	0.126	9.10E-03	-1.202	0.984	6.23E-04	5.00E-03
	δ_w	63.3	104.2	50.1	23.5	0.028	0.026	0.012	0.004	3.142	-2.946	3.142	0.144	2.30E-03	-0.105	0.971	5.36E-04	4.50E-03
	δ_{FE}	46.3	54.2	101.8	41.1	0.175	0.161	0.110	0.065	1.023	-0.769	0.254	3.010	-6.00E-03	0.148	0.994	1.30E-03	7.10E-03
	δ_{FW}	114.7	55.2	28.3	20.3	0.096	0.021	0.019	0.014	-2.501	2.639	0.679	1.922	1.02E-02	-1.008	0.978	4.80E-03	1.36E-02
600S162-33-	δ_B	110.7	200.9	54.9	21.9	0.035	0.025	0.007	0.002	-0.733	-2.088	-0.663	-0.949	2.40E-03	-0.366	0.993	6.12E-05	1.60E-03
	δ_C	66.4	73.9	304.7	31.1	0.041	0.035	0.030	0.006	2.962	-1.588	2.428	1.717	8.90E-03	-1.362	0.994	4.54E-04	4.40E-03
	ϕ	98.5	41.9	174.0	38.6	0.093	0.063	0.046	0.037	-2.603	0.784	-2.199	2.873	3.80E-03	-0.431	0.995	1.10E-03	6.80E-03
	δ_w	65.0	107.0	78.7	50.1	0.065	0.061	0.045	0.027	2.957	-3.142	-3.106	3.062	-4.00E-03	-0.633	0.987	1.80E-03	8.70E-03
	δ_{FE}	40.7	50.1	111.8	32.2	0.081	0.077	0.066	0.024	2.508	1.267	-2.966	3.142	-7.00E-03	-0.316	0.977	3.80E-03	1.23E-02
	δ_{FW}	90.9	68.8	52.0	41.5	0.544	0.426	0.163	0.009	-0.637	1.089	2.089	3.142	-5.80E-03	0.151	1.000	3.54E-04	3.80E-03
600S162-33-	δ_B	92.9	64.0	46.1	39.0	0.066	0.063	0.028	0.013	-3.141	2.946	2.490	3.142	-9.56E-04	0.146	0.995	5.06E-04	4.50E-03
	δ_C	104.7	62.6	50.2	36.1	0.073	0.064	0.047	0.011	-2.817	2.399	3.141	3.109	-2.08E-02	3.166	0.998	2.83E-04	3.30E-03
	ϕ	111.6	56.8	44.5	35.4	0.054	0.030	0.026	0.015	-2.491	0.546	1.994	3.124	1.40E-03	-0.185	0.991	6.23E-04	5.00E-03
	δ_w	39.6	112.7	46.6	34.3	0.099	0.093	0.072	0.045	1.212	-2.446	-0.368	2.633	3.00E-03	-0.513	0.997	5.35E-04	4.60E-03
	δ_{FE}	117.0	54.4	66.1	40.6	0.208	0.171	0.154	0.062	-2.613	3.142	1.849	3.142	-8.20E-03	-0.246	0.998	1.80E-03	8.20E-03
	δ_{FW}	110.8	33.0	45.0	42.7	0.163	0.049	0.028	0.000	-2.744	-3.117	-0.056	-0.049	8.90E-03	-0.845	0.995	2.60E-03	1.03E-02
800S200-33-	δ_B	916.5	358.3	1828.1	157.0	0.114	0.087	0.027	0.011	2.144	1.333	1.103	-0.692	-1.54E-05	0.012	0.998	7.10E-03	5.00E-03
	δ_C	714.8	520.8	298.0	185.6	0.199	0.079	0.032	0.027	1.328	2.440	3.142	0.544	-7.05E-04	0.549	0.994	2.73E-02	9.70E-03
	ϕ	411.2	221.3	286.8	1823.4	0.039	0.036	0.029	0.025	0.476	3.140	1.648	-0.975	-7.82E-05	-0.015	0.965	1.48E-02	7.20E-03
	δ_w	468.2	564.3	251.0	174.0	0.163	0.123	0.108	0.032	0.051	-3.120	-2.863	-0.118	-3.08E-04	0.391	0.999	3.70E-03	3.60E-03
	δ_{FE}	322.5	283.6	762.9	133.8	0.241	0.204	0.141	0.016	1.444	3.142	1.038	1.713	2.57E-04	0.013	0.993	4.04E-02	1.18E-02
	δ_{FW}	229.0	538.2	216.7	296.8	0.250	0.238	0.208	0.141	-2.149	-0.655	0.079	-3.142	-1.71E-04	1.017	0.982	1.96E-01	2.60E-02
800S200-33-	δ_B	813.8	343.5	166.3	236.8	0.174	0.111	0.018	0.014	1.826	0.028	3.142	-1.361	-6.92E-05	0.054	0.999	7.70E-03	5.20E-03
	δ_C	459.6	776.1	170.1	216.0	0.114	0.094	0.029	0.025	0.843	-2.154	1.503	1.940	2.06E-04	-0.161	0.995	2.01E-02	8.30E-03
	ϕ	538.3	299.4	205.5	1828.8	0.086	0.068	0.031	0.009	-0.754	2.969	-1.564	2.627	-2.75E-04	-0.017	0.992	1.52E-02	7.30E-03
	δ_w	795.1	223.4	292.4	152.4	0.287	0.019	0.018	0.013	-1.476	3.142	-2.958	1.923	-1.54E-04	0.275	0.998	2.49E-02	9.30E-03
	δ_{FE}	702.6	408.6	286.6	230.1	0.271	0.271	0.073	0.038	1.287	1.812	2.274	3.142	1.63E-04	0.017	0.996	6.05E-02	1.45E-02
	δ_{FW}	764.4	409.4	278.8	150.8	0.442	0.119	0.044	0.039	-1.490	-2.096	3.142	-1.648	2.76E-04	0.205	0.988	4.30E-01	3.86E-02
1000S200-43-	δ_B	846.8	240.4	482.2	210.0	0.281	0.100	0.070	0.061	-1.393	-3.142	3.142	-1.825	-2.92E-04	0.241	0.996	5.94E-02	1.46E-02
	δ_C	536.2	306.8	1828.8	246.3	0.331	0.159	0.061	0.045	2.471	-0.364	-0.114	1.784	-2.10E-03	1.716	0.999	1.14E-02	6.40E-03
	ϕ	363.0	284.8	801.0	183.0	0.058	0.057	0.050	0.021	2.253	3.142	-0.715	0.556	-4.83E-05	0.241	0.984	1.53E-02	7.40E-03
	δ_w	808.2	253.9	231.7	329.8	0.353	0.353	0.241	0.208	-1.624	-2.389	-0.199	-3.142	8.09E-05	1.262	0.981	6.83E-01	4.92E-02
	δ_{FE}	674.5	521.7	211.0	310.0	0.730	0.513	0.056	0.029	0.878	2.930	0.067	3.142	9.54E-05	-0.674	0.998	5.42E-02	1.39E-02
	δ_{FW}	787.1	366.7	341.3	213.8	0.381	0.381	0.341	0.060	-1.563	-3.113	-0.729	3.142	1.45E-04	1.799	0.982	5.53E-01	4.43E-02
1000S200-43-	δ_B	330.1	345.9	754.8	181.7	0.275	0.144	0.122	0.018	1.683	-0.443	-1.892	2.083	3.32E-04	-0.275	0.984	1.07E-01	1.96E-02
	δ_C	290.3	256.4	227.9	555.9	0.244	0.232	0.135	0.106	-1.770	0.261	2.275	-2.151	1.10E-03	-0.949	0.992	2.93E-02	1.03E-02
	ϕ	302.8	318.6	206.2	1379.6	0.068	0.066	0.030	0.009	1.417	0.077	-2.816	3.142	3.39E-05	0.067	0.990	1.09E-02	6.30E-03
	δ_w	251.4	809.6	229.9	326.7	0.329	0.329	0.225	0.220	-2.448	-1.640	-0.158	-3.142	-1.80E-04	1.596	0.984	5.10E-01	4.27E-02
	δ_{FE}	712.7	563.5	360.1	135.7	0.668	0.331	0.073	0.011	1.040	3.142	1.100	0.819	2.52E-04	-0.801	0.999	1.78E-02	8.00E-03
	δ_{FW}	797.1	334.7	289.0	206.1	0.343	0.209	0.157	0.048	-1.601	-3.142	-1.320	3.142	-2.67E-04	2.187	0.982	4.98E-01	4.24E-02

Table E.5. Imperfection fitted coefficients - distortional specimens.

		L_1	L_2	L_3	L_4	C_1	C_2	C_3	C_4	φ_1	φ_2	φ_3	φ_4	m	b	R^2	SSE	$RMSE$
		(mm)				(mm) or (°)				(rad)				(mm/mm) or (°/mm)	(mm) or (°)			
362S137-68-	δ_B	224.2	178.2	99.9	63.7	0.366	0.282	0.021	0.013	0.421	2.570	2.450	3.142	2.29E-04	-0.070	1.000	7.53E-04	3.10E-03
	δ_C	317.1	602.3	123.5	77.7	0.157	0.076	0.028	0.017	1.330	-0.987	0.585	1.029	-7.38E-04	0.225	0.995	3.70E-03	7.00E-03
	ϕ	187.5	86.8	82.1	147.5	0.241	0.081	0.076	0.052	1.197	-2.716	-0.064	-1.847	3.30E-03	-0.881	0.998	5.70E-03	8.60E-03
	δ_w	297.1	607.7	158.2	68.7	0.133	0.032	0.025	0.004	1.416	-0.156	1.762	-0.857	-4.32E-04	0.269	0.999	3.35E-04	2.10E-03
	δ_{FE}	287.8	175.4	102.9	76.4	0.261	0.118	0.026	0.020	-1.725	3.142	3.142	3.142	1.50E-03	-1.534	0.998	1.11E-02	1.19E-02
	δ_{FW}	242.5	166.2	127.1	93.9	0.426	0.208	0.067	0.017	0.761	1.863	3.142	3.142	-1.70E-03	2.113	1.000	8.56E-04	3.30E-03
362S137-68-	δ_B	234.9	146.3	103.7	75.3	0.157	0.113	0.048	0.028	0.635	1.224	1.555	0.077	6.07E-04	-0.187	0.997	2.50E-03	5.70E-03
	δ_C	177.0	140.7	200.3	119.9	0.272	0.223	0.157	0.113	0.666	1.513	-1.058	2.879	-3.47E-04	0.107	0.996	1.70E-03	4.70E-03
	ϕ	282.2	161.1	93.5	71.2	0.123	0.063	0.049	0.022	1.264	-0.516	2.502	-0.061	3.20E-03	-1.086	0.997	3.60E-03	6.90E-03
	δ_w	292.7	609.0	90.5	141.7	0.132	0.027	0.014	0.010	1.431	0.333	0.722	1.648	-5.32E-05	0.130	0.998	9.18E-04	3.50E-03
	δ_{FE}	267.1	94.7	93.7	56.5	0.277	0.201	0.189	0.004	-2.027	-1.549	1.368	-1.371	1.70E-03	-1.767	1.000	1.40E-03	4.30E-03
	δ_{FW}	183.4	135.2	243.8	99.0	0.258	0.111	0.075	0.025	1.085	2.061	-0.356	3.142	2.60E-03	0.374	0.999	9.01E-04	3.50E-03
600S137-68-	δ_B	239.6	162.6	96.7	73.5	0.146	0.110	0.029	0.021	0.869	1.123	-2.304	3.142	7.05E-04	-0.220	0.999	1.30E-03	4.30E-03
	δ_C	166.6	84.8	609.3	69.7	0.074	0.041	0.023	0.020	-0.839	1.601	3.070	-2.107	6.05E-04	-0.189	0.997	1.10E-03	3.90E-03
	ϕ	256.4	134.6	69.4	44.4	0.095	0.071	0.024	0.012	0.724	1.142	-0.875	-0.825	-2.80E-03	0.691	0.991	5.50E-03	8.60E-03
	δ_w	96.8	128.4	72.5	62.2	0.020	0.012	0.009	0.005	3.102	-3.103	2.546	3.140	9.59E-05	-0.033	0.953	8.21E-04	3.30E-03
	δ_{FE}	258.4	87.9	122.4	72.0	0.147	0.068	0.061	0.041	-2.119	2.874	-3.142	3.142	1.60E-03	-0.419	0.990	1.51E-02	1.40E-02
	δ_{FW}	144.5	110.5	192.5	98.0	0.355	0.241	0.232	0.124	0.820	1.426	-0.236	3.142	4.62E-04	0.216	0.997	3.50E-03	6.90E-03
600S137-68-	δ_B	155.9	180.7	91.0	55.6	0.155	0.137	0.027	0.011	1.908	-0.609	3.142	2.914	6.08E-04	-0.177	0.993	1.70E-03	4.90E-03
	δ_C	211.5	523.9	87.6	66.5	0.120	0.051	0.037	0.011	2.635	1.020	1.079	-0.838	1.90E-03	-0.547	1.000	2.05E-04	1.70E-03
	ϕ	110.3	93.5	71.9	287.3	0.140	0.085	0.030	0.017	-0.076	1.374	2.512	0.403	2.53E-04	-0.459	0.993	2.50E-03	6.00E-03
	δ_w	214.7	179.3	96.4	54.5	0.223	0.151	0.017	0.008	0.447	3.009	3.142	1.795	-2.20E-03	1.052	0.992	4.20E-03	7.70E-03
	δ_{FE}	252.8	118.3	85.8	51.6	0.074	0.074	0.053	0.015	-2.041	-3.063	3.142	1.874	2.30E-03	-0.768	0.976	1.50E-02	1.44E-02
	δ_{FW}	205.1	148.6	105.4	90.8	0.224	0.198	0.103	0.026	0.558	1.046	1.607	3.142	-2.80E-03	1.424	0.998	2.90E-03	6.50E-03
800S250-68-	δ_B	368.8	738.4	227.0	157.2	0.036	0.029	0.026	0.020	0.235	1.784	-3.142	3.142	-1.53E-05	0.012	0.973	1.17E-02	6.40E-03
	δ_C	746.8	386.8	271.8	175.0	0.141	0.103	0.078	0.034	1.594	1.179	1.830	2.160	1.30E-03	-0.979	0.998	1.19E-02	6.40E-03
	ϕ	206.9	181.6	242.7	735.7	0.040	0.032	0.030	0.020	-1.584	-0.648	-2.362	-1.642	-5.87E-05	-0.096	0.988	2.80E-03	3.10E-03
	δ_w	333.6	798.0	254.0	216.2	0.137	0.137	0.137	0.077	-2.526	-1.412	-1.966	-0.556	-1.12E-05	0.798	0.972	2.35E-01	2.85E-02
	δ_{FE}	646.7	484.3	295.4	96.6	0.348	0.222	0.096	0.007	0.791	3.003	3.141	3.142	3.09E-05	-0.689	0.993	5.95E-02	1.44E-02
	δ_{FW}	806.3	255.3	321.5	239.7	0.237	0.237	0.163	0.153	-1.482	-1.616	-3.142	0.778	2.88E-05	-0.782	0.994	9.11E-02	1.77E-02
800S250-68-	δ_B	306.2	347.4	676.3	181.5	0.155	0.150	0.100	0.053	-0.574	3.142	-1.395	-1.641	-1.96E-04	0.150	0.991	2.80E-02	9.80E-03
	δ_C	338.3	188.4	565.1	240.3	0.033	0.024	0.023	0.014	-2.716	1.144	1.213	-0.386	1.88E-04	-0.144	0.991	3.40E-03	3.40E-03
	ϕ	756.5	343.4	182.9	123.7	0.057	0.026	0.017	0.011	1.707	-0.833	-2.176	0.834	-5.05E-05	-0.132	0.984	9.80E-03	5.80E-03
	δ_w	780.2	260.4	314.4	219.7	0.115	0.113	0.109	0.046	-1.383	-1.764	-3.142	-0.382	6.16E-05	0.756	0.981	7.82E-02	1.65E-02
	δ_{FE}	642.3	468.9	347.4	478.8	0.250	0.213	0.080	0.030	1.168	2.157	3.142	1.249	2.15E-04	-0.845	0.997	2.03E-02	8.40E-03
	δ_{FW}	749.7	273.2	341.0	223.8	0.175	0.175	0.160	0.056	-1.588	-1.113	-2.454	-0.199	2.89E-05	-0.823	0.992	6.27E-02	1.47E-02
1200S250-97-	δ_B	797.4	499.8	273.8	159.9	0.157	0.076	0.072	0.032	-1.773	1.715	0.330	-1.329	5.06E-05	-0.040	0.996	2.62E-02	9.50E-03
	δ_C	237.6	226.8	351.1	1188.1	0.157	0.141	0.091	0.015	2.916	-0.229	-0.652	3.029	-8.80E-04	0.687	0.987	3.03E-02	1.03E-02
	ϕ	514.8	248.7	307.1	151.3	0.033	0.028	0.013	0.012	-1.147	0.660	-3.141	-1.412	-2.93E-04	0.201	0.980	6.20E-03	4.70E-03
	δ_w	212.3	870.8	133.0	263.3	0.071	0.039	0.021	0.017	-0.125	2.194	-3.142	0.096	-4.43E-05	0.827	0.966	3.68E-02	1.13E-02
	δ_{FE}	397.8	522.2	285.6	131.3	0.144	0.137	0.086	0.013	1.711	1.177	3.128	0.742	6.09E-04	0.084	0.993	2.93E-02	1.01E-02
	δ_{FW}	382.8	189.3	277.1	911.3	0.042	0.031	0.027	0.018	-2.213	1.902	-0.826	1.324	1.13E-05	0.335	0.838	7.96E-02	1.66E-02
1200S250-97-	δ_B	275.7	478.8	576.9	287.9	0.42	0.40	0.39	0.38	-0.36	3.14	0.32	3.14	-3.66E-05	0.03	0.99	7.47E-02	1.60E-02
	δ_C	224.6	763.9	442.6	196.7	0.12	0.12	0.11	0.06	-1.04	-2.28	0.81	1.45	-1.20E-03	0.92	1.00	3.16E-02	1.05E-02
	ϕ	254.8	235.2	725.0	403.0	0.13	0.13	0.08	0.04	3.14	-0.64	-1.17	3.14	-2.08E-04	0.26	0.95	9.07E-02	1.77E-02
	δ_w	207.3	286.3	649.4	143.7	0.04	0.04	0.03	0.02	2.33	0.05	-2.63	1.35	-1.21E-04	0.81	0.98	1.77E-02	7.80E-03
	δ_{FE}	359.5	266.9	218.9	177.0	0.14	0.08	0.03	0.01	1.73	1.24	2.39	3.14	9.13E-04	0.20	0.98	6.73E-02	1.53E-02
	δ_{FW}	362.2	291.4	579.3	163.5	0.15	0.15	0.06	0.03	-2.04	-0.31	-3.14	0.92	5.98E-05	0.44	0.98	3.72E-02	1.13E-02

References

[E.1] L.E. McAnallen, D.A. Padilla-Llano, X. Zhao, C.D. Moen, B.W. Schafer, M.R. Eatherton, "Initial Geometric Imperfection Measurement and Characterization of Cold-Formed Steel C-Section Structural Members with 3D Non-Contact Measurement Techniques". *Proceedings of the Annual Stability Conference, SSRC 2014*, March 25-28, 2014, Toronto, Canada.

[E.2] Godoy, L.A., "Thin-Walled Structures with Structural Imperfections: Analysis and Behavior". Pergamon Press, Oxford, 1996.

[E.3] Schafer, B.W., Li, Z., Moen, C.D., "Computational modeling of cold-formed steel." Thin-Walled Structures, 48 (10-11), 752-762, 2010.

[E.4] Zeinoddini, V. M., Geometric imperfections in cold-formed steel members. Ph.D. dissertation, Johns Hopkins University, Baltimore, 2011.

[E.5] Moen, C.D., Igusa, T., and Schafer, B.W., "Prediction of Residual Stresses and Strains in Cold-Formed Steel Members." Thin-Walled Structures, 46(11), 1274-1289, 2008.

[E.6] Quach, W.M., Teng, J.G., Chung, K.F., "Residual stresses in steel sheets due to coiling and uncoiling: a closed-form analytical solution." Engineering Structures, 26, 1249-1259, 2004.

[E.7] ASTM-C955, Standard Specification for Load-Bearing (Transverse and Axial) Steel Studs, Runners (Tracks), and Bracing or Bridging for Screw Application of Gypsum Panel Products and Metal Plaster Bases. West Conshohocken, PA. 2009.

[E.8] Schafer BW, Pekoz T. Computational modeling of cold-formed steel: characterizing geometric imperfections and residual stresses. Journal of Constructional Steel Research 1998; 47(3):193–210.

[E.9] Zeinoddini VM, Schafer BW. Simulation of geometric imperfections in cold-formed steel members using spectral representation approach. Thin-Walled Structures 2012; 60:105–17.

[E.10] Rasmussen, K. J. R., and Hancock, G. J., "Geometric imperfections in plated structures subject to interaction between buckling modes." Thin-Walled Structures, 6(6), 433–452, 1988.

[E.11] Young, B., Rasmussen, K.J.R., "Behaviour of cold-formed singly symmetric columns." Thin-Walled Structures. 33 (2) 83-102, 1999.

[E.12] Peterman, K.D., "Experiments on the stability of sheathed cold-formed steel studs under axial load and bending." Master's Thesis, Johns Hopkins University, Baltimore, MD, 2012.

[E.13] EOS Systems Inc., PhotoModeler help topics manual (build 2012.1.1.668), (http://www.photomodeler.com), Vancouver, Canada. 2012.

[E.14] Jolliffe, I., "Principal Component Analysis and Factor Analysis." (2002). Principal Component Analysis, Springer Series in Statistics, Springer New York, 150–166, 2002.

[E.15] Liu, Y.-S., and Ramani, K. (2009). "Robust principal axes determination for point-based shapes using least median of squares." Computer-Aided Design, 41(4), 293–305.

Additional imperfection shapes

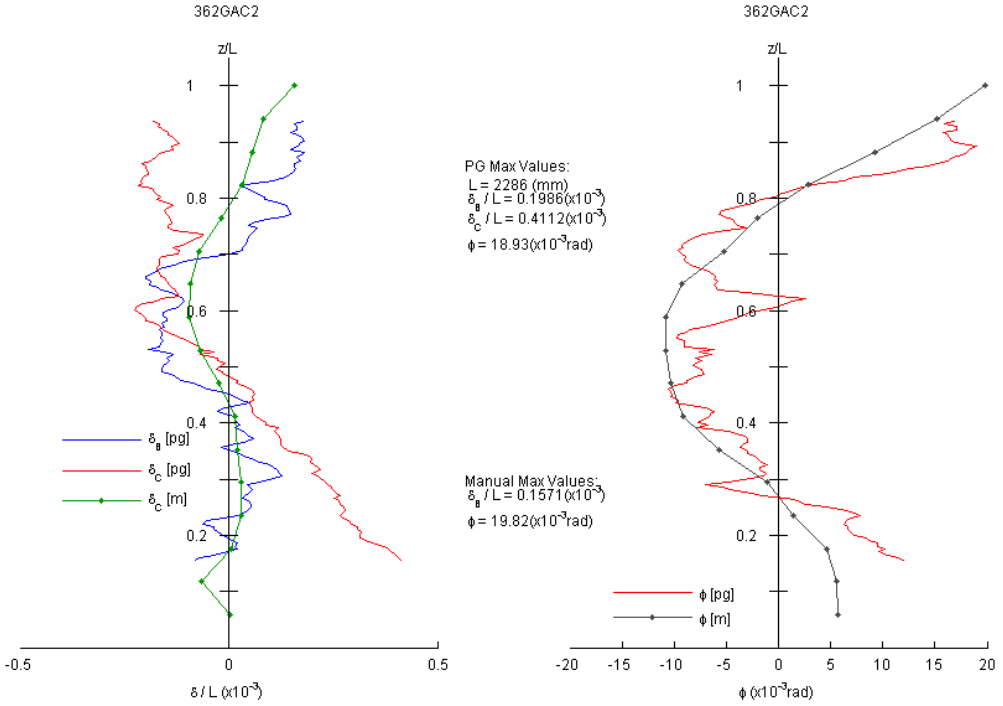

Fig. E.9. Global imperfections for specimen 362S137-68-GAC-2 (pg = photogrammetry, m = manual).

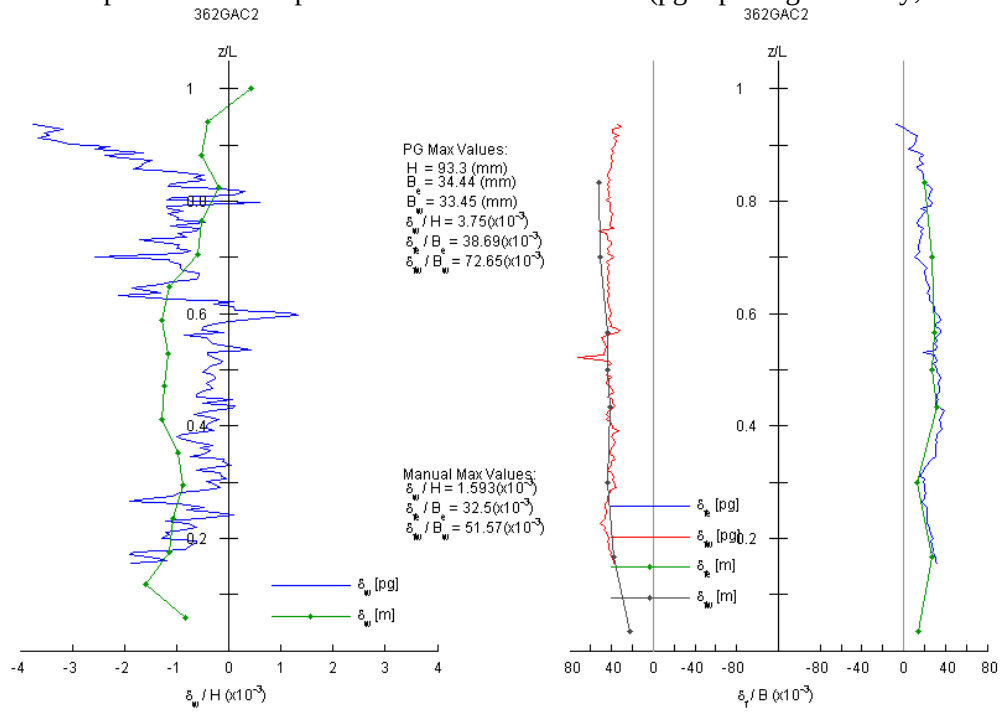

Fig. E.10. Local imperfections for specimen 362S137-68-GAC-2 (pg = photogrammetry, m = manual).

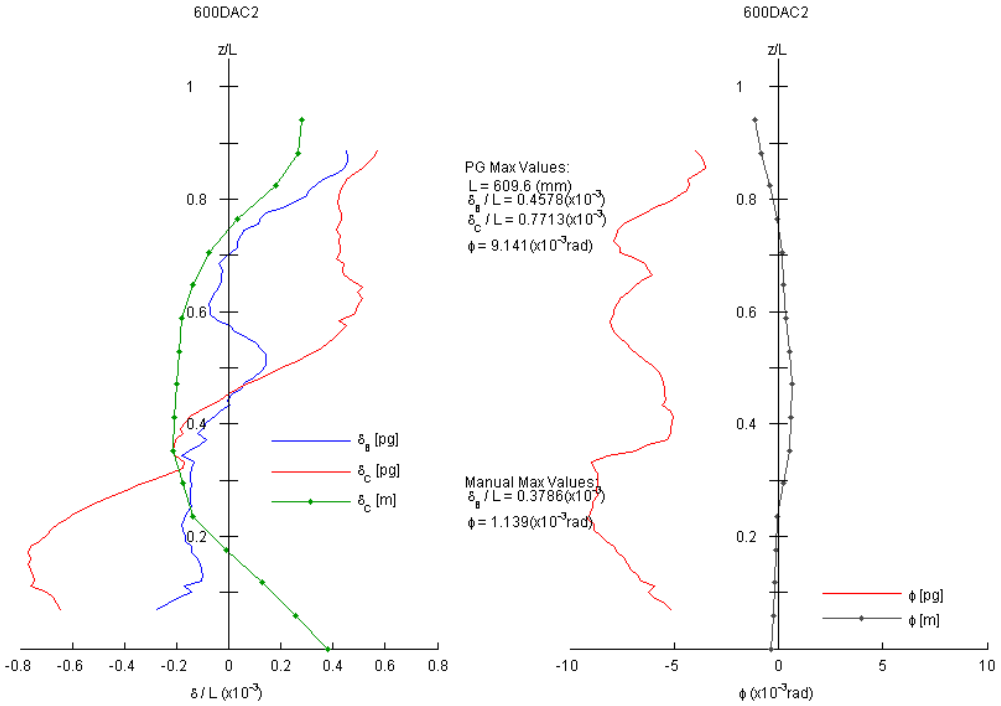

Fig. E.11. Global imperfections for specimen 600S137-68-DAC-2 (pg = photogrammetry, m = manual).

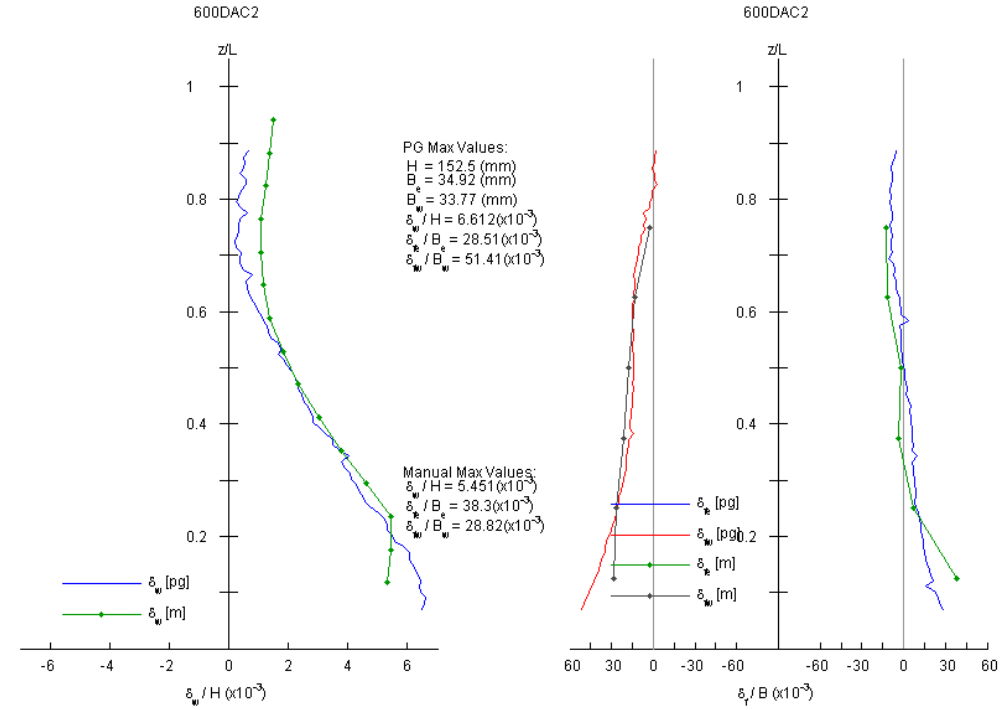

Fig. E.12. Local imperfections for specimen 600S137-68-DAC-2 (pg = photogrammetry, m = manual).

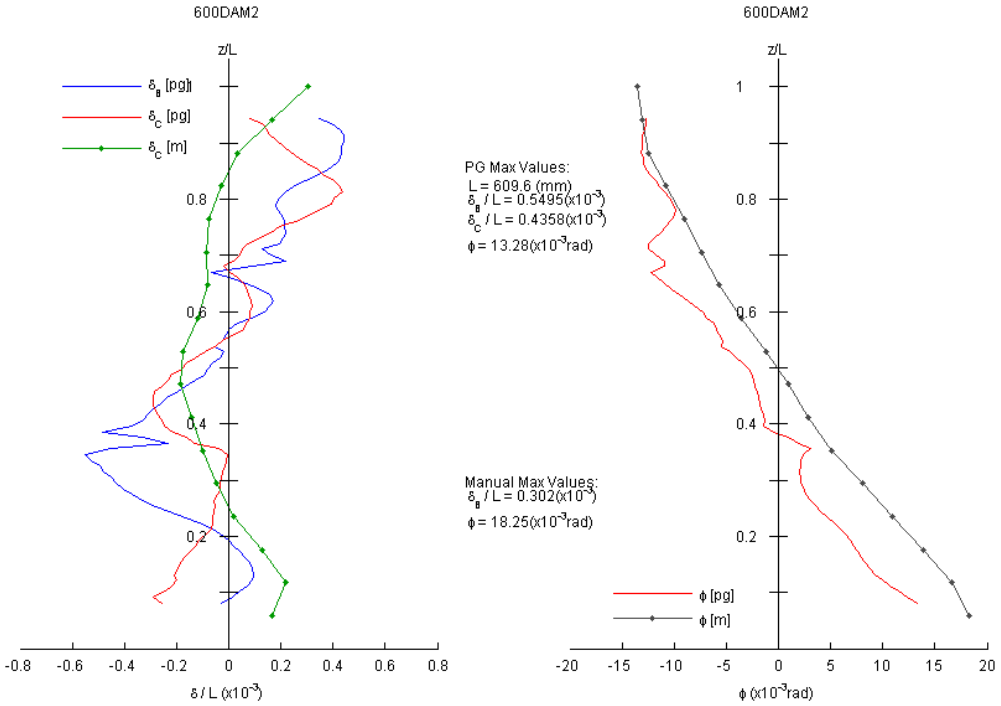

Fig. E.13. Global imperfections for specimen 600S137-68-DAM-2 (pg = photogrammetry, m = manual).

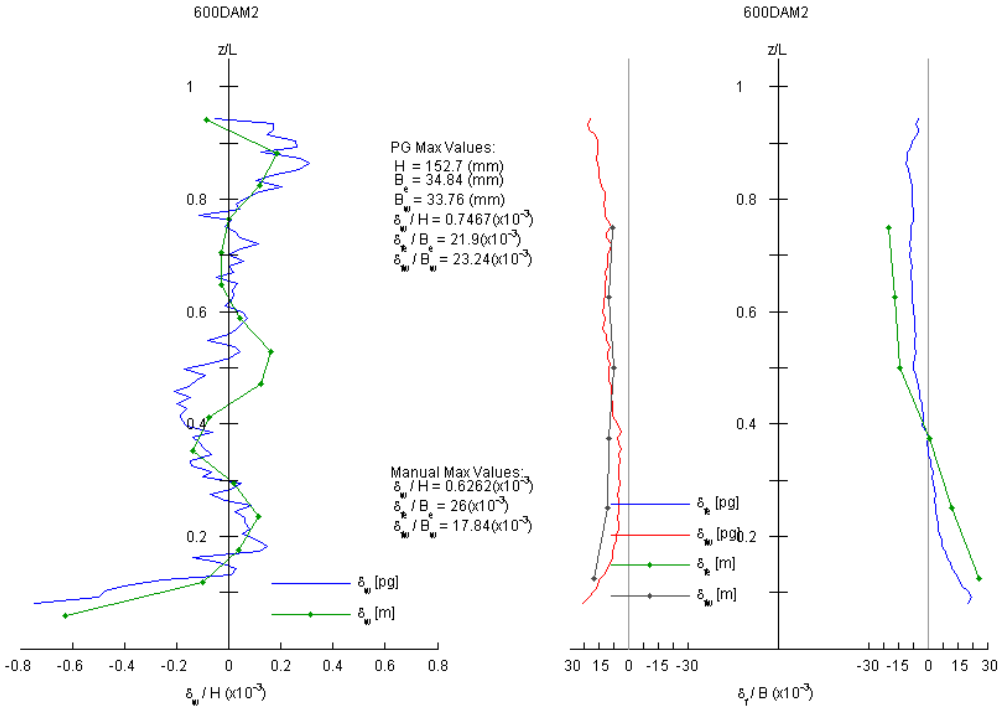

Fig. E.14. Local imperfections for specimen 600S137-68-DAM-2 (pg = photogrammetry, m = manual).

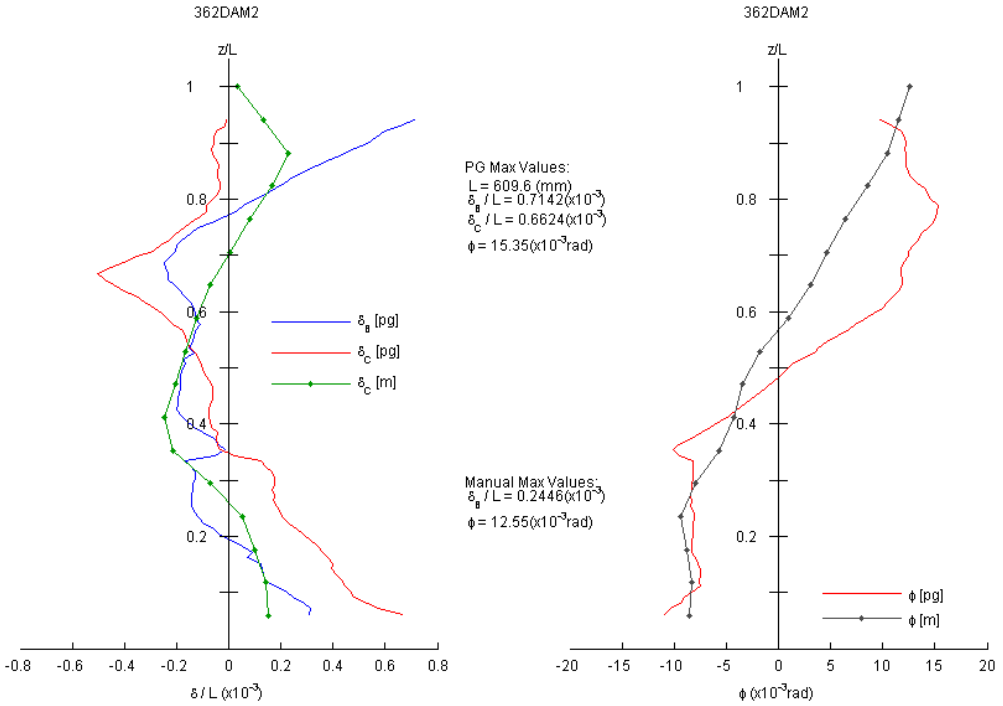

Fig. E.15. Global imperfections for specimen 362S137-68-DAM-2 (pg = photogrammetry, m = manual).

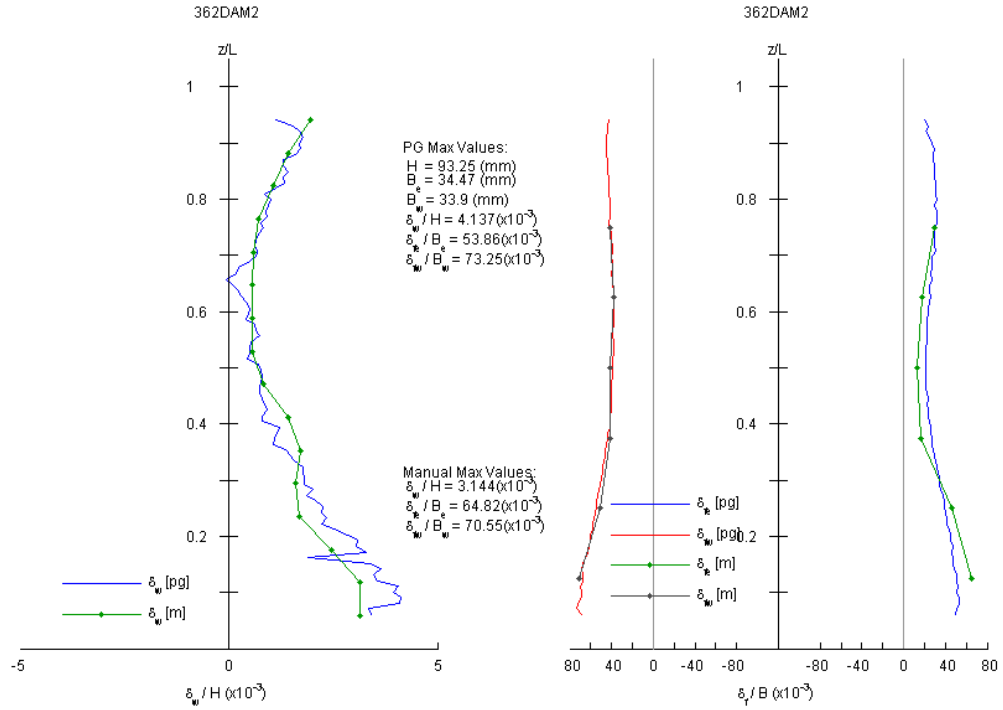

Fig. E.16. Local imperfections for specimen 362S137-68-DAM-2 (pg = photogrammetry, m = manual).

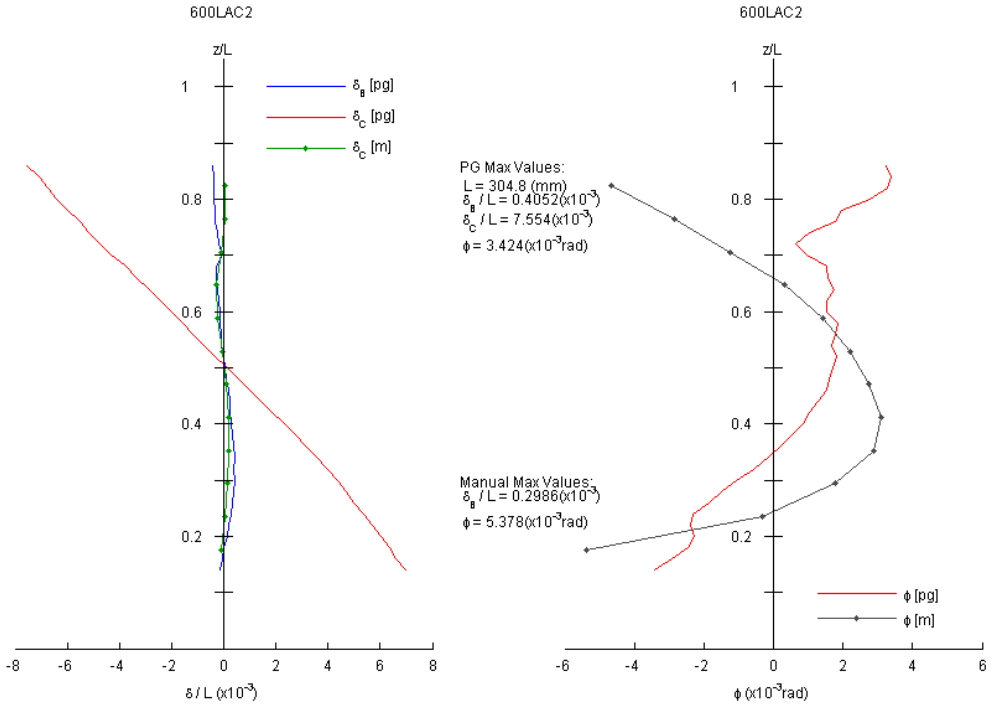

Fig. E.17. Global imperfections for specimen 600S162-33-LAC-2 (pg = photogrammetry, m = manual).

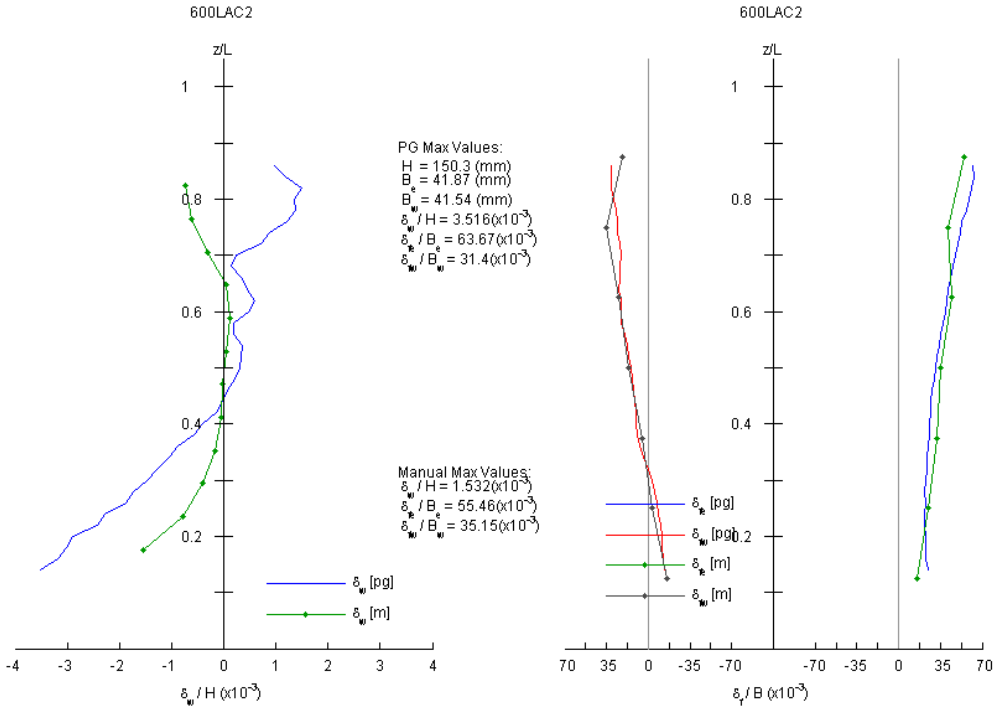

Fig. E.18. Local imperfections for specimen 600S162-33-LAC-2 (pg = photogrammetry, m = manual).

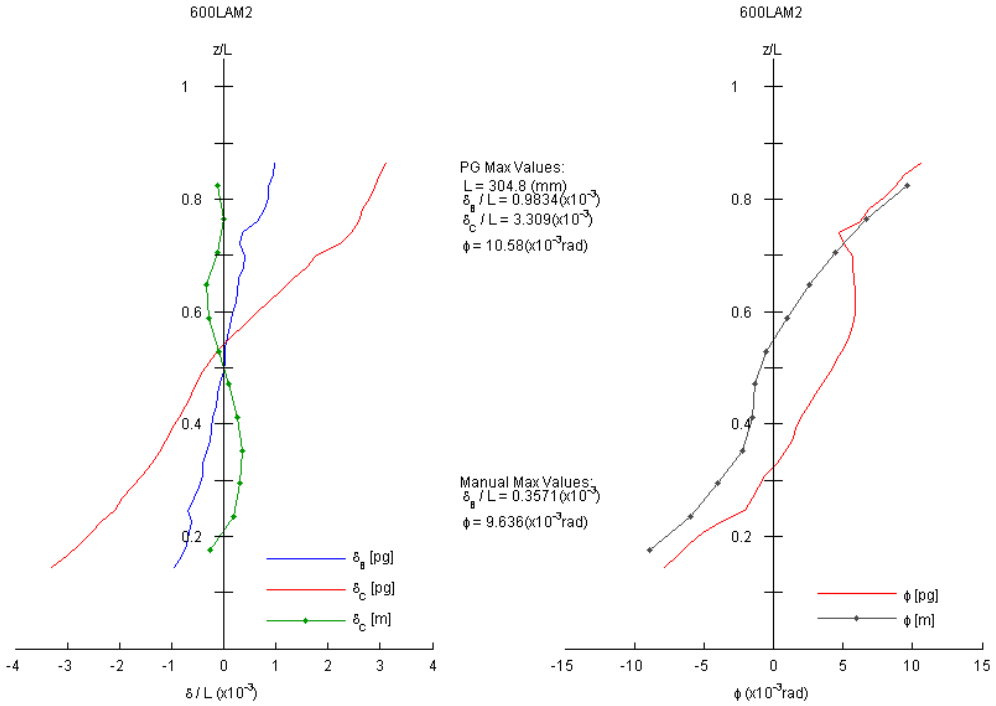

Fig. E.19. Global imperfections for specimen 600S162-33-LAM-2 (pg = photogrammetry, m = manual).

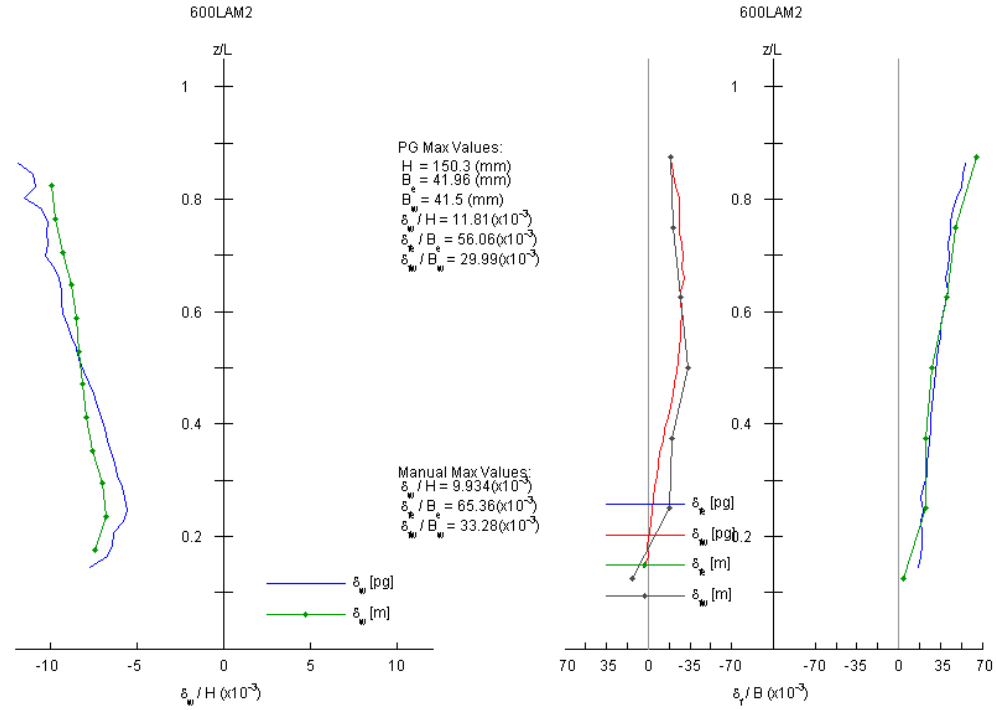

Fig. E.20. Local imperfections for specimen 600S162-33-LAM-2 (pg = photogrammetry, m = manual).

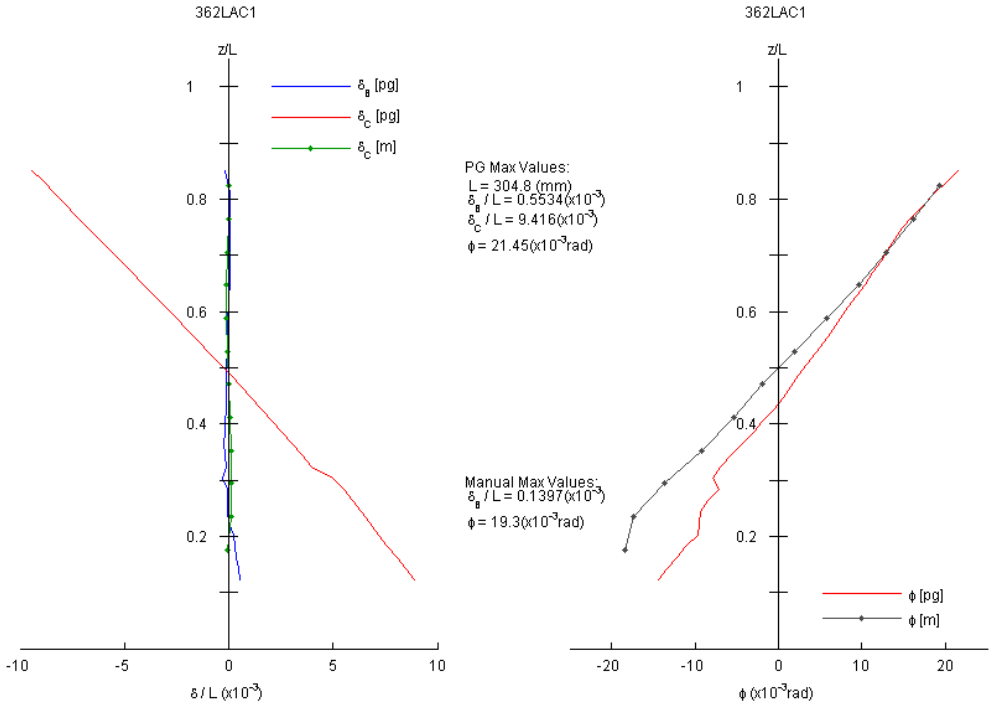

Fig. E.21. Global imperfections for specimen 362S162-54-LAC-1 (pg = photogrammetry, m = manual).

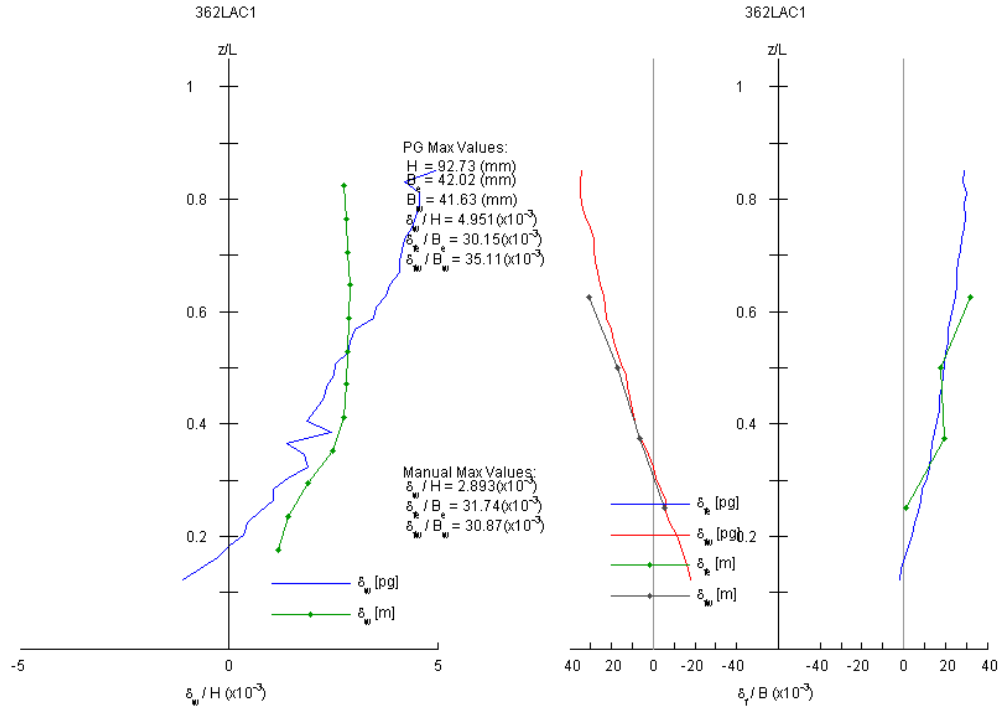

Fig. E.22. Local imperfections for specimen 362S162-54-LAC-1 (pg = photogrammetry, m = manual).

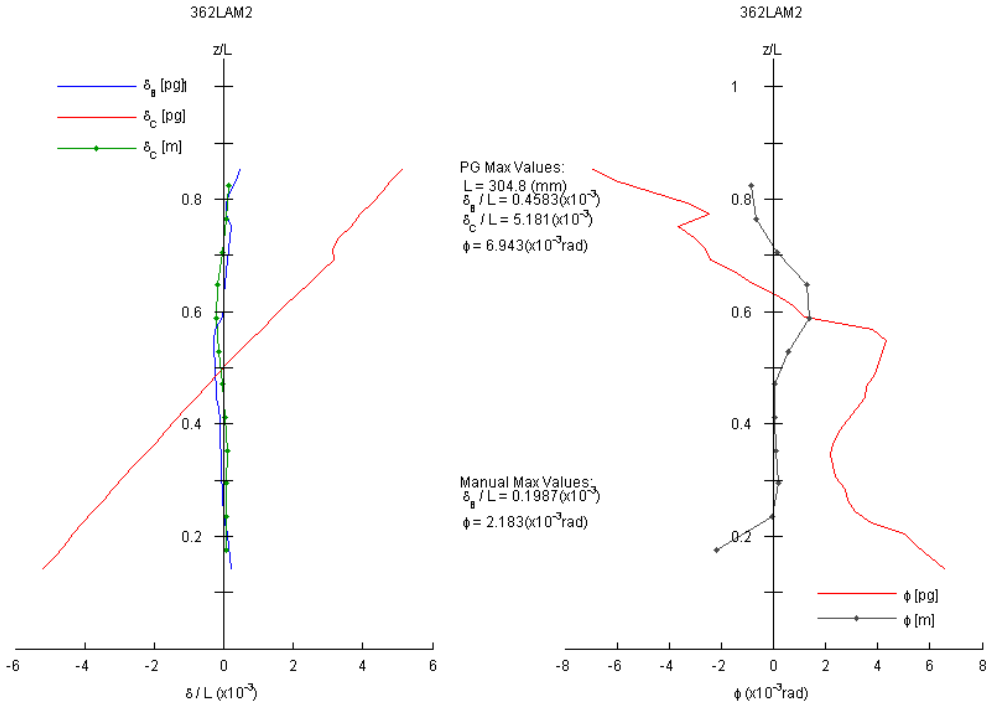

Fig. E.23. Global imperfections for specimen 362S162-54-LAM-2 (pg = photogrammetry, m = manual).

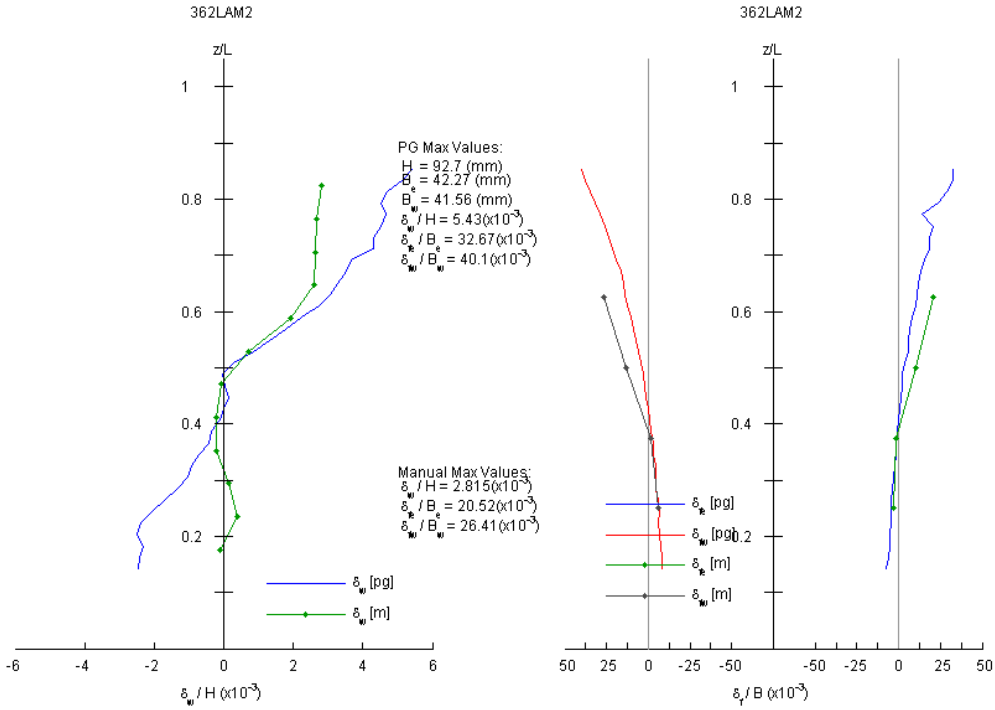

Fig. E.24. Local imperfections for specimen 362S162-54-LAM-2 (pg = photogrammetry, m = manual).

Appendix F MATLAB Code for *asymPinching* Model

The following MATLAB code illustrates the implementation of the tension-to-compression unloading-reloading path definition for the *asymPinching* model described in Chapter 7. The variables in this code follow the same definitions in the original *Pinching4* model. A compiled version of the *asymPinching* model for OpenSees 2.4.5 can be downloaded from http://edcfs.blogspot.com/aTWSection.

```
function [state3Strain,state3Stress] =
getstate3mod(state3Strain,state3Stress,kunload,kElasticNegDamgd,lowTstateStrain,lowTstateStress,
TminStrainDmnd, envlpNegStrain,envlpNegDamgdStress,hghTstateStrain,hghTstateStress,MDL)
    %=========================================================================
    % File Name: getstate3.m
    % Description: Defines the tension-to-compression unloading path using
    %              trial strain and strain rate, especially for state 3.
    %
    %                          Padilla-Llano David (Dec 2014) - dapadill@vt.edu
    %=========================================================================
    kmax = max([kunload kElasticNegDamgd]);
    TperElong = -(state3Stress(4) - kunload*state3Strain(4))/kunload;

    if (state3Strain(1)*state3Strain(4) <0.0) % Trilinear unload reload path expected
        % Calculate Point at 3:-> End of Unloading from Negative Quadrant
        if (TminStrainDmnd < envlpNegStrain(4))
            state3Stress(3) = MDL.uForceN*envlpNegDamgdStress(5);
        elseif (TminStrainDmnd < envlpNegStrain(3))
            state3Stress(3) = MDL.uForceN*envlpNegDamgdStress(4);
        else
            state3Stress(3) = MDL.uForceN*envlpNegDamgdStress(3);
        end

        state3Strain(3) = hghTstateStrain + (-hghTstateStress + state3Stress(3))/kunload;

        % Check Strain at 3 is not in front of Strain at 4
        if (state3Strain(3) > state3Strain(4))
            state3Strain(3) = state3Strain(4) + (state3Stress(3) - state3Stress(4))/kunload;
        end

        %%% Calculate Point at 2:-> Peak in the Unload-Reload path
        if (MDL.uForceN == 0.0)
            state3Stress(2) = lowTstateStress*MDL.rForceN;
        elseif (MDL.rForceN-MDL.uForceN > 1e-8)
            state3Stress(2) = lowTstateStress*MDL.rForceN;
        else
            if (TminStrainDmnd < envlpNegStrain(4))
                st1 = lowTstateStress*MDL.uForceN*(1.0+1e-6);
                st2 = envlpNegDamgdStress(5)*(1.0+1e-6);
                state3Stress(2) = min([st1 st2]);
            elseif (TminStrainDmnd < envlpNegStrain(3))
                st1 = lowTstateStress*MDL.uForceN*(1.0+1e-6);
                st2 = envlpNegDamgdStress(4)*(1.0+1e-6);
                state3Stress(2) = min([st1 st2]);
            else
                st1 = envlpNegDamgdStress(3)*MDL.uForceN*(1.0+1e-6);
                st2 = envlpNegDamgdStress(5)*(1.0+1e-6);
                state3Stress(2) = min([st1 st2]);
            end
        end
```

```
        % Check that Stress is less than the maximum stress from damaged backbone
        if (state3Stress(2) < envlpNegDamgdStress(3))
            state3Stress(2) = envlpNegDamgdStress(3);
        end

        state3Strain(2) = TperElong + envlpNegStrain(3)*MDL.rDispN;

        % Correct Strain at 2 if reload stiffness exceeds kunload or is negative
        k23 = (state3Stress(2)-state3Stress(3))/(state3Strain(2)-state3Strain(3));
        k13 = (state3Stress(1)-state3Stress(3))/(state3Strain(1)-state3Strain(3));

        if ((state3Strain(2) > state3Strain(3)))
            state3Strain(2) = state3Strain(3) + (state3Stress(2) - state3Stress(3))/kunload;
        elseif (k23 > kunload)
            state3Strain(2) = state3Strain(3) + (state3Stress(2) - state3Stress(3))/kunload;
        elseif ( k23 < 0 )
            % Point 3 should be lower than Point 3
            df = abs(state3Stress(3)/1000);
            state3Stress(2) = state3Stress(3) - df;
            if ( k23 < k13 )
                % pt 2 should be along a line between 1 and 3
                du = state3Strain(1)-state3Strain(3);
                df = state3Stress(1)-state3Stress(3);
                state3Strain(2) = state3Strain(3) + 0.5*du;
                state3Stress(2) = state3Stress(3) + 0.5*df;
            end
        end
    else
        % linear unload reload path is expected
        du = state3Strain(4)-state3Strain(1);
        df = state3Stress(4)-state3Stress(1);
        state3Strain(2) = state3Strain(1) + 0.33*du;
        state3Strain(3) = state3Strain(1) + 0.67*du;
        state3Stress(2) = state3Stress(1) + 0.33*df;
        state3Stress(3) = state3Stress(1) + 0.67*df;
    end

    % checkslope and slope are local variables
    checkSlope = state3Stress(4)/state3Strain(4);
    slope = 0.0;
    % Final Check: Enforces monotonic Increasing Load-Response through
    % State 4 if TperElong is zero
    i = 1;
    while (i<4)
        du = state3Strain(i+1)-state3Strain(i);
        df = state3Stress(i+1)-state3Stress(i);
        if (du<0.0 || df<0.0) && (TperElong <= 0)
            du = state3Strain(4)-state3Strain(1);
            df = state3Stress(4)-state3Stress(1);
            state3Strain(2) = state3Strain(1) + 0.33*du;
            state3Strain(3) = state3Strain(1) + 0.67*du;
            state3Stress(2) = state3Stress(1) + 0.33*df;
            state3Stress(3) = state3Stress(1) + 0.67*df;
            slope = df/du;
            i = 4;
        end
        % If the slope from Start to End of State 4 is less than the slope
        % from zero to point 1 of state4 then unload to zero and load
        % linearly to point 4 of state4
        if (slope > 1e-8 && slope < checkSlope)
            state3Strain(2) = 0.0;
            state3Stress(2) = 0.0;
            state3Strain(3) = state3Strain(4)/2;
            state3Stress(3) = state3Stress(4)/2;
        end
        i = i + 1;
    end
end
```